VOLUME 80 JUNE 3, 1976 NUMBER 12

JPCHAx

THE JOURNAL OF PHYSICAL CHEMISTRY

PUBLISHED BIWEEKLY BY THE AMERICAN CHEMICAL SOCIETY

THE JOURNAL OF

PHYSICAL CHEMISTRY

Published by the
AMERICAN CHEMICAL SOCIETY
BOOKS AND JOURNALS DIVISION
D. H. Michael Bowen, Director

Editorial Department: Charles R. Bertsch, Head; Marianne C. Brogan, Associate Head; Celia B. McFarland, Joseph E. Yurvati, Assistant Editors
Graphics and Production Department: Bacil Guiley, Head
Research and Development Department: Seldon W. Terrant, Head

Advertising Office: Centcom, Ltd., 50 W. State St., Westport, Conn. 06880.

Published biweekly by the American Chemical Society at 20th and Northampton Sts., Easton, Pennsylvania 18042. Second class postage paid at Washington, D.C. and at additional mailing offices.

Editorial Information

Instructions for authors are printed in the first issue of each volume. Please conform to these instructions when submitting manuscripts.

Manuscripts for publication should be submitted to *The Journal of Physical Chemistry*, Department of Chemistry, University of Minnesota, Minneapolis, Minn. 55455. Correspondence regarding **accepted papers and proofs** should be directed to the Editorial Department at the ACS Easton address.

Page charges of $60.00 per page are assessed for papers published in this journal. Ability to pay does not affect acceptance or scheduling of papers.

Bulk reprints or photocopies of individual articles are available. For information write to Business Operations, Books and Journals Division at the ACS Washington address.

Requests for **permission to reprint** should be directed to Permissions, Books and Journals Division at the ACS Washington address. The American Chemical Society and its Editors assume no responsibility for the statements and opinions advanced by contributors.

Subscription and Business Information

1976 Subscription rates—including surface postage

	U.S.	PUAS	Canada, Foreign
Member	$24.00	$29.75	$30.25
Nonmember	96.00	101.75	102.25
Supplementary material	15.00	19.00	20.00

Air mail and air freight rates are available from Membership & Subscription Services, at the ACS Columbus address.

New and renewal subscriptions should be sent with payment to the Office of the Controller at the ACS Washington address. **Changes of address** must include both old and new addresses with ZIP code and a recent mailing label. Send all address changes to the ACS Columbus address. Please allow six weeks for change to become effective. **Claims** for missing numbers will not be allowed if loss was due to failure of notice of change of address to be received in the time specified; if claim is dated (a) North America—more than 90 days beyond issue date, (b) all other foreign—more than 1 year beyond issue date; or if the reason given is "missing from files". Hard copy claims are handled at the ACS Columbus address.

Microfiche subscriptions are available at the same rates but are mailed first class to U.S. subscribers, air mail to the rest of the world. Direct all inquiries to Business Operations, Books and Journals Division, at the ACS Washington address or call (202) 872-4444. **Single issues** in hard copy and/or microfiche are available from Special Issues Sales at the ACS Washington address. Current year $4.75. Back issue rates available from Special Issues Sales. **Back volumes** are available in hard copy and/or microform. Write to Special Issues Sales at the ACS Washington address for further information. **Microfilm** editions of ACS periodical publications are available from volume 1 to the present. For further information, contact Special Issues Sales at the ACS Washington address. **Supplementary material** must be ordered directly from Business Operations, Books and Journals Division, at the ACS Washington address.

Microfiche	U.S.	PUAS, Canada	Other Foreign
Photocopy	$2.50	$3.00	$3.50
1–7 pages	4.00	5.50	7.00
8–20 pages	5.00	6.50	8.00

Orders over 20 pages are available only on microfiche, 4 × 6 in., 24X, negative, silver halide. Orders must state photocopy or microfiche if both are available. Full bibliographic citation including names of all authors and prepayment are required. Prices are subject to change.

American Chemical Society
1155 16th Street, N.W.
Washington, D.C. 20036
(202) 872-4600

Member & Subscription Services
American Chemical Society
P.O. Box 3337
Columbus, Ohio 43210
(614) 421-7230

Editorial Department
American Chemical Society
20th and Northampton Sts.
Easton, Pennsylvania 18042
(215) 258-9111

Notice to Authors last printed in the issue of January 1, 1976

THE JOURNAL OF
PHYSICAL CHEMISTRY

Volume 80, Number 12 June 3, 1976

JPCHAx 80(12) 1267–1392 (1976)

ISSN 0022-3654

COMMUNICATIONS TO THE EDITOR

■Supplementary and/or miniprint material for this paper is available separately (consult the masthead page for ordering information); it will also appear following the paper in the microfilm edition of this journal.

* In papers with more than one author, the asterisk indicates the name of the author to whom inquiries about the paper should be addressed.

AUTHOR INDEX

THE JOURNAL OF
PHYSICAL CHEMISTRY

VOLUME 80, NUMBER 12 JUNE 3, 1976

Yield and Decay of the Hydrated Electron from 100 ps to 3 ns

C. D. Jonah,* M. S. Matheson, J. R. Miller, and E. J. Hart

Chemistry Division, Argonne National Laboratory, Argonne, Illinois 60439 (Received November 3, 1975)

Publication costs assisted by Argonne National Laboratory

Energy is deposited by fast electrons in water in small localized volumes called spurs. The decay of the hydrated electron in a spur has been measured to be about 17% between 100 ps and 3 ns. Half of this decay occurs before 700 ps where previous techniques could not observe any decay. The principal reactions of the hydrated electron in the spur are presumed to be $e_{aq}^- + e_{aq}^-$, $e_{aq}^- + H^+$, and $e_{aq}^- + OH$. Scavengers for the hydrogen ion are about equally effective in slowing the decay as are scavengers for the hydroxyl radical except for OH^- which seems unusually effective. This suggests H^+ and OH are distributed similarly with respect to e_{aq}^-. Spur decay is also observed for the products of electron capture, Cd^+ or $RSSR^-$, where RSSR is cystamine. The observations reconcile different methods for measurement of the initial hydrated electron yield to 4.6 ± 0.2 molecules/100 eV, and combined with our earlier data, provide the major features of the history of e_{aq}^- in the spur from 100 ps to the achievement of a homogeneous distribution.

Introduction

For several years radiation chemists have been learning about the deposition of energy by ionizing radiation.[1] As experimental progress has been made in unraveling the processes of energy deposition, more and more detail is needed. It is clear that energy is deposited inhomogeneously.[2-5] For low linear energy transfer (LET) radiation, there are local volumes of energy deposition called spurs. The objective (from the view of radiation chemistry) is to know what species are present, their spatial distribution, and the reactions taking place between the various species.

In water, the primary species are thought to be e^-, H_2O^+, and H_2O^* (where the asterisk indicates an excited molecule). When one reaches chemical times ($\gtrsim 10^{-13}$ s) the species are H_{aq}^+, OH, e_{aq}^-, H, possibly H_2, and a reactive precursor of the hydrated electron, e_{dry}^-. In pure water, after spur reactions have taken place ($>10^{-7}$ s), H^+, OH, e_{aq}^-, H, OH^-, H_2, and H_2O_2 will be the predominant species. To understand the processes occurring which take us from the beginning of the chemical state until the end of spur reactions, we need to know the initial yields and time evolution of all of these species. The yields of each of these species have been measured at the homogeneous limit.[6] The yield of the hydrated electron has been determined at 2.7 ± 0.1 in the long time ($>10^{-7}$ s) limit.[6]

The decay to this limit for the hydrated electron has been determined by several groups starting less than 5 ns after a short pulse of ionizing radiation. All of these data are consistent with a yield of hydrated electrons at 1 ns of 4.1 ± 0.1 molecules/100 eV of energy absorbed. Also some data have been accumulated about the various reactions taking place through studying the time evolution of the hydrated electron with various reactions "turned off" by adding solutes which remove H_{aq}^+ or OH.[4,6,7] Yields at times only a few nanoseconds after the irradiation pulse have also been determined with solutes added, but the significance of these results is unclear since the changes from pure water are small (5%) and possible errors in the extinction coefficient could outweigh these differences.[4,6,7]

Another approach to studying mechanisms is through modeling the chemical reactions using diffusion kinetics.[8,9] Parameters are chosen for the number of radicals in the spur and the distribution of the radicals to give agreement with radiation chemical results. Recently, these calculations have been modified[9] to give good agreement with our data on the time evolution of the hydrated electron.

We have attempted to obtain further information on spur reaction mechanisms in pure water by studying the decay of the hydrated electron from 0.1 to 3 ns. The form of decay was also studied using H^+ and OH scavengers. Ethanol was used as the hydroxyl radical scanvenger, since the reactions are well known and the changes in diffusion in ethanol–water are known.[10,11] Sodium hydroxide, ammonia, and sodium acetate were used as the hydrogen ion scavengers.

Using the decay curves determined in this and earlier work[4] we have used G values for various times after energy deposition determined by ourselves and others to calculate G values at 100 ps.

Experimental Section

The picosecond pulse radiolysis equipment has been previously described in detail.[12] The Argonne microwave linear accelerator generates pulses of 20–22 MeV electrons 60 times per second. Each pulse consists of a main pulse containing greater than 90% of the charge with a width (fwhm) of 30 ps. As focussed for an experiment a single pulse deposited 1.5 krads (10^{17} eV/g) in the irradiated volume. Approximately 30% of the electron beam is intercepted by a cell containing 1 atm of xenon. The Cerenkov light generated by the xenon cell is used as the analyzing light. The remainder (70%) of the electron beam is used for radiolysis. Both the electron beam and the light beam are delayed. The delay of the light beam can be varied so that it reaches the irradiation cell before, during, or after the pulse. By varying the delay of the light beam the transmission of the sample as a function of time is determined.

To improve linearity changes were made in the previously described light detection system. The integrator-stretcher was replaced by a commercial charge sensitive FET preamplifier (Tennelec TC 162). The photomultiplier was an RCA C7253A, a five stage side-on photomultiplier. The primary nonlinearity problems were caused by the analyzing light and the light from the sample cell overlapping in time.[12] To test the system, the absorption of the system at 600 nm was measured in the presence of 4 M perchloric acid. It was assumed that the only absorption at 600 nm would be due to the electron so that any change in the absorption except during the decay of the electron (≈100 ps after the pulse) was assumed to be due to photomultiplier nonlinearity. (It might also be due to a transient decay of absorption in the cell windows.) The total change of the absorption from right after the pulse to 3 ns was less than 0.2% of the total transmission from which we infer that the system is very close to linear.

All chemicals were used as received since, on the experimental time scale, small amounts of impurities would have a negligible effect. Solutions were prepared with deionized or singly distilled water and were degassed by bubbling with helium for 15 min. Approximately 2 l. of solution were used in a recirculating flow system with a flow rate of 100 ml/min. An average run would last 15 min. This would generate 25–50 μM products at the end of the run.

Results and Discussion

Figure 1 shows the raw data as plotted by the computer. Figures 2 and 3 show relative concentration plots. All plots are normalized to one at 100 ps. This is done to facilitate comparison of the decay curves. We do not attempt to compare the yields of absorption, because the presence of added solutes changes the extinction coefficient of the hydrated electron and the amount of energy absorbed per unit volume. The corrections for these effects are too uncertain to make the comparison of yields useful. The curves in Figures 2 and 3 are derived from the data of the type shown in Figure 1 by plotting the log of the optical density as a function of time. The results are of the form shown in Figures 5 and 6. The second absorption step is removed by tracing the data and sliding the curve to match the sections before and after the small pulse. The relatively small absorption in the second pulse means almost all of the decay is due to reactions of hydrated electrons produced by the main pulse. Also, by plotting the log of the optical density,

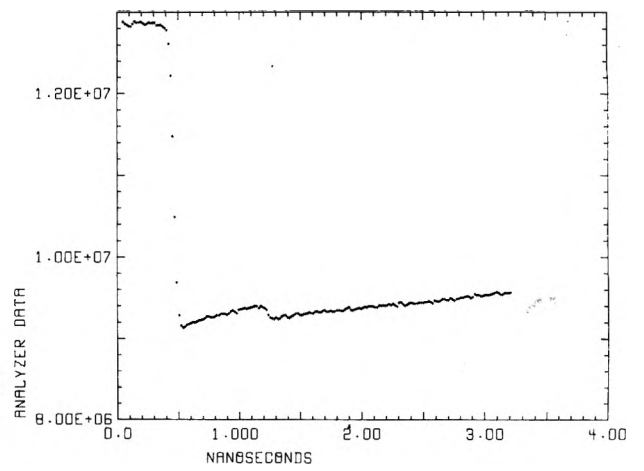

Figure 1. Untransformed output of experiment. The signal is proportional to transmission. 100% transmission corresponds to the level portion on the left. The small step 770 ps after the pulse arises from a small satellite pulse.

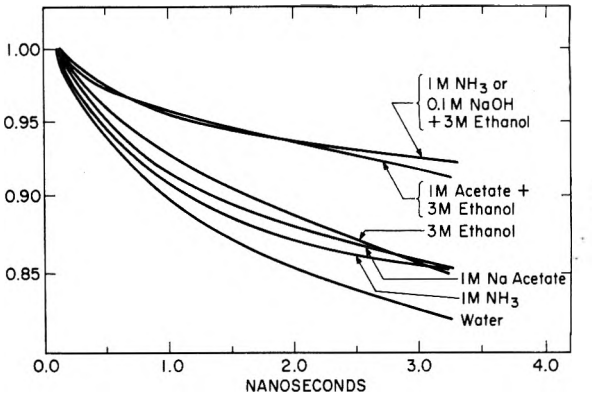

Figure 2. Decay of the hydrated electron in water, 3 M ethanol, 1 M ammonia, 1 M sodium acetate, 3 M ethanol plus 1 M sodium acetate, 3 M ethanol plus 1 M ammonia, and 3 M ethanol plus 0.1 M sodium hydroxide.

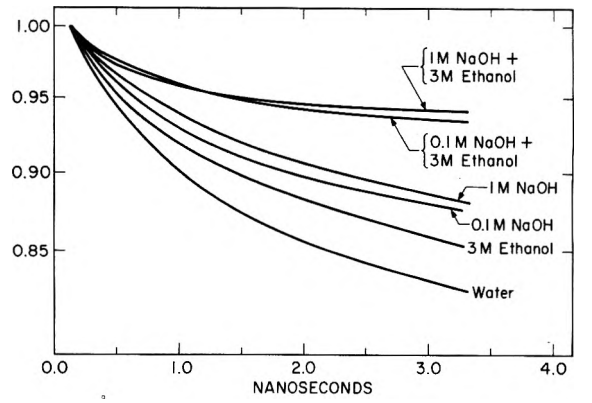

Figure 3. Decay of the hydrated electron in water, 3 M ethanol, 0.1 or 1 M sodium hydroxide, and 3 M ethanol plus 0.1 or 1 M sodium hydroxide.

the effect of the small pulse is decreased even further. The vertical axis in Figures 2 and 3 is not linear but is logarithmic which does not vary greatly from linearity over the range. Differences between curves run on different days are less than 0.5%.

Previously published experimental data for the decay of the

hydrated electron have shown no decay for the hydrated electron within experimental error in the time windows of 20–350 ps or 0.1–1 ns.[4,13,14] The approximately 10% decay which we measure from 0.1 to 1 ns is within the risetime and settling time of our photodiode system (see, for example, Figure 2 of ref 4). We have also been informed that the 3% change in absorbance which we measure from 100 to 350 ps is within the experimental error of the Toronto group.[15] We do not have the capability to go to shorter times so no statement can be made about times earlier than 100 ps.

The major reactions of the hydrated electron in the spur are:

$$e_{aq}^- + H^+ \xrightarrow[1.5 \times 10^{10}]{10^{16}} H \quad (1)$$

$$e_{aq}^- + OH \xrightarrow[3 \times 10^{10}]{10^{17}} OH^- \quad (2)$$

$$e_{aq}^- + e_{aq}^- \xrightarrow[5 \times 10^{9}]{2H_2O\ 10^{17}} H_2 + 2OH^- \quad (3)$$

To study the relative distribution of the radicals as originally formed it would be advantageous to study each reaction by itself. By adding scavengers for H^+ and/or OH reactions 1 and/or 2 may be suppressed.

In 3 M ethanol, the half-life of the hydroxyl radical is about 125 ps. The half-life of the hydrogen ion is 5 and 50 ps in 1 and 0.1 M sodium hydroxide and 30 ps in 1 M ammonia or sodium acetate.[18] Most of the differences between the decay of the electron in the aqueous solutions shown in Figures 2 and 3 occur at times after the primary products we are attempting to scavenge have been eliminated.

In Figure 2 one sees that the decays of e_{aq}^- in 3 M ethanol, 1 M ammonia, or 1 M sodium acetate are reasonably similar (±1% of the concentration of the electron). This implies that OH and H^+ in the spur react equally with the electron. Since the rate constants for reaction of H^+ and OH with the hydrated electron are similar (within a factor of 2), their distributions relative to the electron must be similar. Such a similarity of distribution would be expected for H^+ and OH formed by the fast reaction $H_2O^+ + H_2O \rightarrow H_3O^+ + OH$. (At these short times in the spur, diffusion kinetic calculations show very little difference for the hydrated electron when either H^+ or OH is scavenged if their distributions are identical despite the difference in rate constants implying that the distribution is the more important effect.)

In examining Figure 2, the scavenging of both H^+ and OH is more than twice as effective as scavenging only one of these species. This result can be expected, since, if an electron were "fated" to react with a hydroxyl radical and the radical were not there, it still might react slightly later with the hydrogen ion.

We have carried out diffusion kinetic calculations using the parameters of Kuppermann[9] for water and for hydrogen ion and/or hydroxyl radical scavenging. We find faster decay in our experimental data than in the calculations when scavengers are present. (As graphed in Figure 2 water 0.83 expt, 0.83 calcd; one scavenger 0.86 expt, 0.90 calcd; and two scavengers 0.93 expt, 0.98 calcd. These differences are outside experimental error.) We have not attempted to fit experimental data with the calculations. However, the greater experimental decay might occur in the larger spurs or "short tracks" or it could arise from a lack of a random distribution in the spur.

In Figure 3, the effects of sodium hydroxide and ethanol on e_{aq}^- decays are shown. The difference between the 0.1 and the 1.0 M sodium hydroxide is probably not significant. Sodium hydroxide is clearly more effective in reducing the e_{aq}^- spur decay than are other H^+ scavengers. We have at present no explanation for this unexpected result. The similarity between the 1 and 0.1 M sodium hydroxide eliminates the possibility that the reaction

$$OH^- + H \rightarrow e_{aq}^- \quad (4)$$

gives delayed formation of e_{aq}^- and therefore less apparent decay than is seen with other hydrogen ion scavengers. If G_H were 1 and if no H were lost through side reactions, a 1% difference at 3 ns would be expected with 1 M NaOH. The 0.1 M NaOH would be 1/10 as much. Many possible explanations could be considered for these data. For instance, it could be an excited water molecule reacting with OH^- to generate e_{aq}^- or the OH^- could be eliminating a loss pathway (a dry hole?).

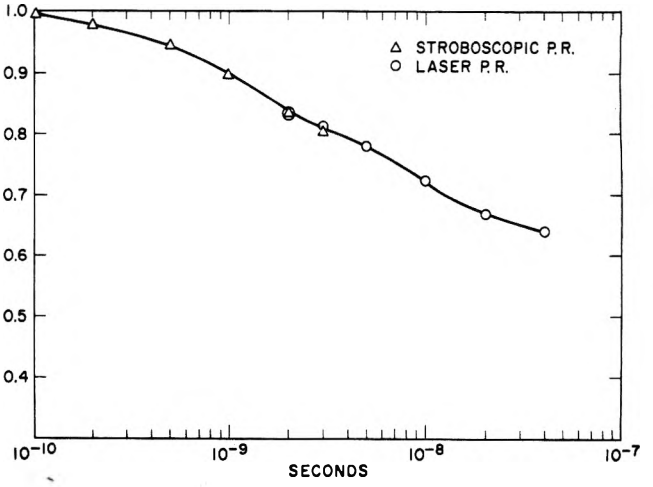

Figure 4. Decay of the hydrated electron in the spur from 100 ps to 40 ns.

TABLE I

Yield	Time, ns	Yield at 100 ps	Ref
3.2	10–15	4.4–4.6	2
4.1	1	4.55	4
3.6	7.5[a]	4.8	5
3.8	2[a]	4.8	19

[a] Time quoted is from end of a 5-ns pulse.

In Figure 4 we have plotted the relative concentration of the hydrated electron as a function of time from 100 ps to 40 ns using the results of Figure 2 as well as the data from our laser pulse radiolysis system. We have used Figure 4 to estimate $G_{e_{aq}^-}$ at 100 ps from measurements reported in the literature using nanosecond pulse radiolysis.[2,5,19] The estimates are listed in Table I. There seems to be fair agreement that the G value is 4.6 ± 0.2 molecules/100 eV. The yield measurements of ref 2, 5, and 19 did not correspond to definite times because of the finite pulse widths used. The estimates in Table I include small corrections for this problem. We have also had to critically reevaluate the time at which our value of 4.1 ± 0.1 was measured.[4] Little concern was given to the time the G value was measured when the experiments were done since it was thought there was no decay before 1 ns. The ~200 ps mentioned clearly was in error since the settling time was cited as 500 ps. After examining original data we feel 1 ns is a reasonable time. If we used 500 psec the G value would be 4.4.

The value from Table I is higher than the value of 4.0 molecules/100 eV at 30 ps previously determined by Hunt and

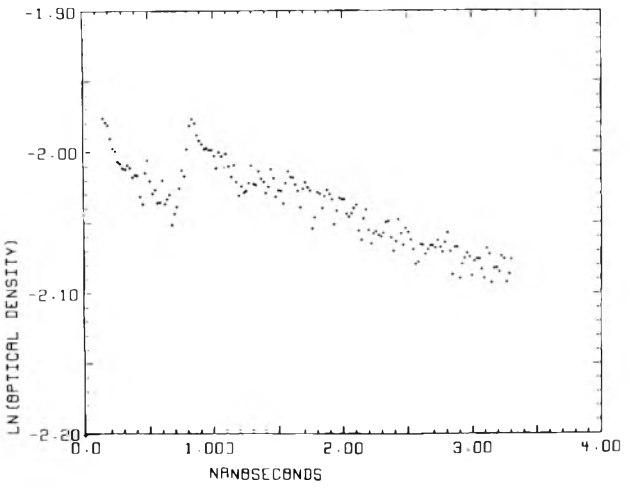

Figure 5. Decay of the absorption at 315 nm of Cd^+ formed in the irradiation of 1 M cadmium perchlorate.

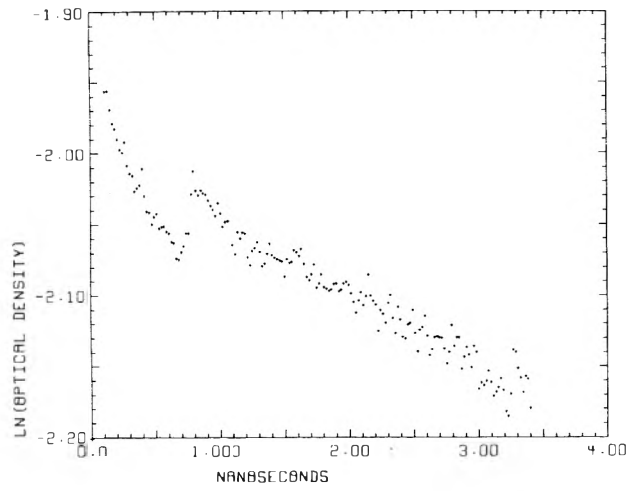

Figure 6. Decay of the absorption at 410 nm of the cystamine anion formed in the irradiation of 2 M cystamine.

coworkers.[7,14] Their results are based on measurements using the stroboscopic pulse radiolysis system.[14] Later experiments[7] measured the yields at 100 ns of either Cd^+ from the irradiation of 1 M $CdClO_4$ or of $RSSR^-$ from the irradiation of 2 M cystamine. (They also measured the yield at 30 ps and 6 ns but these measurements are dependent on the G value assumed for the electron at 30 ps.) These experiments can be interpreted to be consistent with the 4.0 value if one assumes, as they did, that there is no decay of the product species, Cd^+ or $RSSR^-$.

To check the validity of their assumptions, we have measured the product decay in 1 M $Cd(ClO_4)_2$ and 2 M cystamine on the time scale of 100–3000 ps. These data are displayed in Figures 5 and 6. It is clear that there is some spur decay. From these data and the data in ref 7 (methods 1 and 3), their scavenger data are consistent with an e_{aq}^- yield of 4.6 and a dry electron yield of 5.4. This interpretation is reinforced by the scavenger data using cadmium in the presence of *tert*-butyl alcohol where a G value for the dry electron of 5.5 was found.[20]

We feel that several methods are now in agreement to establish that the yield of hydrated electrons in water is 4.6/100 eV at 100 ps. The only data in disagreement with this value are the measurements of the Hunt group[14] and we do not know the reason for the difference.

Conclusions

We have determined the G value for the hydrated electron at 100 ps to be 4.6 ± 0.2 molecules/100 eV. If we use this value with the data of Wolff et al.[14] we derive a value for the yield of dry electrons of 5.4 molecules/100 eV. We have also established the spur decay of e_{aq}^- from 100 ps to homogeneous distribution.

The decay data have shown that H^+ and OH must be relatively similarly distributed relative to the hydrated electron. These data will act as a new test on theoretical calculations.

The decay of the electron is slower in the presence of sodium hydroxide than in the presence of other H^+ scavengers. Further work is needed to identify whether any presently suggested explanation is adequate or whether an as yet unknown process is required.

Acknowledgment. Work performed under the auspices of the U.S. Energy Research and Development Administration.

We are grateful for the assistance of Lee Rawson, Don Ficht, and Benno Naderer who ran the accelerator, when it ran, and got it running when it felt lazy. It is a pleasure to acknowledge the invaluable assistance of Robert M. Clarke in running these experiments.

References and Notes

(1) E. J. Hart and M. Anbar, "The Hydrated Electron", Wiley-Interscience, New York, N.Y., 1970.
(2) J. K. Thomas and R. V. Bensasson, *J. Chem. Phys.*, **46**, 4147 (1967).
(3) G. A. Kenney and D. C. Walker, *J. Chem. Phys.*, **50**, 4074 (1969).
(4) C. D. Jonah, E. J. Hart, and M. S. Matheson, *J. Phys. Chem.*, **77**, 1838 (1973).
(5) G. V. Buxton, *Proc. R. Soc. London, Ser. A.*, **328**, 9 (1972).
(6) I. G. Draganic and Z. D. Draganic, "The Radiation Chemistry of Water", Academic Press, New York, N.Y., 1971.
(7) R. K. Wolff, J. E. Aldrich, T. L. Penner, and J. W. Hunt, *J. Phys. Chem.*, **79**, 210 (1975).
(8) H. A. Schwartz, *J. Phys. Chem.*, **73**, 1928 (1969).
(9) "Diffusion Kinetics in Radiation Biology: An Assessment", A. Kuppermann, in "Physical Mechanisms in Radiation Biology", R. D. Cooper and R. W. Wood, Ed., Technical Information Center, Office of Information Services, U.S. Atomic Energy Commission, 1974.
(10) H. O. Spivey and T. Shedlovsky, *J. Phys. Chem.*, **71**, 2165 (1967).
(11) F. Barat, L. Gilles, B. Hickel, and B. Lesigne, *J. Phys. Chem.*, **77**, 1711 (1973).
(12) C. D. Jonah, *Rev. Sci. Instrum.*, **46**, 62 (1975).
(13) J. W. Hunt, R. K. Wolff, M. J. Bronskill, C. D. Jonah, E. J. Hart, and M. S. Matheson, *J. Phys. Chem.*, **77**, 425 (1973).
(14) R. K. Wolff, M. J. Bronskill, J. E. Aldrich, and J. W. Hunt, *J. Phys. Chem.*, **77**, 1350 (1973).
(15) J. W. Hunt, private communication.
(16) This value is lower than the generally accepted value, since the ionic strength in the spur is relatively high.
(17) M. Anbar, M. Bambenek, and A. B. Ross, *Natl. Stand. Ref. Data Ser., Natl. Bur. Stand.*, **No. 43.**
(18) M. Eigen, W. Kruse, G. Maass and L. DeMaeyer, *Prog. React. Kinet.*, **2**, 287 (1963).
(19) G. V. Buxton, private communication.
(20) C. Stradowski, private communication.

Rates of Electron-Transfer Reactions between Tetracyanoquinodimethane Anion Radical and Substituted *p*-Benzoquinones in Acetonitrile

Akihiko Yamagishi

Department of Chemistry, Faculty of Science, Hokkaido University, Sapporo, 060, Japan *(Received September 5, 1975)*

The reversible electron-transfer reactions between the tetracyanoquinodimethane (TCNQ) anion radical and three kinds of substituted *p*-benzoquinones in acetonitrile have been studied, using a temperature-jump technique. The following forward and backward rate constants ($\vec{k}$ and $\overleftarrow{k}$, respectively) have been determined at 25 ± 2 °C: $TCNQ^-$/*p*-chloranil, $\vec{k} = (5 \pm 2) \times 10^6$ M^{-1} s^{-1}, $\overleftarrow{k} = (2.0 \pm 0.8) \times 10^9$ M^{-1} s^{-1}; $TCNQ^-$/2,3-dicyano-*p*-benzoquinone, $\vec{k} = (1.9 \pm 0.8) \times 10^9$ M^{-1} s^{-1}, $\overleftarrow{k} = (7 \pm 3) \times 10^7$ M^{-1} s^{-1}; $TCNQ^-$/2,3-dichloro-5,6-dicyano-*p*-benzoquinone, $\vec{k} = (5.0 \pm 2.0) \times 10^9$ M^{-1} s^{-1}, $\overleftarrow{k} = (1 \pm 0.6) \times 10^4$ M^{-1} s^{-1}. The measured rate constants are compared with the Marcus electron-transfer theory.

Introduction

The electron-transfer reactions involving organic ion radicals are of interest as examples of the simplest sort of oxidation–reduction reactions of organic molecules. ESR line-shape measurements have been extensively applied to determine the rates of electron exchange between an ion radical and its parent molecule.[1]

$$R^+ \text{ (or } R^-) + R \rightleftharpoons R + R^+ \text{ (or } R^-) \quad (1)$$

As for the electron-transfer reactions between an ion radical and a different kind of neutral molecule

$$R_1^+ \text{ (or } R_1^-) + R_2 \rightleftharpoons R_1 + R_2^+ \text{ (or } R_2^-) \quad (2)$$

the ESR method is confronted with the difficulty that the lifetime of a paramagnetic species is affected not only by the electron-transfer reaction (2) but also by electron exchange (1). This situation makes it extremely difficult to estimate the rates of electron-transfer reactions from the line-shape analysis. Therefore, few attempts have been reported to determine the rates of reaction 2 using the ESR method.[2]

As exemplied by previous studies concerning organic cation radicals, the temperature-jump method is most suitable for the study of rapid reversible reactions such as eq 2.[3] This paper reports the results of the investigation of the electron-transfer reactions between the tetracyanoquinodimethane (TCNQ) anion radical and three kinds of substituted *p*-benzoquinones in acetonitrile. The observed dependence of a rate constant on the free energy change of reaction is compared with the well-known Marcus electron-transfer theory.

Experimental Section

TCNQ, *p*-chloranil (QCl_4), and 2,3-dichloro-5,6-dicyano-*p*-benzoquinone ($QCl_2(CN)_2$) purchased from Tokyo Kasei were sublimed once. Tetraethylammonium (NEt_4^+) salts of these compounds were prepared by reduction with NEt_4I in acetonitrile. Reagent Grade acetonitrile supplied from Wako Pure Chemical Industries was dried over $CaCl_2$, refluxed over P_2O_5, distilled through a distillation column of about 30 cm length, and finally distilled over $CaSO_4$ (water content, 0.5 mg/ml). NEt_4ClO_4 was prepared by adding 1 N $HClO_4$ to a 10% NEt_4OH aqueous solution supplied from Wako Pure Chemical Industries. The sodium salt of 2,3-dicyano-*p*-benzoquinone ($Q(CN)_2$) was kindly donated by Dr. Y. Iida.

The visible spectra were measured with a Hitachi EPS-3T spectrophotometer.

Rate measurements were made with a Union Giken temperature-jump apparatus. This apparatus uses a coaxial cable of 0.02 μF and 200 m length as capacitor.[4] The relaxation was monitored spectrophotometrically by the transmittance change at 740 nm (λ_{max} of $TCNQ^-$). By following the dimerization reaction of $QCl_2(CN)_2^-$, it was assured that the 90% temperature rise was attained within 3 μs for an acetonitrile solution containing 2×10^{-3} M NEt_4ClO_4 as supporting electrolyte.[5] Thus the rates were obtained in presence of $2–5 \times 10^{-5}$ M NEt_4ClO_4.

Results

Equilibrium Measurements. The equilibrium constant of

$$TCNQ^- + Q \rightleftharpoons TCNQ + Q^- \quad (3)$$

is expressed as

$$K = [TCNQ][Q^-]/[TCNQ^-][Q]$$

where Q is a substituted *p*-benzoquinone. In acetonitrile, all anion radicals are assumed to dissociate completely under the condition that the concentration of supporting electrolyte is less than 5×10^{-3} M. In case of $QCl_2(CN)_2^-$, this assumption was previously verified by conductivity measurements.[5]

For $TCNQ^-$/QCl_4, a known amount of QCl_4 is added to a $NEt_4^+TCNQ^-$ solution. The concentrations of QCl_4^- and TCNQ which are produced by eq 3 are equated to the decrease of $[TCNQ^-]$ when QCl_4 is added. The concentration of $TCNQ^-$ is determined using an extinction coefficient ϵ_{840} of 43 300.[6] The gradual decomposition of QCl_4^- in acetonitrile causes about 30% error in determining the equilibrium constant.

For $TCNQ^-$/$Q(CN)_2$, a known amount of TCNQ is added to a $Na^+Q(CN)_2^-$ solution. The concentration of $Q(CN)_2^-$ is determined using an extinction coefficients, ϵ_{590} 4000.[7] The decrease of the concentration of $Q(CN)_2^-$ is equated to the concentration of $Q(CN)_2$.

For $TCNQ^-$/$QCl_2(CN)_2$, a known amount of $QCl_2(CN)_2$ is added to the solution of $TCNQ^-$ containing a large ex-

TABLE I: Equilibrium Constants of Reaction 3

Q	K	$\Delta F°$, kcal mol^{-1}	$\Delta H°$, kcal mol^{-1}	$\Delta E_{1/2}$, kcal mol^{-1} [a]
$Q(CN)_2$	27.2 ± 3 (20 °C)	−1.9		−2.8
QCl_4	(2.6 ± 0.8) × 10^{-3} (25 °C)	+3.6		+4.1
$QCl_2(CN)_2$	(5.9 ± 0.8) × 10^5 (30 °C)	−8.0	−7.6 ± 1.5	−7.4

[a] The difference of the half-wave reduction potential between TCNQ and Q: $E_{1/2}$(TCNQ) = −0.19 V, $E_{1/2}(QCl_4)$ = −0.01 V, $E_{1/2}(Q(CN)_2)$ = −0.31 V, and $E_{1/2}(QCl_2(CN)_2)$ = −0.50 V in MeCN.[8-10]

cess of TCNQ and $NEt_4^+QCl_2CN_2^-$. The concentration of $QCl_2(CN)_2$ is equated to

$$[QCl_2(CN)_2] = [QCl_2(CN)_2]_0 - [TCNQ^-]_0 + [TCNQ^-]$$

where $[QCl_2(CN)_2]_0$ and $[TCNQ^-]_0$ are the added concentration of $QCl_2(CN)_2$ and the initial concentration of $TCNQ^-$, respectively. The concentration of $QCl_2(CN)_2^-$ is determined using an extinction coefficient ϵ_{575} of 6300.[7] The concentration of TCNQ is equated to the initial value, since this species is present in large excess over other components. Knowing the concentrations of all species in this way, the equilibrium constants are calculated.

The results are summarized in Table I. The free energy change of reaction 3, $\Delta F°$, is calculated from the equilibrium constants according to

$$-\Delta F° = RT \ln K$$

$\Delta F°$ is compared with $\Delta E_{1/2}$, the difference of the polographic half-wave reduction potential between TCNQ and substituted quinone

$$\Delta E_{1/2} = E_{1/2}(Q) - E_{1/2}(TCNQ)$$

in which $E_{1/2}$(TCNQ) and $E_{1/2}(Q)$ are the half-wave reduction potentials of TCNQ and substituted p-benzoquinone, respectively. As shown in Table I, $\Delta F°$ obtained in the present work agrees well with $\Delta E_{1/2}$. The table also includes the enthalpy change, $\Delta H°$, for $TCNQ^-/QCl_2(CN_2)$, which is obtained from the temperature dependence of K from 11 to 35 °C. $\Delta H°$ is almost equal to $\Delta F°$, implying that the entropy change for the $TCNQ^-/QCl_2(CN)_2$ system is small. This result may lead to the conclusion that the solvation structure of $TCNQ^-$ is not very different from that of $QCl_2(CN)_2^-$, since the solvation process contributes a great deal to an entropy term.[11]

Measurements of Rates. The rates of reaction 2 are measured with a temperature-jump apparatus. For the $TCNQ^-/Q(CN)_2$ system, a decrease of transmittance is observed at 740 nm after the temperature rise. The synchronous increase of transmittance is observed at 590 nm. These correspond to the concentration changes of $TCNQ^-$ and $Q(CN)_2^-$ caused by the relaxation due to reaction 3. The pseudo-first-order rate constant, k_{obsd}, defined as

$$-d\Delta[TCNQ^-]/dt = k_{obsd}\Delta[TCNQ^-]$$

is related to the forward and backward rate constants of reaction 3, $\vec{k}$ and $\overleftarrow{k}$, respectively, as below.

$$k_{obsd} = \vec{k}\{[TCNQ^-]_e + [Q(CN)_2]_e\} + \overleftarrow{k}\{[TCNQ]_e + [Q(CN)_2^-]_e\} \quad (4a)$$

where the subscript e denotes an equilibrium concentration for the quantity in brackets after the temperature rise. Since the equilibrium measurements are more accurate

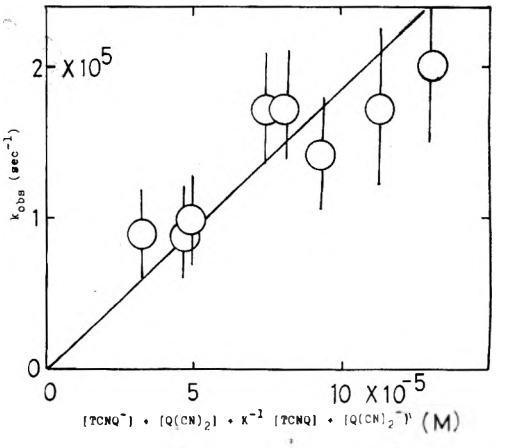

Figure 1. The dependence of k_{obsd} on $\{[TCNQ^-] + [Q(CN)_2] + K^{-1}\{[TCNQ] + [Q(CN)_2^-]\}$ according to eq 4b. Temperature is 25 ± 2 °C. The slope of the straight line gives $\vec{k}$.

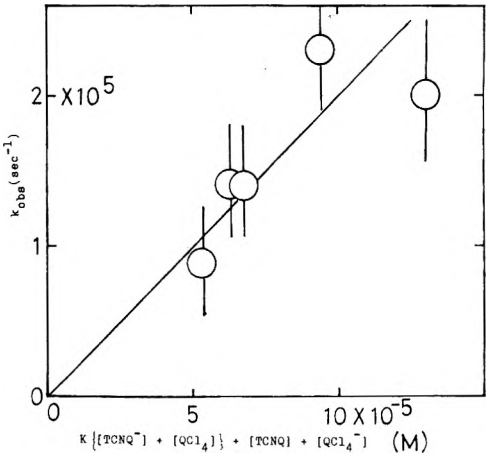

Figure 2. The dependence of k_{obsd} on $[K\{[TCNQ^-] + [QCl_4]\} + [TCNQ] + [QCl_4^-]]$. The slope of the straight line gives $\vec{k}$.

than the rate measurements, the following relation is used in determining the rate constants instead of (4a):

$$k_{obsd} = \vec{k}[[TCNQ^-]_e + [Q(CN)_2]_e + K^{-1}\{[TCNQ]_e + [Q(CN)_2^-]\}] \quad (4b)$$

In Figure 1, k_{obsd} is plotted against the quantity, $[TCNQ^-]_e + [Q(CN)_2]_e + K^{-1}\{[TCNQ]_e + [Q(CN)_2^-]_e\}$. $\vec{k}$ is determined from the slope of the straight line passing through an original point. $\overleftarrow{k}$ is calculated using the relation $K = \vec{k}/\overleftarrow{k}$. The rate constants for $TCNQ^-/QCl_4$ and $TCNQ^-/QCl_2CN_2$ are obtained similarly (Figures 2 and 3). The results of the rate measurements are summarized in Table II.

Discussion

The present results show that the rate constant with the

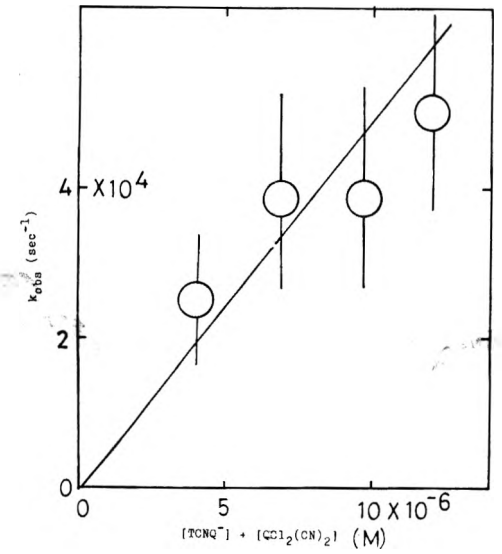

Figure 3. The dependence of K_{obsd} on $[[TCNQ^-] + [QCl_2(CN)_2]]$ according to eq 4a. Temperature is 25 ± 2 °C. The second terms in eq 4a is negligible. The slope of the straight line gives k.

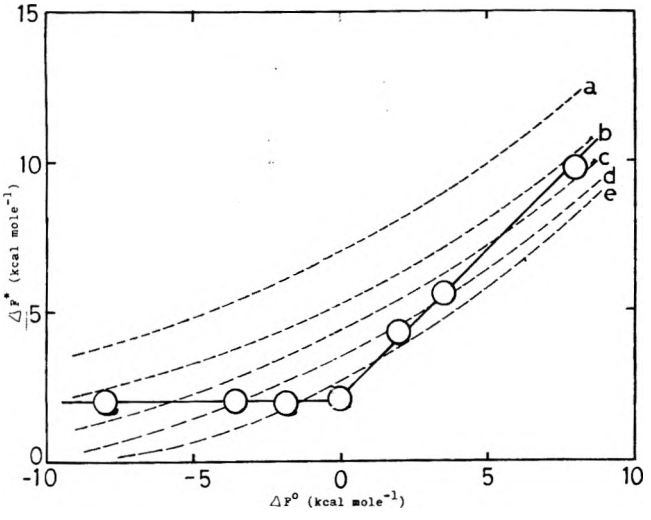

Figure 4. The relation between the rate constants and the free energy changes of reaction. The solid curve is an observed one. The dotted curves are calculated according to the Marcus theory at the assumed effective radii: $a_1 = a_2$ = (a) 3, (b) 4, (c) 5, (d) 6, and (e) 8 Å, respectively.[13] The experimental point at $\Delta F° = 0$ corresponds to the electron exchange of the $TCNQ^-/TCNQ$ system.[12]

negative free energy change of reaction, $\Delta F° < 0$, is close to a diffusion-controlled limit. Thus the activation free energy of reaction 3 in the direction of decreasing $\Delta F°$ is estimated to be less than 2.0 kcal mol^{-1}, the activation energy for diffusion in acetonitrile.[12] On the other hand, the reaction with the positive free energy change, $\Delta F° > 0$, has a definite value of activation free energy, which is obtained from the equation

$$k = Z \exp(-\Delta F^*/RT)$$

in which Z is the frequency of collision, 10^{11} M^{-1} s^{-1}. ΔF^* thus estimated is plotted against $\Delta F°$ in Figure 4.

The present systems provide both the rate constant and the free energy change of reaction rigorously determined under the same condition. It is, therefore, interesting to compare the present results with the Marcus theory of electron-transfer reaction.[13] There is some ambiguity in the effective radii of reactants, a_1 and a_2, since both TCNQ and substituted p-quinones (Q) are quite flat in shape (TCNQ 3 × 9 × 9 Å, Q 3 × 8 × 9 Å). Therefore ΔF^* are calculated at five probable values of a_1 and a_2; $a_1 = a_2 = 3$, 4, 5, 6, and 8 Å (Figure 4).

TABLE II: Rate Constants of Reaction 3 at 25 °C

Q	$\vec{k}$, M^{-1} s^{-1}	$\overleftarrow{k}$ M^{-1} s^{-1}
$Q(CN)_2$	$(1.9 \pm 0.8) \times 10^9$	$(7 \pm 3) \times 10^7$
QCl_4	$(5 \pm 2) \times 10^6$	$(2.0 \pm 0.8) \times 10^9$
$QCl_2(CN)_2$	$(5 \pm 2) \times 10^9$	$(1 \pm 0.6) \times 10^4$

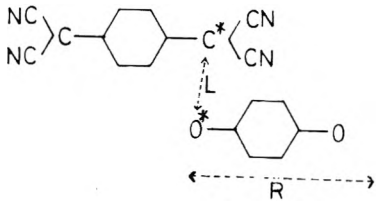

Figure 5. An assumed model of the activated state.

It is apparent that the theory predicts the observed dependence of ΔF^* on $\Delta F°$ in a poor manner at any value of the effective radii. Although one may assume that the effective radii vary from one reacting pair to another, this is improbable on the basis of the touching sphere model. The present results may be rationalized in terms of the more elaborate model for the activated complex. For example, when an electron transfer takes place between two active sites which are embedded in a large dielectrically saturated region, the reorganization parameter, λ, is expressed by

$$\lambda = (\Delta e)^2 \left(\frac{L^2}{3R^3}\right) (1/D_{op} - 1/D_s) \qquad (5)$$

where L is a distance between two active sites and R the effective radius of the dielectrically saturated region.[14] In the present system, one active site may be a carbon atom with a high spin density in $TCNQ^-$, C*, and the other an oxygen atom with high electronegativity in a substituted quinone, O* (Figure 5). Since λ is a function of higher orders of L and R, it will change a great deal for the small change of R and L. Accordingly this modification leads to the variation of λ for one reacting pair to another.

It should be noted that the expression for ΔF^* is derived under the assumption of negligible electronic interaction. However, it is likely that $TCNQ^-$ interacts with substituted p-benzoquinones sufficiently enough to lower such a potential barrier as expected from the theory. Thus the possibility of electronic interaction may also explain the present results that there exists no activation free energy in the direction of the negative free energy change of reaction.

Acknowledgments. The author thanks Professor Masatoshi Fujimoto for his continuous encouragement. Dr. Mitsuyuki Soma made a number of helpful suggestions and it is a pleasure to thank him also. Thanks are also due to Dr. Yoichi Iida for presenting the material.

Appendix

λ is expressed by[13]

$$\lambda = \frac{1}{8\pi} \int (E_c^* - E_c)^2 (1/D_{op} - 1/D_s)\, dV \qquad (6)$$

where E_c^* and E_c are the electric fields which charged reactants and charged products would exert if they were in vacuo, respectively. Under the assumption that C* in TCNQ and O* in Q are charged to be C^{*-} and O^{*-} before and after an electron jump, respectively, $E_c^* - E_c$ is equal to the electric field due to a dipole moment, O*C*. Thus at the point (r, θ)

$$(E_c^* - E_c)^2 = \left(\frac{2(\Delta e)L}{r^3}\cos\theta\right)^2 + \left(\frac{(\Delta e)L}{r^3}\sin\theta\right)^2$$

Substituting this into (6) and integrating the space outside of the sphere with a radius R, eq 5 results.

References and Notes

(1) For the review of the recent progresses, N. Hirota, "Radical Ions", E. T. Kaiser and L. Kevan, Ed., Interscience, New York, N.Y., 1988, p 35.
(2) K. Suga and S. Aoyagi, *Bull. Chem. Soc. Jpn.*, **46**, 755 (1973).
(3) A. Yamagishi, *Chem. Lett.*, 595 (1975).
(4) G. W. Hoffman, *Rev. Sci. Instrum.*, **42**, 1643 (1971).
(5) A. Yamagishi, *Bull. Chem. Soc. Jpn.*, **48**, 2440 (1975).
(6) L. R. Melby, R. J. Harder, W. R. Hertler, W. Mahler, R. E. Benson, and W. E. Mochel, *J. Am. Chem. Soc.*, **84**, 3374 (1962).
(7) Y. Iida, *Bull. Chem. Soc. Jpn.*, **44**, 1777 (1971).
(8) M. E. Peover, *Trans. Faraday Soc.*, **58**, 2370 (1962).
(9) R. M. Scribner, *J. Org. Chem.*, **31**, 3671 (1966).
(10) M. E. Peover, *J. Chem. Soc.*, 4540 (1962).
(11) A. J. Parker, *Quart. Rev., Chem. Soc.*, **16**, 163 (1962).
(12) M. A. Komarynsky and A. C. Wahl, *J. Phys. Chem.*, **79**, 695 (1975).
(13) R. A. Marcus, *J. Chem. Phys.*, **43**, 3477 (1965).
(14) See Appendix.

Radiation Decomposition of *p*-Nitroperoxybenzoic Acid in Solution

Edgar Heckel

Department of Chemistry, East Carolina University, Greenville, North Carolina 27834

(Received September 25, 1975)

Publication costs assisted by the Research Council of East Carolina University

p-Nitroperoxybenzoic acid is reduced by carboxyl radical anions which arise from the interaction of ·OH with formic acid or formate ions at pH >3. The resulting electron adduct of *p*-nitroperoxybenzoic acid (I) eliminates an ·OH radical which subsequently propagates a chain reaction. The inverse square-root law for the dose rate has been confirmed for the chain process. G values >200 were observed for the decomposition of the peroxy acid. An activation energy of 2.7 kcal mol^{-1} has been attributed to the elimination of ·OH from radical anion I. 2-Hydroxyl-2-propyl radicals, formed through hydrogen abstraction from 2-propanol by ·OH, also sustain a chain reaction in solutions of *p*-nitroperoxybenzoic acid, but the kinetic chain length is considerably reduced in comparison with reactions of carboxyl radical anions.

Introduction

In a recent study on the pulse radiolytic decomposition of *p*-nitroperoxybenzoic acid in N_2O saturated aqueous solutions,[1] a chain reaction was observed when isopropyl alcohol was present in the irradiated mixtures. The chain reaction is caused by 2-hydroxy-2-propyl free radicals which arise from the interaction of ·OH with the alcohol under formation of reactive α-hydroxy radicals.[2] The 2-hydroxy-2-propyl radical is known to transfer an electron to acceptors such as nitro compounds[3-5] and hexacyanoferrate(III).[6] The radical anion resulting from the electron transfer to *p*-nitroperoxybenzoic acid eliminates an ·OH radical and forms *p*-nitrobenzoate anion. The ·OH radical subsequently propagates the kinetic chain.

Any compound which efficiently reacts with ·OH forming a species of reducing properties (such as the 2-hydroxy-2-propyl free radical) may sustain a chain reaction in the radiation-induced decomposition of *p*-nitroperoxybenzoic acid. The reactions of formic acid (formate anion) with ·OH radicals and the electron transfer capability of the resulting carboxyl radical in aqueous solutions have been well established.[2,7-11] Therefore we considered it worthwhile to investigate by steady state γ radiolysis the chain reaction mechanism of the decomposition of *p*-nitroperoxybenzoic acid in greater detail using both formic acid and isopropyl alcohol. The results of this study are presented in this paper.

Experimental Section

p-Nitroperoxybenzoic acid was synthesized by the method of Silbert, Siegel, and Swern (which employs 90% hydrogen peroxide and *p*-nitrobenzoic acid; purity 99.5%).[12] Aqueous solutions of 1.6×10^{-3} M *p*-nitroperoxybenzoic acid were prepared and oxygen was removed by bubbling argon through the solutions. Simultaneously oxygen was removed from 45 ml of pH adjusted solution (H_3PO_4/NaOH or $HClO_4$/NaOH mixtures of approximately 0.2 M total solute concentration) by the same technique. The latter solution was then saturated with N_2O (2×10^{-2} M) and 5 ml of 1.6×10^{-3} M peroxy acid solution was added. Nitrous oxide bubbled for 3 min more through the mixture. Portions (4 ml) were transferred to small vials where each sample was again exposed for 30 s to N_2O before the vials were tightly sealed by screw caps.

The samples were irradiated in a 400 Ci Cs-137 γ source (Radiation Machinery Corp.) up to 5 min at a dose rate of 3.1×10^{16} eV g^{-1} s^{-1}. Samples irradiated below or above room temperature were either cooled in ice–water mixtures or heated in warm water just until irradiation. These samples were insulated with asbestos jackets to maintain constant

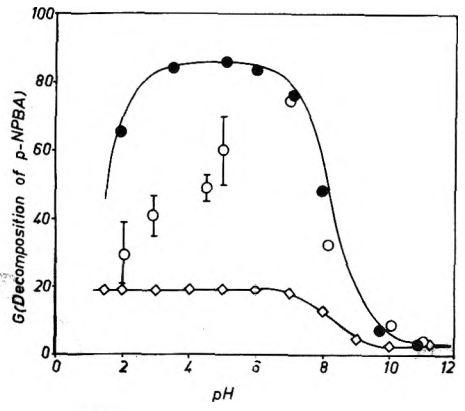

Figure 1. The pH dependence of the G value for the decomposition of *p*-nitroperoxybenzoic acid (1.6×10^{-4} M) in N_2O saturated aqueous solutions of 8×10^{-3} M (◇) 2-propanol and 8×10^{-3} M (○) and 8×10^{-2} M (●) formic acid at 21 ± 1 °C. Dose rate = 3.1×10^{16} eV g^{-1} min^{-1}.

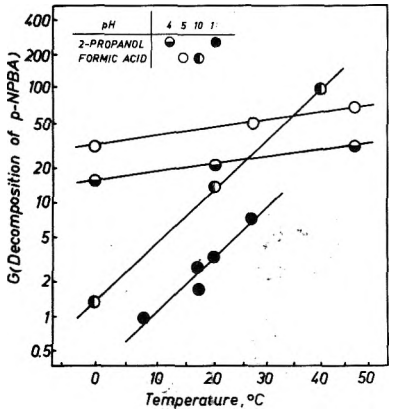

Figure 2. Arrhenius diagram of the decomposition of *p*-nitroperoxybenzoic acid (1.6×10^{-4} M) in N_2O saturated aqueous solutions containing 8×10^{-3} M of either 2-propanol or formic acid. Dose rate = 3.1×10^{16} eV g^{-1} min^{-1}. The $1/T$ abscissa is shown in centigrade notation.

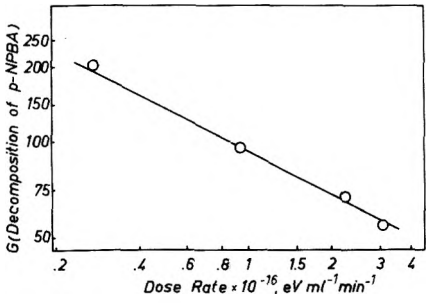

Figure 3. The dose rate dependence of the decomposition of *p*-nitroperoxybenzoic acid (1.6×10^{-4} M) in N_2O saturated aqueous solutions (pH 5) containing 8×10^{-3} M formic acid/sodium formate at 25 °C.

temperature (ΔT <2 °C) during the short irradiation periods. Temperatures pertinent to irradiations are listed in Figures 1–3. Different dose rates (see Figure 3) were obtained through leading shielding of samples.

The amount of *p*-nitroperoxybenzoic acid remaining in the irradiated samples was determined spectrophotometrically in a buffered (10.2 ml of concentrated H_3PO_4 and 170 ml of 0.25 N NaOH in 500 ml of solution, pH 2.0) 1.5×10^{-2} N NaI solution. Portions of the NaI solution (3 ml) were mixed with 3 ml of sample solution and the absorbancy was measured at 345 or 420 nm using a Bausch and Lomb Spectronic 20 spectrophotometer. Experimental errors are approximately ±10% unless specified otherwise.

All solutions were prepared from redistilled (alkaline permanganate) water which was stored in polyethylene containers. All other chemicals were of reagent grade and used without further purification.

Results and Discussion

1. *pH Dependence of Decomposition.* The dependence of the G value (= number of species converted per 100 eV of absorbed energy) of *p*-nitroperoxybenzoic acid upon the pH of the solution is shown in Figure 1. All solvated electrons from the radiolysis of water were converted in our experiments to hydroxyl radicals by nitrous oxide ($N_2O + e_{aq}^- \rightarrow N_2 + OH^- + \cdot OH$), resulting in a total yield of $G(\cdot OH) = 5.5$.[2] Hydroxyl radicals and H atoms ($G = 0.6$) are the initially reactive species in N_2O saturated aqueous solutions.

Solutions Containing 2-Propanol. In the system of 2-propanol, N_2O, and *p*-nitroperoxybenzoic acid (Figure 1) the G value for decomposition is independent of the pH both in acid and alkaline solutions; however, the yield is about ten times greater between pH 1.5 and 6 than above pH 10. The G value of 19 in the pH range 1.5–6 indicates that a chain reaction takes place (chain length ≈ 3–4). We observed a G value of 6.2 for the decomposition of *p*-nitroperoxybenzoic acid in a solution saturated with N_2O but containing no 2-propanol (the mechanism may involve OH radical addition to the benzene ring followed by decomposition of *p*-NPBA). This confirms our previous observation from the pulse radiolysis experiments:[1] ·OH reacts with 2-propanol to form a 2-hydroxyl-2-propyl radical which transfers an electron to *p*-nitroperoxybenzoic acid according to

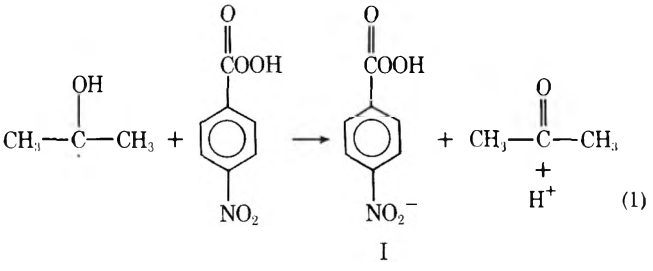

(1)

Electron transfer reactions of this type with other nitroaromatic compounds have been reported previously.[4] The electron adduct of *p*-nitroperoxybenzoic acid (I) eliminates ·OH and forms *p*-nitrobenzoate anion according to

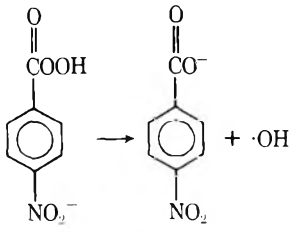

(2)

The hydroxyl radical formed in eq 2 reacts with 2-propanol, and the chain process propagates through another cycle. The small G value of 3.0 in Figure 1 indicates that the chain reaction is not sustained in alkaline solutions. The reduction of the *p*-nitroperoxybenzoate anion by 2-hydroxyl-2-propyl radicals yields a dianion (II).

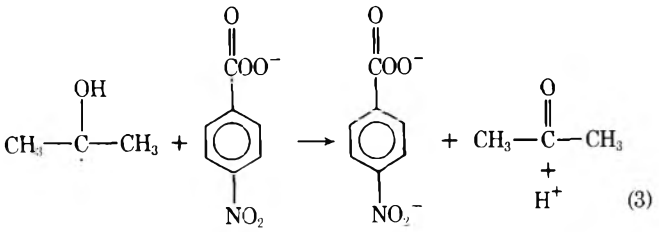

II (3)

The subsequent decomposition reaction to *p*-nitrobenzoate anion and ·O⁻

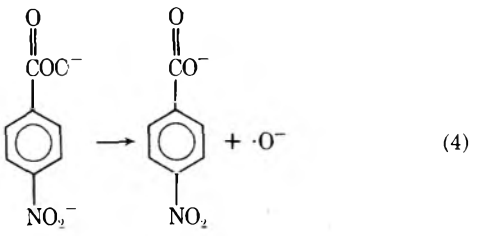

II (4)

is of higher energy of activation (see next section) than the comparable reaction of I, i.e., a chain reaction in alkaline solution is not feasible at room temperature.

In Figure 1, the smooth curve connecting the experimental points in the transition region of pH 6–10 follows the same type of pH dependence as does the degree of dissociation of an acidic species of $pK_a = 8.25$. This pK_a value has been previously identified as the pK_a of anion I.[1] Therefore we assume that the rate-determining processes of the chain mechanism are the decompositions of both I and II.

Solutions Containing Formic Acid. In the mixtures of formic acid, N_2O, and *p*-nitroperoxybenzoic acid, the *G* value for the decomposition of peroxy acid is generally greater than in mixtures containing 2-propanol, but the pH dependence follows identical pattern in both systems above pH 3.5 as shown in Figure 1. Further, the transition from the maximum *G* value into the alkaline region exhibits the same pK_a (= 8.25) dependence as noted for 2-propanol solutions. The *G* value for the reduction of *p*-nitroperoxybenzoic acid, however, depends both on the formic acid concentration (Figure 1) and the concentration of the peroxy acid (Table I) in acid and weakly basic solutions. A *G* value of approximately 3.0 is observed at pH >11 for all solutions investigated, i.e., the decomposition rate is apparently not controlled by the reactivities of carboxyl radical anions and 2-hydroxy-2-propyl radicals toward *p*-nitroperoxybenzoate anions in alkaline solutions.

In N_2O saturated solutions, the ·OH radicals abstract an H atom from formic acid ($k_{5a} = 1.3 \times 10^8$ M^{-1} s^{-1})[13] or from formate anion ($k_{5b} = 3 \times 10^9$ M^{-1} s^{-1})[13]

$$\cdot OH + HCOOH \rightarrow H_2O + \cdot COOH \quad (5a)$$

$$\cdot OH + HCOO^- \rightarrow H_2O + \cdot COO^- \quad (5b)$$

thereby forming radicals which could transfer the unpaired electron to *p*-nitroperoxybenzoic acid molecules according to

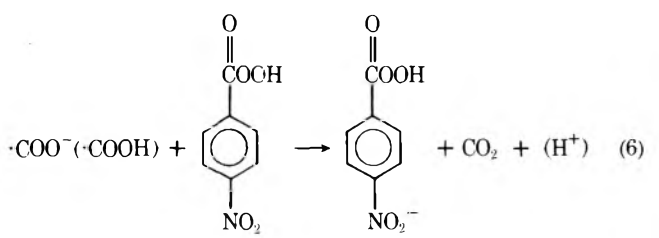

(6)

TABLE I: Dependence of *G* Value of Decomposition of *p*-Nitroperoxybenzoic Acid (*p*-NPBA) on Peroxy Acid Concentration and pH of N_2O Saturated 8×10^{-2} M Formic Acid Solutions[a]

p-NPBA, mM	0.08	0.16	0.32	0.80
pH	*G*(Decomposition of *p*-NPBA)			
1.95		64	69	
3.50	50	84	97	102

[a] Dose rate = 3.1×10^{16} eV g^{-1} min^{-1}.

This reaction corresponds to the electron transfer process described in eq 1 for the 2-hydroxyl-2-propyl radical. Reaction 6 may be followed by either reaction 2 or 4 which complete the chain cycle through formation of ·OH. The reaction proceeds in alkaline solution probably via the carboxyl radical anion according to

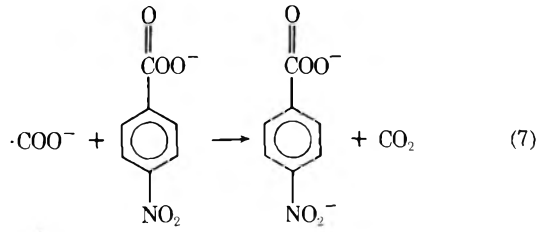

(7)

The decrease in the *G* value at pH <3.5 in solutions containing formic acid is associated with a pK_a of 1.4 which has been reported by Buxton and Sellers[11] for the carboxyl radical.

$$\cdot COOH \rightleftarrows \cdot CO_2^- + H^+ \quad (8)$$

The solid curve referring to these solutions, as shown in Figure 1, was computed via pK_a 1.4 and 8.25 (pK_a of electron adduct of *p*-nitroperoxybenzoic acid) and the maximum *G* value observed in this system. The good agreement between experimental and calculated data of 8×10^{-2} M HCOOH solutions indicates that ·COOH radicals do not (or only inefficiently) react with peroxy acid molecules as no provisions were made for such reaction in our computational procedure.

The dependence of *G*(decomposition) on the concentration of formic acid in acid solutions indicates that not all OH radicals are scavenged by HCOOH molecules at low concentration (8×10^{-3} M) of formic acid. The unscavenged hydroxyl radicals probably add rather rapidly to the benzene ring, e.g., rate constants of 4×10^9 M^{-1} s^{-1} for benzoic acid and 2.6×10^9 M^{-1} s^{-1} for *p*-nitrobenzoate ion have been reported.[13] If we assume a value of 2×10^9 M^{-1} s^{-1} for the addition of OH radicals to *p*-nitroperoxybenzoic acid, approximately 3% of all OH radicals may react with the benzene ring in solutions containing 1.6×10^{-4} M peroxy acid and 8×10^{-2} M formic acid. This compares with 30% in 8×10^{-3} M HCOOH solution and 2% in 8×10^{-3} M 2-propanol ($k_{OH} = 2 \times 10^9$)[13] solution. Under these circumstances, a considerable portion of the ·OH radicals undergoes reactions in 8×10^{-3} M HCOOH solution which do not contribute to the propagation of the chain reaction and, consequently, we observe a smaller *G* value for the decomposition of *p*-nitroperoxybenzoic acid.

Table I shows the dependence of *G* values for the decomposition of *p*-nitroperoxybenzoic acid upon the peroxy acid concentration. The experimental error is about 20% for 0.08 mM solutions because the peroxy acid is totally consumed in less than 3 min of irradiation time. Nevertheless, the *G* value

changes not very much over a tenfold increase of *p*-NPBA concentration, i.e., the rate determining process of the kinetic chain can be described by reactions 2 and 4 as previously stated.

Neutral carboxyl radicals ($2k = 1.7 \times 10^9$ M^{-1} s^{-1})[11] and 2-hydroxyl-2-propyl radicals ($2k = 1.4 \times 10^9$ M^{-1} s^{-1} at pH 6)[14] undergo mutual reactions about twice as fast as negatively charged $\cdot COO^-$ radical anions ($2k = 0.76 \times 10^9$ M^{-1} s^{-1}).[11] However, we cannot assume that the higher G values observed for solutions which contain formic acid in comparison to those containing 2-propanol (Figure 1) result exclusively from the lower rate of $\cdot COO^-$ combination reactions. A great number of chain terminations will not take place via such a reaction mechanism because the steady state concentrations ($\approx 10^{-8}$ M) are low for all three types of radicals under our experimental conditions. Additional reactions must occur (presumably with peroxy acid molecules) which lead to the removal of these free radicals.

Reactions of H atoms ($G = 0.6$) can generally be disregarded in this system since their rate constants are at least one order of magnitude smaller than the rate constants for corresponding reactions involving ·OH radicals.

2. *Energies of Activation.* The Arrhenius diagram of the decomposition of *p*-nitroperoxybenzoic acid in Figure 2 shows that the energies of activation (calculated from the slopes of the curves) do not depend upon the nature of the ·OH scavenger. However, we calculated an energy of activation of 2.7 kcal mol^{-1} for acid solutions and 18.2 kcal mol^{-1} for alkaline solutions. In conjunction with our observation of Figure 1 that the decrease in G(decomposition of *p*-nitroperoxybenzoic acid) exhibits a pK_a dependence expected for the dissociation of I, the results of the study on the activation energies corroborate our previous conclusion that the rate-determining processes of the kinetic chain are the homolytic decompositions of the peroxy bonds via reactions 2 and 4. In addition, it is not very likely, for example, that reactions 1 and 6 would have identical energies of activation, a necessary assumption to explain otherwise our experimental results.

Figure 2 shows that the G values for the decomposition of the peroxy acid are identical in acid and alkaline HCOOH solutions at approximately 35 °C. Solutions containing 2-propanol may have identical decomposition yields at 45 °C.

The experiments at higher temperature and in alkaline solutions were carried out with great care since *p*-nitroperoxybenzoic acid is rather unstable under these conditions and small variations in temperature during irradiation could result in relatively large errors of G(decomposition of *p*-nitroperoxybenzoic acid). However, in preparing the solution as mentioned above and requiring for preparation of peroxy acid solution and irradiation approximately 6 min until mixing with the buffered NaI solution, reproducible data were obtained as shown in Figure 2 for these alkaline solutions.

3. *Dose Rate Dependence.* The kinetic treatment of radiation induced polymerization reactions is applicable to other chain processes which are initiated by ionizing radiation.[15] As it has been shown previously,[16] the G value for the decrease of the substrate depends upon the dose rate DR by an inverse square root law, i.e., in our case G(*p*-nitroperoxybenzoic acid) $\sim DR^{-1/2}$. Figure 3 is a log–log plot of G value vs. DR. The curve exhibits a slope of $-1/2$, which indicates that the decomposition of the peroxy acid is a true chain process.

Acknowledgment. The author wishes to thank Professor R. C. Lamb for a sample of high quality *p*-nitroperoxybenzoic acid. He is also most grateful to Professor A. Henglein for valuable consultations. A grant from the Research Council of East Carolina University to defray publication cost is acknowledged with thanks.

References and Notes

(1) J. Lilie, E. Heckel, and R. C. Lamb, *J. Am. Chem. Soc.*, **96**, 5542 (1974).
(2) K. D. Asmus, H. Möckel, and A. Henglein, *J. Phys. Chem.*, **77**, 1218 (1973).
(3) K. D. Asmus, A. Henglein, M. Ebert, and J. P. Keene, *Ber. Bunsenges. Phys. Chem.*, **68**, 657 (1964).
(4) K. D. Asmus, A. Wigger, and A. Henglein, *Ber. Bunsenges. Phys. Chem.*, **70**, 862 (1966).
(5) J. Rabani, W. A. Mulac, and M. S. Matheson, *J. Phys. Chem.*, **69**, 53 (1965).
(6) G. E. Adams and R. L. Willson, *Trans. Faraday Soc.*, **65**, 2981 (1969).
(7) H. Taube, *J. Am. Chem. Soc.*, **63**, 2453 (1941).
(8) Z. D. Draganic and I. G. Draganic, *J. Phys. Chem.*, **76**, 2733 (1972); **77**, 765 (1973).
(9) N. Basco, G. A. Kenney-Wallace, S. K. Vidyarthy, and D. C. Walker, *Can. J. Chem.*, **50**, 2059 (1972).
(10) R. W. Mathews, J. A. Mahlman, and T. J. Sworsky, *J. Phys. Chem.*, **76**, 2680 (1972).
(11) G. V. Buxton and R. M. Sellers, *J. Chem. Soc., Faraday Trans. 1*, **69**, 555 (1973).
(12) L. S. Silbert, E. S. Siegel, and D. Swern, *J. Org. Chem.*, **27**, 1336 (1962).
(13) L. M. Dorfman and G. E. Adams, Ed., *Natl. Stand. Ref. Data Ser., Natl. Bur. Stand.*, **No. 46.**
(14) M. Simic, P. Neta, and E. Hayon, *J. Phys. Chem.*, **73**, 3794 (1969).
(15) A. Henglein, E. Heckel, Y. Ojima, and G. Meissner, *Ber. Bunsenges. Phys. Chem.*, **67**, 988 (1963).
(16) See, for example, A. Henglein, W. Schnabel, and J. Wendenburg in "Einführung in die Strahlenchemie", Verlag Chemie, Weinheim, 1969, p 305.

Photobleaching of the Biphenyl Anion in γ-Irradiated Rigid Organic Matrices. Dependence on the Matrix Polarity

Tsuneki Ichikawa, Tatsunori Moriya, and Hiroshi Yoshida*

Faculty of Engineering, Hokkaido University, Kita-ku, Sapporo 060, Japan *(Received December 3, 1975)*

Publication costs assisted by Hokkaido University

In order to elucidate the nature of the biphenyl anion formed and trapped in γ-irradiated organic glassy matrices containing biphenyl, its behavior in photobleaching was studied with selected wavelengths of light mostly at 77 K. In nonpolar 3-methylpentane matrix, the excitation spectrum of the photobleaching agrees with the absorption spectrum of the anion. In semipolar 2-methyltetrahydrofuran matrix, the anion is bleached only with light of wavelength shorter than 500 nm. For both the irradiation and bleaching at 4 K, the longer wavelength band of anion (670 nm) is also photosensitive. These results imply that the photoexcited anion releases an electron by an autodetachment mechanism and that the threshold wavelength of photobleaching is dependent on the solvation energy of the anion in the matrices. The change in quantum efficiency of photobleaching, as the bleaching proceeded, was also studied and interpreted in terms of the anion–cation separation distance and the capture of the electron by intact biphenyl. In polar ethanol matrix, it was found that both the blue (~420 nm) and red light (~670 nm) bleached the anion and the quantum efficiency for the blue light remained unchanged. These results seem to indicate that the electron ejected from the anion by the blue light reacts with an ethanol molecule without combining with the cation, whereas the biphenyl anion excited by the red light reacts with a neighboring ethanol molecule.

Introduction

The photobleaching of trapped electrons has been studied extensively in rigid matrices irradiated by ionizing radiations. Threshold energy and quantum efficiency of the photobleaching have provided information essential to radiation chemistry such as the structure of electron traps and the behavior of electrons mobilized in the matrices.[1-5] In the same way it seems worthwhile studying the photobleaching of the anions trapped in the matrices to elucidate the interaction between the anions and the matrix molecules and the behavior of electrons photodetached from the anions. The photobleaching has been studied, for instance, for biphenyl anions in 2-methyltetrahydrofuran (MTHF)[1] and 3-methylpentane (3MP)[6] matrices and for carbanions in alkane matrices.[7] In these studies, the photodetachment of electrons from anions was nicely demonstrated by alternately bleaching trapped electrons and anions.

Among the previous studies on the photobleaching of anions, Dyne and Miller mentioned that the biphenyl anion in the MTHF matrix was bleached at wavelengths of 400 and 433 nm but the longer wavelength band of the anion at 660 nm was not photosensitive.[1] The photoinduced recombination luminescence has been studied for irradiated alkane matrices containing aromatic compounds such as biphenyl.[8-11] The observed excitation spectrum of the luminescence suggests that the biphenyl anion is bleached at any wavelength of light absorbed by the anion. Though many other people may have become aware of such a difference in the behavior of anions depending on the matrix, no systematic studies have been reported on the effect of the nature of the matrix on the photobleaching of anions.

In the present investigation, the photobleaching was examined in detail for the biphenyl anion trapped in γ-irradiated matrices of different polarity. Biphenyl was chosen because it has been widely used in radiation chemical studies as an organic electron scavenger and the absorption spectrum of its molecular anion has been well studied.

Experimental Section

Sample Preparation. 3MP and MTHF were distilled and treated with Na–K alloy under vacuum. 2-Methylpentene-1 (2MP1) and ethanol (EtOH) were distilled. All these solvents were degassed by the freezing–pumping–thawing technique. Biphenyl was zone-refined. Sample solutions were prepared by vacuum-distilling solvents into quartz flat cells or quartz tubes where a measured amount of biphenyl had been placed beforehand. They were sealed under vacuum of about 10^{-5} Torr and irradiated with ^{60}Co γ rays mostly to a dose of 1.6×10^4 rads at 77 K in the dark.

Photobleaching. For photobleaching experiments the sample solutions were put into quartz cells generally of 0.2-cm optical path length. The photobleaching of biphenyl anions was carried out with light from a 500-W xenon lamp through a Toshiba KL-42 or KL-67 band-pass filter (and a neutral density filter, if necessary) and quartz windows of a Dewar vessel. The absorption spectrum of the biphenyl anion consists of two bands, one in the violet and blue region and another in the region from yellow to red as shown in Figure 1. They will be designated as "blue band" and "red band", respectively. These two bands were selectively illuminated by means of the band-pass filters as shown in Figure 1. The number of photons falling on the samples was measured by means of a thermopile standardized by photometry with ferric oxalate solution.

The concentration of biphenyl anions was monitored by measuring the optical density at the absorption maximum at 408 nm with a recording spectrophotometer (Hitachi, Model EPS-3T). The irradiation dose was so low that the initial optical density at 408 nm was less than 0.35 and that the samples were transparent enough to be bleached homogeneously by the light through the band-pass filters. The threshold wavelength of photobleaching was determined by using cutoff filters.

Occasionally the photobleaching experiments were carried out at 4 K (for both irradiations and measurements) by using facilities in the Research Reactor Institute of Kyoto Univer-

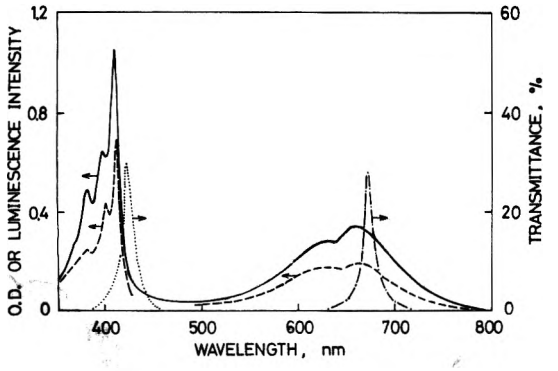

Figure 1. Absorption spectrum (——) and excitation spectrum of recombination luminescence (- - - -) recorded from matrices containing biphenyl irradiated with γ rays at 77 K. The absorption spectrum is due to the biphenyl anion in the MTHF matrix containing 0.2 mol % biphenyl irradiated to a dose of 5.0×10^4 rads. The excitation spectrum was obtained by monitoring the phosphorescence of biphenyl at 460 nm during photobleaching the biphenyl anion in the 3MP matrix containing 0.2 mol % biphenyl irradiated to a dose of 1.6×10^4 rads, and its intensity was shown after the correction of the excitation source spectrum. Transmission spectra of band-pass filters, (· · · · · · · ·) KL-42 and (– · –) KL-67, are also shown for comparison.

sity.[12,13] An incandescent lamp (300 W) with a color temperature of 2836 K was used there as a light source.

Recombination Luminescence. 3MP solutions of 0.2 mol % biphenyl were sealed in quartz tubes of 0.4 cm diameter and frozen at 77 K. Emission and excitation spectra during the photoinduced charge recombination were recorded with a recording fluorescence spectrophotometer (Hitachi, Model MPF-2A) at 77 K. The intensity of exciting light was controlled with neutral density filters if necessary.

Results

Decay of Biphenyl Anion and Calculation of Quantum Efficiency. A typical photobleaching curve of the biphenyl anions is shown in Figure 2 for the illumination at the blue band of the anions in an MTHF matrix at 77 K. If one assumes that the photobleaching quantum efficiency is independent of wavelength within the narrow wavelength region of the bleaching light (see Figure 1), the quantum efficiency, Φ, is derived from the observed photobleaching curves according to the relationship

$$\Phi = \frac{10^{-3}Nl}{\int I_i(\lambda)\{1 - 10^{-\epsilon(\lambda)c(t)l}\}\,d\lambda}\frac{dc(t)}{dt} \qquad (1)$$

where l is the optical path length, $c(t)$ the molar concentration of the anions at the duration of photobleaching, t, N Avogadro's number, $I_i(\lambda)$ the number of incident photons per unit time at wavelength λ (in unit of $cm^{-2}\,nm^{-1}\,s^{-1}$), and $\epsilon(\lambda)$ the molar extinction coefficient of the anions at λ.

The integral in eq 1 gives the number of absorbed photons per unit time. In the present study, the concentration of added biphenyl was sufficiently high, so that no trapped electrons were formed and the only light-absorbing entities present were the biphenyl anions. Therefore, the integral is readily evaluated by using the relationship

$$\epsilon(\lambda)c(t)l = OD_{408}(t)\frac{OD_\lambda(0)}{OD_{408}(0)} \qquad (2)$$

where $OD_\lambda(t)$ represents the observed optical density at λ and at t. The analysis of observed photobleaching curves was performed with a digital computer according to the equation

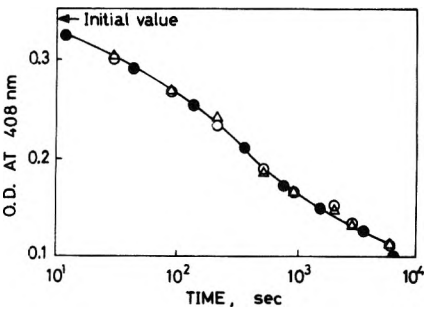

Figure 2. Photobleaching curves of the biphenyl anion observed at 77 K during the illumination at the blue band (420 nm) recorded from the MTHF matrix containing (○) 0.2 and (△) 0.4 mol % biphenyl irradiated to a dose of 1.6×10^4 rads in the cell of 0.2 cm light path length and (●) from the matrix containing 0.2 mol % biphenyl in the cell of 0.1 cm light path length irradiated to a dose of 3.2×10^4 rads. The intensity of light falling on the samples was 5.8×10^{15} photons/cm^2 nm s.

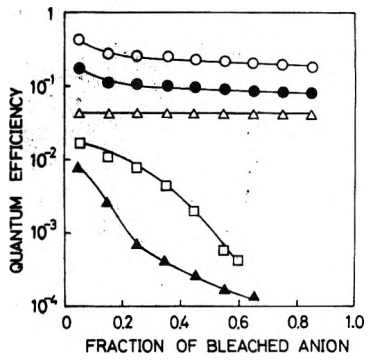

Figure 3. The change in quantum efficiencies of photobleaching the biphenyl anion (○, ●) in the 3MP–2MP1 matrix (8:2 in volume) containing 0.2 mol % biphenyl, (□) in the MTHF matrix containing 0.2 mol % biphenyl, and (△, ▲) in the EtOH matrix containing 0.3 mol % biphenyl irradiated to a dose of 1.6×10^4 rads at 77 K. The open symbols and closed ones indicate the quantum efficiencies at the blue band (~420 nm) and at the red band (~670 nm), respectively.

$$\Phi = \frac{10^{-3}Nl\left|c\left(t - \frac{\Delta t}{2}\right) - c\left(t + \frac{\Delta t}{2}\right)\right|}{\Delta t \int I_i(\lambda)\{1 - 10^{-\epsilon(\lambda)c(t)l}\}\,d\lambda} \qquad (3)$$

In eq 3, Δt is an interval between two successive measurements of OD_{408}. The value of 3.7×10^4 M^{-1} cm^{-1} for $\epsilon(408)$ was used in the calculation.[6]

The quantum efficiency thus obtained is dependent on time: it generally decreases as the survival fraction of the anions becomes smaller, as shown in the following section. However, the shape of photobleaching curves is independent of the initial concentration of the anions, as shown in Figure 2. Therefore, the photobleaching of the anions is a pseudo-first-order process, within the range of low doses examined, and its quantum efficiency is independent of the initial concentration. In addition, it was found that the photobleaching curves were independent of the concentration of biphenyl within its range where the trapped negative charged entities were exclusively the biphenyl anions.

Quantum Efficiency of Photobleaching. Figure 3 shows the dependence of the photobleaching quantum efficiency at 77 K upon the bleached fraction of the biphenyl anions in a nonpolar matrix of 3MP containing 20 vol % of 2MP1, a semipolar matrix of MTHF, and a polar matrix of EtOH. 2MP1 was added into the nonpolar matrix to scavenge biphenyl cations.[14] The illumination at either the blue band or

the red band was found to bleach the anions in the nonpolar matrix, though the quantum efficiency was higher at the blue band than at the red band. The quantum efficiencies for both the illuminations decrease gradually as the photobleaching proceeds. It should be noted that the rate of decrease is identical for both efficiencies, because the two curves for the nonpolar matrix in Figure 3 can be superimposed on each other if normalized at their initial values.

The behavior of the anions is significantly different in the semipolar matrix of MTHF at 77 K. They are not photobleached at all when illuminated at the red band. They are bleached at the blue band, but the quantum efficiency is lower at the beginning and still decreases rapidly as shown in Figure 3. The threshold wavelength of the photobleaching was observed to lie at about 500 nm (2.5 eV) in this matrix. At 4 K where the reorientation of MTHF molecules around the anions seems to be prohibited,[15-17] the anions are bleached not only at the blue band but also at the red band. Because transparent MTHF samples without cracks could not be obtained at 4 K, the quantum efficiency was not determined exactly at this temperature. It was qualitatively suggested that the quantum efficiency at the blue band was higher than that at 77 K, and that it decreased rapidly also at 4 K. It is now evident that the reorientation of solvent molecules is an important factor in determining the threshold wavelength of photobleaching the anions.

In the polar matrix of EtOH at 77 K, the biphenyl anions were reported to disappear slowly and spontaneously by proton transfer from the matrix molecules.[18] However, their decay under photoillumination is much faster than in the dark. The anions were photobleached by illumination at both the blue and red bands. The observed quantum efficiency at the blue band is relatively high and remains unchanged throughout the photobleaching, as shown in Figure 3. The quantum efficiency at the red band is very low and decreases rapidly as the photobleaching proceeds.

The behavior of the biphenyl anions is remarkably dependent on the nature of the matrix. In contrast, their optical absorption spectra (see Figure 1) are independent of the matrix. Neither the change in the spectral shape nor the shift of the absorption maxima could be found at all in the matrices used in the present investigation.

Recombination Luminescence. Biphenyl, as well as some other aromatic compounds, captures both an electron and a positive hole in nonpolar alkane matrices. When exposed to visible or near-ir light, the biphenyl anions in the γ-irradiated matrices release an electron, which combines with the biphenyl cation present in the matrices to yield excited biphenyl and, in turn, to bring about the recombination luminescence of biphenyl.[8-11] This kind of photoinduced recombination luminescence affords us an indirect detection method to study the photobleaching of anions.

In the present study with a concentration of biphenyl as high as 0.2 mol % in the 3MP matrix, only the ionic entities present in the irradiated matrix were the anions and the cations of biphenyl. The photoinduced recombination luminescence was found to be almost exclusively due to the phosphorescence of biphenyl[10] irrespective of the wavelength of excitation (photobleaching). The observed excitation spectrum (see Figure 1) monitored at the peak of the phosphorescence spectrum (460 nm) was essentially the same as that reported previously[8] and its shape was very close to that of the absorption spectrum of the biphenyl anions. This indicates that the observed luminescence spectrum is due to charge recombination, and that the anions in the 3MP matrix can be photobleached with light of any wavelength covering their absorption spectrum.

The intensity of the recombination luminescence decreased during photobleaching, but no change was observed in the shape of the excitation spectrum. The luminescence intensity was found to be proportional to the intensity of the bleaching light. This indicates that photobleaching in the nonpolar matrix, and probably in the other matrices also, is a one-photon process.

Discussion

Four important results were obtained. (1) Light of any wavelength absorbed by the biphenyl anion in the nonpolar matrix causes the photodetachment of an electron, which is a one-photon process. (2) The threshold energy of photobleaching depends on the nature of the matrix; the illumination at either the blue band or the red one bleaches the anion in the nonpolar matrix at 77 K and in the MTHF matrix at 4 K, while only the illumination at the blue band can do so in the semipolar MTHF matrix at 77 K. (3) The photobleaching quantum efficiency decreases in both the nonpolar and semipolar matrices, as the photobleaching proceeds. (4) In the EtOH matrix, the quantum efficiency is relatively high and remains constant for the blue band illumination, while it is low and decreases rapidly for the red band illumination. The implications of these results are discussed below.

Mechanism of Electron Detachment. Although the absorption spectrum of the biphenyl anions is identical in shape with the excitation spectrum of the recombination luminescence and, therefore, with that of the photodetachment of an electron from the anions in the nonpolar matrix, the absorption spectrum cannot be attributed to bound-free transitions of the biphenyl anions. This is because both the absorption and excitation spectra indicate vibrational structure rather clearly, though the bound–free transitions are expected to give a broad structureless spectrum. The free state in the matrices should be matrix dependent, so that the energy of the bound–free transitions should depend on the matrix. However, the absorption spectrum was observed to be independent of the matrix. The primary step of the photobleaching is concluded, therefore, to be the bound–bound transitions of the anions, which is followed by an autodetachment of an electron.

Shida and Iwata observed electronic spectra in the range 300–1500 nm of many aromatic anions formed in the γ-irradiated MTHF matrix and assigned them in terms of molecular orbital calculations.[19] By analogy with these anions, the blue and red bands of the biphenyl anion are believed to be due to the bound–bound transitions. On the other hand, the electron affinity of biphenyl is suggested to be as small as 0.14 eV (slightly smaller than that of naphthalene, 0.15 eV) in the gas phase.[20] It turns out, from consideration of energetics, that the excited states corresponding to the blue (3.0 eV) and red (1.9 eV) bands are high enough to lead to the autodetachment of an electron from the biphenyl anion.

Matrix Effect on Threshold Energy of the Photodetachment of Electron. The threshold energy of the photodetachment of an electron from anions in the gas phase is uniquely given by the electron affinity of their parent molecules. In rigid matrices, however, the threshold energy depends on the nature of the matrix as indicated by the result (2), because the anions as well as the photodetached electrons are more or less solvated. A matrix effect was discussed previously for the photoionization of neutral molecules[3] and for the photoinduced recombination luminescence.[10] Here, let us consider the

threshold of photobleaching of the biphenyl anion observed in nonpolar and semipolar matrices.

The semicontinuum model proposed to account for the solvated electrons[21] seems to be pertinent in considering the matrix effect on the photodetachment of an electron from the anion. Applying the model to the present case (without SCF treatment, because of the complexity and the lack of detailed knowledge about the electronic states of the biphenyl anion), the minimum energy required for the detachment of an electron is expressed by

$$E_{min} = \frac{N\mu e}{r_d^2} + \left(\frac{1}{D_{op}} - \frac{1}{D_s}\right)\frac{e^2}{r_c} + V_0 + E_a \qquad (4)$$

assuming the spherically symmetric solvation of the anion due to the matrix molecules. In eq 4, μ refers to the dipole moment of the matrix molecule, e to the electronic charge, E_a to the electron affinity of biphenyl in the gas phase, V_0 to the quasifree energy of the electron in the matrix medium, and D_{op} and D_s to the optical and static dielectric constants, respectively. The radii, r_d and r_c, are measured from the center of the anion to the molecular point dipoles in the first solvation shell and to the second solvation shell where the continuum begins, as illustrated in Figure 4. N is the number of molecular dipoles in the first solvation shell, which is plausibly 12 based on the close-packed structure.

Taking the average diameter of biphenyl and MTHF molecules, 6 and 5 Å, respectively, r_d and r_c are presumed to be 5.5 and 8.0 Å. In the MTHF matrix at 77 K, the reported values of 1.63 D for μ, 2.00 for D_{op}, and 2.88 for D_s[22] lead to $E_{min} = 1.9 + V_0 + E_a$ in electron volts. If one assumes that V_0 is almost equal to zero, though it has not been determined at 77 K, and if one takes the value of 0.14 eV for E_a, the threshold energy of the photodetachment of an electron is estimated to be 2.04 eV (610 nm). This value is in accordance with the observed threshold wavelength of photobleaching in the MTHF matrix (about 500 nm). Thus the solvation of the anions qualitatively interprets the result that they are bleached at the blue band but not at the red band.

The molecular dipole μ is zero in the nonpolar matrix, though the C–H bond dipoles may contribute somewhat to the solvation.[23] The zero molecular dipole makes the first two terms in eq 4 null, so that E_{min} is as small as E_a (0.14 eV). The biphenyl anions are expected to be photobleached in the nonpolar matrix with visible and near-ir light of any wavelength covering their absorption spectrum. They were found to be bleached at either the blue band or the red one.

According to the previous observations that the solvation of the trapped electrons in the MTHF matrix occurs when the matrix is warmed to 77 K after the γ-irradiation at 4 K,[15,16] the reorientation of the matrix molecules around the anions would be prohibited at 4 K. Therefore, the molecular dipole does contribute little to the solvation of the anions at this temperature, so that they can be bleached even at the red band as in the nonpolar matrix at 77 K.

Quantum Efficiency of Photobleaching. The first step of the photobleaching in the nonpolar and semipolar matrices is the detachment of an electron from the photoexcited biphenyl anions. Then the electron either combines with the cation formed by the ionizing radiation as a counterpart of the anion or is captured by a biphenyl molecule to regenerate the biphenyl anion. The former reaction causes the net decrease in the concentration of the biphenyl anions during photobleaching. The quantum efficiency of photobleaching is therefore given by

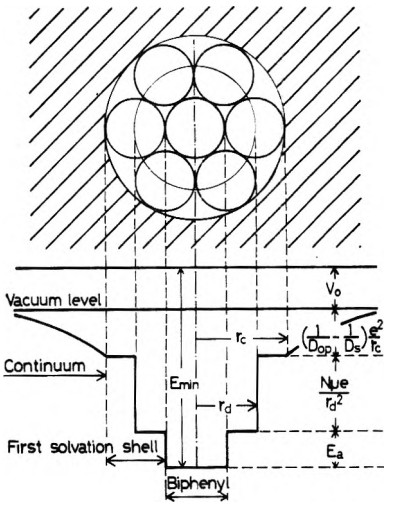

Figure 4. The semicontinuum model for the solvation of the biphenyl anion in organic glassy matrices: V_0, the quasifree energy of an electron in the matrix medium; E_{min}, the threshold energy of photobleaching the biphenyl anion; E_a, the electron affinity of biphenyl. See text also.

$$\Phi = \Phi_d P_r \qquad (5)$$

where Φ_d is the quantum efficiency of the photodetachment and P_r is the probability that the electron combines with the cation. Φ_d is regarded as constant for all biphenyl anions in a particular matrix, as long as the wavelength of bleaching light is unchanged. According to the competition reactions of the electron toward the cation and biphenyl, P_r is dependent on the separation distance between the anion and the cation (path length travelled by an electron before reaching the cation), and it decreases with increasing separation distance. This is the reason why the quantum efficiency of photobleaching decreases during photobleaching.

The quantum efficiency Φ is expressed more exactly with the probability, $W(r,t)$, of finding the anion at distance r from the counterpart cation (the photobleaching process of pseudo-first order indicates that each charge recombination is an isolated event) and at time t and also with the probability, $P(r)$, that the electron detached from the anion at r will reach the cation without being scavenged by biphenyl:

$$\Phi = \Phi_d \int_0^\infty P(r)W(r,t)\,dr \qquad (6)$$

$P(r)$ is a function which decreases with increasing r. $W(r,t)$ has a maximum at a certain distance r, which gradually increases as the charge recombination proceeds, as shown for the isothermal decay of the trapped electrons in a rigid matrix at elevated temperature.[24] The charge recombination occurs more readily in the anion–cation pair of shorter distance, so that the maximum of $W(r,t)$ shifts to the larger r. This shift results in the decrease in Φ during photobleaching.

Although the quantum efficiency in the nonpolar matrix was higher at the blue band than at the red band, the quantum efficiency-bleached fraction curves for both bands could be superimposed on each other if normalized at their initial value. This implies that the difference in the absolute value of quantum efficiency derives from the difference in Φ_d and that the integral in eq 6 is always identical for both bands when the bleached fraction of the anions is the same. It turns out that $P(r)W(r,t)$ depends only on the bleached fraction and, therefore, $P(r)$ is independent of the wavelength of bleaching light. It may be concluded that the excess kinetic energy of the

photodetached electron is dissipated readily and the migration distance of the electron is primarily independent of its initial kinetic energy.

The quantum efficiency in the semipolar MTHF matrix decreased during photobleaching much more remarkably than in the nonpolar matrix. According to eq 6, this is attributed to the stronger dependence of $P(r)$ on r and/or the wider initial distribution of the cation–anion distance $W(r,0)$ in the MTHF matrix. Anyhow, the number of detachment–rescavenging cycles before the charge recombination increases rapidly in this matrix as the photobleaching proceeds.

If the concentration of biphenyl is increased, the average cation–anion distance is decreased because of the larger chance of secondary electrons being scavenged. $W(r,0)$ shifts to smaller r. Upon photobleaching, $P(r)$ is smaller for the higher concentration of biphenyl. These two effects cancel each other and interpret qualitatively the independence of the quantum efficiency of photobleaching on the biphenyl concentration as shown in Figure 2.

Photobleaching in EtOH Matrix. The photobleaching in the EtOH matrix showed some peculiar features. First, the quantum efficiency was unchanged throughout the photobleaching, when the anions were bleached at the blue band. Secondly, the anions were bleached even at the red band. It is expected from eq 4 that the photon energy of the red light is too low to cause the photodetachment of an electron from the biphenyl anions in this matrix, because they cannot be bleached with the red light even in the semipolar MTHF matrix. The threshold, E_{min}, is estimated to be 3.23 eV (380 nm) from the reported values, $D_{op} = 1.85$, $D_s = 3.00$, and $\mu = 1.69$ D[22] and also from the presumed values, $r_d = 4.8$ Å and $r_c = 6.6$ Å (effective diameter of EtOH is 3.6 Å), assuming again that V_0 is zero in the EtOH matrix medium.

Trapped electrons were found, when photoexcited, to disappear in alcoholic matrices in reacting with the matrix molecules, $e^- + ROH \rightarrow RO^- + H$.[25,26] The peculiar features observed here are very probably attributed to this reaction. When the biphenyl anions are highly excited at the blue band, an outer electron of the anions may be delocalized enough to encounter EtOH molecules around the anions and to react with one of them, even though it is not released completely from the anions. The electron cannot escape the deep solvation potential to travel long enough to encounter either the solvent cation or the biphenyl molecules. This may be the reason why the quantum efficiency remains unchanged during the whole bleaching.

When the anions are excited at the red band, the electron cannot be detached at all from the anions. However, the excited anions may transfer an electron to a neighboring EtOH molecule probably in the first solvation shell, owing to an expanded anion orbital. Thereby photobleaching of the anions can occur. Some anions may have a solvation configuration favorable to electron transfer and others may not. This is one of the reasons why the quantum efficiency decreases rapidly during photobleaching, when excited at the red band. Diverse configurations of the trapping sites were assumed also for the trapped electrons in the EtOH matrix in order to interpret the feature of their photoinduced decay.[26-28]

Acknowledgment. The authors express their thanks to Professor T. Higashimura and his research group of the Research Reactor Institute of Kyoto University for giving us the opportunity of using the experimental facilities. This work was supported by Science Fund (No. 978052) provided by Japanese Ministry of Education.

References and Notes

(1) P. J. Dyne and O. A. Miller, *Can. J. Chem.*, **43**, 2696 (1965).
(2) T. Huang and L. Kevan, *J. Chem. Phys.*, **61**, 4660 (1974).
(3) A. Bernas, J. Blais, M. Gauthier, D. Grand, and T. B. Truong, *Int. J. Radiat. Phys. Chem.*, **6**, 401 (1974).
(4) Y. Ishikawa, K. Oka, and S. Sato, *Bull. Chem. Soc. Jpn.*, **48**, 2680 (1975)
(5) K. Harada, M. Irie, and H. Yoshida, *Int. J. Radiat. Phys. Chem.*, in press.
(6) J. B. Gallivan and W. H. Hamill, *J. Chem. Phys.*, **44**, 1279 (1966).
(7) J. E. Willard, *Int. J. Radiat. Phys. Chem.*, **6**, 325 (1974).
(8) A. Dèroulède, F. Kieffer, and M. Magat, *Adv. Chem. Ser.*, **82**, 401 (1968).
(9) A. Dèroulède, *J. Lumin.*, **3**, 302 (1971).
(10) C. Deniau, A. Dèroulède, F. Kieffer, and J. Rigaut, *J. Luminescence*, **3**, 325 (1971).
(11) F. Kieffer, C. Lapersonne-Meyer, and J. Rigaut, *Int. J. Radiat. Phys. Chem.*, **6**, 79 (1974).
(12) A. Namiki, M. Noda, and T. Higashimura, *J. Phys. Chem.*, **79**, 2975 (1975).
(13) A. Namiki, *J. Chem. Phys.*, **62**, 990 (1975).
(14) J. B. Gallivan and W. H. Hamill, *J. Chem. Phys.*, **44**, 2378 (1966).
(15) H. Yoshida and T. Higashimura, *Can. J. Chem.*, **48**, 504 (1970).
(16) H. Hase, T. Higashimura, and M. Ogasawara, *Chem. Phys. Lett.*, **16**, 214 (1972).
(17) H. Yoshida, M. Ogasawara, T. Warashina, and T. Higashimura, *J. Chem. Phys.*, **56**, 4238 (1972).
(18) T. Shida and W. H. Hamill, *J. Am. Chem. Soc.*, **88**, 3689 (1966).
(19) T. Shida and S. Iwata, *J. Am. Chem. Soc.*, **95**, 3473 (1973).
(20) M. Szwarc, "Carbanions, Living Polymers and Electron Transfer Processes", Interscience, New York, N.Y., 1968, p 297.
(21) C. Kevan, *Adv. Radiat. Chem.*, **4**, 286 (1974).
(22) Reference 21, p 184.
(23) D.-F. Feng, L. Kevan, and H. Yoshida, *J. Chem. Phys.*, **61**, 4440 (1974).
(24) T. Ichikawa, H. Yoshida, and K. Hayashi, *Bull. Chem. Soc. Jpn.*, **46**, 812 (1973).
(25) A. Habersberzerova, Lj. Josimovic, and J. Teply, *Trans. Faraday Soc.*, **66**, 656 (1970).
(26) T. Shida and M. Imamura, *J. Phys. Chem.*, **78**, 232 (1974).
(27) B. G. Ershov and A. K. Pikaev, *Adv. Chem. Ser.*, **81**, 1 (1968).
(28) G. V. Buxton, F. S. Dainton, T. E. Lantz, and F. Sargent, *Trans. Faraday Soc.*, **66**, 2962 (1970).

Organic Phase Species in the Extraction of Hydrochloric Acid by Triisooctylamine in Various Organic Diluents

A. S. Vieux* and N. Rutagengwa

Laboratoire de Chimie Analytique, Université Nationale du Zaïre, Campus de Kinshasa, Zaïre *(Received September 5, 1975)*

Publication costs assisted by the Université Nationale du Zaire

The equilibria between triisooctylamine dissolved in several organic diluents and dilute aqueous solutions of HCl have been studied. In 1,2-dichloroethane, dichloromethane, 1,2-dichlorobenzene, and chloroform, the ammonium salts usually exist as ion pairs within the range of concentrations investigated. In the low dielectric constant diluents, benzene, xylene, and carbon tetrachloride, the ion pairs aggregate. The semithermodynamic formation constants for the extraction of the ion-paired triisooctylammonium chloride depends on the polarity or dielectric constant of the diluent and on the chemical nature of the diluent. Chemical methods and ir spectroscopy have been used. The ir method appeared very accurate for equilibrium constant determination.

Introduction

Previous investigations have shown that the extraction of acids and metallic ions by long-chain alkylamines is significantly influenced by the nature of the diluent. It was found in the extraction of acids that complexes of the type $(R_3NHX)_n$ (HX = strong mineral acid; R_3N = tertiary amine) are generally formed.[1-11] The value of n is small at low aqueous acidity with low total amine concentration. Larger aggregated species may exist depending upon aqueous acid concentration and amine concentration.[12] The formation of these larger aggregates is also greatly dependent on the nature of the diluent. Among tertiary amines, trioctylamine and trilaurylamine have been extensively used to study complex formation with acids occurring in the conversion of the base form into the salt,[1-6,9-11] for instance.

Even though the conclusions with trioctylamine and trilaurylamine can be considered as characteristic of the behavior of salt solutions of tertiary amines in equilibrium with the supporting aqueous acid phase, similar investigations with other amines should prove interesting and useful as a guide to further studies of the extraction of metallic anions. Many publications, dealing with the use of triisooctylamine (TIOA), have confirmed its excellent extractive properties. In comparison with trioctylamine and trilaurylamine, however, little has been published on the extraction of mineral acids with triisooctylamine.[3,7,8,13-17]

This paper deals with the extraction of hydrochloric acid by triisooctylamine with respect to widely different diluent character. While studying the extraction of uranyl chloride,[8] we determined the behavior of the organic phase in contact with aqueous hydrochloric acid solution for salt solutions in benzene, xylene, and carbon tetrachloride. It was found that, at low salt concentration, the law of mass action is followed. No attempt was made at that time to elucidate the phenomenon occurring at higher salt concentrations. Because in the extraction of metals, amine salts at rather high concentrations are used, it is important to study the extraction reactions in these conditions. In this paper, an attempt is made to evolve a quantitative description of the extraction equilibria, keeping in mind the possibility of aggregation of the amine salts. We have limited our investigations to the range of aqueous acid concentrations where no uptake of excess mineral acid can occur in the organic phase. That is, we have investigated the range of aqueous acid concentrations where the ratio of the initial amine concentration to the acid concentration in the organic phase is equal to, or smaller than, unity ($[HCl]_o \leq [R_3N]_{oi}$).

The diluents were chosen to cover a wide variation in character, including at the same time the most practical ones and those most commonly used in the extraction of metallic ions by long-chain alkylamines. The diluents used were benzene, xylene, carbon tetrachloride, 1,2-dichlorobenzene, 1,2-dichloroethane, chloroform, and dichloromethane.

The extraction system was studied by the back-extraction technique and by the partition isotherms method. Furthermore, an infrared spectroscopic investigation was undertaken in order to obtain additional information.

The infrared method has proved to be a very accurate method for determination of the equilibrium constant, by following the acidity of the organic phase.

Experimental Section

The amine and the diluents used here, as well as the technique of extraction and the methods of analysis, have been described in previous publications.[8] The extractions were performed at (25 ± 2 °C). The acid content of the aqueous phases was determined either by potentiometric titration or by pH measurements.

For the distribution isotherms technique 1 M (H^+, Na^+)Cl^- solutions were used. Each amine solution of a given concentration was equilibrated with at least ten aqueous acid solutions of variable acid concentrations of constant ionic strength. The acid content of both phases was determined at equilibrium and the pH of the aqueous phase was measured. In some cases, the acid content of the organic phase was obtained by evaluating the difference between the acidity of the initial aqueous phase and the acidity of the aqueous phase at equilibrium.

All determinations were performed under an argon atmosphere. Experimental data agreed within ±1%. Reported results are the averages of at least two determinations. No third phase, or a variation of volume of the two

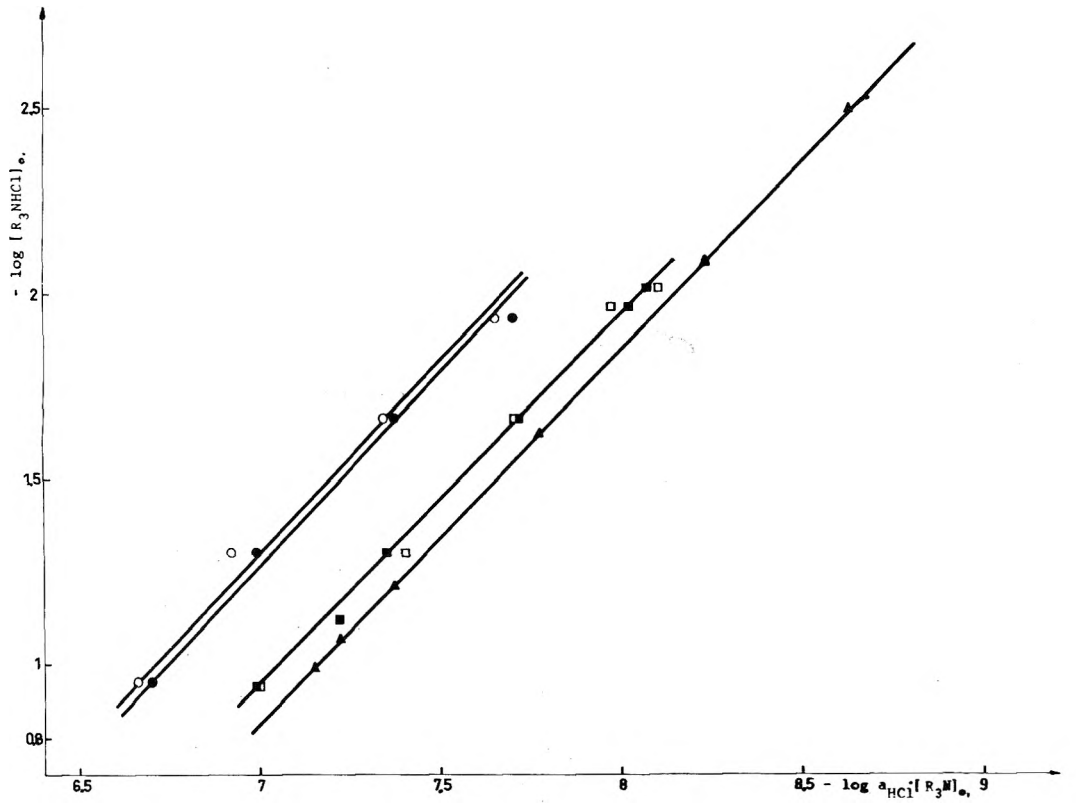

Figure 1. Logarithmic plots of the ammonium salt $[R_3NHCl]_o$ concentration in the organic phase vs. the aqueous acid activity a_{HCl} multiplied by the free amine concentration $[R_3N]_o$. The aqueous acid activity is obtained from pH measurements: in chloroform (O), in 1,2-dichloroethane (□); the aqueous acid activity is obtained from the acid concentration: in chloroform (●), in 1,2-dichloroethane (■), in dichloromethane (△).

TABLE I: Equilibrium Constants of Hydrochloride Salt of Triisooctylamine in Various Diluents by the Back-Extraction Method

Alcalimetry

Diluent	$[H^+]_{aq}$	$\gamma_{\pm HCl}$	$[R_3NHCl]_o$	$\log K_1$
Benzene	2.20×10^{-2}	0.874	7.84×10^{-2}	3.98
	1.98×10^{-2}	0.876	5.52×10^{-2}	3.96
	1.71×10^{-2}	0.882	3.29×10^{-2}	3.92
	1.28×10^{-2}	0.896	1.22×10^{-2}	3.86
	1.01×10^{-2}	0.905	5.70×10^{-3}	3.83
Xylene	3.10×10^{-2}	0.860	7.60×10^{-2}	3.53
	3.10×10^{-2}	0.861	6.76×10^{-2}	3.48
	2.80×10^{-2}	0.866	5.20×10^{-2}	3.50
	2.65×10^{-2}	0.868	4.15×10^{-2}	3.47
	1.67×10^{-2}	0.887	1.03×10^{-2}	3.45
CCl_4	3.20×10^{-2}	0.850	7.85×10^{-2}	3.52
	2.94×10^{-2}	0.862	5.80×10^{-2}	3.48
	2.74×10^{-2}	0.867	4.00×10^{-2}	3.41
	2.18×10^{-2}	0.875	2.10×10^{-2}	3.46

pH Metry

	$[R_3NHCl]_o$	(H^+)	$[R_3N]_o$	$\log K_1$
Xylene	7.5×10^{-2}	2.62×10^{-2}	3.2×10^{-2}	3.53
	6.1×10^{-2}	2.57×10^{-2}	2.9×10^{-2}	3.50
	5.3×10^{-2}	2.55×10^{-2}	2.7×10^{-2}	3.48
	3.7×10^{-2}	2.38×10^{-2}	2.3×10^{-2}	3.45
	1.1×10^{-2}	1.77×10^{-2}	1.4×10^{-2}	3.50
CCl_4	7.85×10^{-2}	2.89×10^{-2}	2.93×10^{-2}	3.50
	5.80×10^{-2}	2.88×10^{-2}	2.70×10^{-2}	3.41
	4.00×10^{-2}	2.36×10^{-2}	2.47×10^{-2}	3.46
	2.10×10^{-2}	1.89×10^{-2}	2.10×10^{-2}	3.44

phases, were observed. The subscript o represents the organic phase, aq the aqueous phase, and i the initial concentration. The symbol ( ) or a represents the activity, and [ ] or C the concentration.

Ir Experiments. Infrared spectra were obtained from liquid film (solutions) using a Perkin-Elmer 221, double-beam instrument with cell windows of sodium chloride. The absorbance due to the diluent was compensated. Spectra were recorded from 4000 to 200 cm^{-1}. Infrared spectra were obtained for TIOA and its hydrochloride salt in chloroform, 1,2-dichloroethane, and carbon tetrachloride.

The acid content of the organic phase was determined for salt solutions in chloroform and 1,2-dichloroethane based on the band at 2360 cm^{-1} attributed to $R_3NH^+ \cdots Cl^-$.

Results

A. *Back-Extraction Method.* The general equation for extraction of HCl by TIOA can be written

$$pR_3N_o + qH_{aq}^+ + qCl_{aq}^- \rightleftarrows [(R_3N)_p(HCl)_q]_o \quad (1)$$

As for the experimental constraint applied in the back-extraction tests, the ammonium salt contains an equal number of moles of amine and acid, hence $p = q$ and the equation for the back-extraction tests becomes as follows:

$$[R_3NHCl]_{p_o} \rightleftarrows pR_3N_o + pH_{aq}^+ + pCl_{aq}^- \quad (2)$$

It has been assumed that the ionic dissociation of amine salts is practically nonexistent in diluents of low dielectric constants.[18] It is also assumed that the free amine concen-

tration $[R_3N]_o$ is equal to the acid concentration in the aqueous solutions at equilibrium. For the amine and its salt, concentrations are used as an approximation to activities. This is the best available expedient, because our results appear to indicate that the organic phase cannot be considered as behaving ideally. Similarly, as an expedient approximation, we shall consider for the aqueous acid, the pH as being equal to log a_{H^+} (and $-pH - \log \gamma_{H^+} \neq \log C_{H^+}$). The activity coefficients used are taken from the literature.[19] Hence application of the law of mass action to eq 2 will give the semithermodynamic salt formation constants in terms of activities and molarities, K_1.

For salt solutions in 1,2-dichlorobenzene, dichloromethane, 1,2-dichloroethane, and chloroform, the different sets of results (available as supplementary material; see paragraph at end of text regarding supplementary material) seem to indicate the absence of any marked reactions in the organic phase, including polymerization, within the concentration range shown. From the slope of the curves (Figure 1), it can be concluded that the ammonium salt exists as undissociated ion pairs up to $\simeq$0.1 M.

For salt solutions in benzene, xylene, and carbon tetrachloride the results (Table I) seem to indicate a progressive variation of the value of K_1 with concentration. However, this variation is not very important in the tenfold range of concentrations studied. One reasonable interpretation could be that in these diluents, the ammonium salt exists mainly as the monomeric species, without excluding the formation, in small amounts, of polymeric species, mainly dimeric ones. This is in agreement with literature data on the extraction of hydrohalic acids with trilaurylamine and trioctylamine in benzene and carbon tetrachloride.[1,2,4]

It appears that the diluent plays an important role in determining the affinity of the amine for the aqueous acid. The mean values of the constants in benzene, xylene, and carbon tetrachloride are in fairly good agreement with the values reported for TOA·HCl in benzene,[20] toluene,[21] and carbon tetrachloride.[22] For salt solutions in dichloromethane and 1,2-dichloroethane the equilibrium constant is a factor of 10^3 greater than for solutions in benzene, xylene, and carbon tetrachloride. In the extraction of hydrogen bromide by solutions of trilaurylamine, a difference between the equilibrium constant of more than 10^5 was reported for salt solutions in chloroform and cyclohexane; for TLA·$HClO_4$, the difference is almost 10^4 for salt solutions in triethylbenzene and 1,2-dichlorobenzene.[1]

In general, the higher the dielectric constant of the diluent, the better the extraction. One explanation for this is that a positive electrostatic free energy obstructs the transfer of ions from a medium of high dielectric constant (water) to one of lower value.

However, the correlation between the ease of extraction and the dielectric constant of the diluent is not very good. For example, here, K_1 is larger in chloroform (Σ = 4.8/20 °C)[23] than in 1,2-dichlorobenzene (Σ = 9.9/25 °C) while there is a difference of more than 10^2 between the K_1 values in 1,2-dichlorobenzene and 1,2-dichloroethane (Σ = 10.4/25 °C), two diluents which have close dielectric constants.

Both "electrostatic" solvation of the ions and a short range "chemical" interaction with the diluent should then be taken into account. Such an argument was suggested to explain $HClO_4$ extraction by TLA in chlorobenzene and anisole.[1] If the diluent is somewhat basic, it may interact with the weakly acidic hydrogen of the ammonium cation.

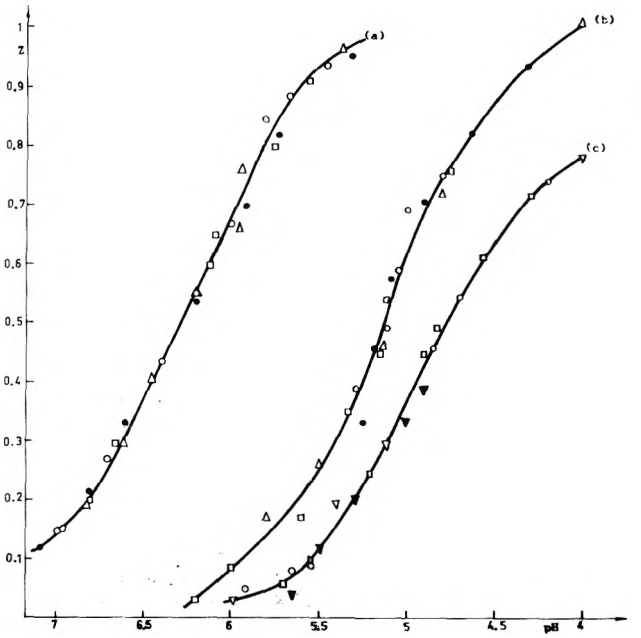

Figure 2. Plots of Z vs. pH for solutions of four different initial concentrations of amine $[R_3N]_i$ in the various diluents. Molarity of the amine in 1,2-dichlorobenzene (a): 0.193 (●), 0.0979 (○), 0.483 (△), 0.0248 (□); in chloroform (b): 0.214 (●), 0.103 (○), 0.0561 (△), 0.0271 (□); and in 1,2-dichloroethane (c): 0.203 (□), 0.109 (○), 0.0508 (△), 0.0253 (▲).

For chloroform which is slightly acidic, there is a possibility of hydrogen bonding to the anion. A consideration of these two aspects of diluent properties may explain the differences in the value of the equilibrium constants reported here.

Many authors[1,2,4] have reported that trialkylammonium salts of long-chain amines in chloroform appear to be monomeric in the range of concentrations used here. Warnquist,[24] however, using the emf titration technique, found that the hydrochloride salt of diisononylamine exists only in the dimeric form. There is much evidence from various experimental methods that (strong) acid salts of long-chain secondary amines generally have a greater tendency to aggregate.

B. *Partition Isotherms Method.* The partition isotherms method, with four different initial amine concentrations in the range between 0.025 and 0.2 M, was used to check independently the results obtained by the back-extraction technique and to find the composition of the aggregates of the amine salt in the organic phase, where aggregation appears to occur.

Since an ionic medium, 1.00 M (Na^+, H^+)Cl^-, was used, the activity coefficients in the aqueous phase may be assumed to be practically constant. Measurements of pH of the aqueous phase were carried out. The acid content of the organic phases was determined by titration, when the results were estimated to be sufficiently accurate. Organic acid content can be calculated as the difference in the HCl concentrations of the aqueous phase before and after equilibrium. The hydrogen ion concentration in the aqueous phase at equilibrium is obtained from pH measurements and activity coefficients.[25] The deviation of $[Cl^-]$ from 1.00 M can be neglected, so that (Cl^-) can be considered constant.[26] Here we use the same expedient approximations which we used for the treatment of the results obtained by

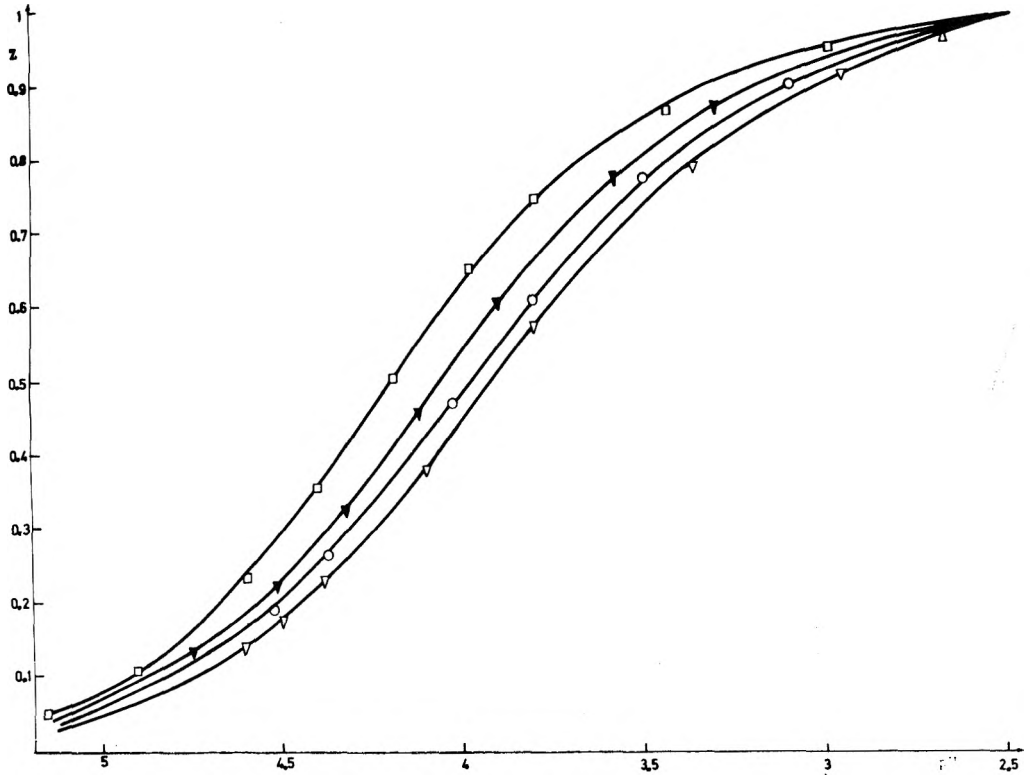

Figure 3. Plots of Z vs. pH for amine $[R_3N]_i$ solutions of four different initial concentrations in benzene; amine molarity: 0.226 (□), 0.0983 (▲), 0.0538 (○), and 0.0240 (△).

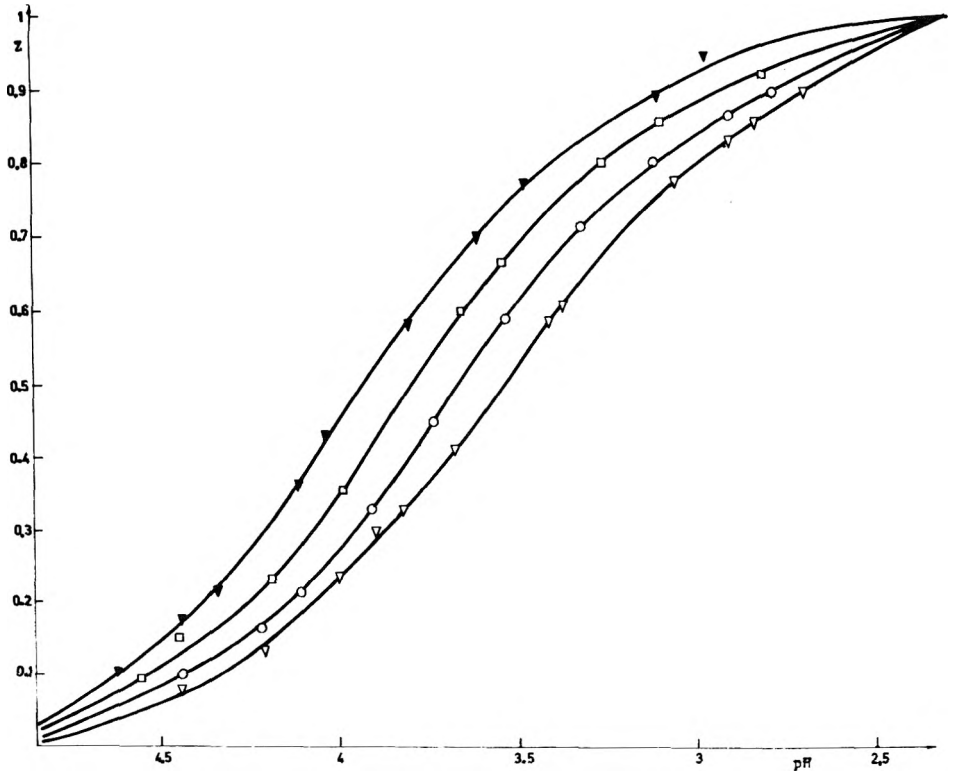

Figure 4. Plots of Z vs. pH for amine $[R_3N]_i$ solutions of four different initial concentrations in xylene; amine molarity: 0.256 (▲), 0.121 (□), 0.0543 (○), and 0.0235 (▲).

the back-extraction method for activities and concentrations.

The results are presented as a function Z of pH, where

$$Z = [HCl]_o/[R_3N]_{oi}$$

For solutions of the four amine concentrations in the various diluents, the plots $Z = f(pH)$ were drawn. We refer to Kojima et al.[27] for the calculation procedure.

The application of the mass action law to eq 1 gives

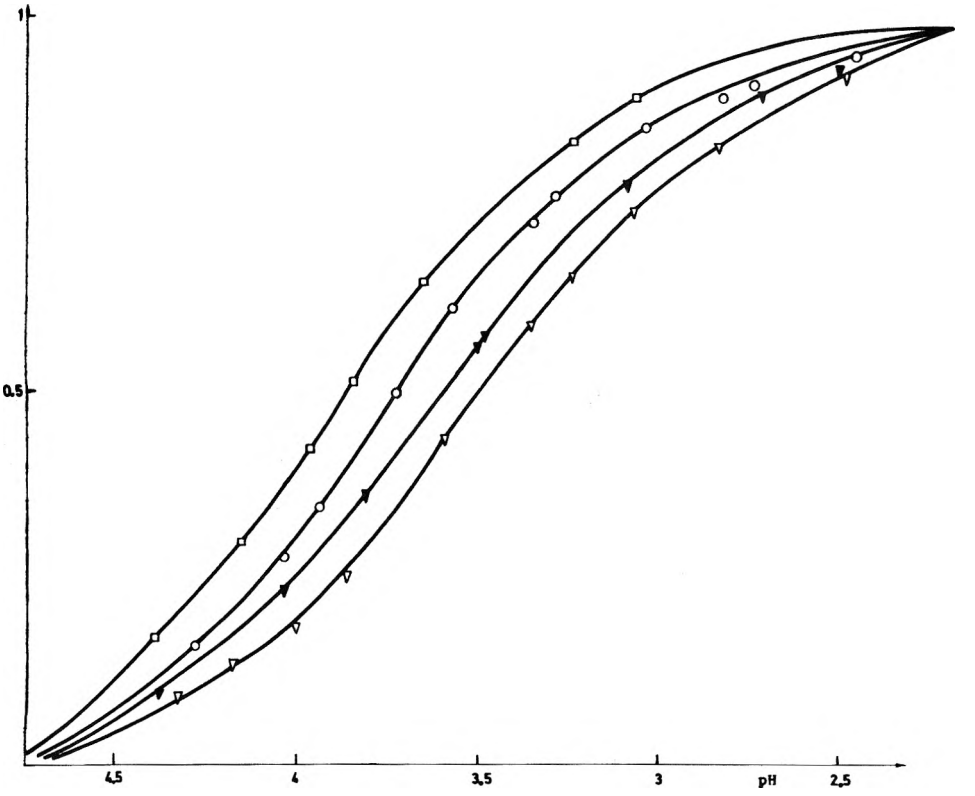

Figure 5. Plots of Z vs. pH for amine $[R_3N]_i$ solutions of four different initial concentrations in carbon tetrachloride; amine molarity: 0.242 (□), 0.113 (○), 0.0542 (▲), and 0.0245 (△).

$$K_{pq} = \frac{[(R_3N)_p(HCl)_q]_o}{[R_3N]_o{}^p(H^+)_{aq}{}^q(Cl^-)_{aq}{}^q}$$

Under our experimental conditions (Cl^-) is constant. It follows

$$K_{pq}' = \frac{[(R_3N)_p(HCl)_q]_o}{[R_3N]_o{}^p(H^+)_{aq}{}^q}$$

$$K_{pq}' = K_{pq}(Cl^-)_{aq}{}^q$$

It is convenient to present our results in two parts, because two distinctly different groups of results were observed with the diluents: 1,2-dichloroethane, 1,2-dichlorobenzene, and chloroform on one side, and benzene, xylene, and carbon tetrachloride on the other.

1. *Solutions of the Hydrochloride Salt of TIOA in 1,2-Dichloroethane, 1,2-Dichlorobenzene, and Chloroform.* Plots of Z = f(pH) are shown in Figure 2. The agreement between different amine concentrations in each plot indicates that $p = 1$. Since under our experimental conditions, excess acid extraction is avoided, hence $q \leq p$ and $q = 1$, so that only the complex R_3NHCl is formed.

The apparent equilibrium constant at 1 M NaCl ionic strength can then be rewritten

$$K_1' = [HCl]_o/[R_3N]_o(H^+)_{aq}$$

The free amine concentration was obtained from the difference between its initial concentration and the acid content of the organic phase.

2. *Solutions of the Hydrochloride Salt of TIOA in Benzene, Xylene, and Carbon Tetrachloride.* Plots of Z vs. pH are shown in Figures 3–5. The lack of agreement between the plots for different TIOA concentrations indicates that one or more polynuclear complexes are formed.

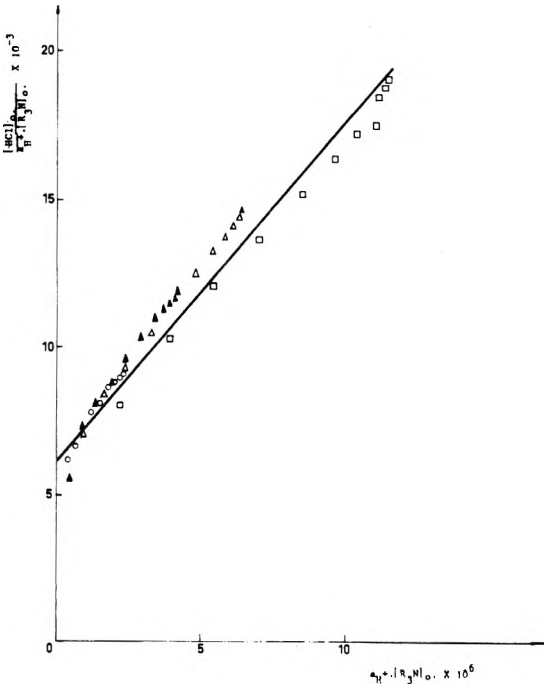

Figure 6. Plots of $[HCl]_o/a_{H^+}[R_3N]_o$ vs. $a_{H^+}[R_3N]_o$ for amine $[R_3N]$ solutions of four different initial concentrations in benzene; amine molarity: 0.226 (□), 0.0983 (△), 0.0538 (▲), and 0.0240 (○).

The calculation method indicated above to obtain the concentration of the free amine can no longer be used. This concentration was obtained from a graphical method.[27]

The values of $[R_3N]_o$ determined from the graphical method using the values of a_{H^+}, $[R_3N]_{oi}$, and Z were found

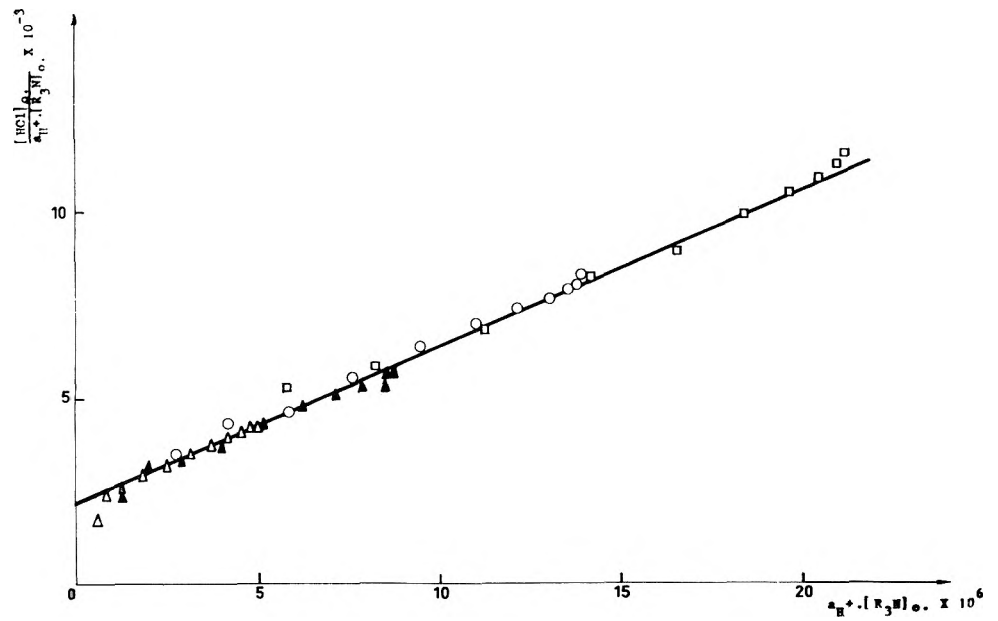

Figure 7. Plots of $[HCl]_o/a_{H^+}[R_3N]_o$ vs. $a_{H^+}[R_3N]_o$ for amine $[R_3N]$ solutions of four different initial amine concentrations in xylene; amine molarity: 0.256 (□), 0.12 (○), 0.0543 (▲), and 0.0235 (△).

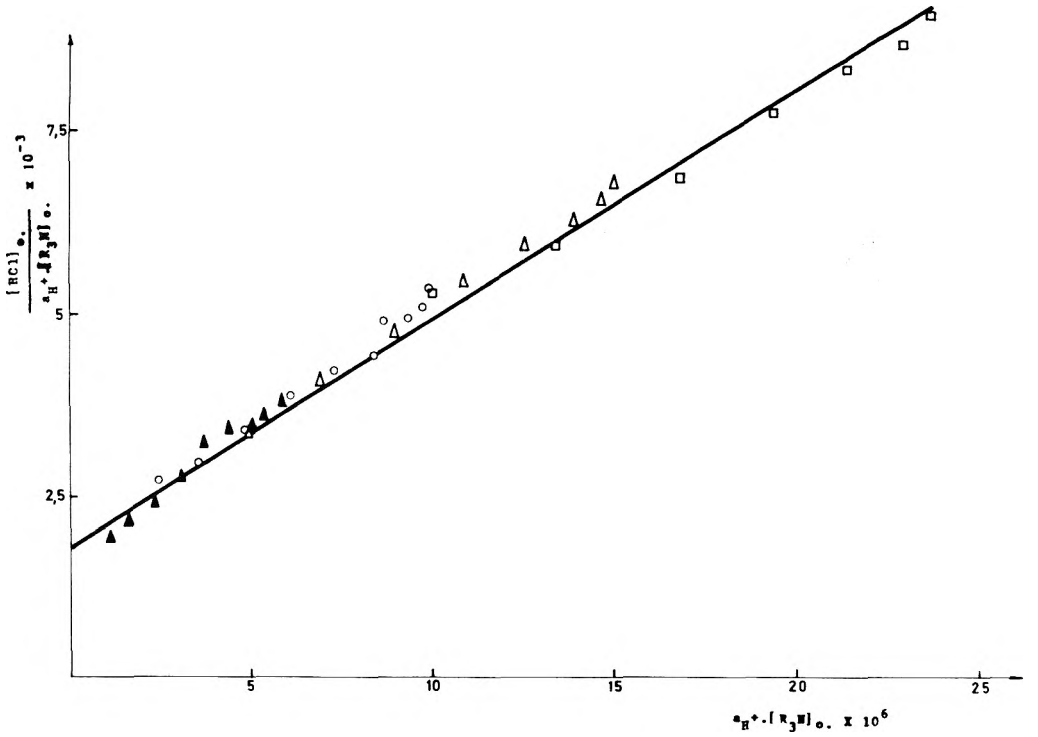

Figure 8. Plots of $[HCl]_o/a_{H^+}[R_3N]_o$ vs. $a_{H^+}[R_3N]_o$ for amine $[R_3N]$ solutions of four different initial concentrations in carbon tetrachloride; amine molarity: 0.242 (□). 0.113 (△), 0.0542 (○), and 0.0245 (▲).

to be identical with the difference between the initial or total amine concentration and the acid content of the organic phase at equilibrium, regardless of the initial or total amine concentration. Hence it can be concluded that $p = q$.

The values of $K_{pp'}$ may be determined with the values of $[HCl]_o$, a_{H^+}, and $[R_3N]_o$. The plots of $[HCl]_o/a_{H^+}[R_3N]_o$ vs. $a_{H^+}[R_3N]_o$ should give a straight line, if the only species present are the monomeric and dimeric ones. This appear to be so, as shown in Figures 6–8. The equilibria involved can then be written

$$R_3N + H^+ + Cl^- \rightleftarrows R_3NHCl$$

$$2R_3N + 2H^+ + 2Cl^- \rightleftarrows [(R_3NHCl)_2]$$

The values of the equilibrium constants of these reactions have been calculated.[28] From the values of K_1' and K_2' obtained, the values of K_1 and K_2 were determined in which the mean activity coefficient of a 1 M NaCl aqueous solution was used as the activity coefficient of the chloride ion. Considering the reaction

TABLE II: Equilibrium Constants of the Hydrochloride Salt of TIOA in Various Diluents

Diluent	log K_1[a]	log K_1[b]	log K_1[c]	log K_1[d]	log K_2	log K_d
Benzene	3.90		3.97	3.88	9.11	1.16
Xylene	3.48	3.47	3.52	3.52	8.67	1.63
Carbon tetrachloride	3.47	3.46	3.42	3.38	8.55	1.70
1,2-Dichlorobenzene	4.97		4.89			
1,2-Dichloroethane	6.07	6.04	6.06			
Dichloromethane	6.15					
Chloroform	5.74	5.67	5.70			

[a] Obtained from back-extraction technique data and alcalimetric determinations of aqueous acid concentrations at equilibrium. [b] Obtained from back-extraction technique data and pH determinations of aqueous acid concentrations at equibrium. [c] Obtained from direct extraction technique. [d] Obtained previously[8] from back-extraction technique data for amine salt concentrations equal to or smaller than 2.5×10^{-2} M, by pH measurements and alcalimetric determinations.

$$2R_3NHCl \overset{K_d}{\rightleftharpoons} (R_3NHCl)_2$$

$$K_d = [(R_3NHCl)_2]/[R_3NHCl]^2 = K_2/K_1^2$$

The data for the values of K_1, K_2, and K_d are summarized as follows:

	K_1	K_2	K_d
Benzene	9.40×10^3	1.30×10^9	14.6
Xylene	3.34×10^3	4.75×10^8	42.6
Carbon tetrachloride	2.66×10^3	3.59×10^8	50.7
1,2-Dichlorobenzene	7.80×10^4		
1,2-Dichloroethane	1.15×10^6		
Chloroform	5.10×10^5		

For the direct extraction method used here, the only direct comparison of our data which can be made is with those of Kojima et al.,[27] who used the same technique for the HCl salt of TOA in benzene. Our results in this diluent are considered to be in fairly good agreement with the corresponding equilibrium constants of $K_1 = (1.51 \pm 0.02) \times 10^4$; $K_2 = (2.92 \pm 0.07) \times 10^9$, and $K_d = 12.9 \pm 0.5$ found by the above mentioned authors for TOA·HCl. The differences which appear could be explained by the difference in the basic character of the two amines.

Our data indicate that the dimer formation ability is influence by the diluent such as benzene < xylene < carbon tetrachloride.

It appears that within the range of concentrations investigated, the aggregation, when it occurs, leads to the formation of dimeric species, excluding higher aggregates. Several investigators have already come to this conclusion.[1,2,4,27,29,30] Müller and Diamond[1] have found this for the hydrohalic salt of trilaurylamine, using the back-extraction technique and vapor pressure measurements (except for solutions in cyclohexane, where tetramers were found to exist). An average value of n from 1.47 to 1.74 is found for the hydrohalic salt of TLA in benzene.[1] Similar conclusions were reached by Fomin and Potapova[29] at a concentrations of 0.1–0.2 M for tri-n-octylammonium nitrate in carbon tetrachloride using boiling point measurements, and by Keder et al.[4] for hydrochloride and nitrate salts of trioctylamine in carbon tetrachloride, using NMR within the concentration range 0.1–0.5 M. Furthermore, a shift of the N–H proton resonances to lower magnetic fields upon dilution suggests that this is due to the break up of dimers.

However, such a simple mechanism leading to an equilibrium monomer $\rightleftarrows$ dimer is not absolute and high multimers seem to sometimes exist predominantly. Hogfeldt's results[12] are a good illustration of this.

TABLE III: Infrared Absorption Frequencies of Pure Triisooctylamine

Absorption frequencies, cm^{-1}	Assignment
1094	The valence vibration C–N
1162, 1360, 1374	Symmetric deformation vibration
1460	The CH_2 deformation vibration and the CH_3 asymmetric deformation vibration
2795	Vibration of C–H coupled to N of TIOA
2864	The CH_3 symmetric valence vibration
2920	The phase valence vibration of CH_2
2950	The CH_3 antisymmetric valence vibration

One interesting feature is that in diluents of low dielectric constant such as benzene, xylene, and carbon tetrachloride, dimer and multimer formation occurs only within a certain range of concentration for ammonium salts of tertiary amines.

There are so many factors which can interfere in the determination of the concentration range where polymerization starts, that it is impossible to give an order of magnitude of this concentration range. However, it is surprising to note an observable divergence while conditions remain nearly unchanged. For instance, Newmann and Klotz[20] suggested a relationship between the failure of the mass action law treatment of the experimental data and specific nonideality caused by polymerization of the monomers over 2×10^{-2} M in the extraction of HCl by TOA in benzene, while according to Mazurova and Gindin,[21] in toluene, up to 0.1 M, only the monomeric species exist. It seems, however, that aggregation is more favored in toluene than in benzene.

However, Mazurova and Gindin found a very slight increase in log K_1 on increasing the amine concentration from 0.0148 to 0.09227 M, which according to them is clearly due to some change in the activity coefficients of the organic phase.

What appears from this is that nonideal behavior has been interpreted by two different meanings. As a matter of fact deviation from Raoult's law may be attributed, at least partially, to nonspecific nonideal behavior of the solutes, e.g., a change in the activity coefficients of the organic phase solutes. Instead, the deviation of alkylammonium salt solutions from an ideal behavior can also be due to the aggregation of the solutes. Both approaches are correct but

TABLE IV: Infrared Absorption Frequencies (cm^{-1}) of TIOA and Its Hydrochloride Salt in Chloroform and 1,2-Dichloroethane

TIOA in $CHCl_3$	TIOA in CH_2Cl-CH_2Cl	Hydrochloride salt of TIOA in $CHCl_3$	Hydrochloride salt of TIOA in CH_2ClCH_2Cl
		1011	
1092		1060	
		1075	
1163		1115	
1364	1364	1365	
1376	1378	1378	1378
1460	1460	1465	1465
1660	1660		1605
1712	1712		
		1720	1720
2800 shoulder	2800 shoulder	2360	2360
2864	2864	2868	2868
2920	2920	2920	2920
2950	2950		

they need to be clearly distinguished and it is usually rather difficult to choose between these two reasons.[31]

In fact experience has shown that the determination of activity coefficients of the organic phase solutes under changing conditions in a multicomponent extraction system is a formidable task. Furthermore, the activity coefficients estimates in various solvent extraction systems are only exceptionally of general thermodynamic validity. Hence, the only quantitative process to be considered is related to aggregation.

The different sets of results for the values of the semithermodynamic equilibrium constants are given in Table II.

These differences are due to the different methods used.

C. *Infrared Study.* Some infrared absorption bands appearing in our spectra are listed in Tables III and IV. The band at 1090 cm^{-1} is assigned to C–N stretching according to Bullock et al.[32] In comparing the spectrum of TIOA with that of TIOA solution in chloroform, a small lowering of the C–N stretching frequency was observed. This could be due to specific interaction (hydrogen bonding) between the diluent and the amine. This band disappears in TIOA·HCl salt solutions, corroborating the data in the literature.[32,33] In the salt solution a frequency shift to 1070 cm^{-1} is observed; this can be interpreted as meaning that the nitrogen doublet is no longer free, the ammonium cation C–N–H^+ being formed. This band appears even to be a doublet with a maximum of low intensities at 1073 and 1060 cm^{-1}.

The origin of the band at 1712 cm^{-1} for the amine solution which is shifted to 1720 cm^{-1} for the hydrochloride salt is not clear. Other authors have also not given any assignment to this band.[32]

The infrared spectrum of TIOA shows a band at 2795 cm^{-1} which is attributed to C–H stretching.

In chloroform solution, the hydrogen is bound to the nitrogen of the amine. There follows a weakening of the bond between the free electrons of the nitrogen and the C–H[33] stretching; the band at 2795 cm^{-1} becomes a small shoulder and shifts to 2800 cm^{-1}. This change cannot be attributed to the diluent for which, in this region, bands are weak or nonexistant, because of the diluent compensation technique.

The protonated form of the amine N–H^+ produces a broad band with a maximum at 2360 cm^{-1} and perhaps at 1011 cm^{-1}. According to Bullock et al.[32] for the MDOA salt of hydrohalic acids, the series of bands in the region 2400–2700 cm^{-1} is assigned to N–H^+ stretching modes in N–H^+···X^-, the frequencies depending on X^-. For the band at 2360 cm^{-1} in chloroform and 1,2-dichloroethane, Beer's law appeared to be valid. No frequency shift or broadening was observed with change of concentration. Complete and partial spectra of the hydrochloride salt of TIOA were taken to determine the acid content of the organic phase. Absorption of standard organic solutions containing respectively 5:7.5:10:20:50:60:70:80:90 and 100 mM were recorded. The plot of log (I_0/I) vs. acid content of the organic phase gives a straight line up to a concentration of 70 mM, where Beer's law ceases to be valid. Very good agreement was found for the acid content determined either potentiometrically or by ir absorbance at 2360 cm^{-1}. The values of the equilibrium constant calculated from ir measurements were consistent within 0.1%.

Supplementary Material Available: a complete listing of the equilibrium constants (6 pages). Ordering information is available on any current masthead page.

References and Notes

(1) R. M. Diamond, "Solvent Extraction Chemistry", North Holland, Amsterdam, 1967, pp 349–361; R. M. Diamond and D. G. Tuck, *Prog. Inorg. Chem.*, **2**, 109 (1960); W. Müller and R. M. Diamond, *J. Phys. Chem.*, **70**, 3469 (1966); J. J. Bucher and R. M. Diamond, *ibid.*, **69**, 1565 (1965); W. Müller, *Actinides Rev.*, **1**, 71 (1967).

(2) G. Duyckaerts, J. Fuger, and W. Müller, EURATOM Report No. EUR 426.F, Brussels, Belgium, 1963; W. Müller, G. Duyckaerts, and J. Fuger in "Solvent Extraction Chemistry of Metals", H. A. C. Mc Kay, T. B. Healey, I. L. Jenkins, and A. E. Naylor, Ed., Macmillan, London, 1966, p 233; W. Müller and G. Duyckaerts, EURATOM Report No. 2246 e, 1965.

(3) F. L. Moore, NAS-NS-3101, National Academy of Sciences, Nuclear Science Series, Office of Technical Services, Department of Commerce, Washington 25, D.C., 1960; F. L. Moore, *Anal. Chem.*, **29**, 1660 5 (1967); **30**, 908 (1958).

(4) W. E. Keder and A. S. Wilson, *Nucl. Sci. Eng.*, **17**, 287 (1963); W. E. Keder, A. S. Wilson, and L. L. Burger, Symposium on Aqueous Reprocessing Chemistry for Irradiated Fuels, Brussels, Belgium, 1963 (HWSA-2959); A. S. Wilson and N. A. Wogman, *J. Phys. Chem.*, **66**, 1552 (1962); W. E. Keder and L. L. Burger, *ibid.*, **69**, 3075 (1965).

(5) C. F. Coleman, *At. Energy Rev.*, 2, 3 (1964); *Nucl. Sci. Eng.*, **17**, 274 (1963); C. F. Coleman and J. W. Roddy, "Solvent-Extraction Chemistry", North-Holland, Amsterdam, 1967, pp 362–367; J. W. Roddy and C. F. Coleman, *J. Inorg. Nucl. Chem.*, **30**, 3600 (1969).

(6) G. Markovits and A. S. Kertes, "Solvent Extraction Chemistry", North Holland, Amsterdam, 1967, pp 390–397; A. S. Kertes and G. Markovits, *J. Phys. Chem.*, **72**, 4202 (1968); A. S. Kertes, *J. Inorg. Nucl. Chem.*, **27**, 209 (1965).

(7) R. Kollar, V. Plichon, and J. Saulnier, *Bull. Soc. Chim. Fr.*, 2193 (1967).

(8) A. S. Vieux, *Bull. Soc. Chim. Fr.*, 3364, 3366 (1969); A. S. Vieux, N. Rutagengwa, J. B. Rulinda, and A. Balikungeri, *Anal. Chim. Acta*, **68**, 415 (1974); A. S. Vieux, *Bull. Soc. Chim. Fr.*, 4281 (1968); *C.R. Acad. Sci.*, **265**, 987, 1158 (1967).

(9) J. M. P. F. Verstegen, *Trans. Faraday Soc.*, **58**, 1878 (1962); J. M. P. F. Verstegen and J. A. A. Ketelaar, *ibid.*, **57**, 1527 (1961).

(10) M. L. Good, *J. Inorg. Nucl. Chem.*, **25**, 467 (1963).

(11) G. Scibona, R. A. Nathan, A. S. Kertes, and J. W. Irvine, Jr., *J. Phys. Chem.*, **70**, 735 (1966); G. Scibona, S. Basol, F. Orlandini, and P. R. Danesi, *J. Inorg. Nucl. Chem.*, **28**, 1441 (1966).

(12) E. Hogfeldt and F. Fredlund, *Acta Chem. Scand.*, **18**, 543 (1964); E. Hogfeldt and F. Fredlund, *Trans. R. Inst. Technol., Stockholm*, **27**, 226 (1964); E. Hogfeldt, B. Bolander, and F. Fredlund, *ibid.*, **225**, 26 (1964); Proceedings of the 7th International Conference on Coordination Chemistry, Stockholm, June 1962, Paper 7 M4; E. Hogfeldt, P. Danesi, and F. Fredlund, *Acta Chem. Scand.*, **25**, 1338 (1971); E. Hogfeldt, *Sven. Kem. Tidskr.*, **76**, 4 (1964); L. Kuca and E. Hogfeldt, *Acta Chem. Scand.*, **25**, 1261 (1961); M. A. Lodhi and E. Hogfeldt, "Solvent Extraction Chemistry", North Holland, Amsterdam, 1967, p 421; E. Hogfeldt and De Jesus Tavares, *Trans. R. Inst. Technol., Stockholm*, 228 (1964); E. Hogfeldt, F. Fredlund, and K. Rasmusson, *ibid.*, 229 (1964).

(13) C. D. Strehlov, M.S. Thesis, MIT, 1964.

(14) W. Knoch, *J. Inorg. Nucl. Chem.*, **26**, 1085 (1964).

(15) C. Peak, M.S. Thesis, MIT, 1959.

(16) J. J. Lawrence, *J. Inorg. Nucl. Chem.*, **11**, 69 (1959).

(17) U. Bertocci, AERE/R 2933 (1959).

(18) C. Krauss, *J. Phys. Chem.*, **60**, 129 (1956).

(19) R. A. Robinson and R. H. Stokes, "Electrolyte Solutions", 2nd ed, Butterworths, London, 1959.

(20) L. Newmann and P. Klotz, *J. Phys. Chem.*, **65**, 796 (1961).
(21) A. A. Mazurova and L. M. Gindin, *Russ. J. Inorg. Chem.*, **10**, 1389 (1965).
(22) J. Bizot and B. Tremillon, *Bull. Soc. Chim. Fr.*, 129 (1959).
(23) G. Charlot and B. Tremillon, Les réactions Chimiques dans les Solvants et les sels Fondus, Gauthier-Villars, Paris, 1963, p 594.
(24) B. Warnquist, *Acta Chem. Scand.*, **21**, 1353–1367 (1967).
(25) R. G. Bates and E. A. Guggenheim, *Pure Appl. Chem.*, **1**, 163 (1960).
(26) H. S. Harned and B. B. Owen, "The Physical Chemistry of Electrolytic Solutions", Reinhold, New York, N.Y., 1950, p 453.
(27) T. Kojima, H. Fukutoni, and K. Kakihana, *Bull. Chem. Soc. Jpn.*, **42**, 875 (1969).
(28) L. G. Sillen and N. Ingri, *Ark. Kemi*, **23**, 97–121 (1964).
(29) V. V. Fomin and V. T. Potapova, *Russ. J. Inorg. Chem.*, **8**, 5098 (1963).
(30) M. Taube, *J. Inorg. Nucl. Chem.*, **12**, 174 (1959); **15**, 171 (1960).
(31) A. S. Kertes, *Natl. Stand. Ref. Data Ser., Natl. Bur. Stand.*, **No.** (G).102.
(32) J. I. Bullock, S. S. Choi, D. A. Goodrick, D. G. Tuck, and E. J. Woodhouse, *J. Phys. Chem.*, **68**, 2687 (1964).
(33) H. Brusset, G. Duboc, and F. Haffner, *Bull. Soc. Chim. Fr.*, 3546–3555 (1968).

Rates of Crystallization and a Model for the Growth of NaY Zeolites

Hartmut Kacirek and Hans Lechert*

Institute of Physical Chemistry of the University of Hamburg, 2 Hamburg 13, Laufgraben 24, Germany *(Received December 5, 1975)*

Publication costs assisted by the Institute of Physical Chemistry of the University of Hamburg

Starting from the results of a previous paper, in which the validity of a simple kinetic equation for the growth of zeolites of the faujasite type has been shown, the influences of various parameters on the rate of crystallization are reported. In the considered range of concentration the linear crystallization rate proves to be proportional to the concentration of the silicate in the solution phase for final products of equal Si/Al ratios. The crystallization rate varies for the growth of zeolite X to that of zeolite Y of an Si/Al ratio of 3.4 over three orders of magnitude. Simultaneously, the apparent activation energy of this growth is increased considerably. Based on the experimental results, a model for the explanation of the crystallization process is developed. The rate-determining step seems to be given by the connection of silicate species, specific for the special structure, to the surface of the crystal.

Introduction

In earlier investigations of Kerr[1,2] and Ciric[3] the crystallization of X- and also of A-type zeolites has been found to be an autocatalytic process. This is in agreement with the observations of Breck and Flanigen[4] and Mirskii and Pirozhkov[5] that generally the formation of zeolites is accelerated by nuclei already present in the reaction mixture. More detailed kinetic studies on the growth of several zeolite species have been reported by Zhdanov,[6] Meise and Schwochow,[7] and Culfaz and Sand.[8]

In previous investigations we were able to achieve a strict separation of the processes of nucleation and growth for the crystallization of faujasite[9] over a wide range of compositions of the final product, by suspending seed crystals of NaX in the aluminosilicate gel. The NaX has the faujasite structure, but a low Si/Al ratio and can be easily synthesized with small particle sizes in contrast to faujasites with high Si/Al ratio. In the previous paper[9] it has been shown that the growth of the faujasites obeys a rather simple equation given by

$$\frac{dx}{dt} = 3kx^{2/3}\left(\frac{x}{\bar{r}_0^3}\right)^{1/3} \qquad (1)$$

In this equation x is the mole fraction for the amount of faujasite already crystallized, where "mole" means in this case a formula unit $NaAlO_2 \cdot nSiO_2$. x_0 is the mole fraction at the time $t = 0$, which is equal to the amount of seeds suspended in the gel in the above mentioned experiment. The value of x_0 is given with respect to the total amount of aluminosilicate. $\bar{r}_0$ is the average radius of the seed crystals. The integrated form of the eq 1 describes the course of the crystallization

$$x = x_0 + 3k\frac{x_0}{\bar{r}_0}t + 3k^2\frac{x_0}{\bar{r}_0^2}t^2 + k^3\frac{x_0}{\bar{r}_0^3}t^3 \qquad (2)$$

Solving the eq 2 to the rate constant k, one obtains

$$k = \left(\sqrt[3]{\frac{x}{x_0}} - 1\right)\frac{\bar{r}_0}{t} \qquad (3)$$

The validity of this equation has been carefully checked in the investigations of the previous paper[9] carrying out experiments with different amounts of seeds x_0 and also with seed crystals with different average radii $\bar{r}_0$. The crystallization time t and the activation energy of the growth has not been studied in detail in the reported investigations. These parameters shall be studied in this paper together with some suggestions on a possible mechanism of the growth of the faujasite crystals.

Experimental Section

a. *Sample Preparation.* The aluminosilicate gels were prepared by mixing water glass solution and alkaline aluminate solutions. Some hours after gelling the seeds of the zeolite NaX have been added under stirring and subsequent shaking. The seeds had an average radius of 0.23 μm and were stored and used as an aqueous suspension. The batches were tempered on a water bath. At time intervals samples were taken, which were filtered and washed to near neutrality.

b. *Analysis of the Products.* The composition of the sam-

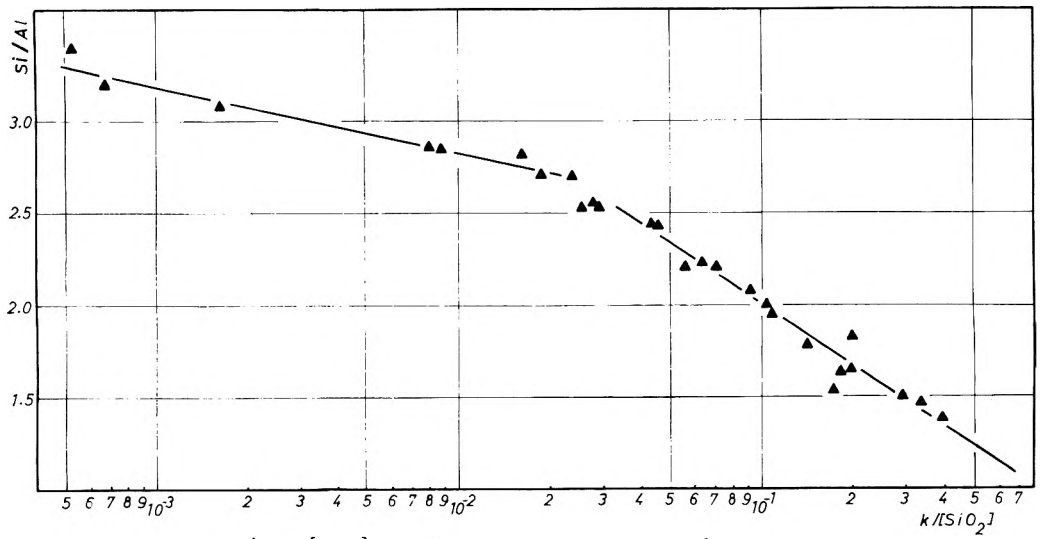

Figure 1. Dependence of rate constants $k' = k/[SiO_2]_{sol}$ on Si/Al ratio of faujasites at 88 °C.

TABLE I: Experimental Determination of the Rate Constants k for the Growth of Faujasite with Different Si/Al Ratios from Batches with Different Compositions

Sample	SiO_2/AlO_2^-	Na–Al/SiO_2	H_2O/AlO_2^-	$SiO_{2\,sol}$, M	10^3k, μm/h	$10^3k/SiO_{2\,sol}$	Si/Al
319	5.0	2.5	400	0.515	200	388	1.39
323	2.1	1.06	160	0.231	75	325	1.47
320	5.0	2.0	400	0.500	145	290	1.50
327 I	2.1	1.06	400	0.102	17	167	1.53
324	2.5	0.98	195	0.380	70	184	1.63
321	5.0	1.5	400	0.477	90	190	1.65
328 I	3.0	0.92	400	0.174	25	144	1.78
325	3.0	0.92	235	0.283	58	205	1.83
322	5.0	1.0	400	0.435	49	110	1.95
326	4.1	0.83	320	0.370	38	103	2.02
290	4.0	0.83	400	0.274	25	91	2.08
329 I	5.0	0.78	400	0.400	28	71	2.20
276	5.0	0.78	400	0.400	22	55	2.20
291	5.0	0.78	400	0.396	25	63	2.22
277	6.0	0.75	400	0.509	23	44	2.40
303	6.0	0.75	400	0.510	24	46	2.43
292	7.0	0.73	400	0.638	17	26	2.52
300	7.0	0.73	400	0.638	19	29	2.52
330 I	7.5	0.72	400	0.706	19	27	2.54
301	8.0	0.71	400	0.756	18	24	2.69
278	8.0	0.71	400	0.755	15	19	2.70
302	9.0	0.70	400	0.830	14	16	2.82
293	10.0	0.69	400	1.02	8	8	2.85
279	10.0	0.69	400	1.02	9	9	2.89
294	12.0	0.67	400	1.27	2.0	1.6	3.08
295	14.0	0.65	400	1.54	1.0	0.7	3.19
296	14.0	0.65	600	1.01	0.53	0.5	3.40

ples has been determined by x-ray analysis. The error limit was less than 4%. Problems arising from the application of this method to the zeolite samples are discussed extensively in the previous paper.[9] The Si/Al ratio was determined by x-ray fluorescence analysis within an error limit 1%. Additionally the particle size distribution was determined from scanning electron micrographs.

Results and Discussion

The first experiments were carried out in which the dependence of the crystallization time on the Si/Al ratio of the final product was studied.

The experiments were done at a temperature of 88 °C. The values of x_0 and $\dot{r}_0$ were kept constant. From the values obtained for x and t, the rate constants then were calculated using eq 3. The results of these experiments are summarized in Table I. From the values given in this table it can be seen that generally the crystallization time increases with increasing Si/Al ratio in the final products, which results in decreasing values of k.

Assuming now that all concentration equilibria between the amorphous solid phase and the liquid phase are established, the Si/Al ratios of the final crystallization products are determined by the ratios $[SiO_2]/[AlO_2^-]$, $[Na–Al]/[SiO_2]$, and $[H_2O]/[AlO_2^-]$. Therefore, it is possible to obtain crystallization products with the same Si/Al ratio from batches with different initial compositions. In these cases, however, the crystallization rates dx/dt are different. A direct relation

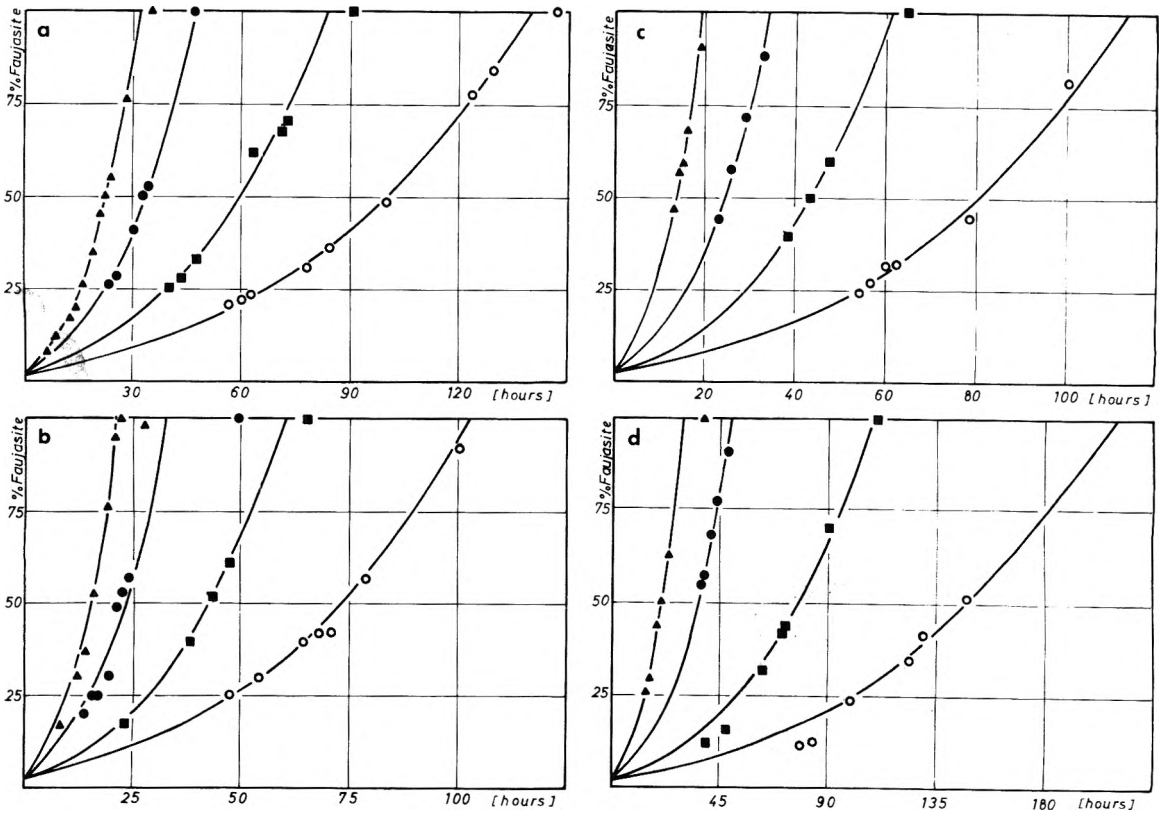

Figure 2. Crystallization curves for faujasite growth of samples 327 (a), 328 (b), 329 (c), and 330 (d) at 58, 68, 78, and 88 °C considering eq 2.

between the Si/Al ratio of the final products and this crystallization rate can be established if the rate is referred to the concentration of the amount of silicate in the solution phase:

$$\mathrm{Si/Al} = \mathrm{f}[k'(T)] \qquad k' = k/[\mathrm{SiO_2}]_{\mathrm{sol}} \tag{4}$$

The concentration $[SiO_2]_{sol}$ of the silicate in the solution has been calculated from the silica content of the batch, the Si/Al ratio, and the amount of crystalline faujasite.

In Figure 2 the crystallization curves for faujasites with different Si/Al ratios at temperatures of 58, 68, 78, and 88 °C are shown. In Figure 3 the rate constant k', taken from these curves, is plotted against the reciprocal temperature. From this plot a relation between the apparent activation energy and the Si/Al ratio can be obtained which is shown by the data of Table II. The values of the Table II show a steady increase of the apparent activation energy with increasing Si/Al ratio.

Our activation energies values agree fairly well with the value of Zhdanov[6] for the growth of zeolite A of 10 kcal/mol as well as with the values of 15 and 14 kcal/mol found by Breck and Flanigen[4] for the formation of X- and Y-zeolites, respectively. It should be kept in mind, however, that under the conditions chosen by the authors, the activation energies are composed of a number of temperature dependent parameters in a quite complicated way.

To further discuss of the mechanism of faujasite growth, the results, obtained in the previous paper[9] and in this paper, important for this discussion are summarized: (a) The rate of the crystal growth can be described by an equation (eq 1) which is identical with that of a homogeneous reaction. (b) The growth of the crystals takes place at the interface between the crystals and the solution and not by a direct conversion of the aluminosilicate gel. (c) The rate of the crystallization is proportional to the actual surface O (x) of the crystals already present in the reaction mixture. (From this statement eq 1–3 have been derived, the validity of which has been shown in the previous paper,[9] as already mentioned.) (d) The rate of the crystal growth of faujasites with equal composition is proportional to the SiO_2 concentration in the liquid phase within the investigated range of concentrations. The concentration of the aluminate has no influence on the crystallization rate. (e) The rate constant k decreases with increasing Si/Al ratio of the crystallization product. Within the range of Si/Al ratios from 1.4 to 3.4 a variation of k over three orders of magnitude can be observed.

Simultaneous Apparent Activation Energy Increases. As the rate-determining step, giving also the activation energy, Culfaz and Sand[8,10] suggest a diffusion process of the reacting species. The high value of 15 kcal/mol, instead of about 3–5 kcal/mol expected for diffusion in solutions, is explained by the high viscosity of the solution in the gel structure. In case of the diffusion as the rate-determining step, however, eq 1–3 which clearly indicate the dependence of the crystallization rate on the surface of the crystals in the reaction mixture, should not be realized. As a first step for an explanation of the crystallization mechanism it seems to be helpful to look at the molecular species being necessary to build up the faujasite structure for different Si/Al ratios and also those present in solution under conditions of the crystallization of these products.

Investigations of McNicol et al.[11,12] indicate that the solutions in equilibrium with aluminosilicate gels used in zeolite synthesis contain different silicate species and only one monomeric aluminate ion. Especially, these investigations show that the solution contains no aluminosilicate. Therefore, the process of the dissolution of the amorphous aluminosilicate is strictly connected with the hydrolysis of all Si–O–Al bonds,

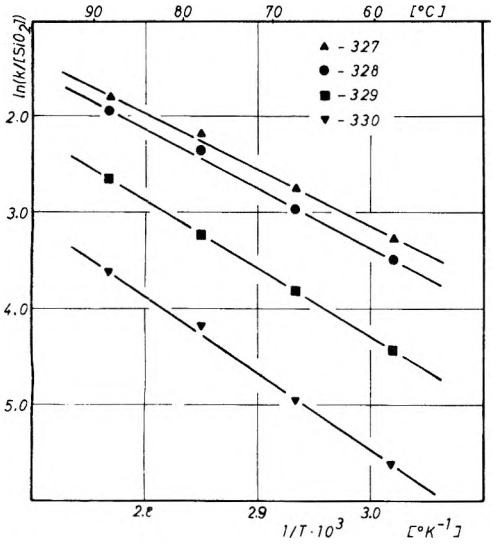

Figure 3. Dependence of rate constant k' for faujasite growth on the reciprocal temperature.

TABLE II

Samples	Si/Al	kcal/mol	Batch composition
327	1.53	11.8	$NaAlO_2 \cdot 2.1(Na_{1.06}H_{2.94}SiO_4)400H_2O$
328	1.78	12.3	$NaAlO_2 \cdot 3.0(Na_{0.92}H_{3.08}SiO_4)400H_2O$
329	2.20	14.1	$NaAlO_2 \cdot 5.0(Na_{0.78}H_{3.22}SiO_4)400H_2O$
330	2.54	15.6	$NaAlO_2 \cdot 7.5(Na_{0.73}H_{3.27}SiO_4)400H_2O$

and the formation of these bonds in the final product must necessarily occur during the crystallization process.

Because of the Loewenstein rule[13] a faujasite with Si/Al = 1 can only be built up by an alternative arrangement of SiO_4 and AlO_4 tetrahedra. The formation of such a structure is only possible by linking monomeric aluminate with monomeric silicate units and the exclusive formation of Si–O–Al bonds. This is demonstrated in Figure 4a by a two-dimensional, "pressed" representation of the faujasite structure.

Representations of this kind prove useful for studies of the possible arrangements of SiO_4 and AlO_4 tetrahedra in the faujasite structure with different Si/Al ratios. For an Si/Al ratio of 1.18 one AlO_4 tetrahedron must be substituted by one SiO_4 tetrahedron in a cuboctahedron. By this procedure four Si–O–Si bonds are formed. Eight SiO_4 tetrahedra in the respective cuboctahedron remain surrounded by four AlO_4 tetrahedra, four SiO_4 tetrahedra are connected with three AlO_4 and one SiO_4, and the replaced SiO_4 is surrounded only by SiO_4 tetrahedra. The whole structure is demonstrated in Figure 4b. The structure of the arrangement of the SiO_4 tetrahedra is shown in the following schematic drawing:

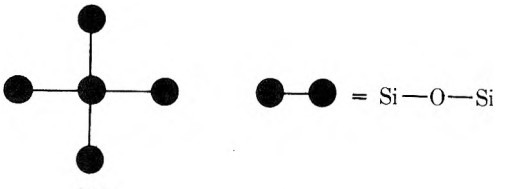

FK

This silica species cannot be expected to exist in solution and must, therefore, be formed in a first crystallization step either from five monomers, from three monomers and one dimer, or from two monomers and one trimer. The process of forming these species is most likely the rate-determining step of the growth.

To an X-type faujasite with Si/Al = 13/11 = 1.18, taking a single cuboctahedron and a statistical distribution of the substituting SiO_4 tetrahedron by a linking of the above discussed arrangements FK, the following average arrangements should occur:

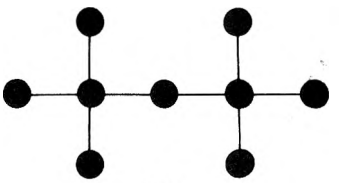

NK

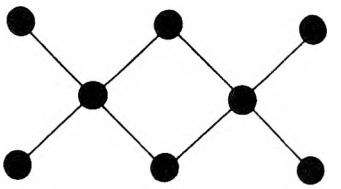

EK

These arrangements are linked in turn to more complicated structures (HK) with a low probability of occurrence. For an X-type faujasite with Si/Al = 1.18, the complete distribution of the mentioned species is given by:

M	FK	NK	EK	HK
61.5%	26.4%	4.4%	5.4%	2.3%

For an Si/Al ratio of 14/10 = 1.4 arrangement FK is proposed to occur twice and also the arrangements derived from FK occur with increased probability (Figure 4c).

Looking at the silicate species which might be present in solution during the crystallization process, it should be mentioned that the species EK can be formed readily by monomer ions and a four-membered ring shaped silicate ion. Proceeding to Si/Al = 15/9 = 1.67, FK occurs three times with a respectively increased probability of the occurrence of the other species (Figure 4d). Deviating from the situation at the lower Si/Al ratios for Si/Al = 1.67, the occurrence of "p-structure" arrangements is possible: The notations "p structure" and "o structure" for the arrangements discussed until now has been chosen by Dempsey[14] according to the notation of the isomers of the substitution products of benzene. Accordingly in an o structure two AlO_4 tetrahedra are separated by one or by three SiO_4 tetrahedra, respectively. In a p structure, on the other hand, these AlO_4 tetrahedra are separated twice by two SiO_4 tetrahedra corresponding to the substituents in a *p*-benzene substitution product (Figure 4e). For mixed o–p structures there are not any characteristic arrangements of SiO_4 tetrahedra. Mainly, the following arrangements occur:

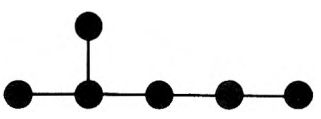

Linking two of these arrangements, for instance, the following is formed:

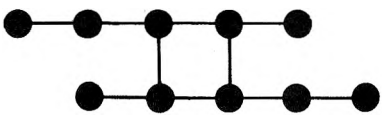

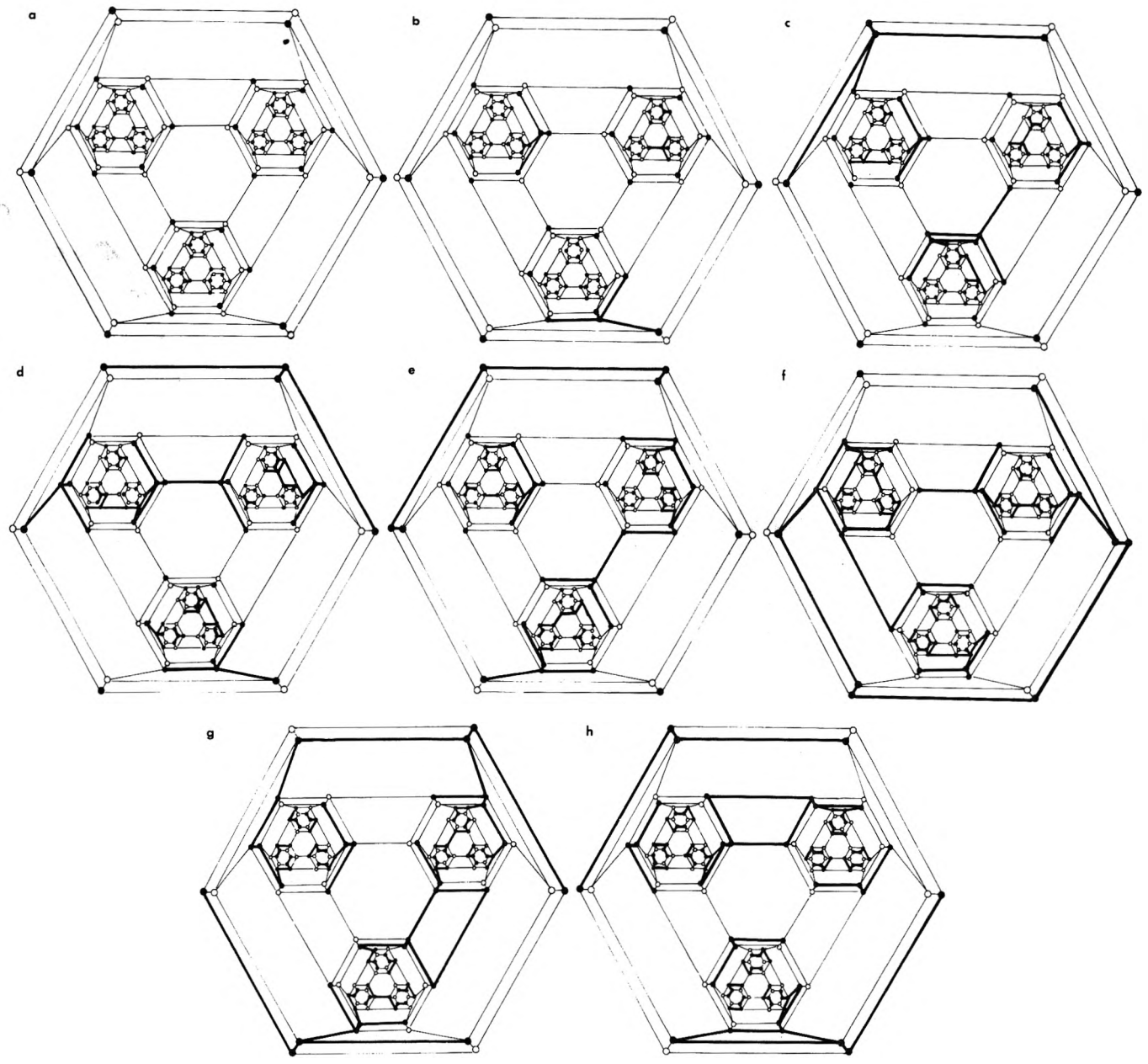

Figure 4. "Pressed" representations of faujasite structure with different Si/Al ratios (O—● = Al–O–Si, ●—● = Si–O–Si): (a) Si/Al = 1.0; (b) Si/Al = 1.18; (c) Si/Al = 1.4; (d) Si/Al = 1.67, o structure; (e) Si/Al = 1.67, o–p structure; (f) Si/Al = 2.0, o–p structure, (g,h) Si/Al = 2.0, p structure.

Beside this, simple dimer silicates can occur:

At Si/Al = 16/8 = 2.0, beside o and o–p structures, the occurrence of pure p structures is possible. These structures can be constructed by using only linear tetramers and its linkages, respectively:

These arrangements may lead to chains of four-membered rings, where the linkage is possible in the 1,2 or in 1,3 position demonstrated in the following:

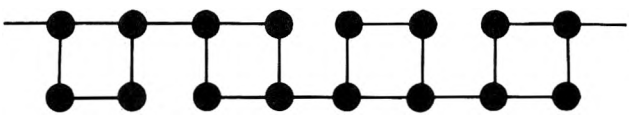

These arrangements are extended over the whole crystal structure. Investigations of the silicate species in alkaline silicate solutions allow at least some qualitative arguments. Following McNicol et al.[11,12] the silicate ion occurs only as monomer in solutions leading to the crystallization of zeolite A. Higher condensed silicates can be found for lower alkali contents and higher silica concentrations. Ir investigations of solutions of this kind, carried out by Beard,[15] show variations of the degree of condensation from 1 to about 10^6 changing only the ratio SiO_2/H_2O. Lagerström[16] has observed in 0.5 *m* solutions, of the composition $Na_mH_{4-m}SiO_4$ with $m = 0.7$ to 1.05, monomers of the kind $Si(OH)_4$, $SiO(OH)_3^-$, $SiO_2(OH)_4^{4-}$, oligomers of the kind $Si_2O_3(OH)_4^{2-}$, and the ring-shaped ion $Si_4O_8(OH)_4^{4-}$. With increasing dilution the ring shaped ion $Si_4O_6(OH)_6^{2-}$ is formed to an increasing extent. Similar results have been reported by Ingri et al.,[17] and in

quite detailed investigations by Aveston[18] and Engelhardt, Wieker et al.[20]

Transferring these results to solutions present in our systems with crystallizing faujasites, it can be seen that under the conditions of the crystallization of the X-type zeolites with low Si/Al ratio, the solution contains preferably monomers and dimers with higher condensed species present only in unimportant amounts.

In the range of Si/Al = 1.4 to 2.0, the so called "transition region", an intermediate degree of condensation from 2 to about 4 can be assumed. For the conditions of synthesis of faujasites of the Y-type from 2.0 to 3.4, the average degree of condensation should be in the range of 4 to 20. For a final elucidation of these problems, further investigations on the relation between the kind of silicate species, the crystallization rate of a special zeolite structure, and the distribution of the AlO_4 and SiO_4 tetrahedra in this structure are necessary. First experiments have been carried out with the molybdato method of Stade and Wieker[19] which allow at least a rough indentification of the silicate species present in the initial solution as well as in a solution obtained by an acid decomposition of the zeolite by attack of the Al–O–Si bonds. These experiments confirm the discussed ideas for low Si/Al ratios, and give some hints on the silicate species present for higher silica contents of the faujasites.

Acknowledgment. The authors thank the "Deutsche Forschungsgemeinschaft" and the "Fonds der chemischen Industrie" for financial support of their work.

References and Notes

(1) G. T. Kerr, *J. Phys. Chem.*, **72**, 1385 (1968).
(2) G. T. Kerr, *J. Phys. Chem.*, **70**, 1047 (1966).
(3) J. Ciric, *J. Colloid. Interface Sci.*, **28**, 315 (1968).
(4) D. W. Breck and E. M. Flanigen, "Molecular Sieves", Society of Chemical Industry, London, 1968, p 47.
(5) Y. V. Mirskii and V. V. Pirozhkov, *Russ. J. Phys. Chem.*, **44**, 1508 (1970).
(6) S. P. Zhdanov, *Adv. Chem. Ser.*, **No 101**, 20 (1971).
(7) W. Meise and F. E. Schwochow, *Adv. Chem. Ser.*, **No 121**, 169 (1973).
(8) A. Culfaz and L. B. Sand, *Adv. Chem. Ser.*, **No. 121**, 140 (1973).
(9) H. Kacirek and H. Lechert, *J. Phys. Chem.*, **79**, 1589 (1975).
(10) A. Culfaz and L. B. Sand, "Proceedings of the Third International Conference on Molecular Sieves", Leuven University Press, 1973, p 21.
(11) B. D. McNicol, G. T. Pott, K. R. Loos, and N. Mulder, *Adv. Chem. Ser.*, **No 121**, 152 (1973).
(12) B. D. McNicol, G. T. Pott, K. R. Loos, and N. Mulder, ref 10, p 23.
(13) W. Loewenstein, *Am. Mineral.*, **39**, 92 (1954).
(14) E. Dempsey in ref 4, p 293.
(15) W. C. Beard, *Adv. Chem. Ser.*, **No 121**, 162 (1973).
(16) G. Lagerström, *Acta Chem. Scand.*, **13**, 722 (1959).
(17) N. Ingri, *Acta Chem. Scand.*, **13**, 758 (1959).
(18) J. Aveston, *J. Chem. Soc.*, 4444 (1965).
(19) E. Thilo, W. Wieker, and H. Stade, *Z. Anorg. Allg. Chem.*, **340**, 261 (1965).
(20) G. Engelhardt, D. Zeigan, H. Jancke, D. Hoebbel, and W. Wieker, *Z. Anorg. Allg. Chem.*, **418**, 17 (1975).

On the Mechanism of Ion Exchange in Zirconium Phosphates. 15. The Effect of Crystallinity of the Exchanger on Li^+/H^+ Exchange of α-Zirconium Phosphate

Abraham Clearfield* and Dinko A. Tuhtar[1]

Department of Chemistry, Ohio University, Athens, Ohio 45701 *(Received November 14, 1975)*

Publication costs assisted by the Petroleum Research Fund

The effect of the crystallinity of α-zirconium phosphate exchangers upon Li^+/H^+ exchange reactions was investigated. The most crystalline exchanger formed three exchanged phases of approximate composition $ZrLi_{0.9-1.04}H_{1.1-0.96}(PO_4)_2 \cdot 4H_2O$, $ZrLi_{1.33-1.50}H_{0.67-0.50}(PO_4)_2 \cdot 4H_2O$, and $Zr(LiPO_4)_2 \cdot 4H_2O$. As the crystallinity of the exchanger decreases the composition ranges of the exchanged phases broaden until with amorphous exchangers only a single solid solution is obtained. The exchange reaction with the amorphous zirconium phosphate is reversible with $K_{Li/H} = 6.2 \times 10^{-5}$.

Introduction

In part II of this series we presented the results of ion-exchange titrations using LiCl + LiOH as titrant on a crystalline zirconium phosphate (α-ZrP) exchanger.[2] Two endpoints were observed, one corresponding to the formation of $Zr(LiPO_4)_{1.33}(HPO_4)_{0.67} \cdot 4H_2O$ and the other to the fully exchanged phase $Zr(LiPO_4)_2 \cdot 4H_2O$. A somewhat similar result was reported by Harvie and Nancollas.[3] Subsequently, Alberti et al. showed that when a highly crystalline sample of α-ZrP is used in the titrations, three endpoints are obtained.[4] A detailed study of the effect of crystallinity on Na^+/H^+ exchange isotherms has in fact shown that significant differences are evident even in highly crystalline α-ZrP samples whose x-ray diffraction patterns appear almost identical.[5] Thus, in order to reconcile the differences in the observed Li^+/H^+ results, a more comprehensive study of the effect of crystallinity of the exchanger on the ion-exchange process was undertaken.

Experimental Section

Preparation of Zirconium Phosphates. The exchanger samples were prepared as described earlier.[6] Portions of an amorphous gel were refluxed in 0.5 M H_3PO_4 for 48 h (0.5:48),

4.5 M H_3PO_4 for 48 h (4.5:48), etc., up to 12:384. The refluxed solids were washed extensively and dried at 50 °C for 1 week.

Characterization of the Exchangers. Zirconium was determined gravimetrically by precipitation with cupferron.[7] The exchanger samples (0.3–0.4 g) were first dissolved in 1 ml of concentrated HF, diluted, and made 10% in H_2SO_4 before precipitation. The phosphate content was determined, on separate samples, spectrophotometrically at 315 nm by the molybdovanadate method.[8] Water contents were determined as loss on ignition to 800 °C. Thermogravimetric analysis (TGA) was carried out at a heating rate of 5°/min under a helium atmosphere on a Tem-Pres Model TG-2A unit. Similarly differential thermal analysis curves (DTA) were obtained with a Tem-Pres DT-712 unit at a heating rate of 17°/min. Reagent grade Al_2O_3 was used as a reference standard. X-ray diffraction patterns were taken with a North American Philips (Norelco) wide angle diffractometer at a scan rate of 1°/min using Ni-filtered Cu radiation (Cu Kα, λ 1.5418 Å). For the Li^+ exchanged samples x-ray patterns were taken of both the wet and dry solids to guard against phase changes which may take place on drying.

Ion-Exchange Studies. Equilibrations of exchanger with titrant (LiCl + LiOH) were carried out by a batch technique at $\mu = 0.1$ and 25 ± 0.1 °C as described before.[6] The solution to solid ratio was 100 ml/g and equilibration times were 48 h. This equilibrium time was chosen on the basis of kinetic experiments. At high loads (~5 mequiv/g) no further change in pH was observed after 20 h equilibration time, but, at low loads (~1 mequiv/g) small changes in pH occurred up to 100 h. However, from 50 to 100 h the change amounted to no more than 0.01–0.02 pH units. Since this represents less than 0.2% of the total exchange reaction, for all practical purposes the reaction is complete after 48 h.

For the titrations in the reverse direction preweighed samples were exchanged to 90% load with LiCl + LiOH and shaken for 48 h. Under these conditions hydrolysis of phosphate groups was very low. The requisite amount of HCl was then added and the whole equilibrated for an additional 48 h. At the completion of the equilibrations the pH was determined on the clear filtrate with a digital Orion potentiometer, Model 801, equipped with a Corning combination electrode (Ag|AgCl internal and glass electrode external). The filtrates were analyzed for Li^+ by flame emission, using a Perkin-Elmer uv-visible spectrometer fitted with a Model 139-0400 flame photometry attachment, for Cl^- gravimetrically and for phosphate spectrophotometrically.[8]

A stock LiCl solution was prepared from reagent grade solid (Fisher Chemicals), filtered, and standardized by gravimetric determination of chloride ion. The LiOH solution was prepared from boiled, deionized water under nitrogen so as to exclude CO_2. This solution was standardized by titration against weighed amounts of NBS potassium acid phthalate. Chem-Tam (Bio-Rad Laboratories) standard 0.100 M HCl was further standardized against the stock lithium hydroxide solution by titration. Distilled, deionized water was used throughout.

Results

Characterization of the Exchangers. Analytical data for the zirconium phosphate preparations are given in Table I. The theoretical elemental analysis for $Zr(HPO_4)_2 \cdot H_2O$, corrected for the presence of approximately 2% Hf, is 30.52% Zr, 20.51% P, and 11.92% H_2O. The major deviation from theoretical stoichiometry is the higher water contents of the less crystalline exchangers. However, it should be noted that the drying procedure was chosen arbitrarily so that this result is an artifact of the chosen conditions and demonstrates the greater tenacity with which the gels hold water. Under more stringent drying the theoretical water content is approached more closely.[9] The high observed phosphate to zirconium ratio for sample 0.5:48 is also a common occurrence with poorly crystalline gels.[9,10] It usually stems from adsorption of excess phosphoric acid which is difficult to wash out.[10] This slight excess seemed to have a negligible effect upon the ion-exchange data as several of the points in Figure 3 were checked with a portion of 0.5:48 which had been exhaustively rewashed and dried. The agreement was within the experimental error indicated by the circles of Figure 3 (~0.2 pH unit).

TABLE I: Analytical Data for Zirconium Phosphate Preparations

Sample	% Zr	% P	% H_2O LOI	P/Zr	pH[a]
UR gel[b]	28.04	18.25	19.56	1.96	3.5
0.5:48	26.78	18.46	20.09	2.07	3.5
4.5:48	29.88	20.09	13.23	1.98	3.9
9:48	30.10	19.93	12.04	1.95	3.7
12:48			11.86		
12:96	30.10	19.90	12.39	1.95	4.0
12:384			11.6		4.0

[a] Represents pH of last washing. [b] Unrefluxed gel.

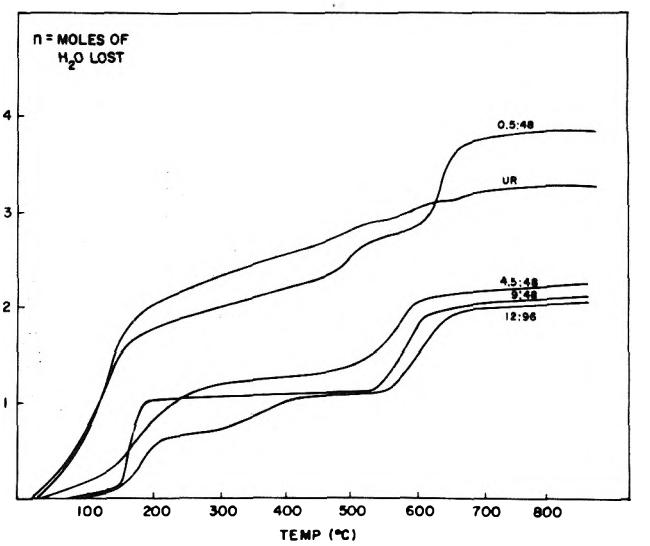

Figure 1. Weight loss vs. temperature curves for zirconium phosphates of different crystallinities as derived from thermogravimetric analysis (heating rate was 5°/min).

Weight loss curves obtained from thermogravimetric analysis are shown in Figure 1 and for 12:384 in ref 11. These curves are similar to those obtained for other refluxed gels with some small differences.[6,10,11,13] Surface and zeolitic water are, in general, lost below 300 °C while phosphate condensation occurs above 500 °C. However, these temperatures are dependent upon the heating rate chosen. Sample 12:96 lost its zeolitic water in roughly two stages up to 400 °C. This is in keeping with our earlier finding[11] that highly crystalline α-ZrP preparations either lose their zeolitic water in this fashion or rapidly over a very narrow temperature range as with sample 9:48. The reasons for this are not clear. The unrefluxed gel lost its last mole of water over a broad temperature range (~150–800 °C) which is also characteristic of the amorphous gel.[12,13] However, even as mild a treatment as refluxing the

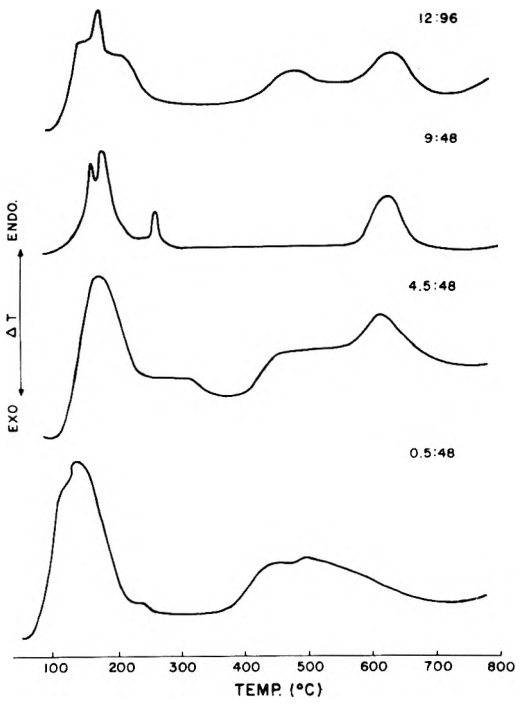

Figure 2. Differential thermal analysis curves for α-ZrP exchangers obtained at a heating rate of 17°/min.

gel in 0.5 M H_3PO_4 induced sufficient order in the structure to cause the bulk of the phosphate condensation to occur above 500 °C.

DTA curves for the exchangers are given in Figure 2 and for 12:384 in ref 11. These curves have been adequately explained for highly crystalline samples.[11] Briefly, the four endotherms clearly seen in the curve for 9:48 result from the following changes:

$$\underset{\alpha\text{-ZrP}}{Zr(HPO_4)_2\cdot H_2O} \xrightarrow{110\ ^\circ C} \underset{\zeta\text{-ZrP}}{Zr(HPO_4)_2\cdot H_2O} \xrightarrow[-H_2O]{-180\ ^\circ C}$$

$$\underset{\zeta\text{-ZrP}}{Zr(HPO_4)_2} \xrightarrow{250\ ^\circ C} \underset{\eta\text{-ZrP}}{Zr(HPO_4)_2} \xrightarrow[-H_2O]{-650\ ^\circ C} ZrP_2O_7$$

These processes are not as clearly differentiated in the curve for sample 12:96. This undoubtedly stems from the very slow rate at which this exchanger loses water as evidenced in its TGA curve (Figure 1). Thus, the water loss and phase changes overlap. The additional endothermic peak occurring at about 450 °C is as yet unexplained but may be due to a disordering of the crystal lattice prior to pyrophosphate formation.[11] With samples of lower crystallinity (4.5:48 and 0.5:48) the initial water loss and phase changes overlap so badly that only a single broad endotherm is observed. Furthermore, for sample 0.5:48, pyrophosphate formation begins at a much lower temperature and occurs over a much broader temperature range.

X-ray diffraction patterns for the exchangers are much like those reported previously.[6] For comparison purposes the crystallite sizes of the present preparations, determined in the same way as for the earlier study, are given in Table II. Since the [002] direction is perpendicular to the layers of α-ZrP and the interlayer distance is 7.56 Å, the number of layers in the average crystallite can readily be calculated.[6] The diffraction peaks for exchanger 0.5:48 were so broad that meaningful measurements could not be obtained. In this respect it is somewhat less crystalline than the corresponding exchanger used for the sodium and cesium ion-exchange studies.[6,14]

TABLE II: Crystallite Sizes of Zirconium Phosphate Exchangers

	D_{002}		Corr D_{hkl}, Å	
Exchanger	Size, Å	No. of layers	D_{110}[a]	D_{112}
4.5:48	300	40	400 (56)	330
9:48	1770	230	1250 (230)	1660
12:48	3020	400	1780 (330)	

[a] The number in parentheses is the number of cavities within a layer.[6]

Ion-Exchange Studies. The ion-exchange data are summarized in Figures 3–5. In these curves and subsequent representations the exchange capacity (7.54 mequiv/g) was calculated on the basis of the weight of anhydrous exchanger (ZrP_2O_7) so as to avoid differences resulting from the variation in water contents of the several exchangers. Figure 3 is a plot of the pH vs. lithium hydroxide added (or HCl added in reverse direction) for exchanger 0.5:48. The exchange appears to be reversible and the curves show no definite endpoint. However, when the actual ion uptake is considered a definite endpoint is observed (Figure 4) at ~7.0 mequiv of Li^+ per gram of zirconium pyrophosphate, somewhat below the theoretical capacity of 7.54 mequiv/g. This reaction is seen to be perfectly reversible and to exhibit the one for one exchange required of a perfect exchanger. Phosphate release to the solution is given by the points at the far left of the figure. The almost constant value of 0.3 mequiv/g must result from the excess H_3PO_4 on the surface,[10] which is calculated from the analysis (Table I) to be 0.26 mequiv/g. The slight increase observed above pH 7 then results from hydrolysis.

The most crystalline exchanger, 12:384, yielded a titration curve consisting of three plateaus (Figure 3). This behavior is in substantial agreement with the results presented by Alberti et al.[4] Three lithium containing phases were observed to form during the course of the titration. As will be seen subsequently these phases have a variable composition. However, as a basis for discussion they will be identified by ideal compositions as phase LiH, $ZrLiH(PO_4)_2\cdot 4H_2O$, phase A (1.33 $Li^+\cdot 4H_2O$), $ZrLi_{1.33}H_{0.67}(PO_4)_2\cdot 4H_2O$, and phase F ($2Li^+\cdot 4H_2O$), $Zr(LiPO_4)_2 4H_2O$. The latter two phases were described in paper II of this series[2] and phase LiH is identical with the one reported by Alberti et al.[4] X-ray diffraction patterns for the phases are given in Table III while their occurrence during the course of the titrations is summarized in Table IV.

Let us now consider the titration curve for 12:384. Initially the pH decreased slightly and this was followed by the first plateau or region of constant pH. Analysis of the Li^+ content of the solution phase showed that it remained constant at 0.1 N so that all of the lithium ion added as hydroxide was exchanged. As seen in Table IV α-ZrP is converted to phase LiH along the plateau (although a minor amount of Li^+ may also be in solid solution in the α-ZrP). Phase rule considerations require that these two solid phases have constant compositions in order to be in equilibrium with a solution of constant composition.[15] However, at about 40% of exchange the pH begins to rise, while the same two phases are still present. Thus, one or both of them must change composition. This is most probably phase LiH since at these high loadings it is quite likely that the α-ZrP phase would have had ample op-

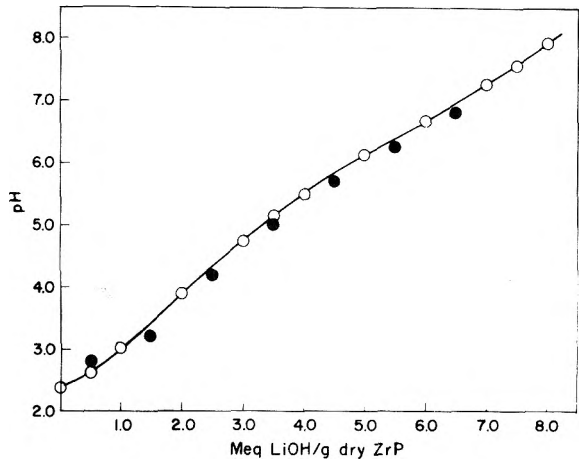

Figure 3. Uncorrected potentiometric titration curve for exchanger 0.5:48. Titrant: forward direction 0.1 N LiOH + 0.1 N LiCl, open circles; backward direction 0.1 N HCl + 0.1 N LiCl, filled circles. The total ionic strength was 0.1.

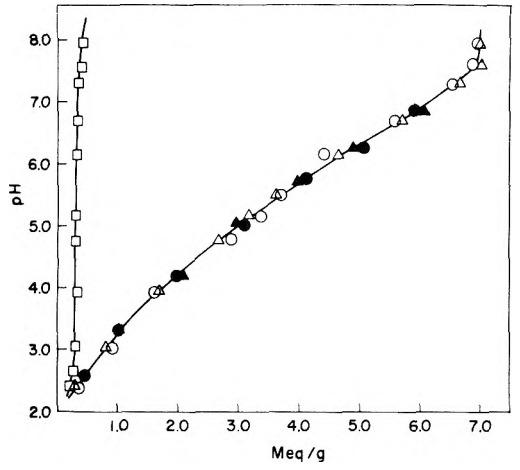

Figure 4. Corrected potentiometric titration curve for exchanger 0.5:48. Symbols are as follows: Li^+ uptake (△), H^+ released to solution (○). Open symbols are for forward direction, closed symbols for backward direction; phosphate ion released to solution (□).

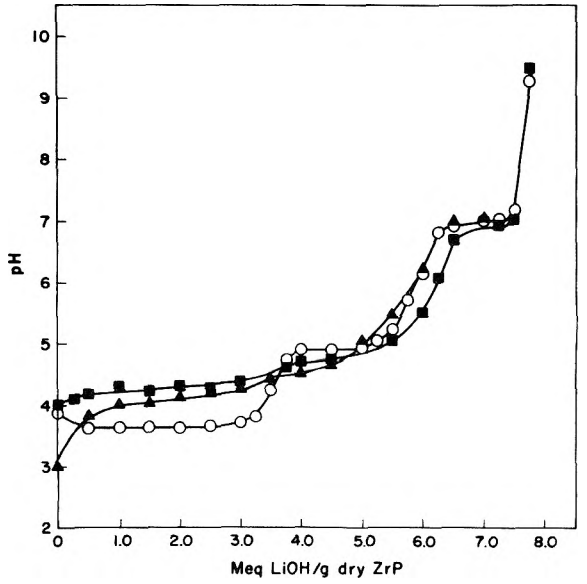

Figure 5. Potentiometric titration curves for zirconium phosphate exchangers (forward direction only). Samples: 4.5:48 (▲), 12:48 (■), 12.384 (○). Titrant: 0.1 N LiOH + 0.1 N LiCl.

TABLE III: X-Ray Diffraction Patterns of Lithium Ion Exchanged α-ZrP

Phase LiH		Phase A		Phase F	
d, Å	I/I_0	d, Å	I/I_0	d, Å	I/I_0
10.3	100	10.2	100	10.2	100
5.0	13	5.06	12	5.01	5
4.63	6	4.55	11	4.68	5
4.50	2	4.11	9	4.53	25
4.36	11	3.89	22	4.24	15
4.22	14	3.30	10	3.81	50
4.10	17	3.11	15	3.41	30
3.56	20	2.99	7	3.27	7
3.42	20	2.71	7	3.03	30
3.32	15	2.68	7	2.67	35
3.10	2	2.63	5	2.58	5
2.99	2			2.42	7
2.83	6			2.11	10
2.74	5			2.00	5
2.69	7			1.90	5
2.67	10			1.70	10
2.54	5			1.65	5

TABLE IV: Phases Present in Solid Exchanger as a Function of Lithium Ion Content

Load as % of total capacity[b]	Phases present in exchanger		
	12:386	12:48	4.5:48
2.6 (0.2)		α-ZrP	α-ZrP
3.3 (0.25)	α + LiH	α + LiH	α-ZrP
6.6 (0.5)	α + LiH	α + LiH	α + LiH
40 (3)	α + LiH	α + LiH	α + LiH
46 (3.5)	Trace α + LiH	α + LiH	α + LiH + A
50.8 (3.83)		α + LiH	
53 (4.0)	LiH + A	Trace α + LiH	α + LiH + A
57 (4.3)	LiH + A	LiH + A	
63 (4.75)	LiH + A	LiH + A	LiH + A
66 (5)	Trace LiH + A	A	LiH + A
73 (5.5)	A	A	A + F
79.6 (6.0)	A + F	A + F	A + F
86.2 (6.5)	A + F	A + F	A + F
92.8 (7.0)	A + F	A + F	A + F
99.5 (7.5)	F	F	F

[a] Numbers in parentheses represent mequiv/g.

portunity to reach its maximum Li^+ content. Thus it is proposed that phase LiH can exist over a range of compositions and that as the loading increases beyond 40% not only is more α-ZrP being converted to phase LiH but this phase is also increasing in Li^+ content. At about 53% of exchange the solubility of Li^+ in phase LiH is exceeded and the new Li^+ rich phase A appears. This is just the point where the second plateau begins. Along the plateau phase LiH converts to phase A until at 67% loading this process is complete. Consequently the pH again rises as phase A changes its composition. Just before the third plateau phase F makes its appearance. Finally phase A converts to phase F along this plateau.

Although the titration curve for 12:48 differs significantly from that of 12:384 the same three lithium containing phases were obtained. Phase LiH was first observed to form at a loading of 3.3% but not at 2.6%. Thus, it is likely that some Li^+ dissolved in the α-ZrP phase initially accompanied by a slight rise in pH. Then from 3.3% of exchange to 53% this phase was converted to phase LiH. It should be noted that this portion of the titration curve nowhere has constant slope so that at

least one of the phases must be changing in composition. Once again at higher loadings phase LiH converts to phase A and this process is completed at roughly 66% Li^+ content. This portion of the curve is relatively flat but not completely so. Phase A then changes composition until somewhere in the region of 75–76% phase F makes its appearance. Once again it should be noted that these two phases coexist along the region of steepest rise in pH. However, at about 86% of exchange their compositions must stabilize since a relatively constant pH plateau is obtained.

The same general sequence of events take place during Li^+ exchange with 4.5:48 but the composition ranges of the exchanged phases are broader. Initially some lithium ion goes into solid solution (Table IV) and this gives rise to the steep increase in pH which is observed at the very beginning of the curve (Figure 3). Then this solid solution is converted to phase LiH. However, phase A makes its appearence at a rather low total loading and before α-ZrP is completely converted to phase LiH. Thus, three phases are present at 46% loading. The α phase dissappears at a loading of somewhat greater than 53% probably because of the large amount of lithium ion required for phase A. Similarly, phase F also is formed at lower loadings (73%) than observed with the more crystalline exchangers and well before the plateau. Even the plateau has a nonzero slope so that here also phase F may be changing its composition.

In our previous study[2] it was shown that the lithium ion exchange reactions with 12:24 were not reversible. Rather the exchanger phase became disordered and did not recrystallize with longer equilibration times. Since 4.5:48 is considerably less crystalline than 12:24 it was of interest to see what would occur in the reverse titration with this exchanger. Here also it was found that the reaction was not reversible. At first the pH in the reverse direction was higher than in the forward direction but then fell to much lower values. In the process, the solid became amorphous.

Determination of Equilibrium Constant for Exchanger 0.5:48. The progress of the exchange reactions with 0.5:48 could not be monitored by x-ray diffraction methods because of the very poor crystallinity of this solid. However, the smooth shape of the titration curve and the reversibility of exchange suggest that the exchanging ions form a single solid solution over the entire range of compositions.[5,13] The total exchange capacity obtained was 7.0 mequiv/g or 92.8% of theoretical. This lower capacity is always obtained with gels of low crystallinity and was explained on the basis of the inability of the cations to pack around the disordered phosphate groups in a complete fashion.[5] Thus, for the purpose of determining the equilibrium constant the capacity of the exchanger is chosen as the theoretical one 7.54 mequiv/g. Furthermore, the water content of the gel 0.5:48, in contact with water in the unexchanged state, is 5 mol per formula weight.[5] This was found to change only slightly when fully loaded with Li^+. Thus, the titration data may be treated by the method of Argersinger et al.[16]

The reaction may be written

$$\overline{RH} + Li^+(aq) \rightleftharpoons \overline{RLi} + H^+(aq) \quad (1)$$

where $\overline{RH}$ represents exchanger 0.5:48 and $\overline{RLi}$ represents the lithium ion exchanged state. The equilibrium constant for this reaction is then

$$K_{Li/H}{}^{0.5} = \bar{a}_{Li}a_H/\bar{a}_H a_{Na} \quad (2)$$

where the barred quantities represent activities of the ions in the solid phase and the unbarred ones activities of the ions in the aqueous phase. Let

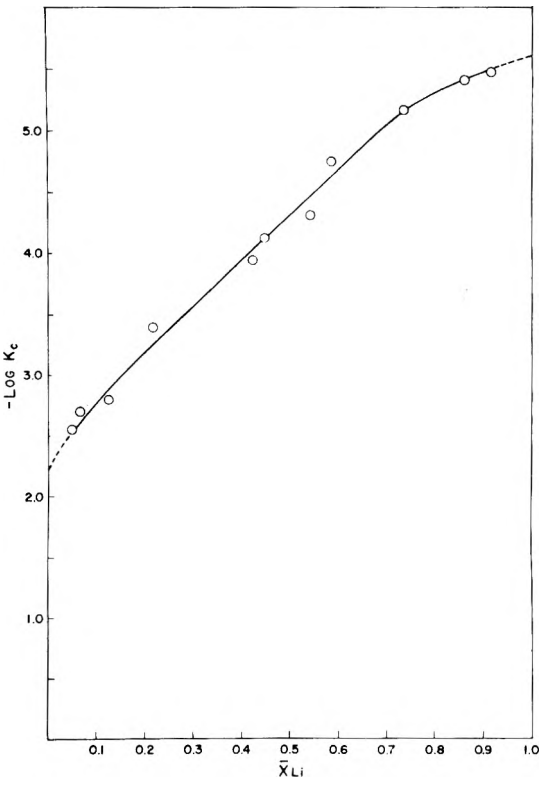

Figure 6. log K_c vs. equivalent fraction of lithium ion in the solid for exchanger 0.5:48.

$$K_C = \bar{X}_{Li}a_H/\bar{X}_H a_{Na} \quad (3)$$

so that according to Argeisinger et al.

$$\log K_{Li/H}{}^{0.5} = \int_0^1 \log K_C \, d\bar{X}_{Li} \quad (4)$$

In eq 3 and 4 $\bar{X}$ refer to equivalent ionic fractions. A plot of log K_c vs. $\bar{X}_{Li}$ is given in Figure 6 and the area under the curve is the value of the integral. In this way the value of $K_{Li/H}{}^{0.5} = 6.2 \times 10^{-5}$ was obtained.

Discussion

It is now necessary to reconcile previous studies with the results of this work. In our earlier study[2] the exchanger examined was 12:24. Its titration curve exhibited features intermediate between those of 12:48 and 4.5:48. Reexamination of the x-ray patterns did indeed reveal that three lithium containing phases were obtained during the course of the titration. Our earlier report was in error because the similarities in the x-ray patterns of phases LiH and A led us to interpret the pattern as a single phase. In fact the x-ray data presented by Alberti et al[4] for their highly crystalline (d.p.) exchanger are almost identical with the ones listed in Table III. Furthermore, the titration curve for their d.p. exchanger is very similar to that of our 12:384 except that with d.p. the third plateau begins at lower Li^+ content (75% vs. 83%). Therefore, they must also have obtained the same three phases reported here. The curve presented by Harvie and Nancollas for 5:100 fits between those of 4.5:48 and 12:24. This position would seem to be reasonable based on the crystallinity to be expected for this exchanger. However, the x-ray patterns presented by them and by Dyer, Leigh, and Ocon[17] contain reflections for partially dehydrated lithium containing phases. These phases will be reported upon subsequently. One point still to be re-

conciled is the observation that with 10:100 the water uptake accompanying Li^+ exchange peaked at 66% of exchange.[4] If in fact phase LiH contains 4 mol of water as does phase A, then the maximum water uptake should still occur at close to 50% of exchange.

The approximate composition ranges of the lithium containing phases could be ascertained from the extent of their occurrence in the x-ray patterns (Table IV). In the case of 12:384 the x-ray patterns indicate that the Li^+ content of phase LiH is close to 1 mol per formula weight of exchanger. This estimate was made from the relative peak heights of the (002) reflections of α-ZrP and phase LiH along the first plateau. No quantitative study was attempted because the x-ray patterns of the wet solids suffered from preferred orientation. Efforts to eliminate this effect were unsuccessful. Nevertheless, these qualitative observations and the extent of the first plateau places the lower limit of Li^+ content of phase LiH between 40 and 50% of the exchange capacity. Thus, we assume this limit at 45% and that along the first plateau phase LiH has a constant composition of approximately $ZrLi_{0.9}H_{1.1}(PO_4)_2 \cdot 4H_2O$. Therefore, at 40% of exchange the solid phase would consist of approximately 10% α-ZrP and 90% phase LiH. However, as additional lithium ion is taken up by the exchanger it is proposed that the composition of phase LiH changes (along with the conversion of the remaining α-ZrP) and eventually achieves a lithium ion content of slightly greater than 50%. The upper limit composition must then be close to $ZrLi_{1.04}H_{0.96}(PO_4)_2 \cdot 4H_2O$. At this point the second plateau is achieved. This plateau ends at 66% of exchange where the solid is now completely phase A. Thus, the lower limit of composition for this phase is close to $ZrLi_{1.33}H_{0.67}(PO_4)_2 \cdot 4H_2O$. The upper limit is about $ZrLi_{1.5}H_{0.5}(PO_4)_2 \cdot 4H_2O$ since at 79.6% of exchange a considerable amount of phase F was already formed.

With exchangers of less crystallinity the composition ranges of these phases increase. In fact even the α-ZrP phase is able to solubilize some Li^+ until eventually in the case of 0.5:48 a single solid solution is obtained. This behavior of expanding composition ranges is similar to that experienced with the Na^+/H^+ and Cs^+/H^+ systems.[6,14] However, it should be remembered that the exchange behavior toward each ion is unique and does not depend upon the acidity of the protons but rather upon the way in which the exchanger can accommodate the different cations in the cavities, i.e., upon the structure of the exchanged phase.

Equilibrium constants have now been measured for exchanger 0.5:48 for Cs^+/H, Na^+/H^+, and Li^+/H^+. Their respective values are 2×10^{-5}, 2×10^{-5}, and 6.5×10^{-5}. This makes the selectivity sequence $Li^+ > Na^+ \simeq Cs^+$. However at very low loads the order is rather $Cs^+ > Na^+ > Li^+$. Thus as loading proceeds selectivity crossovers occur. This is clearly evident in the titration curves presented by Harvie and Nancollas for gel exchangers. This point will be discussed more completely in a future paper.

Finally it should be noted that the maximum uptake by 0.5:48 for Li^+ is 7.0 mequiv/g. The corresponding values for Na^+ and Cs^+ are 6.4 mequiv/g and 5.9 mequiv/g. These values are in the reverse order of the sizes of the unhydrated ions. This is the order to be expected on the basis of our earlier suggestion[6] that four univalent cations pack around each $P-O^-$ group. Because of the disorder of the phosphate groups in 0.5:48 this packing cannot be achieved for each potential exchange site. The larger is the cation the more such steric exclusion is to be expected.

Acknowledgment. Acknowledgment is made to the donors of the Petroleum Research Fund, administered by the American Chemical Society, for support of this work.

References and Notes

(1) Portions of this paper were taken from the Ph.D. thesis of D. A. Tuhtar, presented to the Department of Chemistry, Ohio University, June 7, 1975.
(2) A. Clearfield and J. M. Troup, *J. Phys. Chem.*, **74**, 314 (1970).
(3) S. J. Harvie and G. H. Nancollas, *J. Inorg. Nucl. Chem.*, **32**, 3923 (1970).
(4) G. Alberti, S. Allulli, U. Constantino, M. A. Massucci, and M. Pelliccioni, *J. Inorg. Nucl. Chem.*, **35**, 1347 (1973).
(5) A. Clearfield, A. Oskarsson, and L. Kullberg, *J. Phys. Chem.*, **78**, 1150 (1974).
(6) A. Clearfield, Å. Oskarsson, and C. Oskarsson, *Ion Exch. Membr.*, **1**, 91 (1972).
(7) N. H. Furman, "Standard Methods of Chemical Analysis", 6th ed, Van Nostrand, New York, N.Y., 1962, p 1099.
(8) O. B. Michelsen, *Anal. Chem.*, **29**, 60 (1957).
(9) A. Clearfield and J. A. Stynes, *J. Inorg. Nucl. Chem.*, **26**, 117 (1964).
(10) S. Ahrland, J. Albertsson, A. Oskarsson, and A. Niklasson, *J. Inorg. Nucl. Chem.*, **32**, 2069 (1970).
(11) A. Clearfield and S. P. Pack, *J. Inorg. Nucl. Chem.*, **37**, 1283 (1975).
(12) S. Ahrland, J. Albertsson, L. Johansson, B. Nihlgard, and L. Nilsson, *Acta Chem. Scand.*, **18**, 1357 (1964).
(13) S. Ahrland, J. Albertsson, A. Alnas. S. Hemmingsson, and L. Kullberg, *Acta Chem. Scand.*, **21**, 195 (1967).
(14) A. Clearfield and A. Oskarsson, *Ion Exch. Membr.*, **1**, 205 (1974).
(15) A. Clearfield and A. S. Medina, *J. Phys. Chem.*, **75**, 3750 (1971).
(16) W. J. Argersinger, Jr., A. W. Davidson and O. B. Bonner, *Trans. Kans. Acad. Sci.*, **53**, 404 (1950).
(17) A. Dyer, D. Leigh, and F. T. Ocon, *J. Inorg. Nucl. Chem.*, **33**, 3141 (1971).

On the Mechanism of Ion Exchange in Zirconium Phosphates. 16. Calorimetric Determination of Heats of Li^+–H^+ Exchange

Abraham Clearfield* and Dinko A. Tuhtar[1]

Department of Chemistry, Ohio University, Athens, Ohio 45701 *(Received December 1, 1975)*

Publication costs assisted by the Petroleum Research Fund

The heats of Li^+–H^+ exchange have been measured calorimetrically on zirconium phosphates of different crystallinities. For the most crystalline exchanger the reaction is exothermic up to about 50% Li^+ uptake. This is followed by a mildly endothermic reaction to about 77% lithium loading and a more highly endothermic reaction at still higher loading. These heat effects correspond to the formation of three separate exchange phases identified earlier by x-ray methods. In the case of the nearly amorphous exchanger the reaction is initially very slightly exothermic but soon becomes endothermic. The overall enthalpy is $\Delta H° = 2.57$ kcal/mol and the entropy, $\Delta S° = -10.6$ eu. Qualitative explanations for the enthalpy and entropy effects are presented and the results compared to those obtained with other alkali metal cations.

Introduction

In the preceding paper in this series the effect of crystallinity of the exchanger on Li^+–H^+ exchange of α-zirconium phosphates (α-ZrP) was examined.[2] Three lithium ion containing phases of approximate composition $ZrLi_{0.9-1.04}H_{1.1-0.96}(PO_4)_2{\cdot}4H_2O$, phase LiH, $ZrLi_{1.33-1.50}H_{0.67-0.5}(PO_4)_2{\cdot}4H_2O$, phase A, and $Zr(LiPO_4)_2{\cdot}4H_2O$, phase F, were obtained with a highly crystalline α-ZrP exchanger. As the crystallinity of the exchanger decreased the composition ranges became broader for each phase until with the least crystalline exchanger only a single solid solution was observed. Calorimetric studies have been found to yield valuable information on the exchange process.[3,4] For example, with highly crystalline exchangers sharp breaks in the $\Delta H_x°$ vs. loading curves were obtained at the phase boundaries. Furthermore, in those cases where the reactions are reversible, enthalpy measurements permit evaluation of the differential entropies of exchange. Comparison of such data for a series of ions provides valuable insight into the exchange process. For these reasons we have undertaken the present study.

Experimental Section

Calorimetric Measurements. All solutions were prepared and standardized as described in the previous paper and the exchangers were the same ones described and characterized therein.[2] The calorimetric procedure has also been described in detail[3,4] so that only a brief sketch will be presented here. A constant temperature environment type LKB 8721-1 reaction solution calorimeter with associated thermostat, temperature sensor, and calibration unit was used. A small quantity (0.14–0.40 g) of finely ground exchanger in the hydrogen form was weighed into an ampoule and water (0.5–0.7 ml) added to eliminate heat of wetting effects. The ampoules were then sealed and placed into a four-pronged holder. This holder, which also served as a stirrer, was lowered onto a sapphire tipped glass pin to break the ampoule without interrupting the stirring. For most of the experiments the reaction vessel contained 100 ml of a 0.1000 M LiCl + C mM LiOH solution, where $0 < C < 10$. After each calorimetric determination the extent of exchange was determined by analyzing the solution.[2,5]

Treatment of Experimental Data. The standard heat of partial exchange, $\Delta H_x°$, refers to the reaction

$$H_2ZN_S^{H}H_2O(s) + 2X\,LiCl(aq) + \infty H_2O \rightleftarrows Li_{2x}H_{2-2x}ZN_S^{M}H_2O(s) + (\infty + N_S^{H} - N_S^{M})H_2O + 2X\,HCl(aq) \quad (1)$$

In eq 1 a formula weight of mixed exchanger containing $2X$ mole of Li^+ is formed from 1 formula weight of zirconium phosphate in its pure hydrogen form. All reactants and products are in their standard states. That is, the mixed exchanger is in equilibrium with an infinitely dilute solution of LiCl and HCl in the right proportions to maintain the composition of the exchanger. The pure hydrogen ion and lithium ion forms of the exchangers are in equilibrium with infinitely dilute solutions of HCl and LiCl, respectively. Z denotes one formula weight of the anionic framework of the exchanger while N_S^{H} represents the number of moles of water in 1 formula weight of zirconium phosphate (H_2Z) and N_S^{M} denotes this value for the mixed exchanger. When $X = 1$, we obtain the standard heat of complete exchange, $\Delta H°$. However, since the exchanger greatly prefers hydrogen ion it is necessary to add lithium hydroxide in order that the entire range of lithium ion uptake may be covered. Thus, the reaction for which the heat is measured is

$$H_2ZN_S^{H(V)}H_2O(s) + 2N\,LiCl(aq) + VH_2O + 2Y\,LiOH(aq) \rightleftarrows Li_{2x}H_{2-2x}ZN_S^{M'}H_2O(s) + (V + N_S^{H(V)} - N_S^{M'} + 2Y)H_2O + 2(N - X + Y)LiCl(aq) + 2(X - Y)HCl(aq) \quad (2)$$

In eq 2 $N_S^{H(V)}$ and $N_S^{M'}$ are the number of moles of water in 1 formula weight of exchanger before and after the exchange, respectively. Then following the procedure developed previously,[3] it can be shown that

$$\Delta H_X° = \Delta H_X - 2Y\Delta H_N° - 2(X - Y)\Phi_L(M''_{HCl}) + 2(X - Y)\Phi_L(M''_{LiCl}) + 2Y\Phi_L(M'_{LiOH}) \quad (3)$$

In eq 3 $2Y$ is the number of moles of LiOH consumed by the exchange reaction, $\Delta H_N°$ is the heat of neutralization at 25 °C and infinite dilution, ΔH_X is the measured heat of reaction, and Φ_L denotes the relative apparent molar heat contents of the indicated species and molarity. The values

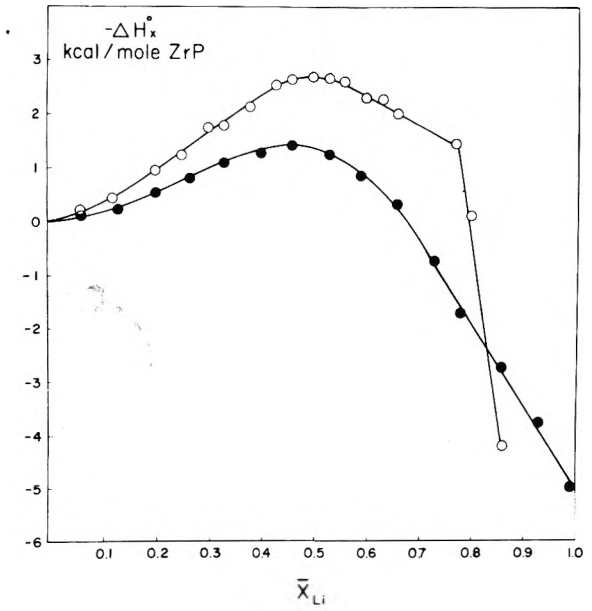

Figure 1. Standard heats of partial exchange as a function of lithium ion loading for exchangers 12:384 (open circles) and 4.5:48 (filled circles).

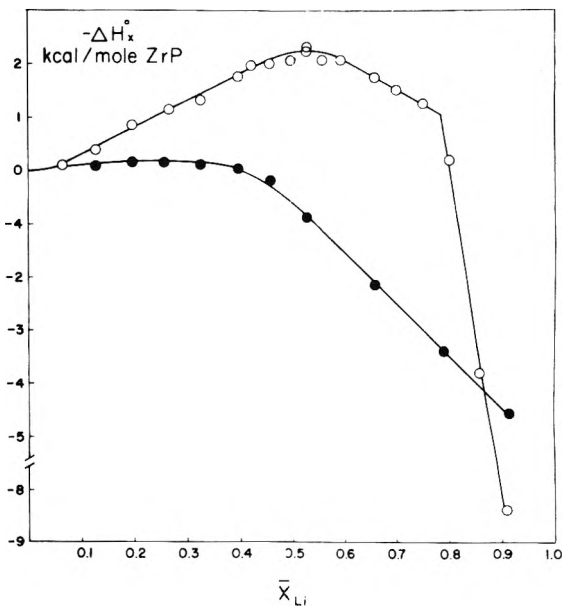

Figure 2. Standard heats of partial exchange as a function of lithium ion loading for exchangers 12:48 (open circles) and 0.5:48 (filled circles).

of the relative apparent molar heat contents were taken from the compilation of Harned and Owen[6] and that for $\Delta H_N°$, −13.34 kcal/mol, from the work of Grenthé and associates.[7]

Under the experimental conditions used in the calorimetric study phosphate release to the solution was negligible for all exchangers except 0.5:48.[2] In this case the maximum release was 0.052 mM/g of exchanger at pH 6.0. At this pH most of the phosphate ion is in the form of $H_2PO_4^{2-}$ so that the hydrolysis reaction occurring is in the main

$$H_2PO_4^- + H_2O \rightleftarrows HPO_4^{2-} + H_3O^+ \quad (4)$$

The enthalpy change for this reaction is 0.8 kcal/mol or a total heat effect of 0.042 cal/g in the worst case. Since the measured enthalpies are of the order of 8–10 cal/g, neglect of hydrolysis is not serious.

Results

Crystalline Samples 12:48 and 12:384. The $\Delta H_x°$ vs. ion uptake curves for these exchangers are given in Figures 1 and 2. At lithium ion loadings of less than 50% the heat effects were usually completed within 5 min. However, progressively longer times were required at higher loadings. For example, at $\bar{X}_{Li} = 0.8$, 20 min was required to achieve a steady state in the resistance vs. time curve for exchanger 12:48 and 60 min for 12:384. In these cases the Regnault–Phaundler method[9] rather than Dickinson's method was used to calculate the experimental heats of reaction. Even so measurements at very high loadings, requiring more than 1 h time, were deemed unreliable and omitted from the curves. Besides the slowness of the reactions another feature of the experimental observations is worthy of note. At $\bar{X}_{Li} > 0.5$ a second small jump in resistance was always observed at times close to the completion of the reaction. This indicates that a second reaction is superimposed upon the first ion-exchange–neutralization reaction. This heat effect may result from the sudden crystallization of one of the exchanged phases (most likely phase A). This point is under investigation.

The $\Delta H_x°$ vs. lithium uptake curves for 12:384 and 12:48 each exhibit three distinct slopes. This correlates well with the ion-exchange titration data.[2] The first exothermic reaction is due to the conversion of α-ZrP to phase LiH. When this process is complete, an endothermic reaction ensues in which phase LiH is converted to phase A. The final highly endothermic portion of the curve corresponds to the formation of the fully exchanged phase F. Although no major differences in the curves for the two exchangers are observed smaller heat effects are noted with the less crystalline exchanger 12:48. Also the maximum in the curve occurred at $\bar{X}_{Li} = 0.53$ for 12:48 as apposed to $\bar{X}_{Li} = 0.5$ for 12:384.

Exchanger 4.5:48. The $\Delta H_x°$ curve for this exchanger (Figure 1) departs from that of the more crystalline samples in that it exhibits only a single endothermic region. At first thought this might seem surprising since 4.5:48 forms the same three phases as the more crystalline samples. However, as was pointed out previously,[2] the composition ranges of the exchanged phases increase with decreasing crystallinity. Thus, a rather smooth transition from one phase to the other seems to occur according to the $\Delta H_x°$ values. This seems plausible for the conversion of phase LiH to phase A judging from the titration curve.[2] However, it is somewhat surprising when applied to the formation of phase F since a distinct plateau was observed in the titration curve for this phase change.

Exchanger 0.5:48. Lithium ion exchange on this almost amorphous exchanger is accompanied by almost negligible heat effects up to about 40% of exchange (Figure 2). At higher loading the $\Delta H_x°$ curve exhibits a negative slope characteristic of an endothermic reaction. Since the Li^+–H^+ exchange reaction has been shown to be reversible, values of the corrected selectivity coefficients were available from the ion-exchange titration data.[2] Thus, it was possible to calculate the differential free energies of exchange defined as

$$-\Delta \bar{G}_x = RT \ln K_c^{Li/H} \quad (5)$$

where $K_c^{Li/H}$ is the corrected rational selectivity coefficient

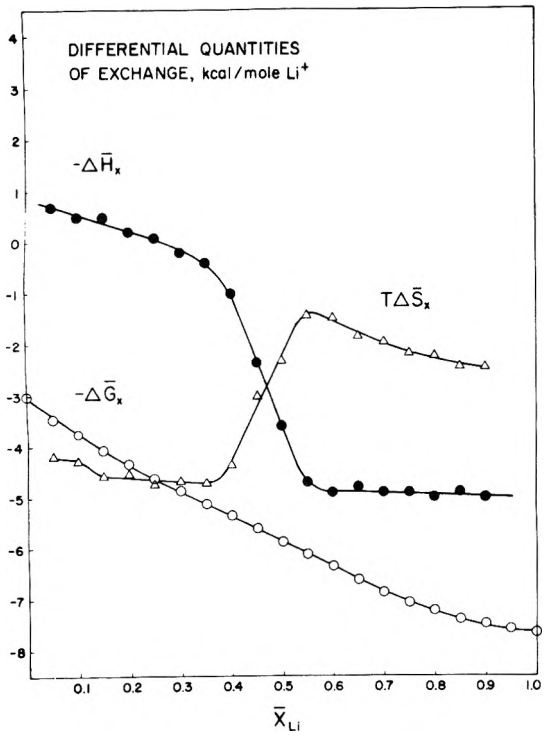

Figure 3. Differential quantities of exchange as a function of lithium ion loading for exchanger 0.5:48.

for Li^+–H^+ exchange with sample 0.5:48. The differential heats of exchange are readily obtained from the standard heats of partial exchange by the relationship

$$\Delta\bar{H}_x = \delta\Delta H_x^\circ/\Delta\bar{X}_{Li} \quad (6)$$

Finally, the differential entropies of exchange can then be calculated from

$$\Delta\bar{S}_x = -(\Delta\bar{G}_x - \Delta\bar{H}_x)/T \quad (7)$$

These differential quantities are plotted in Figure 3. The integral heat of complete exchange, ΔH°, is defined as

$$\Delta H^\circ = \int \Delta\bar{H}_x \, d\bar{X}_{Li} \quad (8)$$

It was evaluated as the area encompased by the $\Delta\bar{H}_x$ vs. $\bar{X}_{Li}$ curve in Figure 3, which amounted to a value of +2.57 kcal/mole. From the previously determined value of the equilibrium constant, 6.2×10^{-5}, ΔG° is calculated to be +5.74 kcal/mol. The standard entropy of exchange derived from these two quantities is then −10.6 eu.

Discussion

The appearance of three distinct slopes in the ΔH_x° vs. $\bar{X}_{Li}$ curves of 12:384 and 12:48 confirms the ion-exchange data that three distinct phases form as lithium ion replaces hydrogen ion. These ion-exchange reactions are not reversible so that it is not legitimate to derive equilibrium constants for them. However, following a procedure previously invoked for Cs^+–H^+ exchange, one can think of the first ion-exchange reaction as being ideally

$$Zr(HPO_4)_2{\cdot}H_2O(s) + 3H_2O + Li^+(aq) \rightleftarrows ZrLiH(PO_4)_2{\cdot}4H_2O + H^+(aq) \quad (9)$$

and

$$K_{Li/H}^{12:384} = a_{H^+}\bar{a}_{Li}/a_{Li^+}\bar{a}_H a_w^3 \quad (10)$$

Along the first plateau one solid of constant composition is converted to another (the half-exchanged phase) of constant composition. Thus the activities of the ions in the solid are constant and

$$K_{Li/H}^{12:384} = a_{H^+}/a_{Li^+}a_w^3 \quad (11)$$

Thus, from the pH of the plateau $K_{Li/H}^{12:384}$ is calculated to be 2.3×10^{-3} and ΔG° = 3.6 kcal/mol. The heat of reaction, from Figure 1, is taken to be −2.69 kcal/mol from which the entropy is determined to be −19 eu. No real thermodynamic significance is to be attached to these values but they afford some insight into the exchange process.

For purposes of this discussion it will be more instructive to compare ΔS_{EX}° values since these represent entropy differences between the corresponding ionic forms of the exchanger. That is, ΔS_{EX}° reflects changes in hydration of the exchanger accompanying the reaction and differences in lattice distortion of the two forms of the exchanger. Sherry has shown[10] that

$$\Delta S_{EX}^\circ = -(S_H^\circ - S_M^\circ) + \Delta S^\circ \quad (12)$$

where $S_H^\circ - S_M^\circ$ refers to differences in entropies of the hydrated ions for the hypothetical reaction

$$H^+(g) + M^+(aq) \rightarrow H^+(aq) + M^+(g) \quad (13)$$

For $M^+ = Li^+$ this entropy difference is 2.4 eu[11] so that ΔS_{EX}° = −21.4 eu. This large negative entropy mainly arises from the binding of 3 mol of water by the exchanged phase. By way of comparison the corresponding ΔS_{EX}° value for formation of the half-exchanged sodium ion phase was −25.9 eu. In this case 4 mol of water was fixed by the new phase. The greater negative entropy effect per mole of water for Li^+ may stem from the smaller interplanar spacing of the lithium phase and the tighter binding of the water by lithium ion compared to sodium ion.

Additionally the observed enthalpy for the formation of phase LiH (−2.69 kcal/mol) is less than half that (−6.9 kcal/mol) for the half-exchanged sodium ion phase. This is to be expected because of the high heat of hydration of lithium ion. Thus, the enthalpy for reaction 13 is −137.7 kcal/mol when M^+ is Li^+ and −163.8 kcal/mol for Na^+. The observed decrease in enthalpy for Li^+ exchange relative to Na^+ exchange more than compensates for the slight entropy increase so that lithium ion is less preferred by crystalline α-ZrP than is sodium ion.

For the gel exchanger 0.5:48 the differential entropy is initially relatively constant at about $T\Delta\bar{S}_x$ = −4.6 kcal/mol or $\bar{S}_x$ = −15.4 eu.

Enthalpies and entropies of exchange are now known for three alkali metal ions on exchanger 0.5:48 permitting some interesting comparisons to be made. In each case the initial exchange reaction is exothermic but as the loading increases becomes endothermic. Cesium ion exchange is initially the most exothermic but eventually becomes the most endothermic. Lithium ion exchange is the least exothermic and at the same time becomes the least endothermic. Sodium ion exchange gives enthalpy values which lie between those of Cs^+ and Li^+. Over the exothermic region of exchange the entropies have high negative values and remain relatively constant. Lithium ion exchange has the highest and cesium ion the lowest entropy values. As the reaction becomes more endothermic the entropies increase with those for Cs^+ and Na^+ becoming highly positive (Cs^+ > Na^+). After an entropy increase from 40 to 60% of exchange, further exchange of Li^+ is accompanied by an en-

tropy decrease (Figure 3). The net result of these effects is an initial weak field selectivity sequence Cs > Na > Li which changes with loading to a strong field selectivity sequence Li > Na > Cs.

The nearly amorphous gel 0.5:48 may be considered to be a weak field exchanger in the sense of Eisenman's theory.[12] This gel swells in contact with water to an interlayer spacing of 11.2 Å.[5] Thus, initially the incoming cations need not approach the negative sites closely but may surround themselves with the excess gel water. The electrostatic effect is therefore small and the reaction is dominated by the hydration effect.[12] This explains the observed order of the enthalpies and entropies. The hydrogen is mainly covalently bonded to phosphate oxygens (although it has been proposed that some is present as ions to account for the swelling of the gel[5]). Thus, on displacement to the solution it hydrates binding a large number of water molecules in the process. Conversely, cesium ion binds water weakly and upon entering the gel experiences a small net change in hydration. In addition it is only weakly attracted to the negative fixed group. The net effect is a large negative entropy and enthalpy. Lithium ion binds water strongly and this ion likely suffers a loss of water to the solution on exchange. Thus, the initial entropy and enthalpy values are expected to be less negative. As the loading increases, the cations are crowded closer together (especially beyond 50% of exchange). Lithium ions, because of their small size, can approach the negative fixed groups closely and thus stay relatively far apart from each other. The much larger cesium ions cannot easily surround the negative sites as the crowding of three or four cations around each fixed group[13] sets up large cation–cation repulsions. It is postulated then that this repulsion effect creates progressively greater internal disorder, i.e., a progressively greater randomization of cations and water molecules. Thus, the entropy progressively increases and the enthalpy decreases. As the size of the incoming cation decreases so does the degree of disorder so that with Na^+ a smaller increase in entropy and a less endothermic reaction is observed. However, Li^+ is so small that it is able to produce a near saltlike arrangement about the negative sites and hold the water molecules in fixed positions. Thus, the entropy does not become positive in the latter stages of exchange. Also the lessened repulsion and closer approach to the negative sites result in a smaller endothermic effect. These ideas will be given a more quantitative expression when the entire series of exchange reactions with alkali metals has been completed.

Our results may be compared to those of an earlier calorimetric study carried out on a weakly crystalline (~0.5:48) zirconium phosphate.[14] That study used empirically determined exchange capacities obtained without use of added LiOH. Thus, a much lower range of ion uptake was examined, i.e., less than 1 mequiv/g. The enthalpy was found to be −1.1 kcal/mol and the entropy −10.0 eu. Our data for 0.5:48 are in the same direction but of somewhat different magnitude when taken over the same loading. Because of the differences in preparation of the two exchangers better agreement is not to be expected.[4]

Acknowledgment. Acknowledgment is made to the donors of the Petroleum Research Fund, administered by the American Chemical Society, for support of this work.

References and Notes

(1) (a) Portions of this paper were taken from the Ph.D. Thesis of D. A. Tuhtar, presented to the Department of Chemistry, Ohio University, June 7, 1975.
(2) A. Clearfield and D. A. Tuhtar, *J. Phys. Chem.*, preceding paper in this issue.
(3) A. Clearfield and L. H. Kullberg, *J. Phys. Chem.*, **78**, 152 (1974).
(4) A. Clearfield and L. H. Kullberg, *J. Phys. Chem.*, **78**, 1812 (1974).
(5) A. Clearfield, Å. Oskarsson, and C. Oskarsson, *Ion Exch. Membr.*, **1**, 205 (1974).
(6) H. S. Harned and B. B. Owen, "Physical Chemistry,of Electrolyte Solutions", Reinhold, New York, N.Y., 1957, p 707.
(7) I. Grenthé, H. Ots, and O. Ginstrup, *Acta Chem. Scand.*, **24**, 1067 (1970).
(8) K. S. Pitzer, *J. Am. Chem. Soc.*, **59**, 2365 (1937).
(9) I. Wadso, *Sci. Tools*, **13**, 33 (1966).
(10) H. S. Sherry, "Ion Exchange", Vol. II, Marcel Dekker, New York, N.Y., 1968.
(11) D. R. Rosseinsky, *Chem. Rev.*, **65**, 467 (1965).
(12) G. Eisenman, "Glass Electrodes for Hydrogen and Other Cations", Marcel Dekker, New York, N.Y., 1967, pp 70–75.
(13) A. Clearfield and Å. Oskarsson, *Ion Exch. Membr.*, **1**, 205 (1974).
(14) G. H. Nancollas and B. V. K. S. R. A. Tilak, *J. Inorg. Nucl. Chem.*, **31**, 3643 (1969).

Comparison of Substituent Effects on Dissociation and Conjugation of Phenols with Those of Carboxylic Acids in Acetonitrile, *N,N*-Dimethylformamide, and Dimethyl Sulfoxide

M. K. Chantooni, Jr., and I. M. Kolthoff*

School of Chemistry, University of Minnesota, Minneapolis, Minnesota 55455 *(Received January 23, 1976)*

Publication costs assisted by the University of Minnesota

Evidence is presented that in the three dipolar aprotic solvents, AN, DMF, and Me_2SO, the ρ value in the Hammett equation is mainly determined by the rate of the proton exchange in the hydrogen bonded primary reaction product between an un-ionized acid and uncharged base, B···HA, to form ionized BH^+A^-. The ρ value for $pK^d(HA)$ of non-ortho-substituted benzoic acids in the solvent AN, which is an extremely weak base, is equal to 2.4, while in the reaction of tetramethylguanidine with these acids in AN, in which salt formation is quantitative, the ρ value for the formation of BH^+A^- is 2.1. In conjugation reactions between an uncharged acid and an anion under conditions in which no proton transfer occurs, ρ values of the hydrogen bonding reaction were found to be much smaller than 2. For $K^f(HR{\cdot}A^-)$, HR being 4-bromophenol and A^- an non-ortho-substituted benzoate, ρ is only -0.6 and -1.2_8 for phenolates. Exactly the same ratio of 2.1 is found for ρ values for $pK^d(HA)$ in water for phenols ($\rho = 2.1$) and benzoic acids ($\rho = 1$). Resolution, R, of acid strength of non-ortho-substituted phenols between water and the three dipolar aprotic solvents, AN, DMF, and Me_2SO, is equal to 2.0 as compared to 2.4 for non-ortho-substituted benzoic acids and 1.9_2 for non-hydroxyacetic acids. This similarity in R is attributed mainly to a similar extent of solvation of phenolate, benzoate, and acetate ions in water.

In the last several years extensive studies have been made in this laboratory of acid–base equilibria in the three dipolar aprotic solvents, acetonitrile (AN), *N,N*-dimethylformamide (DMF), and dimethyl sulfoxide (Me_2SO). Hammett plots of the negative logarithm of the dissociation constant, $pK^d(HA)$, vs. σ of substituted benzoic acids[1a] in these solvents and of a few phenols[1b] in AN have been reported. To obtain reliable ρ values from the Hammett plots of the phenols in the three aprotic solvents, values of $pK^d(HA)$ of 13 non-ortho-substituted phenols have been estimated in the present study.

The reaction between an uncharged acid, HA, and an uncharged base, B, in solvent S[2,3] first involves formation of the un-ionized hydrogen bonded species B···HA, followed by proton transfer to form the ion pair BH^+A^- and finally dissociation into ions. On the other hand, in reactions between an uncharged acid, HA, and an anion base, X^-, (conjugation) only hydrogen bonding occurs under conditions where proton transfer is absent, i.e., when HA is much weaker an acid than HX.

One of the main objectives of this paper is to compare ρ values of reactions between HA and B in AN in which HA are substituted benzoic acids and B is AN ("simple" dissociation of HA), or *N,N*-dimethylbenzylamine (Me_2BA), or tetramethylguanidine (Me_4Gdn). These bases vary widely in strength. With the solvent, S, the primary reaction product is S···HA, whereas with Me_4Gdn salt formation, BH^+A^-, is quantitative. These studies were carried out only with benzoic acids, as phenols, in general, are such weak acids in AN that several of them do not yield complete salt formation with Me_4Gdn, the strongest base available for this purpose.

Also, in this paper, ρ values of the heteroconjugation reactions in AN between substituted benzoic acids or phenols and chloride and substituted benzoates or phenolates with 4-bromophenol (HR) are compared with those of the acid–base reaction between B and HA. Values of $K^f(HA{\cdot}Cl^-)$ of benzoic acids[4] and phenols[1b] in AN as well as $K^f(HR{\cdot}A^-)$ of benzoates in AN, DMF, and Me_2SO[1a] and of a few non-ortho-substituted phenolates in AN[1b] have been determined previously. New data of conjugation of several non-ortho-substituted phenolates with HR in AN, DMF, and Me_2SO are reported; in addition, heteroconjugation constants of a few substituted acetic acids with chloride in AN have been estimated.

Experimental Section

Chemicals. Solvents. Purification and storage of acetonitrile, *N,N*-dimethylformamide, and dimethyl sulfoxide have been described previously.[1a]

Acids. Anhydrous acetic, *n*-butyric, monomethylglutarate, mono- and dichloroacetic, α,β-dibromopropionic acids,[5a,b] 4-bromo-, 3-nitro-, 3-α,α,α-trifluoromethyl-, 4-nitro-, 3,5-dinitro-, 3-chloro-4-nitrophenols,[1b] and 4-hydroxy-, 3-bromo-, 3-nitro-, 3,5-dinitro-, 2,4-dinitro-, and 3-nitro-4-chlorobenzoic acids[4] were used previously. In the present study 3-α,α,α-trifluoromethyl-4-nitrophenol was Baker practical grade, while the other substituted phenols were Aldrich products. 3,4-Dichloro-, 3,5-dichloro-, 3,4,5-trichloro-, and 3-α,α,α-trifluoromethyl-4-nitrophenol were recrystallized from petroleum ether–benzene mixtures, mp 68, 68, 100, and 81 °C, respectively. 3,4-Dinitrophenol was recrystallized from water and air dried, mp 138 °C (*caution, explosive when dry*). 3-Chlorophenol was distilled at atmospheric pressure, bp 212 °C. Aldrich 4-cyanophenol was used without further purification.

Bases. Tetramethylguanidine was the same product used previously,[5c] while 0.9 M tetraethylammonium hydroxide in methanol was prepared as previously.[5a]

Techniques. Conductivity measurements in AN, including those of solutions saturated with potassium chloride in presence of weak uncharged acids, were described elsewhere.[1b] The viscosity correction in the 0.055 M tetramethylguanidine solution in AN is negligible.[5d] Measurements of p_aH using the

TABLE I: Dissociation Constants of Phenols and Heteroconjugation Constants of Phenolates with *p*-Bromophenol

Phenol	pK_{HA} W[l]	pK_{HA} Me_2SO	pK_{HA} DMF	pK_{HA} AN	log K^f(HR·A⁻) and/or log K^f(HR)$_2$A⁻ (in brackets) Me_2SO	DMF	AN	σ
1. Unsubstituted	9.95	16.4[f]	(18.0)[d]	27.2[f] (26.6)[k]				0.00
2. 4-Chloro-	9.42		16.7_8[d]					$+0.22_7$
3. 4-Bromo-	9.36	15.7_3[j]		25.6_0[j]	2.7_0[j]		[5.8][j]	+0.26
4. 3-Chloro-	9.13		16.2_9[d]	25.0_4[j]				$+0.37_3$
5. 3-Trifluoromethyl-	9.06[m]	14.3_0[j]	15.7_0[d]	24.9_0[j]				+0.42
6. 3,4-Dichloro-	8.58	14.2_2[j]		24.0_6[j]				+0.60
7. 3,5-Dichloro-	8.18	13.0_9[j]		23.3_1[j]				$+0.74_6$
8. 3-Nitro-	8.38	13.7_5[j]	13.8_5[c] 15.4_3[d]	23.8[i]	2.1_5[j] [3.6][j]		3.6[i] [7.2][i]	+0.710
9. 3,4,5-Trichloro-	7.90[m]	12.5_8[j]		22.5_4[j]	1.9_2[j] [2.6][j]		[5.3][j]	$+0.97_3$
10. 4-Cyano-	7.95	13.1_0[j]		22.7_7[j]	1.8_5[j] [2.9][j]		[5.3][j]	+1.00
11. 4-Nitro-	7.15	11.0[f] (9.9)[e] 10.4[h] 10.9_3[j]	12.6_4[a] 11.8_4[c] (10.9)[e]	20.9[i] 20.7[k]	1.3_9[j]	1.8_7[j]	2.8[i]	+1.27
12. 3,5-Dinitro-	6.7	10.6[f]	11.2_5[a] 11.4_2[j]	20.5[i]	1.2_8[j] [1.3][j]	1.8_4[j] [2.0][j]	3.0_2[j] [4.1][j]	+1.42
13. 3-Chloro-4-nitro-	6.49[m]	9.8_0[j]		19.9_5[i]	0.8_2[j] [0.5][j]		2.4[i]	+1.64
14. 3-Trifluoromethyl-4-nitro-	6.38[m]	9.3_3[j]	10.3_8[j]	19.3_8[j]	0.9_1[j]	1.2_0[j]	2.2_2[j]	+1.69
15. 3,4-Dinitro-	5.42	7.9_7[j]		17.9_2[j]	0.4_5[j]		2.1_3[j]	+1.98
2-Nitro-	7.21	11.0[f]	12.2_0[b] 12.1_4[c]	22.1[i] 22.0[k]			3.3_2	
2,5-Dinitro-	5.22		8.6_2[b] 8.7_8[c]					
2,4-Dinitro-	4.10	5.2[e] 5.4[j]	6.3_3[a] 6.3_6[c] 6.4_3[j] 6.3_4[b] 6.0[e]	16.0[k] 15.3_4[b]	-0.1_0[j]	0.3_5[j]	1.7[i]	
2,6-Dinitro-	3.71	4.9[f]	6.0_0[a] 6.18[b] 6.0_7[c]	16.4[i]				
2,6-Dinitro-4-chloro-	2.97	3.5[f] 3.6_5[g]	4.7_0[a]	15.0[i]			1.4_3[i]	
4-Nitro-2,6-di-*tert*-butyl	7.2	7.6[i]	8.2_7[j]	19.0[i]				
Picric acid	0.3			11.0[i]			0.2_2[i]	

[a] I. M. Kolthoff, M. K. Chantooni, Jr., and H. Smagowski, *Anal. Chem.*, **42**, 1622 (1970). [b] J. Juillard and B. Loubinoux, *C. R. Acad. Sci., Ser. C*, **264**, 1680 (1967). [c] A. Petrov and I. Umanskii, *Zh. Fiz. Khim.*, **41**, 1374 (1967); **47**, 363 (1973). [d] C. Ritchie and G. Megarle, *J. Am. Chem. Soc.*, **89**, 1447 (1967). [e] B. Clare, D. Cook, S. Ko., Y. Mac, and A. J. Parker, *ibid.*, 88, 1911 (1966). [f] Reference 5c. [g] I. M. Kolthoff and T. Reddy, *Inorg. Chem.*, **1**, 189 (1962). [h] C. Ritchie and R. Uschold, *J. Am. Chem. Soc.*, **89**, 1721 (1967). [i] Reference 1b. [j] This work. [k] J. F. Coetzee, *Prog. Phys. Org. Chem.*, **4**, 45 (1967); J. F. Coetzee and G. R. Padmanabhan, *J. Phys. Chem.*, **69**, 3193 (1965). [l] Values of pK(HA) in water taken from R. A. Robinson, *J. Res. Natl. Bur. Stand.*, **68**, 159 (1964) and G. Kortüm, W. Vogel, and K. Andrussow, "Dissociation Constants of Organic Acids in Aqueous Solution"; A. Biggs and R. Robinson, *J. Chem. Soc.*, 388 (1961). [m] Estimated from Hammett relation pK(HA) = 9.95 − 2.11σ.

glass electrode in the three aprotic solvents have been described.[1a]

Results

Values of pK^f(HA) of Phenols and K^f(HR·A⁻) of Phenolates from Potentiometric Data. Values of pK^d(HA) of phenols in AN and Me_2SO were obtained from paH (a is activity) measurements with the glass electrode in equimolar mixtures of the phenol with its phenolate ($c = 1.5 \times 10^{-3}$ to 2.2×10^{-3} M) using 0.9 M tetraethylammonium hydroxide (in methanol, MeOH) for its preparation. The effect of MeOH on paH was determined separately and taken into account.[5a] The following values of paH were found in the equimolar mixtures of 3,5-dichlorophenol at various dilutions in AN: $c = 1.99 \times 10^{-3}$ M, $c_{MeOH} = 0.067$ M, paH = 23.01; $c = 1.00 \times 10^{-3}$ M, $c_{MeOH} = 0.034$ M, paH = 23.09; and $c = 0.50 \times 10^{-3}$ M, $c_{MeOH} = 0.017$ M, paH = 23.13. For 3,4-dichlorophenol solutions in Me_2SO, $c = 1.98 \times 10^{-3}$ M, $c_{MeOH} = 0.066$ M, paH = 14.08; $c = 1.00 \times 10^{-3}$ M, $c_{MeOH} = 0.033$ M, paH = 14.13; and $c = 0.50 \times 10^{-3}$ M, $c_{MeOH} = 0.017$ M, paH = 14.15. The paH value at zero MeOH concentration was obtained by extrapolation. The largest corrections for the effect of MeOH were 0.30 paH unit in AN and 0.15 in Me_2SO. The corrections for 3,5- and 3,4-dichlorophenol were applied to all the other phenols in AN and Me_2SO. Values of pK^d(HA) are in Table I, in which those of o-nitrophenols are listed separately.

Values of K^f(BHA) and K^d(BHA) of Tetramethylguanidinium Benzoates in AN from Conductometric Data. Plots of Λ vs. $c^{1/2}$ in Figure a have been constructed[6] from conductivity data of 4-hydroxy-, unsubstituted, 3-bromo-, 3-nitro-, 3-nitro-4-chloro-, 3,5-dinitro-, and 2,4-dinitrobenzoic acids from 3×10^{-4} to 1.3×10^{-2} M in 0.055 M Me_4Gdn. The excess of Me_4Gdn was sufficiently large to assure quantitative salt formation (BHA), $(Me_4Gdn)_2H^+$ being negligible.[5d] Values of Λ_0(Me_4GdnHA) and pK^d(Me_4GdnHA) obtained from the Fuoss and Kraus treatment of the data are in Table II. Subtracting the value of the mobility of the tetramethylguanidinium ion, 84,[5d] from Λ_0(BHA) in Table II yields values of $\lambda_0(A^-)$ ranging from 82 to 98, which are reasonable. From the relation[7]

$$\log K^d(\text{BHA}) + \log K^f(\text{BHA}) = \log K^f(\text{BH}^+) - pK^d(\text{HA}) \quad (1)$$

in which $K^d(\text{BHA}) = a(\text{BH}^+)a(\text{A}^-)/a[\text{BHA}]$, $K^f(\text{BHA}) = [\text{BHA}]/[\text{B}][\text{HA}]$, $K^f(\text{BH}^+) = a(\text{BH}^+)/a(\text{H}^+)[\text{B}]$ and using the value of log $K^f(Me_4GdnH^+) = 23.3$,[5c] values of log K^f(BHA)[8] are derived and are included in Table II.

Heteroconjugation of Phenolates with 4-Bromophenol (HR). Heteroconjugation constants of substituted phenolate ions with HR in AN, DMF, and Me_2SO were found from the effect of HR upon paH of equimolar mixtures of the phenol and its phenolate.[1b,6] The results are presented in Figure b.[6]

TABLE II: Formation and Dissociation Constants of Tetramethylguanidinium Benzoates in AN

Substituent	Λ_0(BHA)	pK^d (BHA)[a]	pK^d(HA)	log K^f(BHA)[b]
4-Hydroxy-	166	3.7_4	20.8	6.2_4
Unsubstituted	175	3.4_5	20.7	6.0_5
3-Bromo-	175	3.3_1	19.5	7.1_1
3-Nitro-	175	3.1_0	19.2_9	7.1_1
3-Nitro-4-chloro-	175	3.0_0	18.5_5	7.7_5
3,5-Dinitro-	182	2.8_5	16.9	9.2_5
2,4-Dinitro-	155	2.4_6	16.1_9	9.5_7

[a] K^d(BHA) = [BH$^+$][A$^-$]/[BHA]. [b] K^f(BHA) = [BHA]/[B][HA].

Calculations of K^f(HR·A$^-$) and K^f(HR$_2^-$), taking into account the effect of methanol, have been described previously.[9] These constants are listed in Table I. As found previously, the phenolates, except those which are the weakest bases, form stable diconjugates in AN. Formation of (HR)$_2$A$^-$ was even found in Me$_2$SO, but, as expected, to a much smaller extent than in AN. Proton transfer between A$^-$ and HR and extensive formation of higher heteroconjugates preclude the estimation of K^f(HR·A$^-$) when A$^-$ is a stronger base than 3-nitrophenolate. Values of the logarithm of the overall formation constant K^f(HR)$_2$A$^-$ are in brackets in Table I.

Heteroconjugation of Chloride with Some Non-Hydroxy-Substituted Acetic Acids in AN. From the conductometrically determined increase in ionic solubility of potassium chloride in AN in presence of the substituted acetic acids in Figure c,[6] the formation constants of the 1:1 and 2:1 conjugates were estimated as was done with the substituted benzoic acids.[4] The following values of log K^f(HA·Cl$^-$) and β(HA·Cl$^-$) = K^f(HA)$_2$Cl$^-$/K^f(HA·Cl$^-$) were found: *n*-butyric 2.1_5, 1.6; acetic, 2.2_4, 2.5; methyl biglutarate 2.1_6;[5a] monochloroacetic acid 2.7_3,[10] ~5;[10] α,β-dibromopropionic acid 3.0_2, and dichloroacetic acid 3.4,[10] ~2,[10] respectively.

Discussion

Plots of pK^d(HA) vs. Hammett σ values in Figure 1 of non-ortho-substituted phenols in AN, DMF, and Me$_2$SO are virtually parallel; ρ_{HA} being 4.4 ± 0.1 (Table III). The difference in pK^d(HA) between the solvents S and AN (reference solvent) expressed in terms of transfer activity coefficients, γ^SAN (i), is

$$\Delta^{AN}S\ pK^d(HA) = \log \gamma^S AN(H^+) + \log \gamma^S AN(A^-) - \log \gamma^S AN(HA)$$
$$\simeq \log \gamma^S AN(H^+) + \log \gamma^S AN(A_{el}^-) - \log \gamma^S AN(H_a) \quad (2)$$

where log γ^SAN(H$_a$) denotes the difference in $\Delta G°$ of formation of the hydrogen bond between HA and S and between HA and AN, while log γ^SAN(A$_{el}^-$) is the difference in free energy of the electrostatic part of the solvation of A$^-$, regarded to be close or equal to zero between aprotic solvents.[10] The last part on the right-hand side of eq 2 has been derived assuming that the nonelectrostatic contribution to γ^SAN(A$^-$), denoted as γ^SAN(n), is the same as the neutral non-hydrogen bonded contribution to γ^SAN(HA), i.e., log γ^SAN(HA) = log γ^SAN(n) + log γ^SAN(H$_a$). Considering the solvents AN and Me$_2$SO and using values of log γ^{Me_2SO}AN(H$^+$) = 11.4,[11] and log γ^{Me_2SO}AN(H$_a$) = 1.9[10] and regarding log γ^{Me_2SO}AN(A$_{el}^-$) = 0 in eq 2, the calculated value of Δ^{AN}Me$_2$SO pK^d(HA) is 9.5. This is compared with average values of 9.7_0 of a series of non-ortho-substituted benzoic acids,[1a] 9.7 for non-hydroxy-substituted aliphatic carboxylic acids[5b] and, from Table I in the present paper, 10.1 ± 0.1 for non-ortho-substituted phenols. In DMF relatively few reliable pK^d(HA) values of phenols are available. From those in Table I Δ^{AN}DMF pK^d(HA) = 9.0 as compared to Δ^{AN}DMF pK^d(HA)$_{calcd}$ = 9.2, using log γ^{DMF}AN(H$^+$) = 10.6[11] and log γ^{DMF}AN(H$_a$) = 1.4[10] in eq 2.

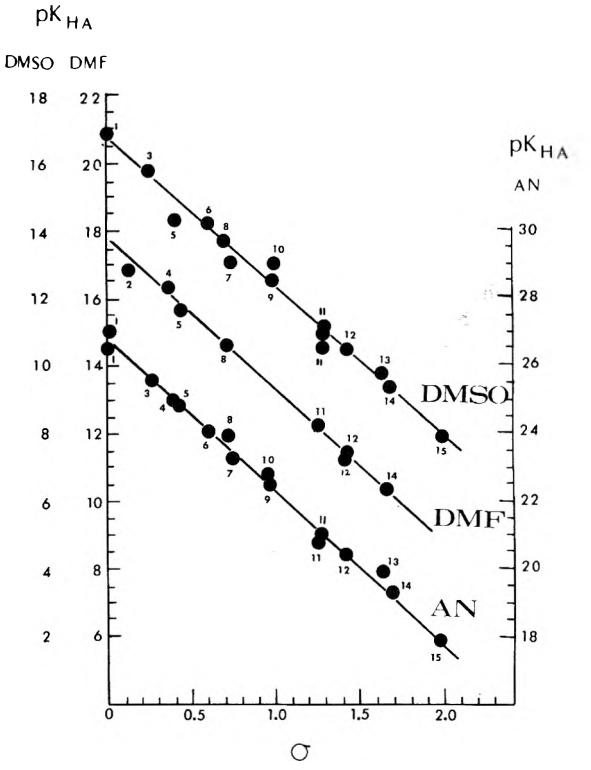

Figure 1. Hammett plots of pK^c_{HA} of non-ortho-substituted phenols in AN, DMF, and Me$_2$SO. Numbers are same as those in Table I. Points 8 and 11 in DMF are average values from two authors.

When σ values are not known reliably, as in the case of Taft σ^* values of some substituted acetic acids, the resolution of acid strength, *R*, is used, defined as

$$R = \rho_S/\rho_W = (pK^d(HA) - pK^d(o))_S/(pK^d(HA) - pK^d(o))_W \quad (3)$$

In eq 3 S is the aprotic solvent, W is water, and pK^d(o) refers to the unsubstituted acid. For non-ortho-substituted phenols ρ in W = 2.1;[12] hence *R* (between W and AN, DMF, or Me$_2$SO) is found equal to 2.0 (Table III) as compared to 2.4 for non-ortho-substituted benzoic acids[1a] and 1.9_2 for non-hydroxy-substituted acetic acids.[5b] (The number of aliphatic carboxylic acids studied was small and a larger number should be investigated.) Thus, the order of magnitude of *R* is the same for phenols and carboxylic acids, which is attributed mainly to the same order of extent of solvation of phenolates and benzoates with water.

In the reaction of Me$_4$Gdn or Me$_2$BA with substituted benzoic acids, HA, in AN little or no substituent effect has been found for the ionic dissociation BHA $\rightleftarrows$ BH$^+$ + A$^-$, ρ values being of the order of 0.5 and ~0, respectively. Considering formation of BHA in these systems, Hammett plots of log K^f(BHA) = log([BHA]/[B][HA]) from Table II are presented in Figure 2. Despite the large difference in strength of the two bases, ρ values are about 2.1 for both bases, which is close to 2.4 for dissociation of benzoic acids in AN (Table III). From the close similarity in ρ values and the likelihood that

TABLE III: Summary of ρ Values and Intercepts of Hammett Plots of pK(HA), pK(BHA), or Heteroconjugation Constants in Various Solvents

Equilibrium	Solvent	ρ values: Benzoic acids	ρ values: Phenols	$\rho_{phenols}/\rho_{benzoic\ acids}$	Intercept[a]: Benzoic acids	Intercept[a]: Phenols
$HA \rightleftarrows H^+ + A^-$ (pK^d)	Me_2SO	2.4^g	$4.2_9{}^f$	1.7_9	$10.9_2{}^g$	$16.5_8{}^f$
	DMF	$2.3_6{}^g$	(4.5)	(1.9_2)	$12.3_3{}^g$	(17.8)
	AN	$2.4_1{}^b$	$4.4_8{}^f$ $4.7_6{}^c$	$1.8_6{}^f$	$20.6_5{}^b$	$26.8_2{}^f$, 27.2^c
	W	1.00	2.1_1	2.1_1	4.2	9.9_5
	Gas phase	12^d	9.7^e	1.2		
$HA + Me_4Gdn \rightleftarrows Me_4GdnHA$ (log K^f)	AN	2.2^f			5.9	
$HA + Me_2BA \rightleftarrows Me_2BAHA$ (log K^f)	AN	2.1^f			1.7	
$A^- + HR \rightleftarrows HR{\cdot}A^-$ (log K^f)	Me_2SO	$0.6_5{}^g$	$1.2_8{}^f$	1.9_7	$1.6_9{}^g$	$3.0_5{}^f$
	DMF	$0.5_7{}^g$	$(1.3)^f$	(2.3)	$2.3_7{}^g$	$(3.4)^f$
	AN	$0.6_2{}^b$	$1.2_8{}^{c,f}$	2.0_6	$3.5_3{}^b$	$4.5_8{}^f$, $4.6_6{}^c$
$HA + Cl^- \rightleftarrows HA{\cdot}Cl^-$ (log K^f)	AN	$+0.4_7{}^b$	$+0.9_9{}^c$	2.1_0	$2.2_3{}^b$	$2.2_3{}^c$

[a] Refers to equilibrium constant involving unsubstituted HA or A^-. [b] Reference 4. [c] Reference 1b. [d] R. Yamdagni, I. Mc. Mahon, and P. Kebarle, *J. Am. Chem. Soc.*, **96**, 4035 (1974). [e] R. Mc. Ives and J. Silvers, *ibid.*, **95**, 8462 (1973). [f] This work. [g] Reference 1a.

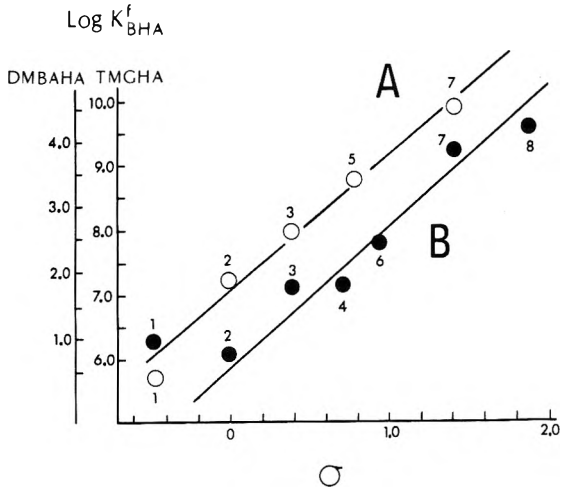

Figure 2. Plots of log K^f(BHA) of tetramethylguanidinium and *N,N*-dimethylbenzylammonium benzoates in AN vs. σ: (A) Me_2BAHA; B, Me_4GdnHA. (1) 4-hydroxy-; (2) unsubstituted; (3) 3-bromo-; (4) 3-nitro-; (5) 4-nitro-; (6) 3-nitro-4-chloro-; (7) 3,5-dinitro-; (8) 2,4-dinitrobenzoates.

BHA is an ionized salt (vide infra) it appears reasonable to conclude that the values of log K^f(BHA) and pK^d(HA) are mainly determined by a proton transfer step in the formation of BH^+A^- or SH^+A^-. Baba et al.[13] have found evidence of formation of an un-ionized solvent-separated ion pair in the 4-nitrophenol–triethylamine system in AN from uv and visible spectral studies. From ir spectra in the crystal state of normal salts of substituted benzoic acids with substituted pyridines Johnson and Rumon[14] concluded that when (log $K^f(BH^+)$ − pK^d(HA)) ≥ 3.7 in water, these salts are present as BH^+A^-. In contrast to the above, 4-nitrophenol–triethylamine systems in the *low dielectric constant* inert solvent isooctane possess uv spectra characteristic of the un-ionized ion pair BHA.[13] In fact, the small ρ values of about unity found from substituent effects on the formation constants of BHA between substituted phenols and a variety of uncharged bases in the low dielectric constant inert solvents, carbon tetrachloride, *n*-heptane, and cyclohexane, have been ascribed to highly incomplete proton transfer.[15]

It was reported previously that the dependence of the 1:1 homoconjugation constant $K^f(HA_2^-)$ of benzoic acids[4] and phenols[1b] on substitution is small in AN, $\rho_{HA_2^-}$ being 0.3_5 and 0.2_9, respectively at 25 °C. This is accounted for by the fact that the increasing hydrogen bond donating capacity of HA is being opposed by the decreasing accepting property of A^-. This should be particularly true when the hydrogen bond in HA_2^- is symmetric. From ir studies symmetric hydrogen bonding was reported in the pentachlorophenol homoconjugate in AN by Pawlak.[16]

For non-ortho-substituted phenolates, A^-, $\rho_{HR\cdot A^-}$ was found equal to -1.2_8 in both AN and Me_2SO from the Hammett plots of values of log $K^f(HR{\cdot}A^-)$ in Table I. Reasons for the fact that $\rho_{HR\cdot A^-}$ is independent of the aprotic solvent have previously been given for benzoate heteroconjugates with HR,[1a] their $\rho_{HR\cdot A^-}$ values being $-0.6_1 \pm 0.0_3$. The same interpretation holds for the phenolates even though they differ drastically in structure from the benzoates. The difference, $\Delta^{AN}Me_2SO$ log $K^f(HR{\cdot}A^-)$, of 1.5 unit (Table I) is mainly attributed to the stronger hydrogen bonding of HR to Me_2SO than to AN and is close to the value of log $\gamma^{Me_2SO}AN(H_a)$ = 1.9.

Heteroconjugation of acetic acids with chloride in AN apparently parallels that of substituted benzoic acids. The same is true for phenols. For phenols log $K^f(HA{\cdot}Cl^-) = 8.1_6 - 0.2_2$ pK^d(HA), for acetic acids log $K^f(HA{\cdot}Cl^-) = 6.0_5 - 0.1_7$ pK^d(HA), and for benzoic acids log $K^f(HA{\cdot}Cl^-) = 6.2_5 - 0.1_9$ pK^d(HA). In Table III it is seen that the ρ values of hydrogen bonding reactions involving an ion as an acceptor with an uncharged donor in which proton transfer is negligible (e.g., $\rho_{HR\cdot A^-}$, $\rho_{HA\cdot Cl^-}$) are much smaller in solvents of intermediate or high dielectric constant than those in which the reaction between HA and an uncharged base involves proton transfer. On the other hand, it is remarkable that the ratio of ρ values of phenols to those of benzoic acids in dipolar aprotic solvents, entered in the fifth column in Table III, is the same and equal to $2.0 \pm 0.1_3$ for the various types of reactions involving hydrogen bonding, irrespective of the extent of proton transfer and dissociation into ions.

Acknowledgment. We thank the National Science Foundation for Grant No. MPS70-01756-A02 in support of this work.

Supplementary Material Available: Figures a, b, and c showing the effect of substitution on conductivity data (4 pages). Ordering information is available on any current masthead page.

References and Notes

(1) (a) I. M. Kolthoff and M. K. Chantooni, Jr., *J. Am. Chem. Soc.*, **93**, 3843 (1971); (b) **91**, 4621 (1969).
(2) I. M. Kolthoff, *Anal. Chem.*, **46**, 1992 (1974).
(3) P. Huyskens, *Rev. Quest. Sci.*, **145**, 521 (1974).
(4) M. K. Chantooni, Jr., and I. M. Kolthoff, *J. Am. Chem. Soc.*, **92**, 7025 (1970).
(5) (a) I. M. Kolthoff and M. K. Chantooni, Jr., *J. Am. Chem. Soc.*, **97**, 1376 (1975); (b) in press; (c) I. M. Kolthoff, M. K. Chantooni, Jr., and S. Bhowmik, *ibid.*, **90**, 23 (1968); (d) **91**, 2875 (1969).
(6) See paragraph at end of paper regarding supplementary material.
(7) I. M. Kolthoff and M. K. Chantooni, Jr., *J. Am. Chem. Soc.*, **87**, 1004 (1965).
(8) Since values of K^t(BHA) of *N,N*-dimethylbenzylammonium benzoates calculated from the location of the maximum of the conductometric titration curve[7] are not very reliable, K^t(BHA) values were estimated from those of K^a(BHA) and $K^t(BH^+)$ using eq 1. The value of $K^t(BH^+)$ in AN is not available and is estimated to be 16.4 from that in water (8.80), assuming that Δ^{W}AN log $K^t(BH^+)$ is the same as was found by Coetzee for tertiary aliphatic amines, i.e., 7.6 units (J. F. Coetzee and G. R. Padmanabhan, *J. Am. Chem. Soc.*, **87**, 5005 (1965)). Uncertainty in the value of $K^t(BH^+)$ in AN does not affect the reported ρ value of formation of BHA.
(9) I. M. Kolthoff and M. K. Chantooni, Jr., *Anal. Chem.*, **39**, 1080 (1967).
(10) M. K. Chantooni, Jr., and I. M. Kolthoff, *J. Phys. Chem.*, **77**, 527 (1973).
(11) I. M. Kolthoff and M. K. Chantooni, Jr., *J. Phys. Chem.*, **76**, 2024 (1972).
(12) R. W. Taft, Jr., and I. C. Lewis, *J. Am. Chem. Soc.*, **80**, 2436 (1958).
(13) H. Baba, A. Matsuyama, and H. Kokubun, *Spectrochim. Acta, Part A*, **25**, 1709 (1969).
(14) S. Johnson and K. Rumon, *J. Phys. Chem.*, **69**, 74 (1964).
(15) J. Hine, "Structural Effects on Equilibria in Organic Chemistry", Wiley, New York, N.Y., 1975, p 201.
(16) Z. Pawlak and L. Sobczyk, *Adv. Mol. Relaxation Processes*, **5**, 99 (1973).

Effect of Structure on the Mesomorphic Properties of Cholesteryl Alkanoates. 6.[1a] Effect of Configuration in Chiral Alkanoates[1b]

Harry W. Gibson

Webster Research Center, Xerox Corporation, Webster, New York 14580

(Received December 1, 1975)

Publication costs assisted by Xerox Corporation

The thermal properties and binary phase diagrams (with cholesteryl nonanoate) of some cholesteryl derivatives of chiral alkanoic acids have been determined. In contrast to the effect on degree of helicity as deduced from the optical properties, chirality in the alkanoate portion causes only minor changes in these properties. Changes in chirality in short chain alkanoates with the chiral center adjacent to the carbonyl have the largest effect. The existence of a thermodynamically stable uniaxial smectic texture of mixtures of branched alkanoates at glass surfaces is rationalized on the basis of steric effects on intermolecular bonding.

Introduction

A knowledge of the effects of structural modifications is a prerequisite to rational design of molecules with optimal properties. On this basis we have engaged in a research program on cholesteryl alkanoates. Initially the nucleation of supercooled liquid crystals was investigated.[2] Then the effects of branching (degree, position, length) in the alkanoate portion on thermal properties were assessed.[3] Subsequently the sensitivity of the structure of the cholesteric mesophase, as measured by its pitch, to molecular alterations was determined.[4] An electric field induced uniaxial to birefringent smectic texture transformation of some binary mixtures of these cholesteryl alkanoates was also studied.[5]

The effects of structure on the thermal properties of cholesteryl *n*-alkanoates have been thoroughly investigated.[6] Binary phase diagrams of *n*-alkanoates[3,7] and branched alkanoates[3] have been determined.

The critical physical properties of cholesteryl alkanoates are explicable in terms of conformational mobility of the alkanoate moiety. Decreased mobility lends to enhanced intermolecular attractive forces (increased melting point, enthalpy, and entropy of fusion, smectic behavior in preference to cholesteric[2b-4]) and decreased molecular volume (increased pitch[4]).

Thus, steric interactions play a significant role in determination of the thermal properties[3] and a dominant role in the determination of the pitch,[4] i.e., helicity, of the cholesteric mesophase. Therefore, changes in configuration of branched cholesteryl alkanoates are expected to alter these characteristics since both intra- and intermolecular forces will be changed. This is demonstrated in Figure 1. In accordance with other findings for conformations of carbonyl compounds,[8] it is assumed that the methyl group of cholesteryl 2-methylbutyrate eclipses the carbonyl in preference to the hydrogen or ethyl moieties. From Figure 1 it is apparent that the relationship of the ethyl group to rest of the molecule is different in the two cases. Indeed the compounds are diastereomers and the relationships are thus diastereomeric. Hence, intramolecular interaction energies are not equal.[9] Important for the mesomorphic properties, intermolecular interactions will have different energetics in principle,[9] i.e., the two compounds will have different physical properties.[9]

The work comprising the present paper and part of a previous one[4] was carried out to determine the magnitude of these effects of chirality, with the ultimate purpose of learning more about the detailed structure of the cholesteric mesophase.

Results and Discussion

The compounds examined are the esters of cholesterol prepared from the following acids: racemic 2-methylbutyric,

TABLE I: Thermal Properties of Cholesteryl Alkanoates

Alkanoate	Structural formula[a]	Transitions,[b] °C	Predicted[c] monotropic transitions	Figure no.	ΔH_f,[d] kcal/mol	ΔS_f,[e] eu
rac-2-Methylbutyrate	$ChOOCCH(CH_3)CH_2CH_3$	K108I	(S89)	3a	4.98	13.0
(*S*)-2-Methylbutyrate	$ChOOCCH(CH_3)CH_2CH_3$	K107I	?	3b	5.45	14.3
rac-2-Methylpentanoate	$ChOOCCH(CH_3)CH_2CH_2CH_3$	K82I	(S68)	4a	9.26	26.1
(*R*)-2-Methylpentanoate	$ChOOCCH(CH_3)CH_2CH_2CH_3$	K90I(68S)		4b	7.17	19.8
(*S*)-2-Ethyl-3-methylbutyrate	$ChOOCCH(C_2H_5)CH(CH_3)_2$	K113I(92S)			5.79	15.0
(*S*)-4-Methylhexanoate	$ChOOC(CH_2)_2CH(CH_3)CH_2CH_3$	K113I	(C69)	6	5.87	15.2
rac-2-Ethylhexanoate	$ChOOCCH(C_2H_5)(CH_2)_3CH_3$	K44S50I			3.13	9.55
(−)-2-Ethylhexanoate	$ChOOCCH(C_2H_5)(CH_2)_3CH_3$	K49S57I		5	3.03	9.41
(*R*)-4-Ethyl-5-methylhexanoate	$ChOOC(CH_2)_2CH(C_2H_5)CH(CH_3)_2$	K80I	C14S13)	7	3.86	10.9
3,3,5-Trimethylhexanoate	$ChOOCCH_2C(CH_3)_2CH_2CH(CH_3)_2$	K111I	(C60S59)	8	5.15	13.4

[a] Ch = cholesteryl. [b] Notation of L. Verbit, *Mol. Cryst. Liq. Cryst.*, **15**, 89 (1971); K = crystal, I = isotropic, S = smectic, C = cholesteric. [c] Predicted by extrapolation of transition lines in binary phase diagrams with cholesteryl nonanoate; see figure indicated. [d] Standard deviation less than 0.1 kcal/mol. [e] Standard deviation less than 0.2 eu.

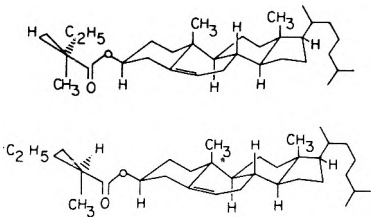

Figure 1. Configurations of cholesteryl (*S*)-2-methylbutyrate (top) and cholesteryl (*R*)-2-methylbutyrate (bottom) showing changes in spatial relationships between the cholesteryl moiety and the methyl and ethyl groups.

(*S*)-2-methylbutyric, racemic 2-methylpentanoic, (*R*)-2-methylpentanoic, (*S*)-2-ethyl-3-methylbutyric, (*S*)-2-methylhexanoic, (−)-2-ethylhexanoic, (*R*)-4-ethyl-5-methylhexanoic, and 3,3,5-trimethylhexanoic. The syntheses of all the esters except those from racemic 2-methylpentanoic and 3,3,5-trimethylhexanoic acids have been described elsewhere.[3,10] The optical purities of the active acids ranged from 84 to 98% with the exception of (*S*)-2-ethyl-3-methylbutyric acid which was 7% optically pure.

A. *Thermal Properties.* The thermal properties of the esters are summarized in Table I. In the three cases where the esters from corresponding active and racemic acids can be compared (2-methylbutyrate, 2-methylpentanoate, and 2-ethylhexanoate) very similar transition temperatures are observed; the diastereomerically pure esters from the active acids have somewhat higher temperatures. This is as expected since the products from the racemic acids are in fact mixtures of diastereomers.

Turning now to the thermodynamic parameters ΔH_f and ΔS_f, significant differences between the products from the active and racemic acids exist, especially in the two shorter acids. In the case of the 2-methylpentanoates the product from the racemic acid has the higher ΔH_f and ΔS_f; apparently ΔH_f for the product from the *S* acid has a high ΔH_f and predominates in the mixture. We believe the configuration of (−)-2-ethylhexanoate (equivalent to 2-*n*-butylbutyrate) is *R* since both (*R*)-2-methylbutyrate and (*R*)-2-methylpenanoate have negative rotation.[4] Thus from comparison of values for esters from racemic and optically pure acids (Table I) ΔH_f and ΔS_f appear to be lower for the *R* configurations. This indicates that the esters from the *R* acids do not pack as well in the crystal as those from the *S* acids (Figure 1). The results for the 2-methylpentanoates suggest that the differences are larger when both of the branches have an odd number of carbon atoms.

With reference to the pitch measurements reported previously, it is noteworthy that using the reported pitch (455 nm)[11] and the present ΔH_f for the ester from the racemic 2-methylpentanoate the pitch–ΔH_f curve[4] for the 2-branched series has the same shape as that of the *n*-alkanoates. That is, as ΔH_f increases the pitch increases to a maximum, then decreases, and finally levels off. In the case of the unbranched alkanates this behavior was attributed to chain folding in the crystalline phase when the carbon number of the alkanoate exceeds eight or nine, while the chains are extended in the cholesteric phase.[4] Recent x-ray studies, however, seem to rule out chain folding in the crystals,[12,13] but do indicate different types of crystal packing. The pitch changes with structure in the 2-branched series seems to follow the trend anticipated based upon the lengths of the two branches. The chain folding explanation cannot in principle apply to the crystalline phases of the 2-branched alkanoates, however, since none of the chains are long enough to fold. The ΔH_f data must reflect differences due to ease of packing in the crystal; this in turn, we believe, is related to the conformational mobilities of the alkanoate chain. There are two opposing and not independent[8] factors: (1) the conformational mobility about the important CO–alkyl bond and (2) the alkyl group flexibility, which depends upon its length. Let us discuss the 2-methylalkanoates, namely, the series isobutyrate, 2-methylbutyrate, 2-methylpentanoate. Referring to Figure 2 we expect that the population of conformation **1a** relative to conformation **1b** will increase as R becomes larger; however, at the same time conformation **1c** also contributes more extensively.[8] In the case of the 2-ethylalkanoates (2-methylbutyrates, 2-ethylbutyrate, and 2-ethylhexanoates) the conformation with H eclipsed with the carbonyl (conformation **2c**, Figure 2) is expected to predominate when R is other than methyl; when R is methyl conformation **2b** predominates.[8] Thus the entire range of conformational mixes (and probably barriers) is covered by these two series of compounds. In addition, we do not have any notion of the effects of these structural changes on the conformations of the O–CO bond. Moreover, the energetics will be different for the two diastereomers. Therefore, we cannot reach any detailed conclusions on the effect of branching on the conformations of these molecules.

B. *Phase Diagrams.* The effects of chirality on the meso-

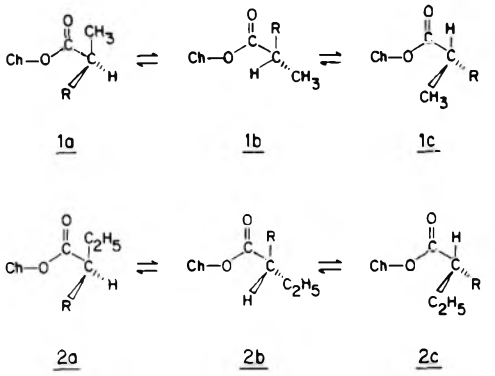

Figure 2. Newman projections of the eclipsed conformations about the carbonyl alkyl bond of cholesteryl 2-methylalkanoates (top) and cholesteryl 2-ethylalkanoates (bottom).

morphic properties might also be expected to manifest themselves in binary phase diagrams (Figures 3–8). First consider the cholesteryl esters derived from racemic and (*S*)-2-methylbutyric acids. Their phase diagrams (Figure 3) reveal clear differences in their mesomorphic tendencies. The mesophases of the *S* ester have much lower stability than those from the racemic acid. The curved lines for the smectic transition (Figure 3a) and smectic and cholesteric lines (Figure 3b) in these two phase diagrams are unique. In our experience[3,7] with cholesteryl derivatives these transition lines are straight, or nearly so, indicating ideal interactions between the two components. The major difference between the two phase diagrams is the lower clearing points for the ester from the active acid.

The results for the esters from racemic and *R* modifications of 2-methylpentanoic acid are shown in Figure 4. The differences are subtle. The domain of the cholesteric phase is about the same and the upper stability limit of the smectic phase is virtually unchanged. The only difference is the higher melting point of the mixture from the *R* acid; this result is expected since there are really three components in the mixtures derived from the racemic acid.

The partial phase diagram of cholesteryl nonanoate–cholesteryl (−)-2-ethylhexanoate (Figure 5) is likewise very similar to that derived from the ester prepared from the racemic acid.[3]

From these three pairs of phase diagrams it can be seen that the transition temperatures of binary mixtures are not very sensitive to configuration; the greatest changes occur in the shorter alkanoates and where the branch is adjacent to the carbonyl group.

A number of phase diagrams of new cholesteryl esters have also been constructed and augment our previous work.[3] The phase diagrams of cholesteryl nonanoate with cholesteryl (*S*)-4-methylhexanoate, (*R*)-4-ethyl-5-methylhexanoate, and 3,3,5-trimethylhexanoate are given in Figures 6–8, respectively. Without detailed discussion, it suffices to say that these results corroborate the conclusions reached in our previous work and outlined in the introduction.

C. *Uniaxial Smectic Textures.* In the course of these studies what is believed to be a unique texture transformation was discovered. It consists of a spontaneous, thermally reversible interconversion of the focal conic and uniaxial textures, presumably of the smectic A phase.[14] The field-induced uniaxial to focal-conic transformation of these systems was previously reported.[5] As noted surface interactions control this transformation; thick samples are uniaxial only near the substrate.

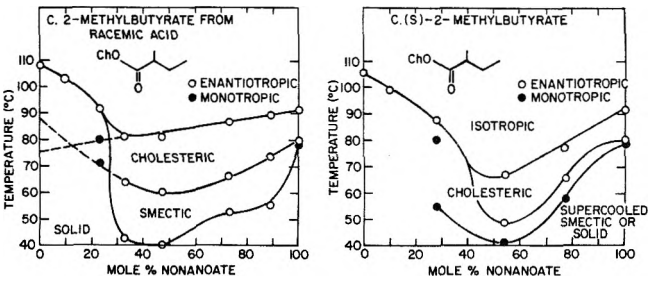

Figure 3. (a) Phase diagram of cholesteryl nonanoate–cholesteryl 2-methylbutyrate from racemic acid (left). (b) Phase diagram of cholesteryl nonanoate–cholesteryl (*S*)-2-methylbutyrate (right).

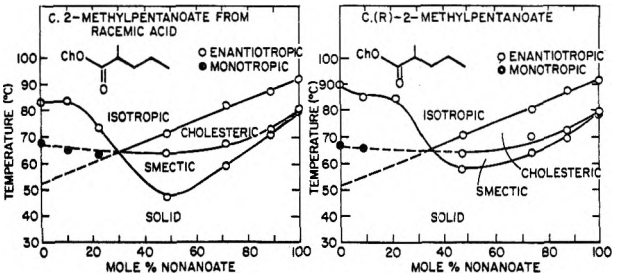

Figure 4. (a) Phase diagram of cholesteryl nonanoate–cholesteryl 2-methylpentanoate from racemic acid (left). (b) Phase diagram of cholesteryl nonanoate–cholesteryl (*S*)-2-methylpentanoate (right).

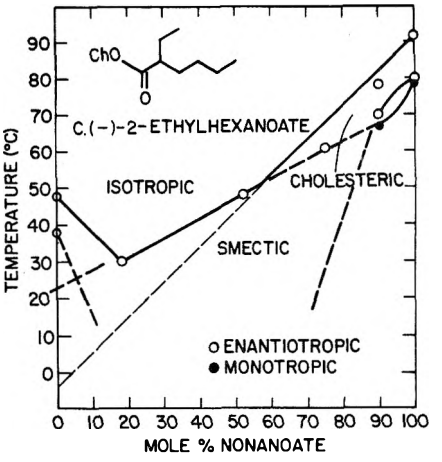

Figure 5. Partial phase diagram of cholesteryl nonanoate–cholesteryl (−)-ethylhexanoate.

The uniaxial textures were first observed in the binary mixtures of the esters of the chiral alkanoates. However, none of these esters by itself nor the esters of achiral acids by themselves exhibit this texture spontaneously, presumably because they cannot be supercooled sufficiently. Further examination showed that chirality in the alkanoate chain is not a prerequisite; branching does seem to be required. In Table II the spontaneous, reversible uniaxial ⇌ focal conic temperatures for 1:1 molar mixtures with cholesteryl nonanoate are listed. As noted the esters of the achiral 2-ethylbutyric and 3,3,5-trimethylhexanoic acids give the uniaxial texture. It is also noteworthy that the transformation temperatures for the esters from active and racemic modifications of an acid are essentially identical.

The fact that branching seems to be a prerequisite for the uniaxial texture can be rationalized on the basis of interaction

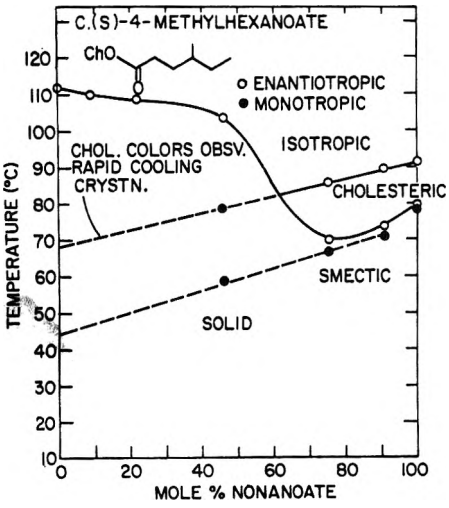

Figure 6. Phase diagram of cholesteryl nonanoate–cholesteryl (*S*)-4-methylhexanoate.

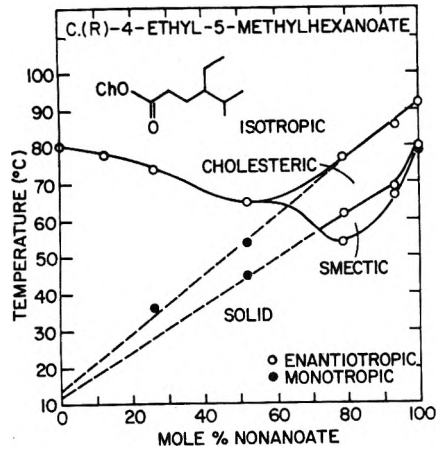

Figure 7. Phase diagram of cholesteryl nonanoate–cholesteryl (*R*)-4-ethyl-5-methylhexanoate.

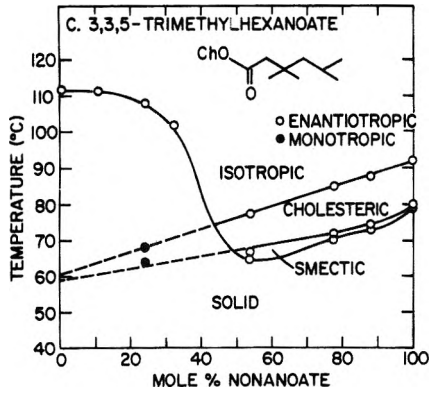

Figure 8. Phase diagram of cholesteryl nonanoate–cholesteryl 3,3,5-trimethylhexanoate.

with the substrate. For nematic systems molecules align parallel to the substrate plane only if the surface energy of the substrate is higher than the liquid crystal surface tension; otherwise a perpendicular arrangement results.[15] The same is very likely true for cholesteric systems. Thus in the smectic phase we would expect to see the uniaxial texture if the substrate surface energy is lower than the surface tension of the mesophase and the focal conic texture otherwise. Another way of stating this is that the uniaxial texture exists when the interaction energy between substrate and liquid crystal is less than the cohesive (intermolecular interaction) energy of the mesophase. Thus as the temperature is raised the displacement of the uniaxial texture by the focal conic indicates that the interfacial interaction energy becomes greater than the cohesive energy. An increase in focal-conic texture would be expected with increasing temperature due to the increasing conformational mobility of the mesomorphic molecules, and the attendant loss of cohesive energy from intermolecular attractions.

TABLE II: Reversible Uniaxial ⇌ Focal Conic Temperatures for 1:1 Molar Mixtures of Cholesteryl Alkanoates and Cholesteryl Nonanoate on Glass Slides

Alkanoate	Temp, °C
2-Ethylbutyrate	40
3,3,5-Trimethylhexanoate	66
(*R*)-2-Methylbutyrate	49[a]
(*R,S*)-2-Methylbutyrate	49[a]
(*R*)-2-Methylpentanoate	65
(*R,S*)-2-Methylpentanoate	63
(*R*)-4-Methylhexanoate	57
(−)-2-Ethylhexanoate	43
(*R*)-4-Ethyl-5-methylhexanoate	50

[a] 1:3 molar mixture of alkanoate:nonanoate.

In these binary mixtures of the branched alkanoates the cohesive energy of the mesophase is high enough to allow the uniaxial orientation; in unbranched systems the cohesive energy must be lower since the uniaxial texture is thermodynamically unstable relative to the focal conic. The higher cohesive energy of the smectic phases in branched alkanoates is consistent with the greater rigidity of the alkanoate chain which permits stronger interaction between the molecules, the carbonyl group probably being a major contributor. Thus, the stability of uniaxial texture is a direct result of the steric effects of branching.

Conclusions

The effects of chirality in the alkanoate portion of cholesteryl alkanoates on thermal properties of pure and mixed esters are relatively minor, in contrast to the significant effects on optical properties. The unique thermally stable uniaxial smectic texture observed in mixtures of branched alkanoates can be rationalized on the same basis as the effects on thermal and optical properties, namely, reduced conformational mobility, which leads to stronger intermolecular interactions.

Acknowledgment. The author wishes to thank Mr. F. C. Bailey for technical assistance, Dr. J. M. Pochan for the ΔH_f measurements, Dr. W. H. H. Gunther for encouragement, and Dr. P. deGennes for a helpful discussion of the smectic phases.

Experimental Section

General. Elemental analyses were performed by Spang Microanalytical Laboratories, Ann Arbor, Mich. Transition temperatures were determined using a Leitz Ortholux polarizing microscope equipped with a Mettler FP5 hot stage; "precleaned" glass microscope slides (Fisher) and cover glasses

(Corning) were employed. Perkin-Elmer differential scanning calorimeters (DSC-1B and 2) were used to determine heats of fusion.

Cholesteryl (R,S)-2-Methylpentanoate. Using the procedure previously reported,[11] this ester was isolated in 72% yield. It was subjected to three recrystallizations from 2-propanol.

Anal. Calcd for $C_{33}H_{56}O_2$: C, 81.76; H, 11.64. Found: C, 81.83; H, 11.93.

Cholesteryl 3,3,5-Trimethylhexanoate. Prepared using the reported general procedure,[11] this ester was purified by two recrystallizations from hexane and one from ethyl acetate.

Anal. Calcd for $C_{36}H_{62}O_2$: C, 82.06; H, 11.86. Found: C, 81.95; H, 11.72%.

Phase Diagrams. The binary mixtures were prepared by mixing weighed samples in the melt, and allowing them to stand several days at room temperature. They were then examined microscopically. Transition temperatures were verified by making more than one determination and cycling the temperature up and down.

References and Notes

(1) (a) References 2-5 comprise papers 1-5 of this series. (b) Presented in part at Vth International Liquid Crystal Conference, Stockholm, Sweden, June, 1974.
(2) (a) J. M. Pochan and H. W. Gibson, *J. Am. Chem. Soc.*, **93**, 1279 (1971); (b) **94**, 5573 (1972).
(3) H. W. Gibson and J. M. Pochan, *J. Phys. Chem.*, **77**, 837 (1973).
(4) H. W. Gibson, J. M. Pochan, and D. Hinman in "Liquid Crystals and Ordered Fluids", J. F. Johnson and R. S. Porter, Ed., Plenum Press, New York, N.Y., 1974, pp 593-606.
(5) J. M. Pochan and H. W. Gibson, *J. Phys. Chem.*, **78**, 1740 (1974).
(6) E. M. Barrall, II, J. F. Johnson, and R. S. Porter, *Mol. Cryst. Liq. Cryst.*, **8**, 27 (1969); G. J. Davis, R. S. Porter, and E. M. Barrall, II, *ibid.*, **10**, 1 (1970); **11**, 319 (1970), and earlier references cited.
(7) A. V. Galanti and R. S. Porter, *J. Phys. Chem.*, **76**, 3089 (1972).
(8) G. J. Karabotsos and N. Hsi, *J. Am. Chem. Soc.*, **87**, 2864 (1965).
(9) E. L. Eliel, "Stereochemistry of Carbon Compounds", McGraw-Hill, New York, N.Y., 1962, pp 21-25, 49; K. Mislow, "Introduction to Stereochemistry", W. A. Benjamin, New York, N.Y., 1966, pp 52-54, 67-70.
(10) H. W. Gibson, *Mol. Cryst. Liq. Cryst.*, **27**, 43 (1974).
(11) H. Hakemi and M. M. Labes, *J. Chem. Phys.*, **58**, 1318 (1973).
(12) J. A. W. Barnard and J. E. Lydon, *Mol. Cryst. Liq. Cryst.*, **26**, 285 (1974).
(13) J. H. Wendorff and F. P. Price, *Mol. Cryst. Liq. Cryst.*, **24**, 129 (1973).
(14) D. Coates and G. W. Gray, *J. Chem. Soc., Chem. Commun.*, 101 (1974).
(15) L. T. Creagh and A. R. Kmetz, *Mol. Cryst. Liq. Cryst.*, **24**, 59 (1973).

Mössbauer Study of Equilibrium Constants of Solvates. 2. Determination of Some Solvation Parameters of Tin Tetrahalides

A. Vértes,* I. Nagy-Czakó, and K. Burger

Department of Physical Chemistry and Radiology, and Department of Inorganic and Analytical Chemistry, L. Eötvös University of Sciences, 1088 Budapest, Hungary

(Received October 8, 1975)

The solvation of tin tetrahalides by donor solvents was studied using Mössbauer spectroscopy. The rate constants of the process $SnX_4 + 2D \rightleftharpoons SnX_4D_2$ for SnI_4 and tetrahydrofuran at 5 °C were found to be $k_1 = 1.1 \pm 0.3$ min^{-1} [mol(kg of benzene)$^{-1}$]$^{-2}$ and $k_2 = 0.06 \pm 0.02$ min^{-1}; the heat of this reaction was $\Delta H = -4.0 \pm 1.0$ kcal/mol. Using Bjerrum's formation function the solvation could be shown to proceed in two steps. The successive equilibrium constants of the formation of the solvate complexes in the system SnI_4–THF at 5 °C were: $K_1 = 0.9 \pm 0.2$ [mol(kg of benzene)$^{-1}$]$^{-1}$ and $K_2 = 13.1 \pm 1.6$ [mol(kg of benzene)$^{-1}$]$^{-1}$ and for the system $SnBr_4$–acetic anhydride: $K_1 = 0.8 \pm 0.2$ [mol(kg of benzene)$^{-1}$]$^{-1}$ and $K_2 = 4.0 \pm 0.6$ [mol(kg of benzene)$^{-1}$]$^{-1}$.

Introduction

Some of the parameters of solvation of tin tetrahalides were studied using Mössbauer spectroscopy in solvent mixtures containing beside the donor solvent an inert solvent of low dielectric constant. The octahedral solvate complex is formed in a reaction leading to equilibrium:[1-3]

$$SnX_4 + 2D \underset{k_2}{\overset{k_1}{\rightleftharpoons}} SnX_4D_2 \qquad (1)$$

where X is the halogen atom, D the donor molecule, and k_1 and k_2 are the rate constants of the two reactions leading to equilibrium.

The equilibrium constant of reaction 1 is

$$K = [SnX_4D_2]/[SnX_4][D]^2 \qquad (2)$$

* Address correspondence to this author at the Department of Physical Chemistry and Radiology.

Equilibrium constant determination by means of Mössbauer spectroscopy has been reported in our previous paper.[3] Now we present some new results in detail.

Solvation Kinetics

When dissolved in benzene tin tetrahalides are not solvated.[3] Upon adding a donor solvent to this solution solvation of tin tetrahalides takes place. Portions of the solution were frozen at different intervals from the time of mixing and by recording their Mössbauer spectra the solvation rate could be followed.

In case of $SnCl_4$ and $SnBr_4$ the areas of the lines assigned to SnX_4 and SnX_4D_2, respectively, did not change with time, while in the SnI_4 system the area of the line pertaining to the solvate SnI_4D_2 definitely increased compared to the area of the line SnI_4. Thus solvation equilibria of $SnCl_4$ and $SnBr_4$ are reached so rapidly that it is impossible to follow them by Mössbauer spectroscopy. (The time needed to reach equi-

librium is less than 1 min.) In the solvation of SnI_4 however equilibrium is reached only after a longer period of time. This different behavior could be due to the differences in the size of the halogen atoms.

Because of the higher rate of the solvation of $SnCl_4$ and $SnBr_4$, respectively, the equilibrium might be shifted during freezing, that is, during cooling from room temperature to the freezing point of the solution: to 5 °C (rate of cooling is 15–20 °C/s). Thus the Mössbauer spectra of the frozen solutions of these two tin tetrahalides permit conclusions only with respect to the state of equilibrium at 5 °C. The solvation equilibrium of SnI_4 is not shifted during the period needed for the solidification of the solutions (1–2 s), thus the equilibrium constant pertaining to room temperature can also be determined from the Mössbauer spectrum.

Starting from the published data of the solvation of tin tetrahalides[1-3] we reckoned only with the presence of nonsolvated SnX_4 and of the solvate complex of the composition SnX_4D_2 in the solution and decomposed the obtained Mössbauer spectra into two lines, and determined accordingly the rate constant of the solvation reaction of SnI_4 on the addition of tetrahydrofuran at 5 °C.

The solution of SnI_4 in benzene was mixed with tetrahydrofuran, the mixture thermostated at 5 °C, and samples were taken at different time intervals. The Mössbauer spectra of these samples were recorded after quick freezing.

Figure 1 shows clearly that as the reaction progresses so does the area of the peak which is proportional to the concentration of the solvate complex increase at the cost of the area of the peak which is proportional to the concentration of unsolvated SnI_4. Figure 2 illustrates the concentration of the complex $SnI_4(THF)_2$ calculated from the spectra vs. time.

The rate of the gross solvation reaction (1) is

$$dc/dt = k_1(M_0 - c)(D_0 - 2c)^2 - k_2c \qquad (3)$$

where M_0 is the initial concentration of SnI_4, D_0 is the initial concentration of the solvating solvent, and c is the concentration of the solvated complex after an interval t from the time of mixing.

The knowledge of $K = k_1/k_2$ made it possible to calculate the rate constants of the solvation of SnI_4 with tetrahydrofuran at 5 °C: $k_1 = 1.1 \pm 0.3$ min^{-1} [mol(kg of benzene)$^{-1}$]$^{-2}$, $k_2 = 0.06 \pm 0.02$ min^{-1}.

The solvation of SnI_4 by donor solvents in benzene is not an instantaneous process, thus the equilibrium reached at various temperatures will not be affected by quick freezing. This offered the possibility of determining the equilibrium constants pertaining to different temperatures (5, 18, and 35 °C) and of calculating the heat of the reaction

$$SnI_4 + 2THF \rightleftharpoons SnI_4(THF)_2 \quad \Delta H = -4.0 \pm 1.0 \text{ kcal/mol}$$

Stability Constants

More detailed study of the solvation of $SnBr_4$ and SnI_4 indicated a concentration dependence of the equilibrium constants determined from the Mössbauer spectra and eq 1 which suggested that solvation proceeds in two steps:

$$M + D \rightleftharpoons MD \qquad (4)$$

$$MD + D \rightleftharpoons MD_2 \qquad (5)$$

where M is SnX_4 and D is the donor–solvent molecule. To clarify this problem measurements were extended to the entire measurable concentration range of the solvation of $SnBr_4$ with acetic anhydride and of SnI_4 with tetrahydrofuran, respectively.

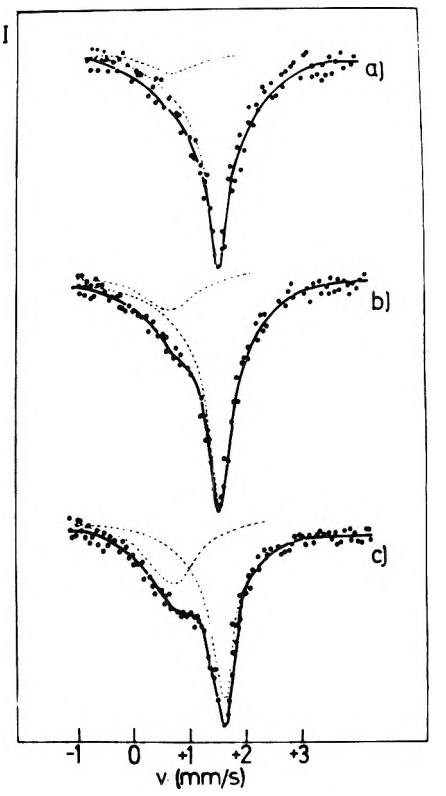

Figure 1. Mössbauer spectrum of the mixture 0.08 mol of SnI_4 + 0.21 mol of THF per 1 kg of benzene, recorded at the temperature of liquid nitrogen: (a) frozen 2 min after the addition of THF; (b) frozen 7 min after the addition of THF; (c) frozen 24 h after the addition of THF.

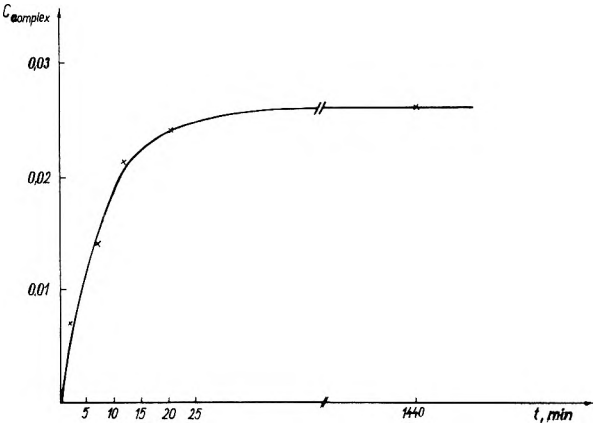

Figure 2. Change in the concentration of the solvate complex $SnI_4(THF)_2$ with time for the mixture 0.08 mol of SnI_4 + 0.21 mol of THF per 1 kg of benzene.

The concentration of SnX_4 was varied between 0.05 and 0.2 M per 1000 g of benzene and the Mössbauer spectrum of the equilibrium system was determined at given SnX_4 content for different concentration ratios of donor solvent:SnX_4.

For the calculation of the equilibrium constants of the solvation reaction Sillen's[4] curve fitting method based on Bjerrum's formation function[5] was used. The essence of which is the fitting of the plotted experimental data to a set of theoretically calculated curves and the calculation of the equilibrium constants from the data of the curve which fits best.

Our experimentally obtained data failed to fit the theoretical curve of the process: $SnX_4 + 2D \rightleftharpoons SnX_4D_2$.

When determining the equilibrium constants of the process

TABLE I

Solvent	Donicity	Dielectric constant	δ_{SnBr_4}, mm s^{-1}	$\delta_{SnBr_4D_2}$, mm s^{-1}	K, [mol kg^{-1}]$^{-2}$	log K
Acetic anhydride	10.5	20.7	1.22 ± 0.08	0.413 ± 0.09	3.2	0.5 ± 0.05
Acetonitrile	14.1	38.0	1.237 ± 0.05	0.385 ± 0.02	25.2	1.40 ± 0.05
Acetone	17.0	20.7	1.176 ± 0.08	0.247 ± 0.04	38.9	1.60 ± 0.10
Tetrahydrofuran	20.0	7.6	1.281 ± 0.041	0.220 ± 0.10	93.2	1.97 ± 0.10

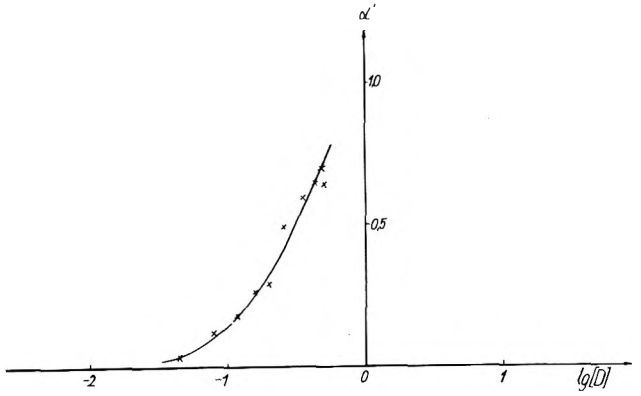

Figure 3. Formation curve of solvated complexes in the SnI_4–THF–benzene system.

corresponding to stepwise complex formation the following facts must be considered: if during solvation the formation of a tin complex with a coordination number of 5 must also be considered, then the corresponding peak on the Mössbauer spectrum should be situated between the peaks of the non-solvated SnX_4 and of the tin complex with a coordination number of 6. According to our earlier findings[6] the isomer shift changes linearly with the coordination number, thus it might be assumed that the peak believed hitherto to be proportional only to the concentration of SnX_4D_2 represents also half of the concentration of the SnX_4D complex present in the system (while the other half of this complex is contained in the peak corresponding to SnX_4). For the study of the system under investigation the following function was introduced:

$$\alpha' = \frac{\frac{1}{2}[MD] + [MD_2]}{[M] + [MD] + [MD_2]} = \frac{\text{area corresponding to the solvate complex in the Mössbauer spectrum}}{\text{total area of the Mössbauer spectrum}} \quad (6)$$

Substitution of the stepwise equilibrium constants

$$K_1 = [MD]/[M][D] \quad (7)$$

and

$$K_2 = [MD_2]/[MD][D] \quad (8)$$

we obtain

$$\alpha' = \frac{\frac{1}{2}K_1[D] + K_1K_2[D]^2}{1 + K_1[D] + K_1K_2[D]^2} \quad (9)$$

For the normalization of eq 9 let us introduce the symbols:

$$\upsilon = K_1[D] \text{ and } p = K_2/K_1 \quad (10)$$

then the normalized form of eq 9 will be

TABLE II

	$SnCl_4$	$SnBr_4$	SnI_4
δ_{SnX_4}, mm s^{-1}	0.88 ± 0.05	1.26 ± 0.04	1.60 ± 0.05
$\delta_{SnX_4D_2}$, mm s^{-1}	0.20 ± 0.10	0.22 ± 0.10	0.72 ± 0.05
log K	2.94 ± 0.15	1.97 ± 0.1	1.12 ± 0.1

$$\gamma = \frac{\frac{1}{2}\upsilon + p\upsilon^2}{1 + \upsilon + p\upsilon^2} \quad (11)$$

When γ is plotted as the function of log υ a set of curves is obtained. Plotting the experimental data on the diagram α' vs. log [D] the values of K_1 and K_2 can be calculated from the data of the best fitting curve of the normalized set of curves.

Figure 3 is the formation curve plotted from the equilibrium data of the system SnI_4–THF. The points are the experimentally obtained data, the full line is the best fitting normalized curve.

The stepwise stability constants of the SnI_4–THF system determined according to the aforementioned method are at 5 °C as follows:

$$K_1 = 0.9 \pm 0.2 \text{ [mol(kg benzene)}^{-1}]^{-1}$$

and

$$K_2 = 13.1 \pm 1.6 \text{ [mol(kg benzene)}^{-1}]^{-1}$$

and the $SnBr_4$–acetic anhydride system:

$$K_1 = 0.8 \pm 0.2 \text{ [mol(kg benzene)}^{-1}]^{-1}$$

and

$$K_2 = 4.0 \pm 0.6 \text{ [mol(kg benzene)}^{-1}]^{-1}$$

Correlation between the Donor Ability (Donicity) of tbe Solvent and the Stability of the Solvate

The influence of the donicity[7] of donor solvents on the equilibrium constant (as defined by eq 1) of the solvation process was studied in the case of $SnBr_4$. Acetic anhydride, acetonitrile, acetone, and tetrahydrofuran with *donicities*[8] increasing from 10.5 to 20.0 in the same order were employed as donor solvents. The results are summed in Table I.

These data show that the coordination of the ligands to the tin atoms reduces the isomer shift which means a reduction of the s electron density at the tin nucleus due to the shielding effect of the 5p and 5d orbitals being filled as a result of coordination. The decrease in isomer shift is greater the higher the donicity of the coordinating solvent. There is a similar unequivocal correlation between the equilibrium constant of solvation and the donicity of the ligand: the equilibrium constant of the process increases with increasing donicity of the solvent.

Effect of the Halogen in SnX_4

The equilibrium constants of the solvation reaction of all

three tin tetrahalides by tetrahydrofuran were determined under identical conditions (0.2 M SnX_4 + 0.2–0.3 M THF/1000 g of benzene).

It appears from Table II that the equilibrium constant increases with decreasing size and increasing electronegativity of the halogen atom. The increasing electronegativity decreases the electron density on the central Sn atom (as shown by the δ values) and promotes the formation of a donor–acceptor bond between the tin and solvent.

Acknowledgment. The authors wish to express their thanks to Professor M. T. Beck for reviewing the manuscript. Thanks are also due to Dr. S. Nagy who helped in the computer evaluation of the results and to Mrs. Suba for her assistance in the recording of the spectra.

References and Notes

(1) U. Mayer and V. Gutmann, *Monatsh. Chem.*, **101**, 997 (1970).
(2) F. Gaizer and M. T. Beck, *J. Inorg. Nucl. Chem.*, **29**, 21 (1967).
(3) A. Vértes, S. Nagy, I. Nagy-Czakó, and É. Csákvári, *J. Phys. Chem.*, **79**, 149 (1975).
(4) L. G. Sillen, *Acta Chem. Scand.*, **10**, 186 (1956).
(5) N. Bjerrum, *Z. Anorg. Chem.*, **119**, 179 (1921).
(6) B. Csákváry, É. Csákváry, P. Gömöry, and A. Vértes, *J. Radioanal. Chem.*, **25**,(2), 275 (1975).
(7) V. Gutmann, "Coordination Chemistry in Non-Aqueous Solutions", Springer Verlag, New York, N.Y., 1968.
(8) The donicity (DN) defined by Gutmann is: the negative reaction heat of solvation of $SbCl_5$ by a donor solvent.

$$SbCl_5 + D \rightleftharpoons SbCl_5D$$

$$DN = -\Delta H$$

Thermodynamic Properties of Liquids, Including Solutions. 12. Dependence of Solution Properties on Properties of the Component Molecules[1]

Maurice L. Huggins

135 Northridge Lane, Woodside, California 94062 *(Received January 7, 1976)*

The fundamental assumptions and equations of the author's recent theory of solution properties are reviewed for specific application to binary mixtures of simple molecules, each treated as a chemically uniform (monotonic) compound. The theoretical equation for the excess enthalpy (H^E) includes three meaningful parameters, each assumed to be independent of concentration. For five systems for which accurate experimental data have been published, it is shown that the calculated H^E curves agree accurately with the experimental ones. The calculated H^E parameters for these and ten other systems are listed. The theoretical equation for the excess entropy of mixing (S^E) involves the ratio of the molal volumes of the components, plus three other meaningful parameters. One of these can be estimated. The other two can then be calculated from the differences between the G^E and H^E curves. The magnitudes of the five contributions to the Gibbs energy of mixing are compared.

1. Introduction

During the past few years[2-7] I have been trying to relate the thermodynamic properties of solutions, using theoretically reasonable equations, to parameters that measure properties of the component molecules and their interactions. Most of this research has been concerned with polymer solutions.

In this paper I treat binary mixtures of simple nonpolymeric molecules. One of my aims is to test the basic equations and assumptions of the theory, using the very accurate data on the concentration dependence of the excess enthalpy and excess Gibbs energy now available for many such mixtures. Another aim is to deduce the parameters in (and magnitudes of) the four contributions to the excess Gibbs energy.

2. Theoretical Approach [2-6]

I make the approximation that the change in energy when two liquids are mixed is the change in the sum of the interaction energies between close-neighbor molecules, assuming in effect that the change in the sum of the interaction energies between non-close-neighbors is negligible.

I assume that the actual energy changes are the same as for a hypothetical mixture in which the molecules have surfaces making mutual contacts, with a constant (concentration-independent) interaction energy per unit area of contact for each type of contact.

For such a solution the relative areas of contact of the three types must be those that give the lowest total Gibbs energy. This requirement is equivalent to requiring that the total areas of contact (σ) of the three types be related to an equilibrium constant by the equation

$$K = \sigma_{12}^2/4\sigma_{11}\sigma_{22} \quad (1)$$

I tentatively assume that, for each type of molecule, the average molecular surface area that makes contact with other molecular surfaces does not change with concentration.

The data now used are all for a temperature of 25 °C and a pressure of 1 atm. I assume that the excess enthalpy (H^E) and excess energy (E^E) are equal, since the difference (PV^E) between these functions is negligible at this pressure.

With these assumptions and approximations, I have deduced[2,3] the relation

$$H^E = \epsilon_\Delta x_1 z_2 g_K \tag{2}$$

Here

$$\epsilon_\Delta = \tau_1{}^0(2\epsilon_{12} - \epsilon_{11} - \epsilon_{22}) \tag{3}$$

measures the change of energy, for a contact area ($\sigma_1{}^0$) equal to the contacting surface area of a type 1 molecule, when like contacts are replaced by unlike contacts.

z_1 and z_2 are "contacting surface fractions", given, for a mixture of monotonic (chemically uniform) molecules, by the equation

$$z_2 = 1 - z_1 = \frac{r_\sigma x_2}{x_1 + r_\sigma x_2} \tag{4}$$

where r_σ is the ratio of the contacting surfaces of the two kinds of molecules:

$$r_\sigma = \sigma_2{}^0/\sigma_1{}^0 \tag{5}$$

g_K is a factor given by the equation

$$g_K = \frac{2}{z_1 z_2 K'}[(1 + K' z_1 z_2)^{1/2} - 1] \tag{6}$$

where

$$K' = 4\left(\frac{1}{K} - 1\right) \tag{7}$$

For perfectly random mixing of the molecules, K and g_K both reduce to unity and eq 2 reduces to

$$H^E = \frac{\epsilon_\Delta r_\sigma x_1 x_2}{x_1 + r_\sigma x_2} \tag{8}$$

H^E thus depends on three meaningful parameters: ϵ_Δ, r_σ, and K.

Figure 1 shows the theoretical dependence of H^E on these parameters. The curves were all drawn for the same energy parameter, ϵ_Δ. Changing this parameter would merely alter the scale of the figure. For curves 1–3 the contacting surface ratio was also assumed constant, equal to 1. These curves are symmetrical, but differ in fatness because of differences in the assumed equilibrium constant, K. Curves 1, 4, and 5 were all drawn for $K = 1$, signifying random mixing. They differ in skewness, because of differences in the contacting surface ratio, r_σ. With the ratio greater than 1, the curve peak is at an x_2 value less than 0.5.

The three parameters are readily calculated from accurate measurements of H^E as a function of the concentration. I customarily use H^E at $x_2 = 0.3$, 0.5, and 0.7, calculated from the experimenters' smoothing equations. Rounded values of the parameters for 15 mixtures are listed in Table I, with the standard deviations of the experimental points from the experimenters' smoothing curves and from the theoretical curves. Similar data for 46 binary systems are given in another paper.[7]

The theoretical equation usually gives practically as good agreement with the experimental points as does the smoothing equation, even though the theoretical parameters were not chosen to give the best *overall* agreement.

H^E curves for six systems are shown in Figure 2. They are both the experimenters' smoothing curves and the theoretical curves, since the differences between the two are less than the widths of the lines.

The assumptions can also be tested by calculating (from the experimental data) one of the three parameters (e.g., r_σ) as a function of concentration, assuming the other two parameters to remain constant. Table II shows the results of such calculations for six systems.

The calculated r_σ values are very constant, with appreciable deviations only at the extreme concentrations, where the experimental smoothing curves, used for the calculation, are relatively unreliable.

Three types of comparison between the experimental measurements and the results of calculations using the theoretical equations thus show excellent agreement. The theo-

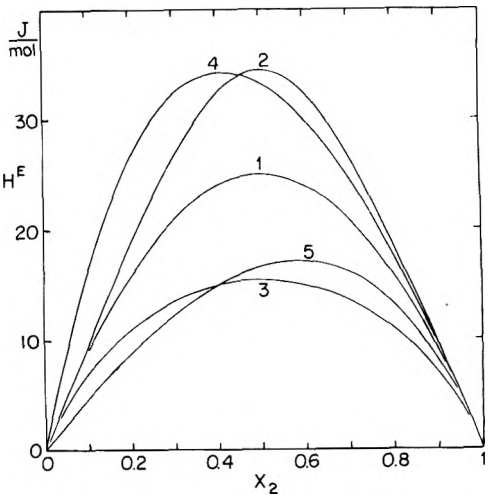

Figure 1. Theoretical curves for excess molal enthalpies, for ϵ_Δ = 100 J: (1) $K = 1$, $r_\sigma = 1$; (2) $K = 5$, $r_\sigma = 1$; (3) $K = 0.2$, $r_\sigma = 1$; (4) $K = 1$, $r_\sigma = 2$; (5) $K = 1$, $r_\sigma = 0.5$. (From ref 5, by courtesy of the Federation of Societies for Paint Technology.)

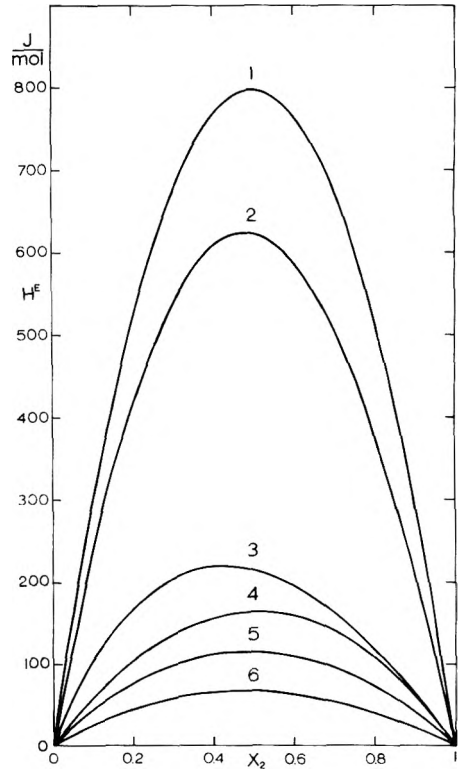

Figure 2. Excess enthalpies: (1) benzene + cyclohexane;[9] (2) cyclohexane + toluene;[14] (3) cyclohexane + *n*-hexane;[13] (4) cyclohexane + CCl_4;[12] (5) benzene + CCl_4;[8] (6) benzene + toluene.[10] The component named first is component 1. (From ref 6, by courtesy of Butterworths.)

TABLE I: Enthalpy Parameters and Standard Deviations

Components[a]	Parameters[c] ϵ_Δ	K	r_σ	Deviations[c] Smoothing eq	Theor	Ref
Benzene +						
CCl_4	476	0.75	1.09	0.06	0.08	8
cyclohexane	3137	0.87	1.12	0.16	0.26	9
toluene	250	1.08	1.16	0.28	0.26	10
CCl_4 + OMCTS[b]	458	0.90	2.68	0.2	0.2	11
Cyclohexane +						
CCl_4	708	0.93	0.91	0.14	0.13	12
cyclopentane	84	1.15	1.79	0.07	0.08	12
n-hexane	685	0.85	1.89	0.09	0.47	13
toluene	2265	1.08	1.18	1.41	0.97	14
Cyclopentane +						
CCl_4	343	0.94	0.89	0.14	0.13	12
cis-decalin	−546	1.02	0.89	0.49	0.49	15
trans-decalin	−1121	1.03	0.92	1.01	1.01	15
tetrachloroethylene	931	0.95	1.05	0.33	0.14	16
Toluene +						
m-xylene	161	1.04	1.11	0.09	0.09	17
o-xylene	185	0.99	1.03	0.15	0.16	17
p-xylene	67	1.02	1.28	0.10	0.11	17

[a] The component named first is component 1. [b] OMCTS = octamethylcyclotetrasiloxane. [c] The ϵ_Δ parameters and standard deviations are in joules per mole.

TABLE II: Dependence of r_σ on Concentration

	x_2 = 0.1	0.2	0.3	0.4	0.5	0.6	0.7	0.8	0.9
Benzene + CCl_4	1.084	1.086	1.086	1.086	1.086	1.087	1.086	1.079	1.038
Benzene + cyclohexane	1.126	1.127	1.126	1.126	1.126	1.127	1.126	1.123	1.105
Benzene + toluene	1.147	1.148	1.148	1.148	1.148	1.148	1.148	1.148	1.148
CCl_4 + cyclohexane	1.106	1.098	1.095	1.095	1.095	1.095	1.095	1.095	1.094
CCl_4 + OMCTS	2.683	2.685	2.685	2.686	2.685	2.685	2.685	2.648	2.543
Cyclohexane + cyclopentane	1.793	1.789	1.788	1.788	1.788	1.788	1.788	1.794	1.845

retical assumptions are thus amply justified, at least for solutions of the sort considered here.

3. Excess Entropy[4]

The excess entropy is in many cases even more important than the excess enthalpy.

Many years ago[18-22] I derived an equation for the combinatorial entropy of a solution—that concerned with the randomness of placing the molecules in the total volume of the solution. Flory[23] independently derived an equivalent relation. We obtained:

$$\Delta S_c = -R(x_1 \ln \phi_1 + x_2 \ln \phi_2) \tag{9}$$

where ϕ_1 and ϕ_2 are volume fractions:

$$\phi_1 = 1 - \phi_2 = \frac{x_1}{x_1 + r_v x_2} \tag{10}$$

Here, r_v is the ratio of the molal volumes:

$$r_v = V_2/V_1 \tag{11}$$

For equal molar volumes of the components the volume fractions become mole fractions, hence ΔS_c equals ΔS_{Raoult}, which leads to Raoult's law. The *excess* combinatorial entropy is thus the relative volume excess entropy:

$$S_{rv}^E = -R[x_1 \ln (\phi_1/x_1) + x_2 \ln (\phi_2/x_2)] \tag{12}$$

Our derivations were specifically for very dilute solutions of flexible chain molecules, but I have since[4] shown that the same relation should apply to any mixture of two components having different molal volumes.

In our derivations, Flory and I both assumed perfectly random mixing of the molecules. Actually, if the equilibrium constant K is not exactly one, there will be a preference for each molecule to have either *like* neighbors (if $K < 1$) or *unlike* neighbors (if $K > 1$). (See eq 1.) To allow for this preference, I have derived the equation

$$S_{cc}^E = \frac{R\sigma^*}{4}\left[z_1(1 - z_2 g_K) \ln \left(\frac{z_1}{1 - z_2 g_K}\right) + z_2(1 - z_1 g_K) \ln \left(\frac{z_2}{1 - z_1 g_K}\right) - z_1 z_2 g_K \ln g_K^2\right] \tag{13}$$

where

$$\sigma^* = x_1\sigma_1^* + x_2\sigma_2^* \tag{14}$$

and σ_1^* and σ_2^* are contacting surface areas per molecule, in a hypothetical solution in which each contact is made independently.

Provisionally, I set

$$\frac{\sigma_2^*}{\sigma_1^*} = \frac{\sigma_2^0}{\sigma_1^0} = r_\sigma \tag{15}$$

(see eq 5) and estimate the smaller of the two constants (σ_1^* and σ_2^*) to have the value 6. This estimate is based on the fact that, in a liquid consisting of close-packed spherical molecules, each molecule contacts 12 others. I guess that the entropy

TABLE III: Entropy Parameters and Gibbs Energy Deviations

Components[a]	r_v	σ_1*	$k_{or,1}$	$k_{or,2}$	$\lvert G_{sm}^E - G_{calcd}^E \rvert_{av}$[b]
Benzene + CCl_4[c]	1.09	6	0.535	−0.400	0.07
Benzene + cyclohexane[d]	1.22	6	0.424	0.453	0.06
CCl_4 + OMCTS	3.21	6	−0.449	1.335	0.10
Cyclohexane + CCl_4[e]	0.89	6.57	0.099	0.058	0.10
Cyclopentane + CCl_4[f]	0.98	6.73	0.131	−0.062	0.01

[a] The references are to the experimental Gibbs energy data. [b] The excess Gibbs energies are in joules per mole. [c] References 24 and 25. [d] References 26 and 27. [e] Reference 29. [f] Reference 30.

TABLE IV: Contributions to the Gibbs Energy of Mixing for Equimolal Mixtures[a]

Components	H^E	$-TS_{rv}^E$	$-TS_{cc}^E$	$-TS_{or}^E$	G^E	$-TS_{Raoult}$	ΔG^M
Benzene + CCl_4	115	−2	11	−42	82	−1718	−1636
Benzene + cyclohexane	799	−12	3	−475	315	−1718	−1403
CCl_4 + OMCTS	163	−401	2	102	−133	−1718	−1852
Cyclohexane + CCl_4	166	−4	1	−93	70	−1718	−1648
Cyclopentane + CCl_4	80	0	0	−46	34	−1718	−1684

[a] The units, for all columns, are joules per mole.

would be the same as for a hypothetical liquid with half as many *independent* contacts. For solutions in which the departure from perfect randomness is not very large, this estimate is probably sufficiently accurate.

In any molecular liquid there is an entropy contribution related to the randomness of instantaneous location and orientation of each molecule (and each rigid segment of a flexible molecule). This randomness is obviously a function of the close-neighbor environment. Using this concept, I have derived, for the orientational, vibrational, and rotational contribution to the excess entropy:

$$S_{or}^E = R[x_1 \ln (1 + k_{or,1} z_2 g_K) + x_2 \ln (1 + k_{or,2} z_1 g_K)] \quad (16)$$

See ref 4, eq 22 (with nN_2 replaced by x_2) and 24 (with k_s' replaced by $k_{or,2}$).

The parameter $k_{or,1}$ (or $k_{or,2}$) measures the change in orientational, vibrational and rotational randomness of a type 1 (or type 2) molecule, when its close neighbors change from all of the same type to all of the other type. In dealing with polymer solutions I have, probably justifiably, neglected the term containing $k_{or,1}$, considering it unimportant relative to that containing $k_{or,2}$. My recent calculations, however, show that for mixtures of simple molecules both terms should be included.

In addition to $k_{or,1}$ and $k_{or,2}$, eq 16 contains the parameters r_σ and K. (See eq 4, 6, and 7.)

If accurate experimental values of G^E and H^E for two or more concentrations are available, S_{or}^E at those concentrations can be calculated from the relation

$$S_{or}^E = \frac{H^E - G^E}{T} - S_{rv}^E - S_{cc}^E \quad (17)$$

Then, using eq 16, $k_{or,1}$ and $k_{or,2}$ can be computed. In the calculations here reported, S_{or}^E was calculated by eq 17 for *three* concentrations (x_2 = 0.3, 0.5, 0.7) and the two parameters calculated to give accurate agreement at x_2 = 0.5, with $k_{or,1}$ having the average of the values giving agreement at x_2 = 0.3 and 0.7. Table III includes $k_{or,1}$ and $k_{or,2}$ parameters, obtained in this way, for five systems. Discussion of their magnitudes will be postponed until after they have been computed for more systems.

4. Gibbs Energy

Using the equation

$$G^E = H^E - TS_{rv}^E - TS_{cc}^E - TS_{or}^E \quad (18)$$

I have calculated G^E at mole fraction intervals of 0.05. Table III gives the average magnitudes of the differences between G^E so calculated and G^E calculated from the experimenters' smoothing equations (extrapolated from higher temperature data, in the cases of the first, second, and fourth systems listed). The averages are for 18 concentrations, x_2 = 0.5 being excluded, since agreement was assumed at that concentration. Considering the probable errors of the H^E and G^E smoothing equations, the average deviations are as small as could be expected.

Table IV lists the (rounded) contributions to the Gibbs energy for equimolal mixtures. At other concentrations the relative contributions of the different terms are not, in general, very different. Note especially the large contribution of the term ($-TS_{rv}^E$) correcting for the relative volumes of the components in the one system in which r_v differs greatly from one. Also note that the contributions of the orientational, rotational, and vibrational term ($-TS_{or}$) are of the same order of magnitude as the excess enthalpy terms.

If the parameters were all independent of temperature, one could easily calculate ΔG^M as a function of temperature and concentration. Because of the relatively large contribution of the Raoult's law entropy term, containing no parameters other than the temperature and concentration, G values so calculated would probably not be far from the true ones for these systems. For greater accuracy, one must await the experimental or theoretical determination of the dependence of the various parameters on temperature. Work on this problem is in progress.

Experimental measurements (of varying degrees of accuracy) of H^E and G^E as functions of concentration and temperature have been reported in the literature for many systems. Applying the equations and procedures of this paper to these data will lead to a better knowledge and understanding of the dependence of the Gibbs energy (and properties deducible therefrom) on temperature, concentration, and meaningful molecular and intermolecular properties than has previously been possible. With this knowledge and under-

standing for many systems, we shall be better able to predict parameters, and so ΔG^M, for other mixtures.

5. Conclusion

I have shown that certain theoretical equations, based on a reasonable model for binary solutions, are in quantitative agreement with very accurate experimental excess enthalpy data. I have shown that these equations, with others for the excess entropy, also lead to good agreement with experimental Gibbs energies of mixing. The parameters in the equations are all reasonably related to molecular and intermolecular properties. Activities, vapor pressures, solubilities, and other measurable thermodynamic properties of solutions are of course readily deducible by rigous equations from the Gibbs energies of mixing.

Acknowledgment. I gratefully acknowledge my indebtedness to the scientists whose fine experimental data I have used and to those with whom I have discussed some of the theoretical aspects of my theory. I also acknowledge the fact that some of the theoretical concepts have previously been used by others. Some pertinent references to this have been given in earlier papers in this series. Finally, I express my gratitude to the Paint Research Institute for some financial assistance.

References and Notes

(1) Presented at the 169th National Meeting of the American Chemical Society, Philadelphia, Pa., April 1975. See *Am. Chem. Soc., Div. Org. Coat. Plast. Pap.*, **35**, 283 (1975).
(2) M. L. Huggins, *J. Phys. Chem.*, **74**, 371 (1970).
(3) M. L. Huggins, *Polymer*, **12**, 389 (1971).
(4) M. L. Huggins, *J. Phys. Chem.*, **75**, 1255 (1971).
(5) M. L. Huggins, *J. Paint Technol.*, **44**, 55 (1972).
(6) M. L. Huggins in "International Review of Science, Physical Chemistry, Series Two, Volume 8, Macromolecular Science", C. E. H. Bawn, Ed., Butterworths, London, 1975.
(7) Fourth International Conference on Chemical Thermodynamics, Montpellier, France, Aug 27, 1975.
(8) R. H. Stokes, K. N. Marsh, and R. P. Tomlins, *J. Chem. Thermodyn.*, **1**, 211 (1969).
(9) M. B. Ewing, K. N. Marsh, R. H. Stokes, and C. W. Tuxford, *J. Chem. Thermodyn.*, **2**, 751 (1970).
(10) J. M. Sturtevant and P. A. Lyons, *J. Chem. Thermodyn.*, **1**, 201 (1969).
(11) K. N. Marsh and R. P. Tomlins, *Trans. Faraday Soc.*, **66**, 783 (1970).
(12) M. B. Ewing and K. N. Marsh, *J. Chem. Thermodyn.*, **2**, 351 (1970).
(13) K. N. Marsh and R. H. Stokes, *J. Chem. Thermodyn.*, **1**, 223 (1969).
(14) A. E. P. Watson, I. A. McLure, J. E. Bennett, and G. C. Benson, *J. Phys. Chem.*, **69**, 2751 (1965).
(15) D. E. G. Jones, I. A. Weeks, and G. C. Benson, *Can. J. Chem.*, **49**, 2481 (1971).
(16) J. Polák, S. Murakami, V. T. Lam, and G. C. Benson, *J. Chem. Eng. Data*, **15**, 323 (1970).
(17) S. Murakami, V. T. Lam, and G. C. Benson, *J. Chem. Thermodyn.*, **1**, 397 (1969).
(18) M. L. Huggins, *J. Chem. Phys.*, **9**, 440 (1941).
(19) M. L. Huggins, Colloid Symposium Preprint (1941); *J. Phys. Chem.*, **46**, 151 (1942).
(20) M. L. Huggins, *Ann. N.Y. Acad. Sci.*, **41**, 1 (1942).
(21) M. L. Huggins, *J. Am. Chem. Soc.*, **64**, 1712 (1942).
(22) M. L. Huggins, "Physical Chemistry of High Polymers", Wiley, New York, N.Y., 1958.
(23) P. J. Flory, *J. Chem. Phys.*, **10**, 51 (1942).
(24) G. Scatchard, S. E. Wood, and J. M. Mochel, *J. Am. Chem. Soc.*, **62**, 712 (1940).
(25) G. Scatchadd and L. B. Ticknor, *J. Am. Chem. Soc.*, **74**, 3724 (1952).
(26) G. Scatchard, S. E. Wood, and J. M. Mochel, *J. Phys. Chem.*, **43**, 119 (1939).
(27) S. E. Wood and A. E. Austin, *J. Am. Chem. Soc.*, **67**, 480 (1945).
(28) K. N. Marsh, *Trans. Faraday Soc.*, **64**, 883 (1968).
(29) G. Scatchard, S. E. Wood, and J. M. Mochel, *J. Am. Chem. Soc.*, **61**, 3206 (1939).
(30) T. Boublik, V. T. Lam, S. Murakami, and G. C. Benson, *J. Phys. Chem.*, **73**, 2356 (1969).

Generalized Integral Equations of Classical Fluids

H. S. Chung

Central Research Division Laboratory, Mobil Research and Development Corporation, Princeton, New Jersey 08540
(Received October 6, 1975)

Publication costs assisted by Mobil Research and Development Corporation

Parametrized integral equations of classical fluids have been derived within the framework of functional differentiation. The first-order theory is examined in detail for rigid spherical and Gaussian molecules. In the region of lower densities, it appears that the lowest order theory is numerically quite similar, in the case of rigid spheres, to the schemes of Rowlinson and of Hurst which are based on different (diagrammatic) arguments. For the Gaussian molecules, the virial coefficients up to the fourth are given correctly by this method. Extension of this parametrization to second and higher order theories is indicated.

I. Introduction

Functional analysis offers a powerful technique for systematically improving the integral equations of classical fluids. Thus, by retaining the quadratic term in the functional Taylor expansion, Verlet[1] has indicated how the original Percus–Yevick and hypernetted chain (hereafter referred to as PY-1 and HNC-1) theories may be generalized to what are subsequently known as the PY-2 and HNC-2 equations. One of these second generation theories, the PY-2, has been extensively studied and the most important conclusions drawn from this work[2] is that ". . . when the PY-1 equation is a decent first approximation, that is for high temperatures or around the critical point, the PY-2 equation significantly improves over those results, and is a useful equation. On the other hand, for dense fluids at low temperatures where the PY-1 and HNC-1 equations are poor, the PY-2 equation is also bad . . ." In view of these assertions, it seems that further progress in the theory

of fluids may be more readily attained, not in the retention of the numerically difficult, still higher order terms of the functional expansion, but in the formulation of better first approximations upon which these more accurate equations are based.

There have been several investigations of this nature, the more significant being those of Rowlinson,[3] Carley and Lado,[4] Rushbrooke and Hutchinson,[5] and Hurst.[6] The common feature among these studies is the introduction into the appropriate integral equation a parameter whose value may be determined within the framework of the theory. The justifications for the parametrization are often couched in "diagrammatic" terms, e.g., the heuristic summation of a fraction of graphs of a certain class. Perhaps the most cogent argument in favor of these procedures is the fact that thermodynamic functions and virial coefficients thus derived are often superior to those of the original unparametrized theory. Despite some improvements, the modified theories are still not sufficiently accurate at all temperatures and densities so extensions of these techniques are evidently desirable. However, in terms of the diagrammatic formulations, it is not immediately apparent how this kind of parametrization can be further developed in a systematic fashion. Functional analysis provides such a method. It is the purpose of this study to examine the parametrization approach within the context of functional differentiation.

II. The Parametrized Integral Equations

In the grand canonical ensemble, the n-particle generic distribution function $\rho^{(n)}(1, \cdots, n)$ is related to that of the $(n + 1)$ particles by

$$\rho^{(n+1)}(1, \cdots, n+1)/\rho^{(n)}(1, \cdots, n) = \rho^{(1)}(n+1|U_n)$$

$$= \Xi^{-1} \sum_{t \geq 1} \frac{z^t}{(t-1)!} \int \cdots \int \mathrm{d}(t-1) \exp\{-\beta[U_t + U(n|t)]\} \quad (1)$$

$$\Xi = \sum_{t \geq 0} \frac{z^t}{t!} \int \cdots \int \mathrm{d}(t) \exp\{-\beta[U_t + U(n|t)]\} \quad (2)$$

Here, we have followed essentially the notations and formalism of Rice and Gray.[7] Briefly, $\beta = 1/kT$ where k is the Boltzmann constant and T the absolute temperature. The quantity $(1, \cdots, n)$ denotes $(\mathbf{R}_1, \cdots, \mathbf{R}_n)$ where $(\mathbf{R}_i) = (X_i, Y_i, Z_i)$, the positional coordinates of the ith particle: $\mathrm{d}(N) = \mathrm{d}\mathbf{R}_1 \cdots \mathrm{d}\mathbf{R}_N$ where N is the total number of molecules in the system. $\rho^{(1)}(n+1|U_n)$ is the singlet distribution function when the system is subjected to an external potential field arising from n fixed molecules. $U(n|t)$ represents the interaction of n particles in the field of t particles. Finally Ξ and z are, respectively, the grand partition function and activity.

Let us consider the function $\mathrm{F}(2|U(1)) \equiv \alpha^{\ln \rho^{(1)}(2|U(1)) \exp \beta u(1,2)}$ (where u is the pair potential) as a functional of $\mathrm{G}(3|U(1)) \equiv \rho^{(1)}(3|U(1))$ in which "α" is a parameter whose value will be determined by methods described later. By performing a functional Taylor expansion, one finds

$$\mathrm{F}(2|U(1)) = \mathrm{F}(2) + \int \mathrm{d}(3) \left.\frac{\delta \mathrm{F}(2|U(1))}{\delta \mathrm{G}(3|U(1))}\right|_{U(1)=0} [\mathrm{G}(3|U(1)) - \mathrm{G}(3)] + (1/2!) \int\int \mathrm{d}(3)\,\mathrm{d}(4) \left.\frac{\delta^2 \mathrm{F}(2|U(1))}{\delta \mathrm{G}(3|U(1)) \delta \mathrm{G}(4|U(1))}\right|_{U(1)=0} \times [\mathrm{G}(3|U(1)) - \mathrm{G}(3)][\mathrm{G}(4|U(1)) - \mathrm{G}(4)] + \ldots = \alpha^{\ln \rho^{(1)}(2)} + \int \mathrm{d}(3) \left.\frac{\delta \alpha^{\ln \rho^{(1)}(2|U(1)) \exp[\beta u(1,2)]}}{\delta \rho^{(1)}(3|U(1))}\right|_{U(1)=0} \times [\rho^{(1)}(3|U(1)) - \rho^{(1)}(3)] + \ldots;$$

$$\mathrm{F}(2) = \mathrm{F}(2|U(1))|_{U(1)=0} \quad (3)$$

Through straightforward manipulation, it can be readily shown that

$$\left.\frac{\delta \alpha^{\ln \rho^{(1)}(2|U(1)) \exp[\beta u(1,2)]}}{\delta \rho^{(1)}(3|U(1))}\right|_{U(1)=0} = (\ln \alpha)\, \alpha^{\ln \rho^{(1)}(2)}\, \mathrm{c}(2,3) \quad (4)$$

The function c(2,3) is the direct correlation function which is related to the pair distribution function g(2,3) by the Ornstein-Zernike equation

$$\mathrm{g}(1,3) - 1 = \mathrm{c}(1,3) + \rho \int \mathrm{d}(2)\, \mathrm{c}(2,3)\, (\mathrm{g}(1,2) - 1) \quad (5)$$

Neglecting quadratic and higher order terms in the Taylor expansion and simply combining eq 3–5, one arrives at the following parametrized integral equation:

$$\mathrm{Q}(1,2) = \rho \int \mathrm{d}(3)\, (\mathrm{g}(2,3) - 1)[(\ln \alpha)\, (\mathrm{g}(1,3) - 1) - \mathrm{Q}(1,3)] \quad (6a)$$

and

$$\mathrm{Q}(i,j) = \alpha^{\ln \mathrm{g}(i,j) \exp[\beta u(i,j)]} - 1 \quad (6b)$$

It is interesting to note that if the function $\mathrm{Q}(i,j)$ is expanded in a series and only the leading term is retained, i.e.

$$\mathrm{Q}(i,j) \simeq (\ln \alpha) \ln \{(\mathrm{g}(i,j) \exp[\beta u(i,j)]\} \quad (7)$$

one finds the replacement of $\mathrm{Q}(i,j)$ by that given in eq 7 leads to the HNC-1 equation which is of course independent of the parameter α. On the other hand, if α is set equal to e, eq 6 is reduced to the PY-1 equation. Thus, this parametrized integral equation encompasses both the HNC-1 and PY-1 formalisms and it is in this sense that it resembles the method of Rowlinson which has a diagrammatic basis. It should be emphasized that more refined versions of the theory, which bear the same relation to the PY-2 and HNC-2 equations as the present one does to the PY-1 and HNC-1, may be constructed from this scheme by keeping additional terms of the functional Taylor expansion. Therefore, this method provides a means of systematically correcting for the current approximate integral equations of fluids.

There are two ways of demonstrating the improvements resulting from this parametrization vis-a-vis the PY-1 and HNC-1 equations. The first is the complete solution of eq 6 for all temperatures and densities. This involves a means of uniquely specifying the parameter α, e.g., through the minimization of the Helmholtz free energy. This will form the subject of a separate communication. The second is the study of the low density properties of the integral equation via the virial coefficients. In the following sections, we shall consider this approach for rigid spherical and Gaussian molecules.

III. The Virial Coefficients

A. *Rigid Spherical Molecules.* We seek the solution of eq 6 for the radial distribution function g(1,2) in the form of a density expansion

$$\mathrm{g}(1,2) = (\exp[-\beta u(1,2)]) \left(1 + \sum_{k=1}^{\infty} \mathrm{g}_k(1,2) \rho^k\right) \quad (8)$$

The coefficients appearing in the expansion of the compressibility factor (the symbols have their customary significance)

$$P\beta/\rho = 1 + B\rho + C\rho^2 + D\rho^3 + E\rho^4 + \ldots \quad (9)$$

may be expressed in terms of the functions $\mathrm{g}_k(1,2)$. We find that $\mathrm{g}_1(1,2)$ and consequently the coefficients up to the third (C) are given correctly and that $\mathrm{g}_2(1,2)$ and $\mathrm{g}_3(1,2)$ may be written as:

TABLE I: Comparison of Virial Coefficients of Rigid Spherical Molecules Derived from Various Integral Equations of Fluids

Method	K	D_p^*	D_c^*	E_p^*	E_c^*
$D_p^* = D_c^*$	−0.165 637	0.2824	0.2824	0.0844	0.1119
$D_p^* = D_{exact}^*$	−0.189 184	0.2869	0.2803	0.0845	0.1105
$D_c^* = D_{exact}^*$	−0.113 188	0.2721	0.2869	0.0843	0.1149
PY-1		0.2500	0.2969	0.0859	0.1211
HNC-1		0.4453	0.2092	0.1447	0.0493
Exact[a]		0.2869	0.2869	0.1103	0.1103

[a] References 8.

TABLE II: Comparison of Virial Coefficients of Gaussian Molecules Derived from Various Integral Equations of Fluids[a]

Method	K	D_p^*	D_c^*	E_p^*	E_c^*
$D_p^* = D_c^*$	−0.646 4464	−0.1255	−0.1255	−0.0050	0.0439
$D_p^* = D_{exact}^*$	−0.646 4446	−0.1255	−0.1255	−0.0050	0.0439
$D_c^* = D_{exact}^*$	−0.646 4474	−0.1255	−0.1255	−0.0050	0.0439
PY-1		−0.1540	−0.0732	0.0683	0.0139
HNC-1		−0.1098	−0.1540	−0.0408	0.0554
Exact		−0.1255	−0.1255	0.0133	0.0133

[a] Please note that the values of E_c^* for the PY-1 and HNC-1 theories were incorrectly given in ref 11.

$$g_2(1,2) = g_2^{PY\text{-}1}(1,2) - (K/2)\, g_1^2(1,2) \quad (10)$$

$$g_3(1,2) = g_3^{PY\text{-}1}(1,2) - K\, I(1,2) - K\, g_1(1,2)\, g_2^{PY\text{-}1}(1,2) + (K/6)(2K+1)\, g_1^3(1,2); \quad K = (\ln \alpha) - 1 \quad (11)$$

The function I(1,2) is defined in terms of f_{ij} (= $\exp -\beta u(i,j) - 1$):

$$I(1,2) = \int d(3)\, f_{13}(1 + f_{23})\, g_1^2(1,2) \quad (12)$$

For rigid spherical molecules

$$f(r_{ij}) = -1 \text{ if } r_{ij} < \sigma$$
$$= 0 \text{ if } r_{ij} > \sigma \quad (13)$$

The superscript PY-1 in $g_k(1,2)$ denotes quantities to be evaluated according to the PY-1 theory. Next, we designate the virial coefficients obtained from the pressure equation

$$P\beta/\rho = 1 - (2\rho\pi\beta/3) \int_0^\infty dr\, r^3\, g(r)\, (du(r)/dr) \quad (14)$$

by C_p, D_p, E_p, . . . , and those from the compressibility equation

$$\beta^{-1}\partial\rho/\partial P = 1 + 4\rho\pi \int_0^\infty dr\, r^2\, (g(r) - 1) \quad (15)$$

by C_c, D_c, E_c, etc. The formulas for D_p and D_c deduced from the above equations for a system of rigid spherical molecules may finally be expressed as

$$D_p^* = D_p^{*PY\text{-}1} - (25K/128) \quad (16a)$$

and

$$D_c^* = D_c^{*PY\text{-}1} + (2357K/26\,880); \quad D_k^* = D_k/B^3 \quad (16b)$$

Similarly, the equations for the fifth virial coefficients assume the following form:

$$E_p^* = E_p^{*PY\text{-}1} - K\, I^*(1) - (5K/8) D_p^{*PY\text{-}1} + (125K\,(K+1))/3072 \quad (17)$$

and

$$E_c^* = E_c^{*PY\text{-}1} + K(56\,269 - 20\,954K)/1\,075\,200 \quad (18)$$

where

$$E_k^* = E_k/B^4,\ I^*(1) = I(1)/B^3$$

and

$$I(R) = (\pi^3/R)[(87/4480) - (2357R/22\,680) + (251R^2/5760)]; \quad 1 \le R \le 2 \quad (19)$$

$$I(R) = (\pi^3/R)[(3159/4480) - (2673R/840) + (2187R^2/640) - (9R^3/8) - (15R^4/64) + (9R^5/40) - (31R^6/960) - (17R^7/2520) + (5R^8/2688) - (R^{10}/51\,840)]; \quad 2 \le R \le 3$$

$$I(R) = 0; \quad R > 3$$

From these equations, it is evident that once the parameter K (or α) is specified, the coefficients can be immediately evaluated. There are three ways of determining K within the present framework: (a) by requiring the coefficients derived from eq 14 and 15 be identical, i.e., $D_p = D_c$. This is a self-consistency argument; (b) by setting $D_c = D_{exact}$(known), and (c) by letting $D_p = D_{exact}$(known). Table I summarizes the results of considering these three cases.

From this table, one notes that the virial coefficients derived from this first-order parametrized integral equation are in significantly better accord with the known values than either the PY-1 or the HNC-1 theory. Also, the self-consistent ($D_p = D_c$ case) results are quite similar to those of the formally different theories of Rowlinson and Hurst, i.e., the values of the fourth virial coefficient are identical but those of the fifth vary somewhat. It appears that, in the region of lower fluid densities, our procedure is numerically analogous to these diagrammatic schemes.

B. *Gaussian Molecules.* Whereas the rigid spherical molecules we have just considered interact with a "hard" repulsive force which is infinite at a distance corresponding to the diameter of the molecules, we now wish to examine the case of a "soft" repulsive force, one in which the Mayer f function is given by

$$f(r) = -\exp[-(r/a)^2]; \quad (\sigma/a)^3 = 3\sqrt{\pi}/4 \tag{20}$$

Here, r is the intermolecular separation and a a size parameter whose value is to be selected so that the resulting second virial coefficient is the same as that of the rigid spheres of diameter σ. This system has been analyzed in various context by Uhlenbeck and Ford,[9] Helfand and Kornegay,[10] and Chung and Espenscheid.[11] In the evaluation of the fourth and fifth virial coefficients, cluster integrals over multidimensional Gaussians are involved; these integrals may be computed exactly for this model. For example, a p point diagram with k f bonds has the general form

$$J(1,2) = (-1)^k \int \ldots \int d(3) \ldots d(p) \exp[-\sum_{i,j} M_{ij} \mathbf{r}_i \cdot \mathbf{r}_j] \tag{21}$$

where $\mathbf{M}$ is a $p \times p$ cluster matrix whose elements are

$$\begin{aligned} M_{ij} &= -1 \text{ if points } i \text{ and } j \text{ are connected by a f bond} \\ &= 0 \text{ otherwise} \end{aligned} \tag{22}$$

and M_{ii} is equal to the number of f bonds emanating from point i. Helfand and Kornegay showed that

$$J(r) = (-1)^k (a^3\pi^{3/2})^{p-2} (M^{11;22})^{-3/2} \times \exp\left[-(r/a)^2 \left(\frac{M^{11}}{M^{11;22}}\right)\right] \tag{23}$$

where M^{11} is the 1,1 minor of $\mathbf{M}$ and $M^{11;22}$ is the 1,1;2,2 second minor. Using this result, we found that for the Gaussian model

$$D_p^* = D_p^{*\text{PY-1}} - (2^{-9/2})K \tag{24a}$$

$$D_c^* = D_c^{*\text{PY-1}} + (K/8)(1 - 2^{-3/2}) \tag{24b}$$

and

$$E_p^* = E_p^{*\text{PY-1}} + K[2(3)^{-5/2} - (8/3)(5)^{-5/2} + 48(11)^{-5/2} - 160(21)^{-5/2}] + (2/3)(5)^{-5/2} K^2 \tag{25a}$$

$$E_c^* = E_c^{*\text{PY-1}} + K[(3)^{-5/2} - (53/3)(5)^{-5/2} + (48/5)(11)^{-3/2} - (32/5)(21)^{-3/2}] + [(2/3)(5)^{-5/2} - (2/5)(3)^{-5/2}]K^2 \tag{25b}$$

The values of these virial coefficients are presented in Table II. Again, one finds that the parametrized integral equation leads to large improvements over the PY-1 and HNC-1 equations. In fact, for this molecular model, the fourth virial coefficients are in complete agreement with the exact, known results. The fifth virial coefficients derived from the three methods of specifying K are numerically the same and they are comparable to those of the PY-1 and HNC-1 theories.

Further comparisons at higher densities must await the solution of the integral equations for various molecular models. At present, suffice it to say that, with the method of functional differentiation, successively better parametrized theories can be developed. It is anticipated, for example, that the second-order theory (inclusion of the quadratic term in the Taylor expansion) of the parametrized integral equation will provide more satisfactory results at all temperatures and densities than the PY-2 and HNC-2 equations.

References and Notes

(1) L. Verlet, *Physica*, **30**, 95 (1964).
(2) L. Verlet and D. Levesque, *Physica*, **36**, 254 (1967).
(3) J. S. Rowlinson, *Mol. Phys.*, 9, 217 (1965).
(4) D. D. Carley and F. Lado, *Phys. Rev.*, **137**, A42 (1965).
(5) G. S. Rushbrooke and P. Hutchinson, *Physica*, 29, 675 (1963).
(6) C. Hurst, *Proc. Phys. Soc.*, **86**, 193 (1965).
(7) S. A. Rice and P. Gray, "The Statistical Mechanics of Simple Liquids", Interscience, New York, N.Y., 1965.
(8) F. H. Ree, R. N. Keeler, and S. L. McCarthy, *J. Chem. Phys.*, **44**, 3407 (1966).
(9) G. E. Uhlenbeck and G. W. Ford, "Studies in Statistical Mechanics", Vol. I, J. deBoer and G. E. Uhlenbeck, Ed., North Holland Publishing Co., Amsterdam, 1962.
(10) E. Helfand and R. L. Kornegay, *Physica*, **30**, 1481 (1964).
(11) H. S. Chung and W. F. Espenscheid, *Mol. Phys.*, **14**(4), 317 (1968).

Semiconducting Potassium Tantalate Electrodes. Photoassistance Agents for the Efficient Electrolysis of Water

Arthur B. Ellis, Steven W. Kaiser, and Mark S. Wrighton*

Department of Chemistry, Massachusetts Institute of Technology, Cambridge, Massachusetts 02139 *(Received October 30, 1975)*

Single crystals of the perovskites $KTaO_3$ and $KTa_{0.77}Nb_{0.23}O_3$ are shown to be efficient photoassistance agents for the electrolysis of water. These n-type semiconductors are photostable in concentrated alkaline solutions where they serve as the anode in the electrolysis reaction. Experiments with ^{18}O-enriched water identify the electrolyte, not the crystal, as the source of the evolved oxygen. Stoichiometric data show the ratio of moles of electrons to moles of hydrogen to moles of oxygen produced to be nearly 4:2:1 as expected for the electrolysis reaction. Consistent with band gaps in the tantalates of ~3.5 eV, light of wavelengths shorter than ~390 nm produces photocurrent. Quantum yields for electron flow at 254 nm are as high as 0.3 to 0.5. The onset of anodic photocurrent is ~−1.25 V vs. SCE in 8.6 M NaOH. These electrode photoassistance agents can operate with no external bias. Crystals of $KTa_{0.77}Nb_{0.23}O_3$ reduced with H_2 at various temperatures show modest variations in current–voltage properties. Optical to chemical energy conversion efficiencies of ~6% for the $KTaO_3$ crystals and ~4% for the $KTa_{0.77}Nb_{0.23}O_3$ crystals are possible. The tantalates examined compare favorably with other electrodes capable of photoassisting the electrolysis of water.

Introduction

The reported[1] use of n-type TiO_2 as the photoelectrode in an electrode system to photoassist the electrolysis of water, reaction 1, has aroused a great deal of interest as a means of

$$H_2O \xrightarrow[\text{(photoassistance agent)}]{h\nu} H_2 + \tfrac{1}{2}O_2 \qquad (1)$$

converting optical to chemical energy.[2] It has been found that the long-term stability of the TiO_2 photoelectrode is offset by such undesirable features[2a,d,g,3-5] as a photoeffect onset near 400 nm, the need for a bias, and low quantum efficiency at small bias. Another semiconductor photoelectrode having a rutile structure, SnO_2, exhibited similar characteristics.[6]

Recent results with a reduced $SrTiO_3$ photoelectrode indicate that the perovskite family could be a new source of robust n-type semiconductors capable of effecting reaction 1.[7] Reduced $SrTiO_3$ is a remarkable electrode in that it photoassists electrolysis without an external bias; for wavelengths below 330 nm and for applied voltages of $\geq$1.5 V, the quantum efficiency for electron flow is unity. Significantly, the optical to chemical energy conversion efficiency can be as high as 20–25%.

In this paper we report results for n-type semiconducting perovskites, $KTaO_3$ and $KTa_{0.77}Nb_{0.23}O_3$, and demonstrate that they serve as the photoreceptor in electrode systems for the photoelectrolysis of water. Quantum yields, stoichiometry, wavelength response, and current–voltage properties of these photoassistance agents are given below. To our knowledge, there has been only one other study[8] of the electrode properties of $KTaO_3$.

Experimental Section

Crystals of n-type semiconducting $KTaO_3$ and $KTa_{0.77}Nb_{0.23}O_3$ were grown by the top-seeded solution technique. These materials have been kindly supplied to us by Dr. Arthur Linz of the Department of Electrical Engineering. All of the samples are at least partially reduced. The actual donor in the $KTaO_3$ is probably calcium. The donor densities in all cases are likely ~10^{19} cm^{-3}. Suitable samples of ~1 mm thickness were cut from each crystal and the faces were polished. Samples designated A, B, and C with approximate cross sections (mm) 15 × 13, 12 × 10, and 3 × 3, respectively, were obtained from the $KTaO_3$ crystal; similarly D, E, and F (5 × 7, 7 × 7, and 5 × 5 mm, respectively) were obtained from the $KTa_{0.77}Nb_{0.23}O_3$ crystal. Samples E and F were subsequently reduced with H_2 for 2 h at 900 and 1050 °C, respectively. Electrodes were fashioned by rubbing gallium–indium eutectic on one face of the crystal and attaching this to a glass-encased copper wire whose end had been coated with silver epoxy. All exposed metal was then insulated with ordinary epoxy.

Two basic photoelectrochemical cells were used in this study. One cell consists of a Pt-wire (~1 mm × 25 mm) cathode and the semiconductor photoelectrode with a variable power supply (HP Model 6241A) and a small resistor (15 Ω) in the external circuit. The potential drop across the resistor was used to measure the current, and this was continuously monitored against time using a Varian Model A-25 recorder. This basic cell is schemed in Figure 1. Such a cell was used for product identification and stoichiometry studies and for determining photocurrents as a function of *applied potential from the power supply*. The second cell is a very similar one except the photoelectrode was potentiostatted vs. a saturated calomel electrode (SCE) using a Heath EUA-19-2 polarography module. The potentiostatted system was used to measure current–voltage (vs. SCE) curves of the photoelectrode as shown in Figures 2 and 3. The Heath potentiostat will not operate at currents in excess of 1.0 mA, and consequently, we used a neutral density filter to limit photocurrents to less than 1.0 mA. The light source was a Bausch & Lomb SP200 equipped with an Osram HBO-200W super high pressure Hg arc lamp. Excessive heat from the focused light beam was dissipated by passing the beam through 18 cm of water.

Gases evolved in the stoichiometry experiments were collected by displacing the electrolyte from 10-ml graduated cylinders which were inverted above the electrodes. A photoassisted electrolysis of ^{18}O-enriched water (obtained from Stohler Isotope Chemicals) was conducted in a small, sealed, U-shaped Vycor vessel designed for gas collection from each

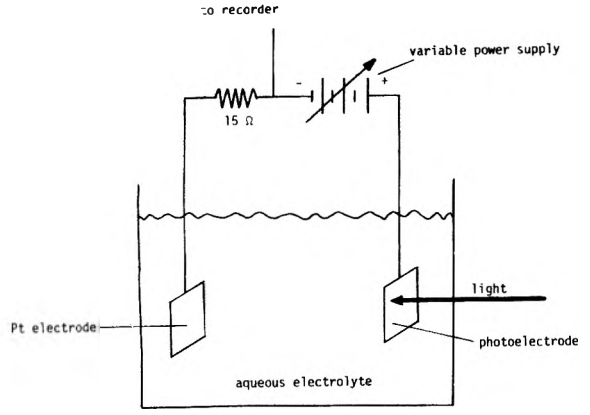

Figure 1. Typical photoelectrochemical cell used in this work for stoichiometry studies. A Hewlett Packard Model 6241A power supply was the variable source indicated in the circuit and a Varian A-25 recorder was used :o monitor current.

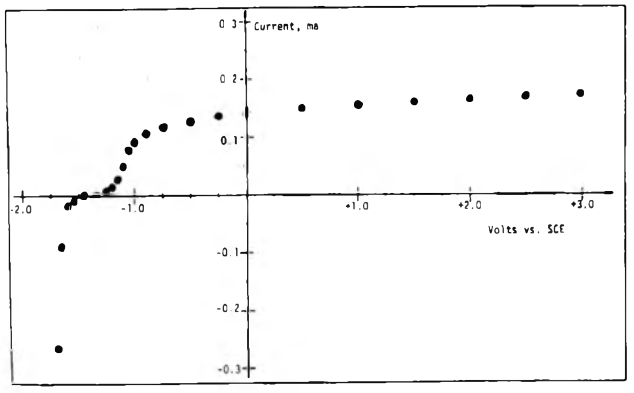

Figure 2. Current–voltage curve for the $KTa_{0.77}Nb_{0.23}O_3$, crystal D, photoelectrode vs. SCE in 8.6 M NaOH. The curve was obtained using the Heath potentiostat (during uv irradiation).

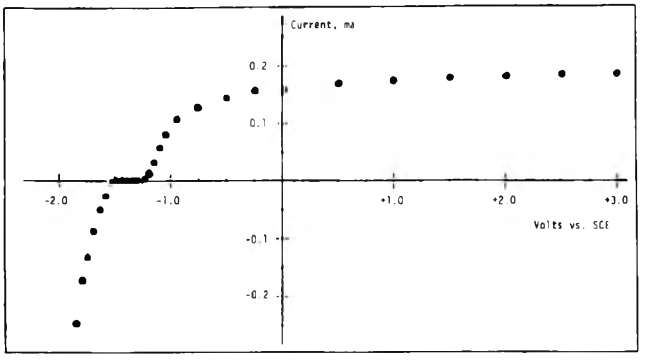

Figure 3. Current–voltage curve for the $KTaO_3$, crystal A, photoelectrode vs. SCE in 8.6 M NaOH. The curve was obtained using the Heath potentiostat (during uv irradiation).

electrode. The gases were analyzed on a Hitachi Perkin-Elmer RMU-6 mass spectrometer.

An Aminco-Bowman SPF-2 emission spectrometer with a 150-W xenon excitation lamp was used with an HP 7044A x–y recorder to obtain relative photocurrent as a function of exciting wavelength. A Vycor cell was placed in the sample chamber such that the photoelectrode was in the path of the light beam. The observed curve was corrected for Vycor absorption and for variation in lamp intensity as a function of wavelength using a rhodamine B quantum counter.[9] Light

TABLE I: Electrode Stability[a]

Crystal	Weight, g		Moles × 10^4		Moles O_2 evolved × 10^4
	Before	After	Before	After	
A	1.4758	1.4751	55.33	55.31	1.29
B[b]	0.8942	0.8908	33.53	33.40	1.38
C	0.1438	0.1433	5.392	5.373	0.876
E	0.3865	0.3864	15.60	15.60	0.53

[a] All data were collected at 25 °C at potentials of less than 2.0 V applied and where the stoichiometry corresponded to the electrolysis of water. [b] Part of this crystal chipped when it was demounted and could not be recovered.

intensities in quantum yield measurements were measured with ferrioxalate actinometry[10] using the Bausch & Lomb source coupled to a Bausch & Lomb high-intensity monochromator.

Results and Discussion

Upon irradiation of the n-type tantalates in the cell shown in Figure 1, electrons flow from the semiconductor toward the Pt electrode. Gases are evolved at each electrode in quantities proportional to the light intensity. Photoelectrode stability was confirmed by experiments carried out with ^{18}O-enriched water and by lack of weight loss of the photoelectrode. Using crystal C mounted in the sealed cell equipped with gas collection tubes (cf. Experimental Section), the identity of the gases evolved from each electrode was determined by mass spectroscopy. With 9.9 N NaOH in $H_2{}^{16}O/H_2{}^{18}O$ (4:1) as the electrolyte, oxygen was collected at the photoelectrode (anode) and hydrogen at the platinum electrode (cathode). A peak at m/e 34 ($^{16}O^{18}O$), roughly one-half the size of the m/e 32 ($^{16}O_2$) peak, confirmed that water is being oxidized and that the O_2 evolved does not originate from decomposition of the electrode. Further, electrode stability was determined directly by measuring the weight loss of the photoelectrode under conditions where the amount of O_2 evolved is of the same order of magnitude as that potentially available from the crystal. These results are shown in Table I. Thus the photoelectrode is stable under the conditions required to electrolyze water. In no case have we found deterioration of electrode properties as a consequence of prolonged irradiation.

The results of quantitative measurement of integrated current in the external circuit, H_2 production, and O_2 production are collected in Table II. A stoichiometric ratio of 4:2:1 for moles of electrons to moles of H_2 to moles of O_2 should result from the electrolysis of water, reaction 1. The data are generally consistent with the electrolysis of water; however, the H_2/O_2 ratio is often greater than 2.0, while the ratio of moles of electrons to moles of hydrogen is always about 2.0. This O_2 deficiency has been observed with other photoelectrodes and attributed to the incomplete decomposition of H_2O_2, a possible intermediate[6,7] in the formation of O_2.

A summary of the I–V characteristics of the tantalate electrodes relative to SCE appears in Table III. Representative curves are pictured in Figures 2 and 3. Anodic currents could only be obtained by irradiation, while dark cathodic currents were not influenced significantly by irradiation. The electrodes examined here are all similar to reduced $SrTiO_3$ in that they yield photocurrent at zero bias (Figure 4). Only for crystals A and B, however, could we verify that this photocurrent corresponds to the electrolysis of water (Table II). For electrodes C, D, E, and F very small sustained currents at

TABLE II: Stoichiometric Data[a]

Crystal	Applied potential, V[b]	Average current, mA[c]	Irradiation time, h	Mol × 10^4		
				Electrons	H_2	O_2
A	0.00	0.17	11.0	0.70	0.35	0.13
B	0.00	0.08	22.75	0.75	0.33	0.16
B	0.25	0.69	18.3	4.85	2.82	1.22
C	1.00	0.95	8.0	2.85	1.55	0.49
C	0.25	0.30	13.3	1.49	0.73	0.39
D	1.20	0.49	25.0	4.32	2.16	0.96
E	0.15	0.48	16.5	2.95	1.58	0.53

[a] 8.6 N NaOH electrolyte, 25 °C. [b] Positive lead to the photoelectrode. [c] Determined by measuring the potential drop across a 15-Ω resistor in series in the circuit.

TABLE III: Current–Voltage Characteristics

Crystal	Anodic onset voltage[a]	Width of voltage plateau, V[b]	$I\ (V_{appl} = 0.00)/I\ (V_{appl} = 4.00)$[c]
A	−1.25	0.30	0.15
D	−1.35	0.17	0.035
E	−1.30	0.25	0.061
F	−1.20	0.35	0.085

[a] Voltage vs. SCE at which anodic photocurrent appears ±0.02 V in 8.6 M NaOH solution. [b] Difference between onsets of anodic photocurrent and dark cathodic currents ±0.04 V in 8.6 M NaOH solution. [c] Ratio of currents (±10%) at the applied voltages of 0.0 and 4.0 in 8.6 M NaOH solution. These values are obtained from plots of photocurrent vs. applied potential such as that shown in Figure 4 using the cell schemed in Figure 1.

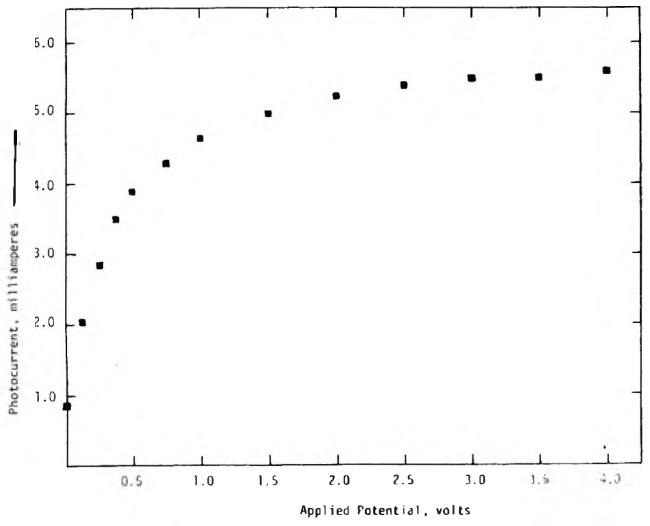

Figure 4. Relative photocurrent vs. applied potential (positive lead to photoelectrode) for $KTaO_3$, crystal B, in 8.6 M NaOH. This curve was determined using the cell schemed in Figure 1.

zero-bias precluded collection of measurable quantities of gases. The data in Table III suggest that reasonable rates of H_2 and O_2 evolution would be expected at zero bias. However, generally, the initially high photocurrents fall to lower values with prolonged irradiation. The photocurrent never reached zero, but to maintain a prolonged, steady photocurrent a small (~0.05–0.19 V) anodic bias is required. Data summarized in Table III and presented in Figures 2–4 represent information recorded over a period of the order of 10 min.

The effect of the reduction with hydrogen for crystals D, E, and F seems to be a slightly steeper anodic rise, a shift in the onset of anodic photocurrent to more positive voltage, and an increase in the width of the plateau separating the onsets of anodic and cathodic current regions. The most highly reduced crystal of the trio, F, was the only one which had reached a saturated photocurrent by 4.0 V applied. Even A, B, and C, which had very high photocurrents at 0.0 V applied and steep anodic rises, did not completely saturate by 4.0 V applied. This is in contrast to reduced $SrTiO_3$ which reached saturation at ≤1.5 V applied. These observations serve notice that variations in the overall cell efficiency will be dependent on the particular electrode material and its preparation.

The absolute photocurrent at 4.0 V applied for the tantalate photoelectrodes ranged from 2 to 6 mA at the highest light intensities used. Current densities of >10 mA/cm^2 have been observed. The maximum current density only depends on the light intensity in the range we have investigated, and the photocurrent is directly proportional to light intensity.

Representative wavelength response curves (relative photocurrent as a function of exciting wavelength) are presented in Figure 5. The onset of photocurrent generally corresponds to the energy of the valence band to conduction band transition in the semiconductor, i.e., the band gap. Band gaps reported for reduced $KTaO_3$[11] and $KTa_{0.65}Nb_{0.35}O_3$[12] are 3.5 and 3.6 eV, respectively, in general agreement with our curves. The photoresponse edge for the tantalates, A, B, and C, appears to be about 370 nm (3.3 eV). Values for the niobate–tantalates D, E, and F are 400, 390, and 380 nm, respectively, thus showing a slight blue shift of absorption edge with reduction. All of the wavelength response curves seem to level off between 270 and 300 nm.

Quantum efficiency for electron flow was determined for electrodes A, B, and E and is summarized in Table IV. These values are reported at 4.0 V applied, but since the photocurrent had not yet saturated at this value, larger quantum yields would obtain at higher potentials. The ratios of these observed quantum yields at various wavelengths agree with the relative wavelength response curves of Figure 5 as required. In no case have we observed a quantum efficiency which is near unity. The possible reasons for this inefficiency are currently under study in these laboratories.

At this point detailed comparisons of these electrode photoassistance agents and those based on TiO_2,[3] SnO_2,[6] and $SrTiO_3$[7] are really inappropriate, since the actual ultimate efficiencies in these systems vary somewhat with electrode preparation, surface treatment, and other materials variables. However, the results reported herein do support the claim that these tantalates are at least as good at TiO_2 in overall energy conversion efficiency, are better than SnO_2, but seem slightly inferior to $SrTiO_3$. We have used[3,7] eq 2 to define the optical

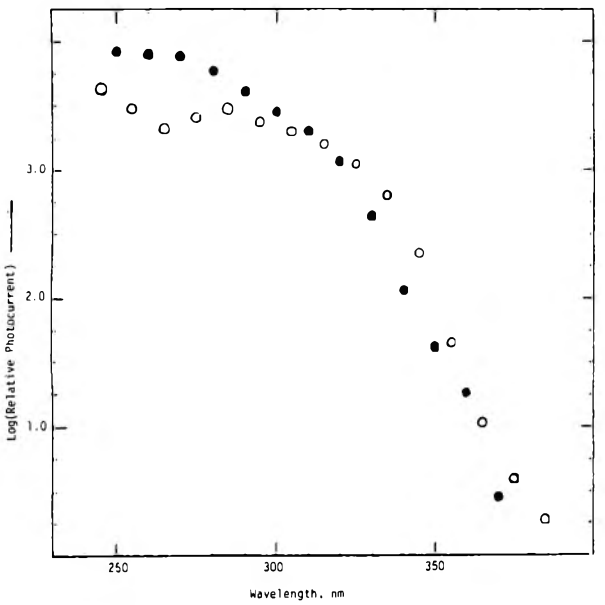

Figure 5. Wavelength response curves for $KTaO_3$, crystal A (●), and $KTa_{0.77}Nb_{0.23}O_3$, crystal E (○). The relative photocurrents shown have been corrected for variation in the light intensity as a function of wavelength.

TABLE IV: Quantum Efficiency for Electron Flow

Crystal	Wavelength, nm[a]	Intensity, einstein/s	$\Phi(\pm 0.2\Phi)$[b]
A	254	7.00×10^{-10}	0.47
B	254	7.4×10^{-10}	0.41
	313	7.75×10^{-9}	0.14
E	254	2.48×10^{-10}	0.33
	313	2.37×10^{-9}	0.28
	313	1.69×10^{-10}	0.28
	336	2.18×10^{-10}	0.16

[a] Bausch & Lomb source with monochromator. [b] In 8.6 M NaOH at 4.0 V applied.

to chemical energy conversion efficiency, η. The value of η can be calculated from data given in the results using eq 3 where

$$\eta = \frac{[\text{energy stored as } H_2] - [\text{energy in from power supply}]}{[\text{energy from light}]} \quad (2)$$

$$\eta = \frac{[\Phi][(0.5)(56.7) - (23.07)(V_{appl})]}{[h\nu \text{ (in kcal/einstein)}]} \quad (3)$$

Φ is the quantum efficiency for electron flow at an applied potential, V_{appl}, and a photon energy $h\nu$ in kilocalories per einstein. The stored energy from the H_2 is 56.7 kcal/mol, the change in free energy associated with reaction 1.[13] The factor of 0.5 is introduced to take into account the fact that two electrons flow per H_2 molecule, and the 23.07 converts volts to kilocalories per mole.

The thermodynamic reversible electrolysis potential for H_2O is 1.23 V, and thus if the applied potential from the power supply is less than this value then optical energy is being utilized. In the cases at hand the electrolysis can even be realized with no bias whatsoever. However, the maximum photoeffect occurs at some positive applied potential (power supply assisting the process). Applied potentials exceeding 1.23 V would yield negative optical → chemical energy conversion efficiency, since in principle, two good electrodes could be used to electrolyze H_2O just above 1.23 V. Thus, the maximum optical → chemical energy conversion will occur somewhere between the onset applied potential and 1.23 V.

For $SrTiO_3$ the maximum value of η obtained was ~0.20 at ~0.35 V_{appl} and 330 nm.[7] For TiO_2 we[3] obtained a maximum value of $\eta \sim 0.02$ and for SnO_2 the efficiency would be even lower since the band gap is larger and higher applied potentials are required.[6] For the tantalates we see from Figure 5 that the maximum efficiency is achieved at ~300 nm (95.3 kcal/einstein), and by using the data in Table IV and Figure 4 we can determine values of η as high as ~0.06 near 0.25 V ($\Phi_{obsvd} \simeq 0.25$). In a similar way $KTa_{0.77}Nb_{0.23}O_3$ gives a value of η_{max} of 0.04. Thus, these tantalates are fairly efficient photoelectrodes. We stress firmly that these determinations are to be used only as a rough guide, since we have not determined the full range of behavior of any system upon wide variation in the material preparation. These initial studies, though, which show that ~6% of the light energy can be converted to stored chemical energy without deterioration of the system, provide real reason for further detailed studies of the perovskites as photoelectrode materials. A good working model for photoelectrochemical cells has already been advanced,[14] and it was pointed out that one of the crucial needs is the discovery and characterization of *stable* photoelectrodes. The perovskites provide rich territory for new detailed studies, but with respect to practical optical energy conversion devices, materials with lower band gaps are required. In this regard we note with interest the recent results on stabilizing small band gap photoelectrodes by thin metal coatings on the semiconductor surface exposed to the electrolyte.[15]

Acknowledgment. We wish to thank Dr. Arthur Linz and Peter Wolczanski of MIT for providing the crystals used in this study. We acknowledge the National Aeronautics and Space Administration for their support of this research. M.S.W. acknowledges support as a Fellow of the A. P. Sloan Foundation, 1974–1976, and A.B.E. as a Fellow of the Fannie and John Hertz Foundation.

References and Notes

(1) A. Fujishima and K. Honda, *Nature (London)*, **238**, 37 (1972); *Bull. Chem. Soc. Jpn.*, **44**, 1148 (1971).
(2) (a) J. Keeney, D. H. Weinstein, and G. M. Haas, *Nature (London)*, **253**, 719 (1975); (b) F. Mollers, J. J. Tolle, and R. Memming, *J. Electrochem. Soc.*, **121**, 1160 (1974); (c) H. Yoneyama, H. Sakamoto, and H. Tamura, *Electrochem. Acta*, **20**, 341 (1975); (d) W. Gissler, P. L. Lensi, and S. Pizzini, *J. Appl. Electrochem.*, **6**, 9 (1976); (e) K. L. Hardee and A. J. Bard, *J. Electrochem. Soc.*, **122**, 739 (1975); (f) M. D. Archer, *J. Appl. Electrochem.*, **5**, 17 (1975); (g) A. Nozik, *Nature (London)*, **257**, 383 (1975).
(3) M. S. Wrighton, D. S. Ginley, P. T. Wolczanski, A. B. Ellis, D. L. Morse, and A. Linz, *Proc. Natl. Acad. Sci. U.S.A.*, **72**, 1518 (1975).
(4) A. Fujishima, K. Kohayakawa, and K. Honda, *Bull. Chem. Soc. Jpn.*, **48**, 1041 (1975).
(5) T. Ohnishi, Y. Nakato, and H. Tsubomura, *Ber. Bunsenges. Phys. Chem.*, **79**, 523 (1975).
(6) M. S. Wrighton, D. L. Morse, A. B. Ellis, D. S. Ginley, and H. B. Abrahamson, *J. Am. Chem. Soc.*, **98**, 44 (1976).
(7) M. S. Wrighton, A. B. Ellis, P. T. Wolczanski, D. L. Morse, H. B. Abrahamson, and D. S. Ginley, *J. Am. Chem. Soc.*, in press.
(8) P. J. Boddy, D. Kahng, and Y. S. Chen, *Electrochim. Acta*, **13**, 1311 (1968).
(9) W. H. Melhiush, *J. Opt. Soc. Am.*, **52**, 1256 (1962).
(10) C. H. Hatchard and C. A. Parker, *Proc. R. Soc., Ser. A*, **235**, 518 (1956).
(11) D. Khang and S. H. Wemple, *J. Appl. Phys.*, **36**, 2925 (1965).
(12) M. DiDomenico, Jr., and S. H. Wemple, *Phys. Rev.*, **166**, 565 (1968).
(13) W. J. Moore, "Physical Chemistry", 3rd ed, Prentice-Hall, Englewood Cliffs, N.J., 1962, p 172.
(14) H. Gerischer, *J. Electroanal. Chem.*, **58**, 263 (1975), and references therein.
(15) Y. Nakato, T. Ohnishi, and H. Tsubomura, *Chem. Lett.*, 883 (1975).

Exoelectron Emission from Ground Aluminum Powder and Its Relationship to the Adsorption of Oxygen, Water, and Some Organic Compounds

Yoshihiro Momose,* Yasuo Iguchi, Sakae Ishii, and Kazuei Komatsuzaki

Department of Industrial Chemistry, Faculty of Engineering, Ibaraki University, Hitachi, Ibaraki, Japan *(Received December 3, 1975)*

Publication costs assisted by Ibaraki University

The surface properties of mechanochemically altered aluminum powder have been studied by means of optically stimulated exoelectron emission (EEE). The "glow-curve" characteristics of EEE from the powder ground in air were strongly influenced by the kind of organic vapor contained in the Geiger-counter gas. The vapors are listed in the descending order of the emission as: $(n\text{-}C_3H_7)_2NH > n\text{-}C_3H_7NH_2 > CH_3COOC_2H_5 > C_6H_6 > C_2H_5OH > (CH_3)_2CO > CH_3CN > n\text{-}C_4H_9Cl$. The emission is correlated with the dielectric constant or acidity constant of the organic compounds, by which the electric field formed on the surface may be influenced. When the powder ground in air was exposed to air for a longer time, the emission became weaker and decreased with an increase of the air humidity. The decay of the emission may be associated with the growth of oxide film and the more amorphous layer formed by condensation of water molecules. The powder ground in various environments (vacuum, O_2, H_2O, C_2H_5OH, and $n\text{-}C_3H_7NH_2$) gave a quite different "glow curve". The emission for vacuum was weaker than that for other environments and the emission varied with increasing vapor pressure of H_2O, C_2H_5OH, and $n\text{-}C_3H_7NH_2$. The surface altered in these environments exhibited a different emission decay during exposure to air, which indicates that the modified surface has a specific chemical activity.

Introduction

Exoelectron emission phenomena have been reviewed from time to time.[1-3] From the viewpoint of whether the phenomena are due to processes inherent to metals or result from interaction with the environment, Ramsey[4] has used the terms "intrinsic" EEE and "extrinsic" EEE, respectively. The latter means that adsorption, the presence of oxide, or some other external material factor is essential for EEE and the present paper is associated with this type of EEE.

The surface phenomena of aluminum is of considerable interest in view of the wide-spread use of this metal because of its light weight, mechanical workability, and remarkable resistance to atmospheric corrosion. Therefore, there is great interest in the role of exoelectrons in mechanochemical reactions[5-8] in adhesion or corrosion phenomena and further in the role of these electrons in heterogeneous reactions.

Few reports are available concerning the effect of adsorption of gases other than water and oxygen[9,10] on the emission from aluminum. However, Polyakov and Krotova[11] have reported that the emission rate upon detachment of polymers from glass is determined primarily by the type of functional groups in the polymer. The present work was undertaken to investigate the interaction between ground aluminum powder and some gaseous compounds by means of EEE: the effect of organic vapor in the Geiger-counter atmosphere on the exoelectron "glow curves" (the change of the emission intensity with temperature) for powder ground in air or in various environments containing the organic vapors, water vapor, and oxygen, and also the "glow curves" as a function of grinding time and exposure time to air after grinding.

Experimental Section

Materials. Commercial aluminum powder (purity 99.5%, 115–200 mesh, Wako Chemicals) was used. Its surface would, of course, be covered by an oxide film. The surface of the powder received no special preparation other than storing in air dried with phosphorus pentoxide for 1 or more days before use. The purity of the oxygen used was 99.99%. The water used was redistilled. The organic vapors were identical with those in earlier papers[12,13] and we used the following compounds: di-*n*-propylamine, *n*-propylamine, ethyl acetate, benzene, ethanol, acetone, acetonitrile, and *n*-butyl chloride.

Grinding. The grinding of the powder was performed by use of a magnetic stirrer in two experimental methods. In one method, the powder (0.50 g) was introduced into a glass vessel (16 mm in diameter and 55 mm deep) with an aluminum plate laid at the bottom and then ground in air (18–24 °C, 32–62% relative humidity (RH)) for a given time (usually 10 min). The powder was broken between a rotator (a small iron bar, 350 rpm) and the aluminum plate to become a finer powder. The sample was kept in air for a given time (usually 1 to 1.5 min) after grinding (this time will be termed exposure time) and then spread evenly in a gold vessel (20 mm in diameter and 3 mm deep). This sample will be termed the A sample. In the other method, the powder (20.0 g), having been introduced in a larger glass vessel and outgassed under vacuum below 10^{-3} Torr for 15 min, was ground between a magnet rotator (600 rpm) and an aluminum plate for 30 min in the presence of various gases (O_2, H_2O, C_2H_5OH, and $n\text{-}C_3H_7NH_2$) or in vacuo. The reaction vessel volume was 424 cm^3. The grinding was started the moment the gas was admitted into the vessel. The initial pressure of gas will be termed P_0. The pressure change of the reaction vessel with time was measured manometrically. We note that some welding between the powder and the aluminum plate took place in vacuo and in oxygen and that in the presence of water or organic vapors, the plate surface became rough or glossy, respectively. The exposure time in air (15–23 °C, 35–59% RH) was usually 10 min and 0.50 g of the sample was used for the EEE measurement. This sample will be termed the V sample.

Exoelectron Counting. EEE was measured by use of a modified Geiger counter. The counter-gas composition was a mixture of the organic vapor (20 Torr) and argon (84 Torr)

TABLE I: Dependence of "Glow-Curve" Characteristics of Ground Aluminum Powder on Organic Vapors [a]

Organic vapor	Intensity at 25 °C, count/s	Peak intensity, count/s (temp, °C)	Intensity at 239 °C, count/s	Total count (25–239 °C)
$(n\text{-}C_3H_7)_2NH$	50	150(88)	30	61 900
$n\text{-}C_3H_7NH_2$	50	100(106)	25	45 400
$CH_3COOC_2H_5$	12	No peak	83	29 200
C_6H_6	7	34(108)	16	15 800
C_2H_5OH	10	19(72)	11	8 300
$(CH_3)_2CO$	9	19(66)	1	5 700
CH_3CN	2	9(80)	1	2 700
$n\text{-}C_4H_9Cl$	0.5	2.5(110)	ca.0 (230 °C)	900 (25–230 °C)

[a] Grinding time, 10 min; air exposure time, 1–1.5 min.

except that of $(n\text{-}C_3H_7)_2NH$ (14 Torr) and Ar (90 Torr). These counter gases gave the same counting rate for a radioisotope. An A or V sample in the gold vessel was mounted on the sample holder in the counter. The counter was then evacuated and flushed with argon, and the counter gas was admitted. After the emission had been measured at 25 °C for 1 min, the "glow curves" were examined by heating the sample to 239 °C (230 °C only for $n\text{-}C_4H_9Cl$) at the rate of 19 °C/min. In the case of the A sample, the sample was illuminated by a weak fluorescent light (wavelength of light > 295 nm) during measuring of the emission, because in this case the inside of the counter had been exposed to the light in the laboratory through quartz glass, and the number of the "glow curves" examined was 7 to 16 for each counter gas. In the case of the V sample, a 20-W bulb was used as a light source (wavelength > 300 nm), and the number of the "glow curves" was 3 to 5 for each grinding environment. A counter gas of C_2H_5OH–Ar was used for the samples treated in the vapors of O_2, H_2O, and C_2H_5OH, and both counter gases of C_2H_5OH–Ar and $n\text{-}C_3H_7NH_2$–Ar were used for those in $n\text{-}C_3H_7NH_2$ vapor and in vacuo. In all experiments an accelerating voltage of 96 V was applied. Both the total count (25–239 °C) and the counting rate were recorded by a scaler and a ratemeter. The value of the total count given in the text does not contain the count at 25 °C for 1 min.

Results

(a) *A Samples.* The "glow-curve" behavior in different counter gases differed widely in spite of identical mechanical treatment. The "glow curves" except that in the $CH_3COOC_2H_5$–Ar counter gas exhibited an emission peak. The emission for the latter increased with temperature with a discernible shoulder near 150 °C. Table I shows the relationship between the median values of the "glow-curve" characteristics and the kind of organic vapor contained in the counter gas. The organic compounds are arranged in the descending order of the value of the total count. In all the experiments the mean deviation from the median value was less than ±28% for the total count, ±35% for the intensity of the peak emission, and ±14 °C for the peak temperature. The intensity of emission was strongly influenced by the kind of organic compounds and the order of the compounds was very similar to that for both sandblasted mild steel[12] and iron surfaces exposed to a discharge from a Tesla coil.[13] The range of the peak temperatures over all the compounds was much wider, compared with that for the sandblasted steel (55–66 °C) and the iron surface (152–173 °C for the main peak). Judging from the peak temperature deviations of ±14 °C, there are two groups of the peak temperatures (on the average

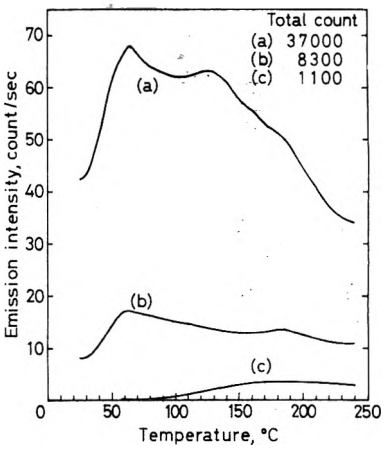

Figure 1. Effect of grinding time on the "glow curve" (air exposure time, 1–1.5 min): (a) 60 min, (b) 10 min, (c) untreated powder.

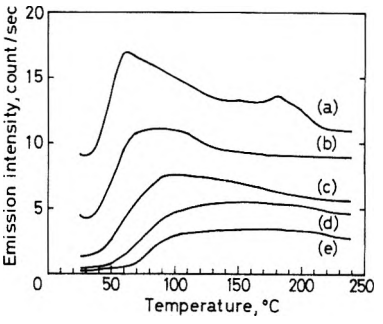

Figure 2. Dependence of the "glow curve" of ground aluminum powder on time of exposure to air (22 °C, 50% RH) after grinding: (a) 0.02 h; (b) 0.5 h; (c) 3 h; (d) 21 h; (e) 44 h.

108 °C for $n\text{-}C_4H_9Cl$, C_6H_6, and $n\text{-}C_3H_7NH_2$, and 77 °C for $(n\text{-}C_3H_7)_2NH$, CH_3CN, C_2H_5OH, and $(CH_3)_2CO$).

The effect of the grinding time and exposure time to air on the emission was examined by use of a counter gas of C_2H_5OH–Ar. Figure 1 shows typical "glow curves" for two grinding times together with that of the untreated powder. In the case of 60-min grinding time, the ground powder became slightly black. The emission increased with an increase of the time of grinding. This indicates that the intensity of emission is regarded as a measurement of the extent of the mechanical damage, though the emission would be expected to reach a maximum and plateau with continued grinding. Figure 2 shows the "glow curves" as a function of the time of exposure to air (22 °C, 50% RH). The emission was gradually suppressed by exposure to air, the temperature for the emission peak

TABLE II: Dependence of "Glow-Curve" Characteristics of Ground Aluminum Powder on Exposure Time to Air after Grinding [a]

Temp and humidity of air	Exposure time, h	Intensity at 25 °C, count/s	Peak intensity, count/s (temp, °C)	Intensity at 239 °C, count/s	Total count (25–239 °C)
22 °C ca. 0% RH	0.5	6.2	16.0(82)	12.0	7900
	3	2.7	12.8(95)	9.5	5900
	21	0.9	*b*	6.1	3200
	43	0.5	*b*	6.0	2200
22 °C ca. 50% RH	0.5	4.6	11.1(92)	9.0	5600
	3	1.3	7.6(97)	5.6	3900
	21	0.4	5.5(148)	4.6	2800
	44	0.2	3.4(182)	2.5	1600
22 °C ca. 100% RH	0.5	2.2	8.3(121)	6.5	3700
	3	1.0	6.0(140)	4.6	3000
	21	0.3	4.2(170)	3.0	1800
	42	0.3	3.4(193)	2.6	1300

[a] Grinding time, 10 min. [b] The intensity of emission gradually increased with increasing temperature.

became increasingly higher, and the "glow curve" for 44-hr exposure time was quite similar to that of the untreated powder. Table II shows the relationship between the "glow-curve" characteristics and the time of exposure to air of different humidities in which the sample has been stored immediately after grinding in air (22 °C, 50% RH). Relative humidities of 0 and 100% refer to ambient air dried by phosphorus pentoxide and air saturated with water vapor, respectively. The variation of the characteristics with exposure time depended strongly on the moisture content of the atmosphere. Figure 3 shows plots of the total count (T) vs. exposure time (t) in each ambient air on a semilogarithmic scale. The points fell on a straight line, represented by the equation $T = B - k \log t$, in each case, and further the slope became steeper with decreasing humidity. The values (k) of the slope were 2910 (0% RH), 2000 (50% RH), and 1290 (100% RH).

The "glow curves" in the absence of light illumination were also examined. Even a counter gas of $(n\text{-}C_3H_7)_2NH$–Ar, giving the largest amount of electrons emitted under light illumination, gave rise to only very weak emission: the peak intensity was 2 count/s at 143 °C and the total count was 400; for the C_2H_5OH–Ar counter gas the total count was about 200. This clearly indicates that photon energies are essential for producing emission from the ground aluminum powder. On the other hand, in the presence of illumination by much stronger light (wavelength > 300 nm), such as sunlight, the emission for a C_2H_5OH–Ar counter gas was a factor of 60 larger over the entire temperature range, but the emission peak was located at almost the same temperature.

(b) *V Samples.* Table III shows the "glow-curve" characteristics (median values) of the optically stimulated emission from samples ground in various gaseous environments. It is clear that the mechanochemically altered surface has still maintained an essentially different nature even under exposure to the same counter-gas atmosphere. In the environment of O_2, H_2O, $n\text{-}C_3H_7NH_2$, and under vacuum, an emission peak was observed at almost the same temperature (near 110 °C), but in the case of C_2H_5OH, a broad emission curve with a slightly elevated intensity at about 50 °C and sometimes about 170 °C, similar to curve b in Figure 1, was observed. It may be noted that the values of the total count both for the environments of $n\text{-}C_3H_7NH_2$ and under vacuum and for outgassing alone were a factor of 6 or more larger in the case of the $n\text{-}C_3H_7NH_2$–Ar counter gas than in the case of C_2H_5OH–Ar, the same as shown inTable I, but the emission peak for each case

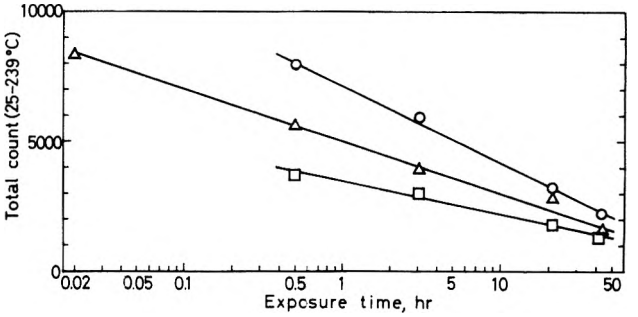

Figure 3. Plots of total count of ground aluminum powder vs. time of exposure to air (22 °C): (○) 0% RH; (△) 50% RH; (□) 100% RH.

was located at almost the same temperature. The emission for C_2H_5OH environment increased by grinding for 3 hr, but the pressure decrease for this time was almost the same as curve f in Figure 5. Figure 4 shows the dependence of the total count on the initial pressure of the vapors. The values for both $n\text{-}C_3H_7NH_2$ and C_2H_5OH were largest at 4.1 Torr and decreased, more rapidly in the latter case, with an increase of initial pressure, but those for H_2O indicated an ascending tendency. Figure 5 shows the pressure change with the time of grinding in various environments. The curve for O_2 (g), H_2O (b,c), and C_2H_5OH (f) showed considerably large variations which are caused by mechanochemical reactions. The curve for $n\text{-}C_3H_7NH_2$ was almost independent of the grinding time in spite of a larger initial pressure range. Table IV shows the dependence of the representative "glow-curve" characteristics for various environments on the time of exposure to ordinary air. In the case of the samples ground both during outgassing and in H_2O vapor, the characteristic values for 0.17–0.19-hr exposure time differed markedly from those for times longer than this time. In the case of C_2H_5OH and $n\text{-}C_3H_7NH_2$, the values varied gradually in the same manner as shown in Table II. The peak temperatures for $n\text{-}C_3H_7NH_2$ was virtually independent of the exposure time, compared with those for C_2H_5OH. The values (k) of the slope obtained from the plots of the total count vs. air exposure time were 1210 for C_2H_5OH and 16 700 for $n\text{-}C_3H_7NH_2$. The former is approximately equal to the value for 100% RH air obtained from Table II.

Discussion

(a) *Effect of Organic Vapor in the Counter Gas on the*

TABLE III: "Glow-Curve" Characteristics of Aluminum Powder Ground in Various Environments [a]

Counter gas	Grinding environment	Pressure (P_0), Torr	Intensity at 25°C, count/s	Peak intensity, count/s (temp, °C)	Intensity at 239°C, count/s	Total count (25–239 °C)
C_2H_5OH + Ar	Vacuum [b]		2.0	8(109)	6.0	3 800
	O_2	16.8	9.0	31(100)	20	15 700
	H_2O	4.2	3.0	11(107)	9.0	5 200
	H_2O	8.2	5.0	16(100)	11	7 700
	C_2H_5OH	4.1	21	25(93)	21	17 500
	C_2H_5OH	8.3	10	13(50)	13	8 500
	C_2H_5OH	16.8	8.0	11(60)	7.0	5 100
	C_2H_5OH [c]	16.5	12	18(54)	15	10 100
	n-$C_3H_7NH_2$	16.9	13	26(111)	15	12 600
	Outgassing [d]		ca.0	3.0(168)	2.0	900
n-$C_3H_7NH_2$ + Ar	Vacuum [e]		18	65(121)	43	34 500
	n-$C_3H_7NH_2$	4.1	55	175(121)	65	80 000
	n-$C_3H_7NH_2$	16.6	65	190(111)	35	75 200
	n-$C_3H_7NH_2$	81.3	20	150(148)	50	58 700
	Outgassing [d]		2.0	32(161)	12	9 900

[a] Grinding time, 30 min; air exposure time, 10 min. [b] This includes grinding during and after outgassing. [c] Grinding time, 3 h. [d] Only outgassing (15 min) without grinding. [e] Grinding after outgassing.

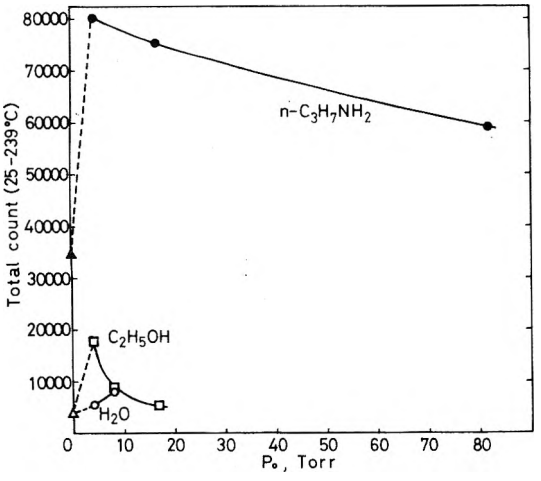

Figure 4. Plots of total count vs. initial pressure (P_0) of vapor: (△, ○, □) C_2H_5OH–Ar counter gas; (▲, ●) n-$C_3H_7NH_2$–Ar counter gas.

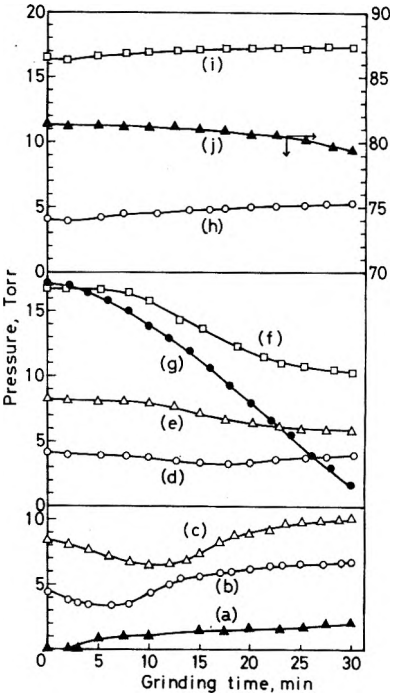

Figure 5. Pressure change with grinding time in various environments: (a) after outgassing; (b) H_2O (P_0, 4.3 Torr); (c) H_2O (P_0, 8.4 Torr); (d) C_2H_5OH (P_0, 4.1 Torr); (e) C_2H_5OH (P_0, 8.2 Torr); (f) C_2H_5OH (P_0, 16.7 Torr); (g) O_2 (P_0, 17.1 Torr); (h) n-$C_3H_7NH_2$ (P_0, 4.1 Torr); (i) n-$C_3H_7NH_2$ (P_0, 16.6 Torr); (j) n-$C_3H_7NH_2$ (P_0, 81.5 Torr).

Emission (A Sample). According to Scharmann,[3] EEE caused by mechanical treatment is based on the following three effects: (a) creation of fresh metal surface on which adsorption takes place, (b) imperfections in the metal, and (c) imperfections in the covering oxide. In this experiment the oxide film on the aluminum powder is broken even with very small loads by grinding to reveal the bare metal surface, perhaps because the substrate metal is softer than its oxide so that the latter cracks easily. The freshly exposed aluminum may interact with oxygen, water vapor, and other gases present in air immediately after grinding and oxide film may be formed again. Thus, the oxide film is thought to contain a great many defects, notably vacancies, which aid in the diffusion of metal ions and the growth of the oxide layer[2] and to be partly hydroxylated, because under atmospheric conditions alumina contains physically adsorbed water, surface hydroxyl groups, and possibly hydroxyl groups incorporated in the bulk lattice; the adsorbed molecular water can be easily removed, whereas the hydroxyl groups can hardly be removed completely even under the most stringent conditions.[14] Ramsey[9] and Linke and Meyer[10] have reported that the emission from abraded aluminum results from the adsorption of water molecules as a hydrogen outward orientation of either H_2O molecules or OH radicals, which lowers the work function. We will explain the experimental results in terms of an electron trap model shown in Figure 6. Figure 7 shows the relationship between the total count shown in Table I and the reciprocal dielectric constant ($1/\epsilon$) of each organic compound. It is apparent that the amount of emitted electrons is closely correlated with the dielectric constant except for both n-C_4H_9Cl and C_6H_6. This suggests that the emission occurs perhaps under the influence of the electric field (E) produced by the surface hydroxyl groups, namely, that as a result of the introduction of the substances into the surface, the electric field strength reduces from the

TABLE IV: Dependence of "Glow-Curve" Characteristics for Each Grinding Environment on Exposure Time to Air after Grinding

Grinding environment (P_0, Torr)	Exposure time, h	Intensity at 25°C, count/s	Peak intensity count/s (temp, °C)	Intensity at 239 °C, count/s	Total count (25–239° C)
During outgassing[a]	0.19	2.0	8.0(136)	6.0	3 800
	1.0	0.5	3.5(93)	3.0	1 500
	3.0	ca. 0	3.0(104)	2.0	1 300
	24.0	ca. 0	3.0(114)	1.5	1 100
	48.3	ca. 0	2.5(126)	1.5	1 000
H_2O[a] (8.2)	0.17	2.0	8.0(129)	7.0	4 600
	1.0	1.0	3.5(95)	2.5	1 600
	3.0	0.5	4.0(93)	2.0	1 500
	23.2	ca. 0	3.0(95)	1.5	800
C_2H_5OH[a] (16.8)	0.20	9.0	12 (63)	7.0	5 800
	1.0	6.0	9.0(72)	7.0	4 900
	3.0	4.0	7.0(72), 6.5(181)	6.0	4 200
	24.0	2.5	5.5(79), 5.5(165)	5.0	3 200
	48.0	2.0	5.5(198)	5.0	3 000
n-$C_3H_7NH_2$[b] (81.3)	0.17	30	150(121)	50	63 300
	1.0	22	140(126)	55	59 600
	3.0	16	90(133)	45	42 500
	24.1	9	66(144)	41	30 800
	47.7	8	54(150)	34	25 300

[a] C_2H_5OH–Ar counter gas. [b] n-$C_3H_7NH_2$–Ar counter gas.

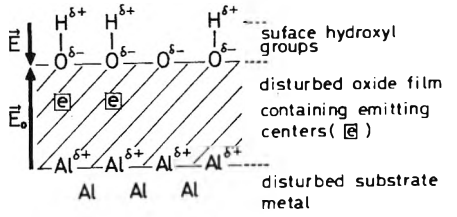

Figure 6. Electron trap model: ($\vec{E}$) the vector of electric field strength due to adsorbed surface hydroxyl groups onto which the organic molecules may be adsorbed; (E_0) the vector of electric field strength across the oxide film, which forces aluminum ions from the metal through the oxide film to the surface, to react with oxygen gas.

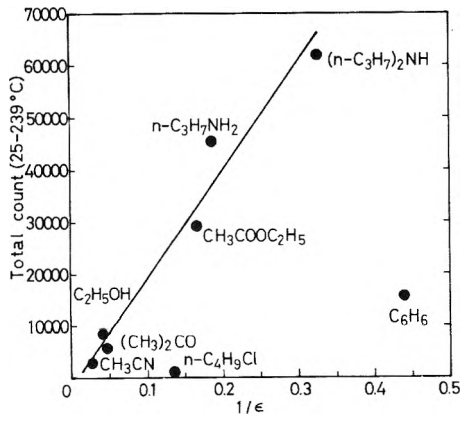

Figure 7. Total count of emitted electrons as a function of reciprocal dielectric constant ($1/\epsilon$) of organic compounds.

value (E) to the value (E/ϵ). In order to expand and clarify the role of the simultaneous optical and thermal stimulation in relation to both the proposed surface field and oxide imperfections, it would be useful to refer to the concept proposed by Claytor and Brotzen,[15] who used a similar technique on aluminum deformed in tension. They have associated thermal stimulation with vacancy diffusion to the surface, where then some of vacancies create preferential sites for optically stimulated emission. The electrons trapped in such sites are removed by light absorption at photon energies lower than those for the original oxide-coated surface. The fact that hardly any emission was observed in the dark seems to be attributable to the diffusion of electrons trapped at vacancies through the oxide film to adsorbed oxygen, giving rise to O^- ions instead of electron emission. It should be noted that this electric field does not deal with a model of the transversal electric field across the fissures created in the oxide layer, as proposed by Gieroszyński and Sujak.[16]

Dear et al.[17] have reported that substances such as C_6H_6 and n-C_4H_9Cl fit a plot of the heat of immersion of aluminum powder against dipole moment, but that n-C_4H_9OH and n-$C_4H_9NH_2$ show a much higher heat than that corresponding to their dipole moments, which may be attributed to hydrogen-bond formation. The molecules on the straight line in Figure 7 may presumably be adsorbed through hydrogen bonding. In previous papers,[12,13] it has been proposed that the emission may be strongly associated with the proton attracting interaction between the functional groups of organic molecules adsorbed and the hydroxyl groups on the damaged solid surfaces. The dielectric constant of organic compounds used is correlated with the negative logarithm of the acidity constant, pK_{BH^+}, for conjugated acids (BH^+) of organic compounds as conjugated bases (B), as follows.[18–20]

B	ϵ	pK_{BH^+}
$(n$-$C_3H_7)_2NH$	3.068	11.00
n-$C_3H_7NH_2$	5.31	10.69
$CH_3COOC_2H_5$	6.02	−6.2
$(CH_3)_2CO$	20.70	−7.2
CH_3CN	37.5	−10.12

This suggests that the hydrogen-bond formation plays an important role in the emission and that the emitting centers may have existed in the vicinity of Brönsted acid sites on the disturbed oxide surface.

Greenler[21] has reported that when aluminum oxide has been exposed to ethanol vapor, the observed surface species are a weakly bound layer of liquid alcohol, a surface ethoxide, and an acetate-like compound. In the experiment for C_2H_5OH–Ar counter gas such a destructive action of ethanol on the surface may have taken place, resulting in a broad emission "glow curve". As for $CH_3COOC_2H_5$–Ar counter gas, ethyl acetate reacts with the oxide film above about 150 °C, increasing the emission, because such an abnormal behavior was not observed in the case of sandblasted mild steel.[12]

(b) *Effect of the Exposure Time to Air after Grinding on the Emission (A Samples).* As the disintegration by means of grinding becomes more severe, the area of the damaged surface increases and results in the increase of emission, as represented in Figure 1. As the time of exposure to air becomes longer, the oxide layer grows thicker and so causes the continuous decrease of emission with a faster decay at lower temperatures, as indicated in Figure 2. It is very interesting that thus the photoelectric work function of the solid surface can be changed reversibly. Arnott and Ramsey[22] have reported that with the emission from aluminum deformed in tension a pressure dependent photostimulated emission occurs in thin oxide films (less than 45 nm) and results from the lowering of work function due to the adsorption of oxygen and water molecules. On the other hand, the emission even without optical stimulation has been observed in many oxides and oxidized metals under various conditions,[22-25] and Saito et al.[26] have reported that an emission "glow curve" of aluminum exposed to x-rays, giving two peaks at 120 and 240 °C, is uninfluenced by light illumination. Therefore, the mechanism of optically stimulated emission quite differs from that of the emission without optical stimulation. Grunberg and Wright[27] have reported that the rate of the optically stimulated emission from abraded aluminum increases with increasing concentration of oxygen. Ramsey[9] has reported that the decay of the optically stimulated emission from aluminum may be correlated with a law for the growth of thin oxide film, represented by the equation: $1/x = B' - k' \log t$ (x is the thickness, t the time). Therefore, the linear plots in Figure 3 suggest that the emission may be reduced as a result of the growth of oxide film being accompanied by the vanishing of defects containing emitting centers. In this connection Yashiro[28] has reported that the surface potential of annealed aluminum after tensile deformation decreases linearly with the logarithm of time in air to its original value, suggesting that this may be caused by the growth of the oxide coating.

As shown in Table II, when the sample having been ground in air of 50% RH was stored in 0 or 100% RH air, the "glow-curve" characteristics obtained was markedly different from those for 50% RH air. Hunter and Fowle[29] have reported that atmospheric moisture breaks down the natural barrier-type oxide film to form an outer porous portion, and that the times required to complete barrier formation are much shorter in the absence of moisture, though the oxide layer formed in this experiment should be amorphous.[29,30] From this, in the environment of 0% RH air a more compact layer may be formed by desorption of adsorbed water molecules, and also in 100% RH air a more porous or amorphous layer by condensation of water molecules, the former increasing the emission and the latter decreasing the emission. It is of considerable interest that the oxide layer containing emitting centers can be recovered by storing in dry air, and therefore in this experiment it is unlikely that the emission from oxides such as Al_2O_3 results from the desorption of water, as observed by Krylova.[31] The slope (k) of the plots for each ambient air appears to be associated with the rate of oxidation, which is dependent on the extent of the interference from water molecules adsorbed or condensed on the surface.

(c) *Effect of the Surfaces Mechanochemically Altered in Various Environments on the Emission (V Samples).* First, it should be noted that since the method of grinding is quite different between A and V samples, we are unable to compare directly the characteristic values of the V sample with those of the A sample. In Figure 5, the gradual increase of pressure for curve a may be due to the evolution of hydrogen gas having been contained in the aluminum powder,[32] which is caused by grinding. In the initial stage for curves b and c the hydration on the oxide film which gives two Al–OH groups and the formation of Al_2O_3 retaining hydrogen held as OH groups[33] may occur, followed by the evolution of hydrogen in the latter stage. Curves d, e, and f for C_2H_5OH may be attributed to the formation of Al–OC_2H_5 and Al–OH.[14] Curve g for O_2, of course, represents the chemisorption on the freshly exposed aluminum. Curves h, i, and j for n-$C_3H_7NH_2$ suggest little interaction between aluminum and n-$C_3H_7NH_2$. As shown in Table III, it is evident that the environment of other vapors as well as O_2 yields much more defects containing emitting centers than that of vacuum. In the case of O_2 and H_2O the increase of emitting centers is associated with the freshly formed oxide film. In the case of C_2H_5OH and n-$C_3H_7NH_2$ the emission behavior is strongly governed by the organic coating formed on the surface, which may suppress the interaction such as the adsorption of moisture during exposure to air or the hydrogen-bond formation between the surface and the organic vapor in the counter-gas atmosphere, because the decrease of the total count with the initial pressure is observed, as shown in Figure 4; a larger variation of the pressure for C_2H_5OH indicating a higher mechanochemical reactivity, as shown in Figure 5, gives a steeper curve in the plot in Figure 4, compared with that for n-$C_3H_7NH_2$.

From Table IV, it is apparent that the surfaces formed in the environment of O_2 and H_2O are remarkably influenced by hydration or oxidation at the beginning of the exposure to air and then gradually approach a stable state. On the other hand, the surfaces in the environment of C_2H_5OH and n-$C_3H_7NH_2$ are more stable against exposure to air and the characteristic values gradually change from the beginning of the exposure. From the values (k) for n-$C_3H_7NH_2$ and C_2H_5OH, it is suggested that the surface for the former may undergo oxidation more easily than that for the latter, because the organic coating formed from C_2H_5OH would more effectively suppress the adsorption of oxygen.

Acknowledgment. The authors wish to thank Professor Yasukatsu Tamai of Tohoku University for his continuing interest and encouragement.

References and Notes

(1) L. Grunberg, *Brit. J. Appl. Phys.*, 9, 85 (1958).
(2) F. R. Brotzen, *Phys. Status Solidi*, **22**, 9 (1967).
(3) A. Scharmann, *Int. Symp. Exoelectron Emission Dosimetry (Proc.), 4th, 1973*, 12 (1974).
(4) J. A. Ramsey, *Int. Symp. Exoelectron Emission Dosimetry (Proc.), 4th, 1973*, 193 (1974).
(5) M. C. Shaw, *J. Appl. Mech.*, **15**, 37 (1948).
(6) H. A. Smith and R. M. McGill, *J. Phys. Chem.*, **61**, 1025 (1957).
(7) H. H. Uhlig, "Corrosion and Corrosion Control", Wiley, New York, N.Y.,

1963, in a Japanese translation, p 107.
(8) Y. Momose, K. Yamada, and K. Nagayama, *J. Polym. Sci., Polym. Lett. Ed.*, **12**, 623 (1974).
(9) J. A. Ramsey, *Surface Sci.*, **8**, 313 (1967).
(10) E. Linke and K. Meyer, *Surface Sci.*, **20**, 304 (1970).
(11) A. M. Polyakov and N. A. Krotova, "Research in Surface Forces", Vol. 3, B. V. Deryagin, Ed., Consultants Bureau, New York, N.Y., 1971, p 394.
(12) Y. Momose, *Z. Phys.*, **250**, 198 (1972).
(13) Y. Momose and H. Okazaki, *Jpn. J. Appl. Phys.*, **12**, 1890 (1973).
(14) H. Cochrane and R. Rudham, *Trans. Faraday Soc.*, **61**, 2246 (1965).
(15) R. N. Claytor and F. R. Brotzen, *J. Appl. Phys.*, **36**, 3549 (1965).
(16) A. Gieroszyński and B. Sujak, *Acta Phys. Polon.*, **28**, 337 (1965).
(17) D. J. A. Dear, D. D. Eley, and B. C. Johnson, *Trans. Faraday Soc.*, **59**, 713 (1963).
(18) J. A. Riddick and W. B. Bunger, "Organic Solvents" in "Techniques of Chemistry", Vol. II, A. Weissberger, Ed., Wiley, New York, N.Y., 1970.
(19) J. B. Hendrickson, D. J. Cram, and G. S. Hammond, "Organic Chemistry", McGraw-Hill, Kogakusha, Tokyo, 1970, p 303.
(20) Z. V. I. Rappoport, "Handbook of Tables for Organic Compound Identification", The Chemical Rubber, Cleveland, Ohio, 1967, p 439.
(21) R. C. Greenler, *J. Chem. Phys.*, **37**, 2094 (1962).
(22) D. R. Arnott and J. A. Ramsey, *Surface Sci.*, **28**, 1 (1971).
(23) H. Hieslmair and H. Müller, *Z. Phys.*, **152**, 642 (1958).
(24) A. Scharmann and G. Seibert, *Z. Phys.*, **183**, 249 (1965).
(25) A. Gieroszyński and B. Sujak, *Acta Phys. Polon.*, **28**, 311 (1965).
(26) Y. Saito, Y. Shinata, and Y. Hasegawa, *Nippon Kinzoku Gakkaishi*, **38**, 1006 (1974).
(27) L. Grunberg and K. H. R. Wright, *Proc. R. Soc. London, Ser. A*, **232**, 403 (1955).
(28) Y. Yashiro, *Oyo Butsuri*, **28**, 289 (1959).
(29) M. S. Hunter and P. Fowle, *J. Electrochem. Soc.*, **103**, 482 (1956).
(30) P. E. Doherty and R. S. Davis, *J. Appl. Phys.*, **34**, 619 (1963).
(31) I. V. Krylova, *Phys. Status. Solidi, (a)* **7**, 359 (1971).
(32) H. Shigematsu, *Nippon Kinzoku Gakkaishi, Ser. A*, **24**, 177 (1960).
(33) D. D. Eley and P. R. Wilkinson, *Proc. R. Soc., London, Ser. A*, **254**, 327 (1960).

Generation of Catalytically Active Acidic OH Groups upon CO_2 Neutralization of Basic Sites in Mg- and Ca-Y Zeolites

Claude Mirodatos, Pierre Pichat, and Denise Barthomeuf*

Institut de Recherches sur la Catalyse CNRS, 39 boulevard du 11 novembre 1918, 69626, Villeurbanne, France

(Received December 23, 1975)

Publication costs assisted by the Centre National de la Recherche Scientifique

The effect of CO_2 in the 25–500 °C temperature range on the OH groups of various Y zeolites exchanged with NH_4^+ and Mg^{2+} or Ca^{2+} cations has been examined in connection with its influence upon the catalytic cracking of isooctane. Because of their changes with cation nature and contents, the infrared bands at 3685 (Mg-Y) or 3675 cm^{-1} (Ca-Y) seem to refer to OH groups associated with the divalent cations. From the influence of CO_2 between 150 and 400 °C, it is inferred that these OH groups have a basic character. On CO_2 adsorption, they give rise to unidentate carbonate species and to new acidic OH groups, probably in the vicinity of these carbonates. Other, less symmetric, unidentate carbonate species are also formed. On evacuation between 400 and 500 °C, the changes in OH groups are reversible; the carbonate species behave differently: the more symmetric types are removed, the others subsist. The increase in isooctane cracking due to CO_2 introduction in the reactants parallels the intensity changes of the bands due to the new acidic OH groups, whereas the stable unidentate carbonates involve inactive sites.

Introduction

The investigations on the surface sites of zeolites have been mainly devoted to the determination of the nature, number, and strength of acid sites. Little information is available about basic sites which may be involved in catalytic processes.[1,2] Concerning, more particularly, the OH groups of zeolites, it has been established that those responsible for the ir bands around 3640 and 3550 cm^{-1} are acid. The acidic character of those vibrating around 3600 and 3690 cm^{-1}, which are observed for ultrastable materials[3-6] and polyvalent cation exchanged zeolites,[6-12] is less well defined. The OH groups corresponding to bands at ca. 3600 cm^{-1} have been reported to react with NaOH;[10,13] their reactivity toward NH_3 is weak[5] or nonexistent[3,6,8,10] and that toward pyridine partial[4] or nonexistent.[7,10,13] The OH groups referring to bands in the 3700-cm^{-1} region may react with NH_3[5] or not;[3] they are insensitive to pyridine.[4,7,13] The nature of these OH groups has been a matter of debate. In the case of zeolites containing alkaline earth cations, they have been attributed to water molecules,[3,7] $M-OH^+$ species,[3,7,14] or associated with aluminum deficient sites as for ultrastable zeolites.[6] To our knowledge, their possible basicity has not been studied.

In this work, the effect of CO_2 on the OH groups of various zeolites exchanged with NH_4^+ and Mg^{2+} or Ca^{2+} cations is examined in connection with its influence on the catalytic cracking of isooctane. Indeed it is known that CO_2 may increase the catalytic properties of some zeolites[15] and it has been suggested that this increase may be due to a surface weakly bonded form of CO_2.[16] Up to now, infrared studies of the action of CO_2 on zeolites have been mainly carried out to determine cation locations[9] and the isotopic exchange of oxygen atoms.[2] At high temperatures, unidentate carbonate species are formed.[2,9,17] No detailed investigation on the influence of CO_2 on the OH groups of zeolites has been reported.

* Address correspondence to this author at the Laboratoire de Catalyse Organique, L.A. CNRS No. 231, Ecole Supérieure de Chimie Industrielle de Lyon, 43 boulevard du 11 novembre 1918, 69621 Villeurbanne, France.

Experimental Section

Materials. Samples were prepared from Union Carbide Na-Y zeolite. Ca-Y zeolites were obtained by exchange of Na^+ ions for Ca^{2+} ions in chloride solutions. Subsequently, partial exchange with NH_4^+ ions of Ca^{2+} ions yielded various Ca-NH_4-Y materials. For Mg-Y zeolites, Na-NH_4-Y samples were first prepared, then exchanged by Mg^{2+} ions from chloride solutions. Two or three treatments with the chloride solution were required to obtain high magnesium levels. For the sample with the highest magnesium content, the exchange was performed at 100 °C. The zeolites were heated at 380 °C in a dry air flow for 15 h in order to evolve NH_3 and then at 550 °C for the same time. This heating procedure tends to avoid ultrastabilizing effects. Chemical compositions of the catalysts referred to by the total number of equivalents of cation per unit cell are given in Table I. X-ray diffraction measurements showed the zeolites to be highly crystalline.

Ir Studies. Wafers (18-mm diameter) of 30–40 mg of zeolite were inserted in a quartz sample holder which was introduced into the infrared cell as previously.[18] The samples were heated (5 deg/min) to 465 °C in a dry oxygen flow in order to evolve carbonaceous deposits. After 15 h at this temperature, the cell was closed and cooled to room temperature. Oxygen was pumped off at room temperature and the samples were heated again either under vacuum at 400 or 465 °C, or in a hydrogen flow at 465 °C for 15 h. The hydrogen treatments were carried out to obtain samples similar to those used in the catalytic experiments.

CO_2 was introduced in the infrared cell at room temperature under a 100 Torr pressure. Its purity was better than 99.998% and further it was thoroughly dried by a series of distillations under vacuum. The zeolites were heated in CO_2 at various temperatures (25 to 500 °C) for 15 h. Spectra were recorded at room temperature.

Deuterated samples were obtained by heating O_2-pretreated wafers in D_2O (~20 Torr) at 200 °C for 4 h. The procedure was repeated four times with intermediate evacuations at 200 °C.

Spectra were scanned on a Perkin-Elmer Model 125 grating spectrophotometer. The reference beam was attenuated.

Results and Discussion

I. *Magnesium Zeolites.* 1. *Hydroxyl Groups.* Samples which have been heated under oxygen and then under hydrogen give the spectra shown in Figure 1. The 3740-cm^{-1} band occurs in all spectra. Only materials containing magnesium give rise to a band near 3685 cm^{-1} with a weak shoulder at 3670 cm^{-1}. The intensity of this band is weak for zeolites containing a low amount of divalent cation. It increases for a number of cation equivalents greater than 32.1 per unit cell. The band near 3640 cm^{-1} also increases similarly. The 3640-cm^{-1} band is more intense than the 3685-cm^{-1} band for the sample containing the highest magnesium level. No other significant OH band is observed in the lower frequency range. As it has been previously pointed out for Mg-Y[19] and La-Y[10] zeolites, the low frequency bands in the 3560–3600-cm^{-1} region have a weaker thermal stability than the higher frequency bands. So, their absence in the present spectra is not unexpected.

In the case of the hydrogen treated zeolites, a weak band at 1625 cm^{-1} was observed and attributed to the deformation vibration of water molecules. In order to eliminate these molecules, samples treated at 465 °C under vacuum instead of hydrogen were examined. Their spectra do not exhibit a band at 1625 cm^{-1}. The 3500–3800-cm^{-1} region is displayed in Figure 2. With the exception of the 3740-cm^{-1} band, the intensities of the OH bands are much weaker than after H_2 treatments and well-resolved bands are observed only for samples with a high magnesium content (Mg 32.1 and Mg 46.1). Besides the fact that these experiments show the lower stability of OH groups under vacuum, they also indicate that the 3685-cm^{-1} band may exist in the absence of the deformation band of water molecules. Therefore the assignment

TABLE I: Analysis and Structural Parameters of the Zeolites

Catalysts	Na^+ ions per unit cell	Mg^{2+} (or Ca^{2+}) ions per unit cell	Total cation equiv per unit cell[a]	T–O asymmetric stretch, cm^{-1}	Unit cell size, Å
Na H Y	7.5	0	7.5	1020	24.65
Mg series					
Mg 17.7	7.1	5.3	17.7	1020	24.45
Mg 23.4	8.2	7.6	23.4	1020	*b*
Mg 26.2	9.1	9.1	26.2	1020	*b*
Mg 32.1	7.1	12.5	32.1	1020	*b*
Mg 37.5	8.1	14.7	37.5	1020	24.63
Mg 46.1	7.5	19.3	46.1	1020	24.64
Ca series					
Ca 23.4	3.5	10	23.4		
Ca 40.7	3.5	18.6	40.7		
Ca 51.2	3.5	23.9	51.2		

[a] The difference with 56 (number of charges to be neutralized) represents the theoretical number of H^+ per unit cell after the NH_4^+ decomposition. [b] Not determined.

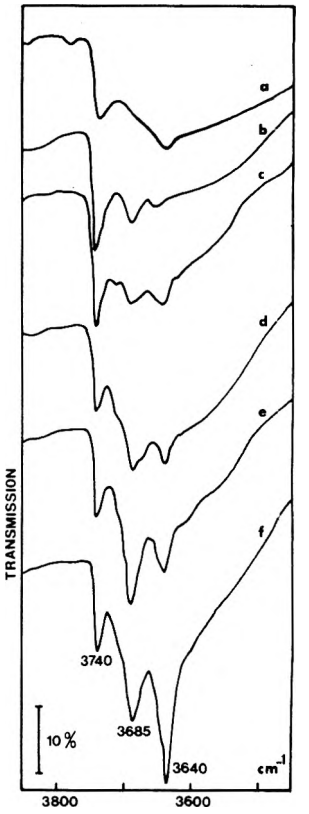

Figure 1. Spectra of OH groups on various zeolites, O_2 treated, then H_2 treated at 465 °C: (a) Na-H-Y 7.5; (b) Mg 23.4; (c) Mg 26.2; (d) Mg 32.1; (e) Mg 37.5; (f) Mg 46.1.

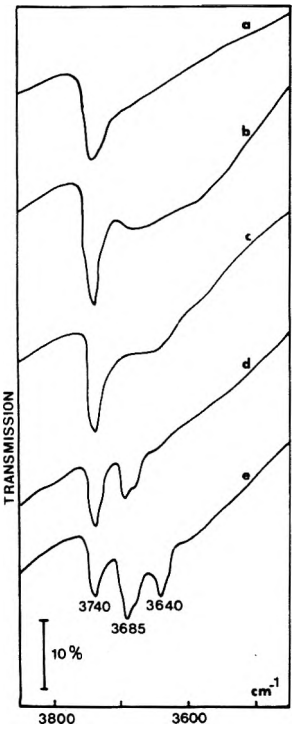

Figure 2. Spectra of OH groups on various zeolites, O_2 treated, then evacuated at 465 °C: (a) Na-H-Y 7.5; (b) Mg 17.7; (c) Mg 26.2; (d) Mg 32.1; (e) Mg 46.1.

of this band to vibrations of water molecules is ruled out in the present case.

Since, for polyvalent cation exchanged Y zeolites or "deep-bed" treated zeolites, OH bands in the same region have been related to a hydrolyzing process (dealumination),[6,10] the question arises as to whether this phenomenon has to be considered here. The heat treatment at 380–550 °C in dry air flow to obtain Na-Mg-HY samples was done very carefully to avoid this effect. If, however, dealumination occurs, it would change structural features. The absorption maximum of the framework T–O bond vibrations near 1020 cm^{-1} would increase with dealumination[10,20] and the unit cell parameter would decrease.[21,22] Table I indicates the vibration frequency of T–O bonds. The low value (1020 cm^{-1}) and the constancy of this frequency with the magnesium content changes show that dealumination does not occur. The 400 °C evacuations carried out on the ir wafers do not affect this frequency either.

Some unit cell parameters are also given in Table I. No unit cell shrinkage is observed for samples showing the 3685-cm^{-1} band. That noted for the Mg 17.7 sample may be due to the preferential location of the first exchanged divalent cations in S_I sites.[23] Consequently, in the present case, the 3685-cm^{-1} band does not seem to be related to dealumination.

The occurrence of $Mg(OH)_2$ deposits in our samples might also be suggested. The OH groups of magnesium hydroxide vibrate at frequencies close to 3700 cm^{-1} [24] but the bands disappear after a few hours of evacuation at 400 °C. The high thermal stability of the 3685-cm^{-1} band and also the difficulty of introducing large amounts of magnesium in the zeolites under study do not seem to be consistent with the formation of magnesium hydroxide.

Accordingly, the OH groups corresponding to the 3685-cm^{-1} band described in this work do not seem to be due to water molecules or OH groups at Al deficient sites. The dependence of this band on magnesium content suggests that it is associated with the divalent cations located in the supercage. Assuming that Mg^{2+} cations fill at first S_I sites, about 25 to 32 equivalents of magnesium cations per unit cell would be necessary for the 16 S_I sites, i.e, 32 to 39 equivalents of cations $Na^+ + 2Mg^{2+}$, depending on the simultaneous presence of Na^+ ions in these sites. Indeed, the 3685-cm^{-1} band starts to increase markedly above this cation content range. All these remarks suggest that the 3685-cm^{-1} band we observed may be associated with $Mg(OH)^+$ species located in the supercages and resulting from a reaction of the type[7]

$$Mg^{2+} + H_2O \rightleftharpoons Mg(OH)^+ + H^+$$

As often proposed, the released proton produces acid OH groups which explain the growth of the 3640-cm^{-1} band on increasing magnesium content.

2. *Acid–Base Properties of the OH Groups.* Pyridine adsorption performed as previously[4] showed that the OH groups associated with the 3640-cm^{-1} band are acid, whereas those corresponding to the 3685-cm^{-1} band are not.

Adsorption of CO_2 at 400 °C was used to study the basicity of the OH groups of samples heated under vacuum or in a hydrogen flow. The results obtained with both types of samples are similar. Because the observed effects are more pronounced for zeolites with high magnesium contents, i.e., exhibiting an intense 3685-cm^{-1} band, spectra of Figure 3 refer to the Mg 46.1 sample. Treatment with CO_2 at 400 °C does not affect the 3740-cm^{-1} band, reduces considerably the 3685-cm^{-1} band, increases the 3640-cm^{-1} band, and produces a new OH band at ca. 3550 cm^{-1} (Figure 3b). Evacuation of CO_2 at 400 °C for 15 h (Figure 3c) causes the opposite effects. After 3 h desorption at 500 °C, the initial spectrum is nearly restored (Figure 3d). Hence CO_2 reacts reversibly with the OH groups vibrating at 3685 cm^{-1} and simultaneously new OH groups are reversibly formed. In order to make sure that these new OH groups do not arise from traces of water introduced with CO_2, deuterated zeolites were prepared. Figure 4a shows the spectrum of the starting Mg 46.1 sample evacuated at room temperature after the 465 °C oxygen treatment. After four successive treatments with D_2O, spectrum 4b shows that most of the OH groups have been exchanged. The OD bands at 2750, 2710, and 2680 cm^{-1} correspond to the 3740-, 3685-, and 3640-cm^{-1} OH bands, respectively. After CO_2 adsorption at 400 °C, the 2710-cm^{-1} band has disappeared, the one at 2680 cm^{-1} has become broader, and a new OD band at 2610 cm^{-1}, equivalent to the 3550-cm^{-1} OH band, has occurred. As a result of CO_2 desorption at 500 °C the initial OD bands are restored with, however, some slight intensity changes. This experiment indicates that the D atoms of the new OD groups referring to the 2610-cm^{-1} band originate from the solid, probably from the OD groups which disappear upon reaction with CO_2 (2710-cm^{-1} band).

As new OH groups arising from the CO_2 reaction have the usual frequency (3550 cm^{-1}) of acid OH groups in Y zeolites, their acid character was examined using NH_3. It was found that they react with this base at room temperature.

3. *Carbonate Species and Correlations with the OH Groups.* As a result of reaction with CO_2 in the 150–400 °C temperature range, bands appear in the 1400–1700-cm^{-1} region of the zeolite spectra. Their number and relative intensities depend on the Mg content and the temperature of reaction.

The most complete set of bands was observed in the case of the Mg 46.1 sample heated in CO_2 at 400 °C. Absorption maxima were found at 1580, 1520, 1490, 1450, and 1410 cm^{-1} (Figure 5d). For the same CO_2 reaction temperature, the in-

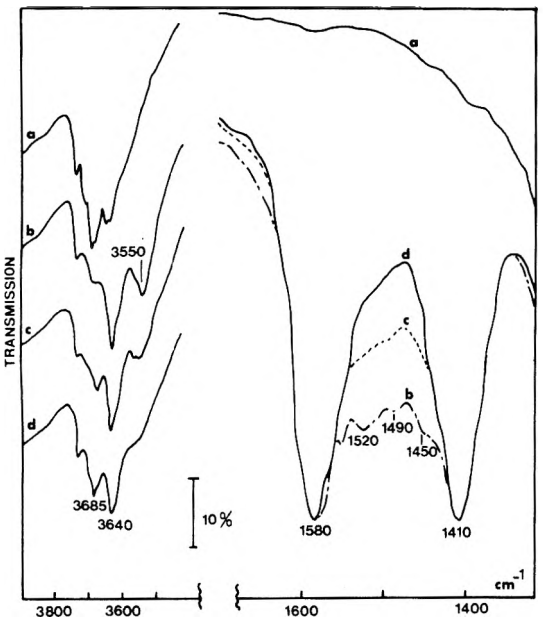

Figure 3. Spectra of the Mg 46.1 zeolite: (a) evacuated at 400 °C for 15 h; (b) heated in 100 Torr of CO_2 at 400 °C for 15 h, then evacuated at room temperature for 30 min; (c) evacuated at 400 °C for 15 h; (d) evacuated at 500 °C for 3h.

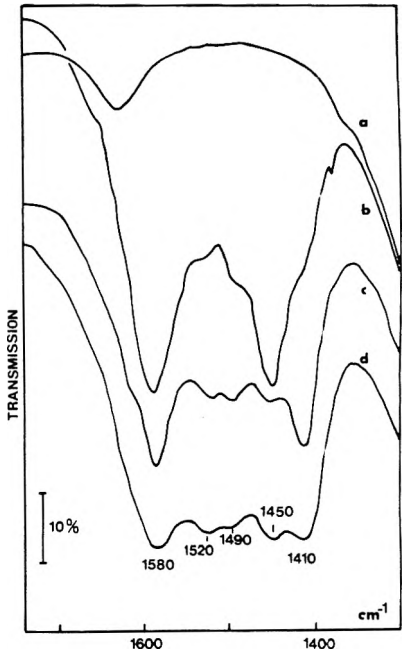

Figure 5. Spectra of various zeolites after CO_2 action at 400 °C: (a) Na-H-Y 7.5; (b) Mg 23.4; (c) Mg 37.5; (d) Mg 46.1.

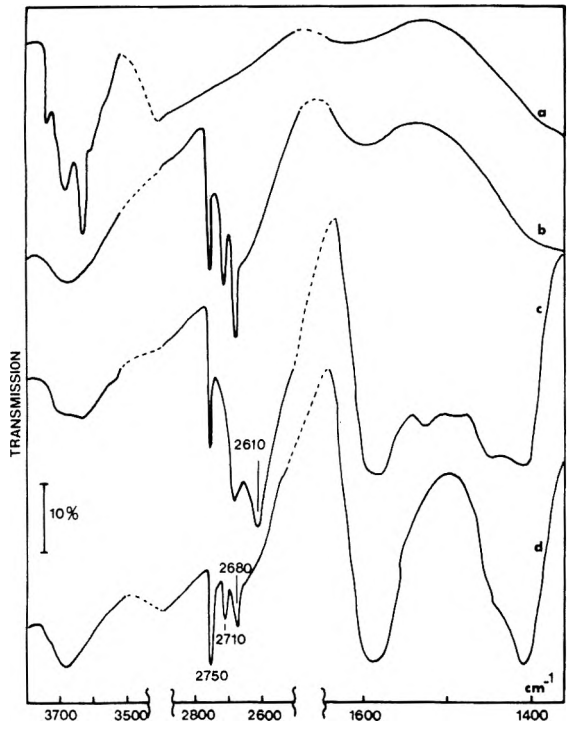

Figure 4. Spectra of the Mg 46.1 zeolite: (a) O_2 treated at 465° for 15 h, then evacuated at room temperature for 30 min; (b) after four successive exchanges with D_2O; (c) heated in 100 Torr of CO_2 at 400 °C for 15 h, then evacuated at room temperature for 30 min; (d) evacuated at 500 °C for 15 h.

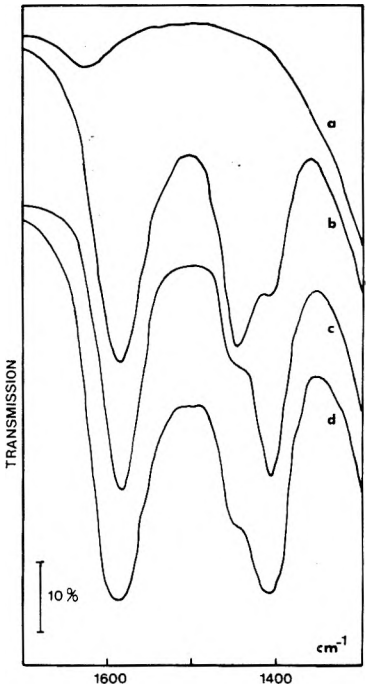

Figure 6. Spectra of various zeolites after CO_2 action at 400 °C then evacuated at 500 °C for 6 h: (a) Na-H-Y 7.5; (b) Mg 23.4; (c) Mg 37.5; (d) Mg 46.1.

tensities of the bands at 1520 and 1490 cm^{-1} increased with increasing Mg content (Figure 5). Overlapping of the bands at 1410 and 1450 cm^{-1} does not allow an easy comparison of their relative intensities as a function of Mg content. Nevertheless, it may be seen from Figure 6, referring to 500 °C evacuated samples, that the 1410-cm^{-1} band becomes preponderant for high Mg content. No band in this spectral region was found for the sample which did not contain Mg^{2+} cations (Figures 5a and 6a).

The influence of temperature on the formation and disappearance of the species responsible for these bands was examined. In the case of the Mg 46.1 sample, the bands do not exist after heating in CO_2 at 100 °C. They begin to appear at 150 °C and their intensity increases on raising the temperature to 400 °C (Figure 7). On evacuation at a series of increasing temperatures, the bands at 1520 and 1490 cm^{-1} are progres-

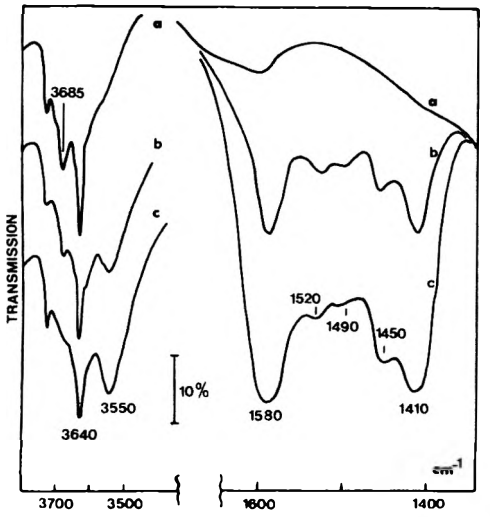

Figure 7. Spectra of the Mg 46.1 zeolite O_2 treated then evacuated at 465 °C: heated in 100 Torr of CO_2 at indicated temperatures for 15 h, then evacuated at room temperature for 30 min; (a) 100 °C; (b) 150 °C; (c) 400 °C.

sively reduced in intensity. They are completely eliminated as a result of a 15-h evacuation at 500 °C (Figure 3d). The other bands withstand this 500 °C evacuation (Figure 3d, 4d, and 6).

The effect of the pressure of CO_2 has also been briefly examined. Exposures of the Mg 46.1 sample to very low pressures of CO_2 at 400 °C caused the appearance of the 1580-, 1450-, and 1410-cm^{-1} bands only.

In regard to these most stable species, it was expected that the influence of electron-donating molecules may help to determine their nature. D_2O, H_2O, and NH_3 were employed. Figure 8A shows that, as a result of D_2O reaction at 25 °C, the spectrum of Mg-Y zeolite was substantially modified. The bands at 1580 and 1410 cm^{-1} have disappeared, the one at 1450 cm^{-1} has increased and two new strong bands have occurred around 1510 and 1650 cm^{-1}. Evacuation at 400 °C restored the starting spectrum (Figure 8Ac). H_2O and NH_3 also caused the disappearance of the 1580-cm^{-1} band. However, the other spectral features are less visible because of the presence of vibrational modes of H_2O, NH_3, and NH_4^+ in the region considered.

Bands in the spectral region considered may be assigned to three types of carbonates (symmetric, and uni- and bidentate), to bicarbonates, and to carboxylates.[25] Usually, assignments are made by analogy between the spectra of solid compounds and those of surface species. Particularly in the absence of information on the 1300–700-cm^{-1} region because of the poor transmission of the zeolites, they remain tentative, since, first, there is some overlapping of the absorption ranges referring to the different species, and secondly, surface species in various environments may be subject to perturbations which influence their spectra in an unknown manner.

Bands at 1580, 1450, and 1410 cm^{-1}. The band at 1450 cm^{-1} is assigned, as usual, to symmetric carbonate species.[25] Bands at 1589 and 1414 cm^{-1} have already been observed for Mg-Y zeolites containing a high magnesium content and exposed to CO_2 at ~500 °C.[17] By contrast, CO_2 reacts with MgO at room temperature, giving rise to bands in different regions (1625–1670 and 1275–1325 cm^{-1}) which have been attributed to two types of bidentate carbonates.[26-28] Though bands close to those considered here (1550–1560 and 1390–1410 cm^{-1}) were also found for MgO[27,28] in conditions similar to those of

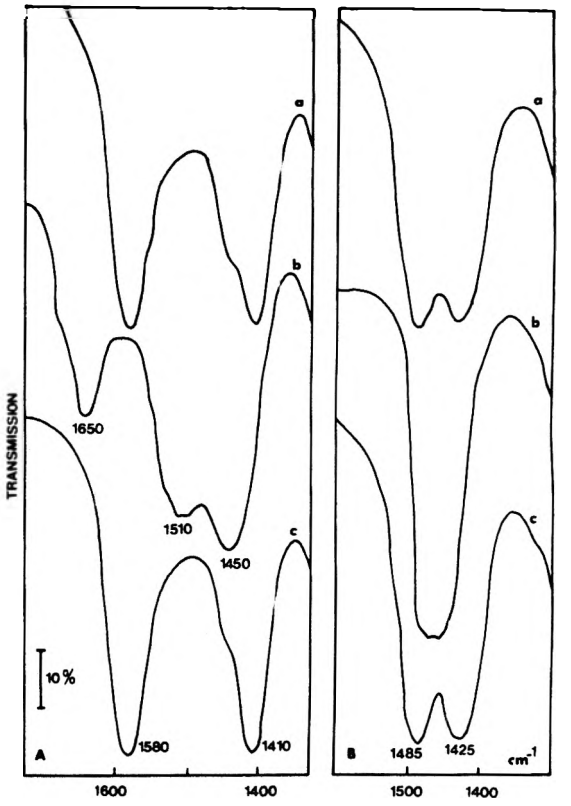

Figure 8. Spectra of the Mg 46.1 (A) and the Ca 51.2 (B) zeolites showing the action of D_2O on the surface carbonate species: (a) evacuated at 500 °C for 6 h after reaction with CO_2 at 400 °C; (b) D_2O (~20 Torr) adsorbed at room temperature; (c) then evacuated at 400 °C for 4 h.

the present work, the differences in reactivity at room temperature are in favor of the absence of any significant formation of MgO in our samples.

Table II shows the absorption ranges of carboxylate and unidentate carbonate species. Attribution of the 1580- and 1410-cm^{-1} bands to either species is not clear-cut. However, the influence of D_2O on these bands gives support to the previous attribution to unidentate carbonates,[17] since it is reasonable to think that this influence, which is reversible, results in a mere change in the symmetry of a unidentate carbonate species. Increasing the symmetry of this species decreases the frequency difference between the asymmetric and symmetric ν(CO) vibrational modes, so that the bands at 1580 and 1410 cm^{-1} are shifted to 1510 and 1450 cm^{-1}, respectively (Figure 8A). This increased symmetry may be interpreted by assuming that a D_2O molecule gives electrons to a Mg^{2+} cation, thus reducing the formal positive charge of the cation and its attractive power toward the carbonate species. Consequently, the three C–O bonds of the unidentate carbonate become more equivalent. This influence of H_2O or D_2O molecules has been already pointed out for Co-Y zeolites and explained by the formation of hydrogen bonds between these molecules and the surface carbonate species without further detail.[17] Also, it may be noted that MgO behaves quite differently, since the initial bidentate carbonate is transformed by H_2O into a unidentate carbonate whose vibrations are at 1510 and 1390 cm^{-1}.[26]

In contrast to previous data relative to Co-Y zeolites,[17] we observed that the 1650-cm^{-1} band forms under the effect of D_2O as well as that H_2O, so that this band cannot be ascribed to the H_2O deformation mode. It may correspond to the

TABLE II: Absorption Ranges (in cm^{-1}) of Surface Carboxylate and Unidentate Carbonate Species

Modes	Asymmetric stretch	Symmetric stretch
Carboxylate[a]	1575–1510	1410–1330
Unidentate carbonate[b]	1550–1460	1435–1350

[a] References 25, 29, and 30. [b] References 2, 9, 17, and 25–30.

ν(C=O) vibration of a bidentate carbonate species whose other vibrational modes are not observed because they are below 1300 cm^{-1}. However, the role of D_2O in reversibly forming this species from the initial unidentate carbonate is not clear. Alternatively, the 1650-cm^{-1} band also falls in the absorption region of the asymmetric CO stretching vibrations of bicarbonate species[26] and the formation of such species on exposure to D_2O would not be surprising. However, another band, which is expected in the 1290–1410-cm^{-1} region,[26] was not found. Therefore, the origin of the 1650-cm^{-1} band remains dubious.

Bands at 1520 and 1490 cm^{-1} and Correlations with the OH Bands. These bands are in the absorption range of the asymmetric ν(CO) vibration of unidentate carbonate species. The symmetric stretch may contribute to the 1410–1450-cm^{-1} absorption region. Changes in these carbonate bands, according to various parameters, are concomitant to the changes in the OH bands. First, these carbonate bands start to increase appreciably for the same Mg content in the zeolite as the 3685-cm^{-1} band. This Mg content probably corresponds to the saturation of inaccessible sites with Mg^{2+} cations. Secondly, for increasing temperatures in the 150–400 °C range, the bands around 1520 and 1490 cm^{-1} become progressively more intense as well as the OH bands at 3550 cm^{-1} and, to a lesser extent, at 3640 cm^{-1}, whereas the 3685-cm^{-1} band becomes weaker. This effect has been observed for the Mg 37.5 and Mg 46.1 zeolites. Thirdly, on evacuation between 400 and 500 °C, the considered carbonates and the new acidic OH groups are removed, whereas the 3685-cm^{-1} band reappears, i.e., the phenomena observed on heating in CO_2 are reversible. Finally, for low amounts of CO_2, the 3685-cm^{-1} band is not affected and those at 1520 and 1490 cm^{-1} do not occur.

The above data suggest that these unidentate carbonate species are formed as a result of the reaction of CO_2 with the OH groups responsible for the band at 3685 cm^{-1}. This reaction also yields new acidic OH groups. Scheme I tentatively

Scheme I

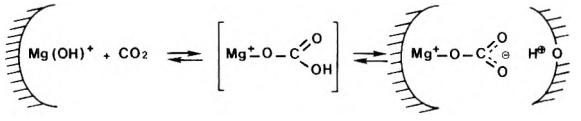

indicates how this may take place. The zeolitic hydrogen atoms, which initially correspond to the 3685-cm^{-1} band, would be transformed into acid protons referring to either the 3640- or 3550-cm^{-1} band, depending upon the zeolitic oxygen atoms with which they interact. This transformation may occur through a species of bicarbonate type; however, if it exists, this species is unstable since no infrared band was found in the 1660–1620-cm^{-1} region. The existence of two bands around 1520 and 1490 cm^{-1} may arise from two different environments for the unidentate carbonate species in the zeolite supercages and it is tentatively suggested that this corresponds to the formation of the two types of acid OH groups. The unidentate carbonate species probably remain in the vicinity of these OH groups, since CO_2 action is reversible. Also, the decrease in stability of the OH groups thus formed as compared with those of a H-Y zeolite indicates that the removal of CO_2 from the unidentate carbonates is easier than the condensation of hydroxyl groups to form water.

There is some analogy between these results and those found on exposing, at room temperature, polyvalent cation-exchanged Y zeolites to HCl or *n*-propyl chloride.[32] The chloride ion becomes associated with the cation, whereas the proton of HCl (introduced or formed in situ) reacts with a framework oxygen atom. The resulting OH groups also have a lessened stability.

Finally, the difference in symmetry between the unidentate carbonates species stable and unstable at 500 °C may stem from their formation. The former type involves certain lattice oxygen atoms whose reactivity is due to the presence of Mg^{2+} cations. The unstable types incorporate oxygen atoms from the $Mg(OH)^+$ species (see Scheme I). Since these hydroxylic oxygen atoms do not belong to the zeolite framework and therefore are expected to be more labile, it is conceivable that the corresponding unidentate carbonate species are more symmetric.

II. *Calcium Zeolites.* Some experiments were carried out with calcium zeolites. Figure 9 shows the spectra obtained in the absorption regions of the OH groups and carbonate species under conditions analogous to those used for magnesium materials. In the case of the Ca 51.2 sample evacuated at 400 °C, the stronger band is at 3675 cm^{-1} and weak bands are observed at 3740 and 3630 cm^{-1} as well as a weak shoulder at 3560 cm^{-1}. Reaction with CO_2 at 400 °C (Figure 9b) decreases the 3675-cm^{-1} band and increases considerably the 3630- and 3560-cm^{-1} bands. Two strong and broad bands occur at 1485 and 1425 cm^{-1}. Moreover, the presence of an absorption without defined maximum is observed between them. Evacuation at 500 °C nearly restores the starting spectrum in the OH region and the absorption between the bands at 1485 and 1425 cm^{-1} disappears. On the contrary, these latter bands subsist. The Ca 40.7 sample undergoes a weaker interaction with CO_2.

By comparison with the data obtained for the Mg-Y samples, we attribute the bands around 1485 and 1425 cm^{-1} to unidentate carbonate species, which is in agreement with previous work.[17] As a result of exposure to D_2O at 25 °C (Figure 8B) these bands are replaced by a broad and very intense band in the 1450–1475-cm^{-1} region. This indicates that the stable unidentate carbonates, which are more symmetric (i.e., less tightly coordinated) than in the case of the Mg-Y zeolites, become still more symmetric because of the influence of D_2O. However, as for Co-Y zeolites,[17] no absorption is found around 1650 cm^{-1}. The above discrepancies are due to the nature of the divalent cations. The question also arises as to the existence of symmetric carbonate species for the Ca-Y samples. Although no band around 1450 cm^{-1} is really distinguishable after evacuation of CO_2 at 500 °C, their existence cannot be entirely dismissed, because of the possible overlapping with the intense bands at 1485 and 1425 cm^{-1}.

The presence of Ca-O in our samples is ruled out, since CO_2 reaction with Ca-O gives rise, at room temperature, to bands at 1510 and 1415 cm^{-1} assigned to a unidentate carbonate, whereas evacuation at 460 °C produces bands at 1550 and 1315 cm^{-1} assigned to a bidentate carbonate.[28] Therefore, the behaviors of Ca-O and Ca-Y zeolites deeply differ.

Concerning the reversible reaction of CO_2 with the surface OH groups, the behavior of Ca- and Mg-Y zeolites appear, in

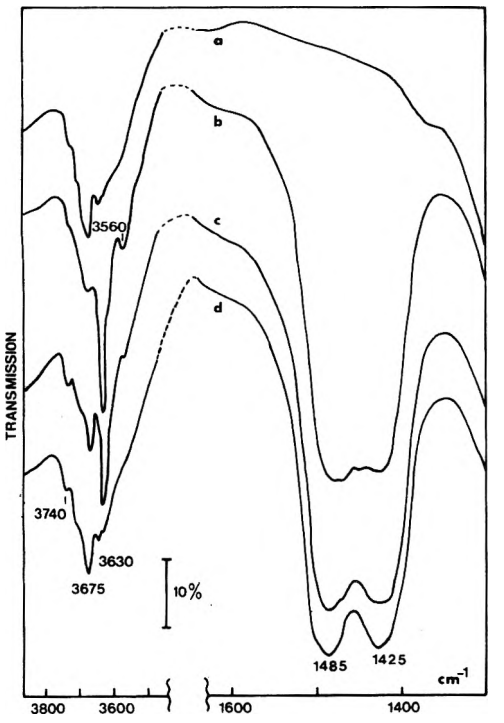

Figure 9. Spectra of the Ca 51.2 zeolite: (a) O_2 treated then evacuated at 400 °C for 15 h; (b) heated in 100 Torr of CO_2 at 400 °C for 15 h, then evacuated at room temperature for 30 min; (c) evacuated at 400 °C for 15 h; (d) evacuated at 500 °C for 1 h.

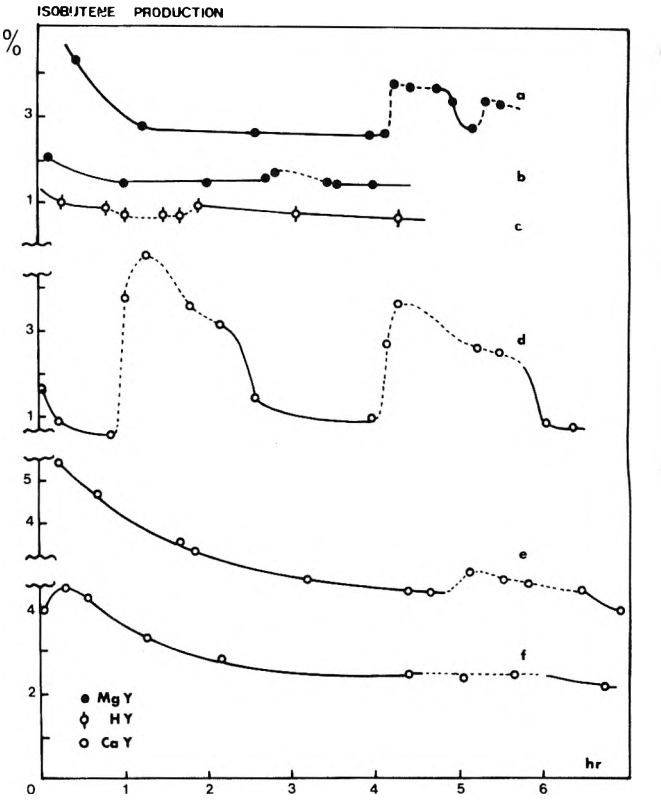

Figure 10. Influence of CO_2 on the catalytic activity of various zeolites for isooctane cracking (pressures:isooctane 100 Torr, CO_2 40 Torr) (—) without CO_2 and (- - -) in presence of CO_2: (a) Mg 46.1; (b) Mg 23.4; (c) Na-H-Y 7.5; (d) Ca 51.2; (e) Ca 40.7; (f) Ca 23.4.

the main, similar. However, differences may be noted. (i) The OH groups which exhibit a basic character vibrate at 3675 cm^{-1} for the Ca-Y zeolites instead of 3685 cm^{-1}. This decrease in wavenumber with increasing cation radius[7] is in favor of the attribution to OH groups linked to the cations or, at least, perturbed in some way by them. The existence of this OH band cannot be associated with the possible formation of $Ca(OH)_2$, since the corresponding hydroxyl groups vibrate at 3650 cm^{-1} and do not withstand to a few hour evacuation at 500 °C.[33] (ii) The increase in acidic OH bands is more pronounced for the Ca-Y than for the Mg-Y zeolites. Moreover, the main growth in intensity is observed for the 3630-cm^{-1} band instead of that at 3550 cm^{-1}. It is admitted that the former band refers to O_1 oxygen atoms[11] and the latter to the other types of oxygen atoms.[10,34] Since the Ca^{2+} and Mg^{2+} cation locations in the supercages may differ, it is not unreasonable to expect that the intermediate bicarbonate species whose formation is suggested (Scheme I) interact preferentially with different types of framework oxygen atoms.[32] (iii) The small difference in frequency between the two stretching vibrations of the unidentate carbonate indicates that this carbonate is more symmetric than in the case of the Mg-Y zeolites. On the other hand, the neighboring positions of these bands hamper the observation of a still more symmetric unidentate carbonate species as for the Mg samples; only a broad absorption without a defined maximum is found.

III. *Catalytic Activity.* The favoring influence of CO_2 on the catalytic activity of zeolites in various reactions has been pointed out.[15] In order to determine whether there is any correlation between this influence and the present results the activity in isooctane cracking was measured for some of our samples. These measurements were carried out at 465 °C in a microreactor as previously described[35] using hydrogen as the carrier gas. The activity was expressed in percent of isobutene formed. A first series of experiments was done by pretreating the catalyst at 465 °C in CO_2 and carrying out the reaction without CO_2 in the reactants. No change in activity was noted. Referring to the thermal stability of the various carbonate species, it may be inferred that under these catalytic conditions, only stable unidentate carbonates exist on the catalyst. Hence stable unidentate carbonates do not involve active sites for the cracking reaction. A second series of experiments was performed by continuously introducing CO_2 during the catalytic test (partial pressure 40 Torr) for 0.5–1.5-h periods. In that case the symmetric unidentate carbonate species and the newly created OH groups are present in the zeolite. Figure 10 shows the results obtained for various magnesium and calcium samples. The H-Y and Ca 23.4 samples did not exhibit any variation in activity (Figures 10c and 10f). For higher bivalent cation content (Mg 23.4 and Ca 40.7) a small increase in isobutene formation was observed (Figures 10b and 10e). For the Mg 46.1 and Ca 51.2 zeolites, a marked increase in activity occurred (Figures 10a and 10d). Stopping the CO_2 gas flow reduced the activity. Cycles of successive increases and decreases in activity could be thus followed according to the presence or absence of CO_2 in the reactants. The increase was greatest for calcium zeolites. Only small changes in selectivity were observed with addition of CO_2 to the reactants. It was found that, at the beginning of each CO_2 introduction, the selectivity was that of the fresh catalyst, as if fresh active sites had been formed. It then rapidly returned to the usual value.

The catalytic results compared with the ir studies show that CO_2 increases activity only when new acidic OH groups are present. The extent of the activity increase parallels the increase of the ir band intensity as a function of cation nature,

of cation contents, and of the presence of CO_2. These correlations suggest that the cracking, which involves acid sites, is enhanced by the acidic OH groups formed on CO_2 adsorption. As usual for acid sites, these centers partly loose their activity upon aging.

In conclusion, this study indicates that acidic OH groups can be created on CO_2 adsorption at the expense of basic hydroxyls groups in magnesium and calcium Y faujasites. The increase in cracking activity relates to the presence of these acidic OH groups. The reversibility of CO_2 action at 465 °C explains that a certain CO_2 partial pressure is required to raise the catalytic activity.[16] The improvement of catalytic properties by other acidic reactants (SO_2, CS_2, . . .)[15] might perhaps be interpreted on a similar basis. Also, zeolites exchanged with transition metal cations might exhibit similar activity enhancements.

Acknowledgment. The authors thank the Laboratory of Chemical Analysis and Dr R. Beaumont for the gift of the Ca samples. This work was assisted by the DGRST (Contract No. 74.7.1157).

References and Notes

(1) A. Bielanski and J. Datka, *J. Catal.*, **32**, 183 (1974); T. Yashima, H. Suzuki, and N. Hara, *ibid.*, **33**, 486 (1974).
(2) J. B. Peri, *J. Phys. Chem.*, **79**, 1582 (1975).
(3) P. Jacobs and J. B. Uytterhoeven, *J. Catal.*, **22**, 193 (1971).
(4) R. Beaumont, P. Pichat, D. Barthomeuf, and Y. Trambouze, *Catal., Proc. Int. Congr. 5th, 1972*, 343 (1973).
(5) J. B. Peri, *Catal., Proc. Int. Congr. 5th, 1972*, 329 (1973).
(6) P. A. Jacobs and J. B. Uytterhoeven, *J. Chem. Soc., Faraday Trans. 1*, **69**, 373 (1973).
(7) J. Ward, *J. Phys. Chem.*, **72**, 2689, 4211 (1968).
(8) J. B. Uytterhoeven, R. Schoonheydt, B. V. Liengme, and W. K. Hall, *J. Catal.*, **13**, 425 (1969).
(9) P. A. Jacobs, F. H. Van Cauwelaert, E. F. Vansant, and J. B. Uytterhoeven, *J. Chem. Soc.*, **69**, 1056 (1973).
(10) J. Scherzer and J. L. Bass, *J. Phys. Chem.*, **79**, 1200 (1975).
(11) J. Ward, *Adv. Chem. Ser.*, **No. 101**, 380 (1971).
(12) See D. W. Breck, "Zeolite Molecular Sieves", Wiley, New York, N.Y., 1974, p 484.
(13) J. Scherzer and J. Bass, *J. Catal.*, **28**, 101 (1973).
(14) J. Ward, *J. Catal.*, **9**, 225 (1967).
(15) Kh. M. Minachev and Ya. I. Isakov, *Adv. Chem. Ser.*, **No. 121**, 451 (1973).
(16) Kh. M. Minachev, G. V. Isagulyants, Ya. I. Isakov, N. Ya. Usachev, and N. N. Rozhdestvenskaya, *Izv. Akad. Nauk SSSR, Ser. Khim.*, **1**, 42 (1974).
(17) C. L. Angell and M. V. Howell, *Can. J. Chem.*, **47**, 3831 (1969).
(18) M. V. Mathieu and P. Pichat, in "La catalyse au laboratoire et dans l'industrie", B. Claudel, Ed., Masson et Cie, Paris, 1967, p 319.
(19) J. Ward, *J. Catal.*, **26**, 451 (1972).
(20) P. Pichat, R. Beaumont, and D. Barthomeuf, *C. R. Acad. Sci.*, **272**, 612 (1971); *J. Chem. Soc., Faraday Trans. 1*, **70**, 1402 (1974).
(21) P. Gallezot, R. Beaumont, and D. Barthomeuf, *J. Phys. Chem.*, **78**, 1550 (1974).
(22) C. V. McDaniel and P. K. Maher in "Molecular Sieves", Society Chemical Industry, London, 1968, p 186.
(23) H. Bremer, W. Mörke, R. Schödel, and F. Vogt, *Adv. Chem. Ser.*, **No. 121**, 249 (1973).
(24) P. J. Anderson, R. F. Horlock, and J. F. Oliver, *Trans. Faraday Soc.*, **61**, 2754 (1965).
(25) L. H. Little, "Infrared Spectra of Adsorbed Species", Academic Press, London, 1966, pp 74–89, and references therein.
(26) T. V. Evans and T. L. Whateley, *Trans. Faraday Soc.*, **63**, 2769 (1967).
(27) S. J. Gregg and J. D. Ramsay, *J. Chem. Soc. A*, 2784 (1970).
(28) Y. Fukuda and K. Tanabe, *Bull. Chem. Soc., Jpn.*, **46**, 1616 (1973).
(29) P. Pichat, J. Veron, B. Claudel, and M. V. Mathieu, *J. Chim. Phys.*, **63**, 1026 (1966); P. Pichat and G. Brau, *ibid.*, **66**, 724 (1969).
(30) V. G. Amerikov and L. A. Kasatkina, *Kinet., Katal.*, **12**, 165 (1971).
(31) N. D. Parkyns, *J. Phys. Chem.*, **75**, 526 (1971).
(32) C. L. Angell and P. C. Schaffer, *J. Phys. Chem.*, 69, 3463 (1965); C. L. Angell and M. V. Howell, *ibid.*, **74**, 2737 (1970).
(33) T. Iizuka, H. Hattori, Y. Ohno, J. Sohma, and K. Tanabe, *J. Catal.*, **22**, 130 (1971).
(34) P. A. Jacobs and J. B. Uytterhoeven, *J. Chem. Soc., Faraday Trans. 1*, **69**, 359 (1973).
(35) D. Barthomeuf and R. Beaumont, *J. Catal.*, **30**, 288 (1973).

Dimeric Properties of Rhodamine B in Glycerol, Ethylene Glycol, and Acetic Acid

Jun'ichiro Muto

Department of Instrumentation Engineering, Faculty of Engineering, Keio University, 832 Hiyoshi, Kohoku, Yokohama 223, Japan
(Received October 6, 1975)

Publication costs assisted by Keio University

Absorption spectra of rhodamine B are examined in solutions of glycerol, ethylene glycol, and acetic acid. Particular attention is given to the absorption spectra of monomers and dimers of rhodamine B in these solutions. Furthermore, dimeric structures of rhodamine B in these solutions are also investigated.

1. Introduction

Rhodamine B, one of the most widely used dye laser materials, has been found to lase in alcohol, water, and PMMA.[1–4] The appearance of the rhodamine B organic dye laser in the various media mentioned above has stimulated a further study on spectroscopic and structural properties of this dye in relation to the lasing mechanism.[5–14]

In aqueous solution, rhodamine B has a tendency to aggregate and form dimers with increasing concentration. Furthermore, the fluorescence quantum efficiency of aqueous rhodamine B was found to be greatly affected by dimerization, since dimers of rhodamine B in water were recognized to make little contribution to fluorescence, though they were capable of optical absorption.[9,10] In glycerol, however, rhodamine B was observed to have a fluorescence quantum efficiency of nearly unity.[12]

The absorption spectrum of rhodamine B is greatly influenced by addition of acid. On the other hand, the absorption spectrum of rhodamine B in acetic acid is quite similar to that in nonacidic solution such as alcohol or acetone.[10] In addition to the use for dye lasers as mentioned before, rhodamine B in ethylene glycol is commonly used as a quantum counter.[15]

Under these circumstances, it will be quite important to examine absorption spectra of rhodamine B in glycerol, ethylene glycol, and acetic acid in some detail with emphasis on determining the monomeric and dimeric absorption spectra in these solutions. Furthermore, dimeric configurations of rhodamine B in these solutions are also investigated.

2. Experimental Section

Rhodamine B, used in our experiment, was obtained commercially (reagent grade, Tokyo Kasei Industries) and no further purification was done in our laboratory.

To eliminate the efficient light from the dye and to select only the transmitted light from the sample solution, absorption measurements at various concentrations and solutions are done by using two monochromators. Details of the experimental apparatus are found in the literature.[10]

3. Results and Discussions

Absorption coefficients in the photon energy region between 2.1 and 2.5 eV are measured at room temperature in solutions of glycerol and ethylene glycol. The obtained results are shown in Figures 1a and 1b. As seen from the figures, the absorption spectra are somewhat different at various concentrations and at various solutions. However, the existence of a main absorption peak around 2.15 eV and a broad shoulder at about 2.35 eV are clearly recognized at all concentrations in the solutions examined. Similar spectral behaviors have already been reported in case of acetic acidic–rhodamine B.[10]

Monomer and Dimer Spectra. In this section, we shall determine the absorption spectra of the monomer and dimer separately from the observed total absorption spectra, and then calculate the equilibrium constant of a monomer–dimer equilibrium state.

First, we write for the relations of various absorption coefficients for the monomer–dimer equilibrium

$$\alpha(E) = \alpha_m(E)x + \alpha_d(E)(1 - x) \quad (1)$$

where $\alpha(E)$, $\alpha_m(E)$, and $\alpha_d(E)$ are the observed total molar absorption coefficient and those of monomers and dimers, respectively, at photon energy E, and x denotes the fraction of monomer.

From the law of mass action for the monomer–dimer equilibrium, we have

$$K = 2Cx^2/(1 - x) \quad (2)$$

in which K expresses the equilibrium constant for the process [monomer + monomer = dimer], and C, the total concentration.

The free energy ΔG for the dissociation of the dimer is written as

$$\Delta G = -RT \ln K \quad (3)$$

where R denotes the gas constant and T the absolute temperature.

Now, integrating eq 1, we have

$$\int \alpha(E)\, dE = I_1 x + I_2 \quad (4)$$

where $I_1 = \int [\alpha_m(E) - \alpha_d(E)]\, dE$, and $I_2 = \int \alpha_d(E)\, dE$. In eq 4, the integrated molar absorption coefficient, $\int \alpha(E)\, dE$, increases with increasing x, if I_1 is positive, while it decreases with increasing x, if I_1 is negative.

As is found in eq 2, x (fraction of monomer) increases with a decrease of C (total dye concentration), since K (equilibrium constant) is positive and x is positive and less than unity.

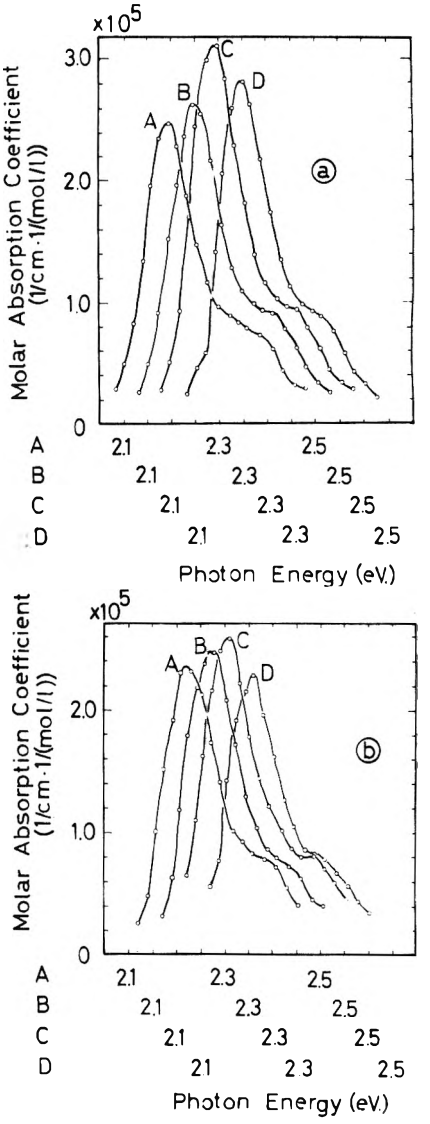

Figure 1. Molar absorption spectra of rhodamine B in (a) glycerol (b) ethylene glycol. A indicates absorption spectrum at 10^{-5} M, B at 5 × 10^{-5} M, C at 10^{-4} M, and D at 10^{-3} M.

Therefore, the integrated molar absorption coefficient in eq 2 decreases with an increase of concentration when I_1 is positive and decreases when I_1 is negative.

Now, let us examine the results of the experiments. The concentration dependence of the integrated absorption coefficients in various solutions is shown in Figure 2. The results of glycerol– and ethylene glycol–rhodamine B are graphically obtained from Figure 1, and those of water and acetic acid from previously reported results.[10] In case of glycerol, ethylene glycol, and acetic acid, the obtained integrated absorption coefficients show close resemblance with each other in that they are found to increase with their increasing concentrations in the lower concentration range ($\leq 10^{-4}$ M), while they decrease in the higher concentration range ($>10^{-4}$ M).

Taking into account the above mentioned discussions on the concentration dependence of integrated absorption coefficients, and also our experimental results described above, we conclude that the monomer–dimer equilibria are realized in these solutions at lower concentrations ($\leq 10^{-4}$ M). The decrease of integrated absorption coefficients at the

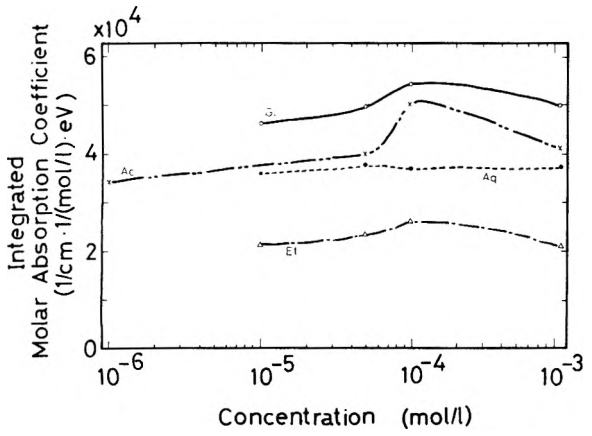

Figure 2. Concentration dependence of integrated molar absorption coefficient of rhodamine B in (Gl) glycerol, (Ac) acetic acid, (Eg) ethylene glycol, and (Aq) water.

higher concentrations ($>10^{-4}$ M) might be attributed to the formation of trimers and/or higher polymers.

In contrast with the experimental results of glycerol, ethylene glycol, and acetic acid, the integrated molar absorption coefficients of aqueous rhodamine B show slight changes with decreasing concentration (see Figure 2). Since the monomer–dimer equilibrium of aqueous rhodamine B is shown to exist in the range of 10^{-5} to 10^{-3} M,[9,10,16] the area of the monomer spectrum becomes the same as the area of the dimer spectrum; that is, the two joined ions of rhodamine B in water have an absorption equal to that of the separate ions. Similar spectral behavior has been observed in case of aqueous Na-fluorescein.[17]

Next, we shall calculate the monomer and dimer spectra of rhodamine B in the following way:[7,19] (1) First, we assume various values of K in eq 2 and calculate the corresponding x for a concentration C. (2) Using these values, $\alpha_m(E)$ and $\alpha_d(E)$ are obtained from eq 1, by the method of a least-squares fit. (3) Once we determine the best-fit monomer and dimer spectra for a given K, then we calculate the average standard deviations between the observed $\alpha(E)$ and the best-fit $\alpha(E)$ for the data at all concentrations. (4) Finally, we determine the best values of K, $\alpha_m(E)$, and $\alpha_d(E)$ on the basis of the minimum average standard deviation.

As discussed previously, the monomer–dimer equilibria of rhodamine B in glycerol, ethylene glycol, and acetic acid seem to exist at the lower concentrations ($\leq 10^{-4}$ M). Then, the best-fit spectra of monomers and dimers in these solutions are calculated using the experimental results obtained in the above mentioned concentration range. In Figures 3a, 3b, and 3c, the absorption spectra of monomers have definite maxima at about 2.2 eV, although details of the spectra are different for different solutions, whereas, dimeric absorption spectra show rather complicated structure as will be discussed below. In case of glycerol, one main band appears in the lower energy region, and a subsidiary band, in the higher energy region. In ethylene glycol, subsidiary bands of H_1 and H_2 appear and the lower energy band is graphically found to result from the overlapping of the two bands with peak positions of 2.155 and 2.195 eV. While in acetic acid, two larger bands in addition to two smaller bands are clearly recognized.[18] The obtained values of peak positions, in addition to the dissociation constants and the free energies of rhodamine B in these solutions are presented in Table I.

Structure of Dimer. When two dye molecules come together

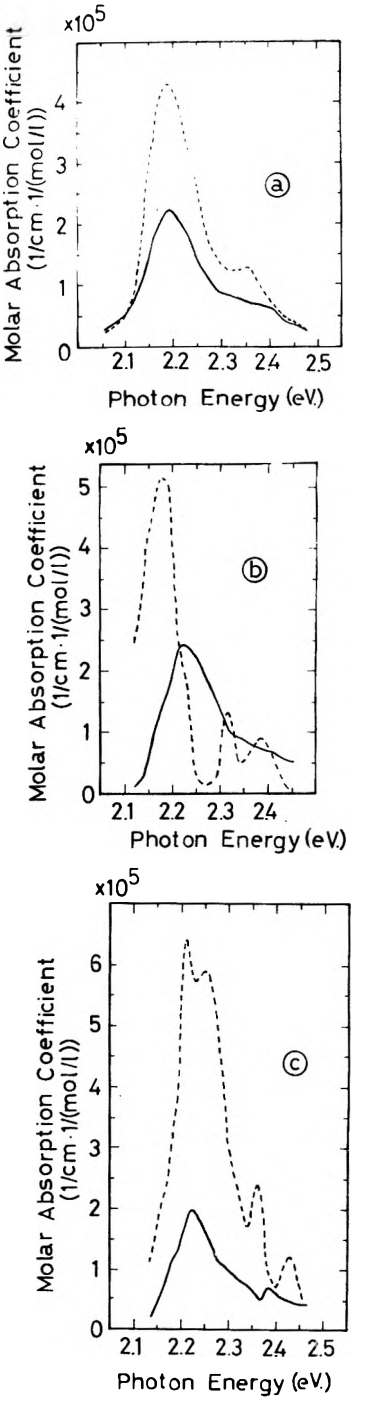

Figure 3. Molar absorption spectra of monomeric (solid curves) and dimeric (broken curves) rhodamine B in (a) glycerol, (b) ethylene glycol, (c) acetic acid.

to form a dimer unit, the monomer absorption peak splits into two peaks (see Figure 4): H band (higher energy band) and J band (lower energy band). The splitting is caused by a point dipole–dipole interaction between adjacent molecules in the dimer. The resulting splitting depends upon the spacing and the directional orientation of the adjacent molecules. The relative orientation of the two molecules also has an effect on the relative strength of the H band and the J band.[19-23]

The simple exciton theory of the point dipole approximation mentioned above gives the expectation that the H band is always larger than the J band in the parallel plane dimer configuration, while the J band is allowed to be larger than the

TABLE I: Results Obtained for Various Parameters for Rhodamine B Dimer[a]

Solution	Dimer peak	eV	α, deg	L, Å	K, M	ΔG, kcal/mol
Glycerol[c]	J	2.19	138	10.4	2.1×10^{-4}	5.0
	H	2.36				
Ethylene glycol[c]	J_1	2.155	135	10.4	6.3×10^{-4}	4.4
	J_2	2.195				
	H_1	2.32	127	9.8		
	H_2	2.39				
Acetic acid[c]	J_1	2.21	132	9.5	6.3×10^{-4}	4.4
	J_2	2.26				
	H_1	2.36	132	9.7		
	H_2	2.43				
H_2O[d]	J	2.183[a]	52[a]	8.3[a]	6.8×10^{-4}[b]	4.2[b]
	H	2.375[a]				

[a] Experimental results are from ref 6. [b] Experimental results are from ref 7. [c] Rhodamine B forms an oblique plane dimer. [d] Rhodamine B form a parallel plane dimer.

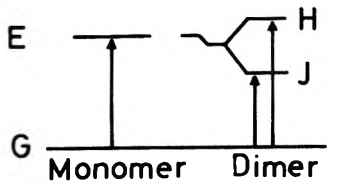

Figure 4. Energy level diagram for monomer and dimer electronic energy levels and optical transitions. E and G indicate excited states and ground state, respectively. H means H band and J shows J band.

H band in the oblique plane dimer structure.[22] The parallel plane and the oblique plane dimers are schematically shown in Figure 5.

Aqueous rhodamine B, similarly to aqueous methylene blue, was proved to have a parallel plane configuration by dimerization, since the H band of these dyes in water was observed to be larger than the J band. In contrast to the results of aqueous rhodamine B and methylene blue mentioned above, the J band is found to be larger than the H band in glycerol–, ethylene glycol–, and acetic acidic–rhodamine B. Therefore, rhodamine B molecules in these solutions are expected to dimerize in order to have oblique plane configurations. Similar dimeric configuration of the oblique structure is observed in alcoholic chlorophyll.[24]

It follows from the simple exciton theory[19-23] that the dipole strength for the H band of the dimer is given by $D(1 + \cos\theta)$, and that for the J band of the dimer, $D(1 - \cos\theta)$, where θ is the relative orientation and D, the monomer dipole strength. The angle θ may be determined from the relative oscillator strength of the split bands

$$\theta = 2\tan^{-1}(E_H f_J / E_J f_H)^{1/2} \quad (5)$$

where E_H, E_J, f_H, and f_J are the peak positions and oscillator strength of the H and J bands, respectively.

The oscillator strength of the monomer f_M is determined by integrating the molar absorption coefficient $\alpha_m(E)$ over the monomer band[25]

$$f_M = 1.51 \times 10^{-5} \int \alpha_m(E)\, dE \quad (6)$$

in which the energy E is given in electron volts.

The energy splitting ΔE of the oblique plane dimer is derived as

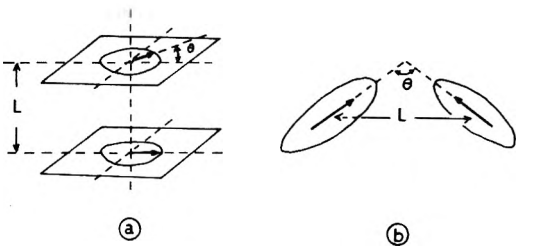

Figure 5. Schematic representations of simple dimer structures: (a) "parallel plane dimer", (b) "oblique plane dimer". The ovals in the figures correspond to the molecular profiles, the arrows the transition dipole moments in the individual molecules at an angle θ with each other, and L shows the distance between dimer molecules.

$$\Delta E = 2DA/L^3 \quad (7)$$

where A is equal to $(3 - \cos\theta)/2$ and L indicates the spacing of the dimer molecule.

The monomer dipole strength is related to the oscillator strength by[19]

$$D = (3h^2e^2/8\pi^2m)(f_M/E_M) \quad (8)$$

in which h is Planck's constant, e the electron charge, and m indicates the electron mass.

Then, the intermolecular distance L of the oblique plane dimer is solved as

$$L = [3.29 \times 10^2 f_M A/(E_M \Delta E)]^{1/3} \quad (\text{Å}) \quad (9)$$

in which E_M denotes the monomer peak energy and ΔE the splitting in electron volts.

The obtained dimeric configurations and spacings of rhodamine B in solutions are listed in Table I.

So far the observed results were analyzed by the simple exciton theory and valuable information was obtained by it. However, some more complicated phenomena were also observed. As mentioned previously, dimers of rhodamine B in ethylene glycol and acetic acid have absorption spectra with two J bands and two H bands. The simple exciton theory does not seem to explain the complicated character of the absorption curves. An explanation of these behaviors will need more detailed study concerning the mutual orientations of atoms in the dimer molecules and the role of molecular vibrations and the vibronic coupling between various states of the dimer.[13] The simple exciton theory may be an oversimplified one, because it assumes a molecule as a point dipole and only the electronic states are taken into account.

The "H" class dimer is thought to be nonfluorescent, while the "J" class dimer is fluorescent.[7] As a matter of fact, molecules of rhodamine B in water were proved to become nonfluorescent by dimerization, since these dimers show strong "H" absorption,[9,10] whereas, our results show larger J-bands absorption in case of glycerol, ethylene glycol, and acetic acid. Similar spectral occurrence of strong "J" absorption has been observed for rhodamine B in EPA.[7] As was described previously, the absorption spectra of rhodamine B in all solutions we examined are shown to be composed of those of fluorescent monomers and of fluorescent dimers. In the present work, glycerol–rhodamine B is seen to have the highest total absorption intensity (see Figure 2) and then, seems to show most efficient fluorescence. Actually, rhodamine B is said to show a fluorescence quantum yield of nearly unity in viscous solutions such as glycerol.[12] Details of the fluorescence processes will be clarified through studies on the fluorescence spectra,

the relaxation times, and the quantum yields of both monomeric and dimeric rhodamine B in solution.

Acknowledgments. The author is indebted to K. Asakura and T. Yamaguchi for their technical assistances. The author also wish to thank Professor J. Yamashita for reading the manuscript. A part of this work is supported by financial aid from the Matsunaga Science Foundation.

References and Notes

(1) E. P. Schaefer, W. Schmidt, and K. Marth, *Phys. Lett.*, **24A**, 280 (1967).
(2) B. B. McFarland, *Appl. Phys. Lett.*, **10**, 208 (1967).
(3) O. G. Peterson and B. B. Snavely, *Appl. Phys. Lett.*, **12**, 238 (1968).
(4) S. A. Tuccio and F. C. Strome, Jr., *Appl. Opt.*, **11**, 64 (1972).
(5) R. W. Chambers and D. R. Kearns, *J. Phys. Chem.*, **72**, 4718 (1968).
(6) K. K. Rohatgi, *J. Mol. Spectrosc.*, **27**, 545 (1968).
(7) J. E. Selwyn and J. I. Steinfeld, *J. Phys. Chem.*, **76**, 762 (1972).
(8) J. Ferguson and A. W. H. Mau, *Chem. Phys. Lett.*, **17**, 543 (1972).
(9) J. Muto, *Jpn. J. Appl. Phys.*, **11**, 1217 (1972).
(10) J. Muto, Keio Engineering Report No. 25, 71, 1972.
(11) K. H. Drexhage, *Laser Focus*, **9**, 35 (1973).
(12) K. H. Drexhage, "Dye Lasers", Vol. 4, "Structure and Properties of Laser Dyes", E. P. Schaefer, Ed., Springer-Verlag, New York, N.Y., 1973, p 114.
(13) R. W. Chambers, T. Kajiwara, and D. R. Kearns, *J. Phys. Chem.*, **78**, 380 (1974).
(14) M. M. Wong and Z. A. Schelly, *J. Phys. Chem.*, **78**, 1891 (1974).
(15) W. H. Melhuish, *J. Opt. Soc. Am.*, **52**, 1256 (1962).
(16) Th. Foerster and E. Koening, *Z. Elektrochem.*, **61**, 344 (1957).
(17) V. L. Levshin and K. V. Krotova, *Opt. Spectrosc.*, **13**, 457 (1962).
(18) Discussion in ref 10 that the chemical reaction of monomers with the solvent is responsible for the spectral behaviors of acetic acidic-rhodamine B is thought to be erroneous.
(19) A. R. Monahan and D. F. Blossey, *J. Phys. Chem.*, **74**, 4014 (1970).
(20) G. S. Levinson, W. T. Simpson, and W. Curtis, *J. Am. Chem. Soc.*, **79**, 4314 (1957).
(21) G. Hoijtink, *Z. Elektrochem.*, **64**, 156 (1960).
(22) M. Kasha, H. R. Rawls, and M. A. El-bayoumi, *Pure Appl. Chem.*, **11**, 371 (1965).
(23) S. S. Brody and M. Brody, *Nature*, **189**, 547 (1964).
(24) Influence of the internal field, such as the Lorentz field or Onsager field, on the oscillator strength is not taken into account in eq 6.

Structure of Aqueous Solutions. Librational Band Studies of Hydrophobic and Hydrophilic Effects in Solutions of Electrolytes and Nonelectrolytes

David W. James, Richard F. Armishaw,*

Chemistry Department, University of Queensland, St. Lucia, Queensland 4067, Australia

and Ray L. Frost

Chemistry Department, Queensland Institute of Technology, Brisbane, Queensland 4067, Australia *(Received August 29, 1975)*

The infrared librational spectrum of water has been examined for aqueous solutions of a series of alkyl substituted ureas and thioureas, formamide, acetamide, acetone, and a series of symmetrical tetraalkylammonium nitrates. The spectra enable separation of effects which can be described as structure making and structure breaking. The unique solution behavior of urea is shown to be dependent on its ability to hydrogen bond in a pseudo-tetrahedral pattern. The tetraalkylammonium salts are shown to decrease the tendency of water to hydrogen bond to four adjacent molecules but at the same time increase the strength of the remaining hydrogen bonds.

There have been several studies of the vibrational spectra of solutions of nonelectrolytes most of which have examined the OH stretching region or overtone region in the infrared spectra.[1-5] There has been one Raman study[6] and one recent infrared study[7] of the librational region of aqueous solutions of sucrose and urea. It is expected that a study of the librational band of water in aqueous solution will give direct information on the nature and extent of hydrogen bonded interactions. We report here a systematic study of the librational band in solutions of substituted ureas and some related solutes and the results are compared with those obtained for solutions of tetraalkylammonium nitrates.

The properties of aqueous solutions of urea have been extensively studied. Although dielectric constant measurements indicate that there is an increase in hydrogen bonding in solutions,[8] other studies indicate that urea destroys the long-range order of water.[9-11] Thus it has been shown that urea raises the critical micelle concentration of dodecylpyridinium iodide and various dodecyl sulfates[9] and this was attributed to a decrease in the ordering of the water. In an examination of the ability of urea to denature proteins it was noted that addition of urea to solutions of serum albumin caused denaturation[8,10] while alkyl ureas have the opposite effect to an extent which is dependent on the length of the alkyl chain and the number of alkyl substituents.[10,11] Certain nonelectrolytes (dextrose and tetramethylurea) were found to be nondenaturants while acetamide and methylurea were found to be weak denaturants.[11] Thermodynamic studies have confirmed the different behavior of urea and substituted ureas in solution.[12]

Aqueous solutions of symmetrical tetraalkylammonium salts have been extensively studied and the results have been recently reviewed.[13] It is concluded that in dilute solution salts containing large cations, for example, tetrapropylammonium (Pr_4N^+) or tetrabutylammonium (n-Bu_4N^+), produce a structure enhancement, while at higher concentration the effect of ion-ion interaction becomes important.

The nature of the structure enhancement is at present not clear. On the basis of the Raman spectrum in the OH stretching region it has been concluded that Bu_4NBr in concentrated solution produced an increase in water structure.[14]

It is anticipated that the presence of ionic charges may have a dominating influence on the observed properties of the tetraalkylammonium salt solutions (as opposed to the solutions of uncharged organic solutes). Extensive studies of solutions of perchlorates, nitrates,[15] and halides[16] have laid the basis for an understanding of observed changes. When the cation is Li^+, Na^+, K^+, or NH_4^+ and the anion is Cl^-, Br^-, I^-, ClO_4^-, or NO_3^- the librational band observed for the salt solution is always at lower frequency and has a higher integrated intensity than for pure water. The changes observed have been discussed in detail elsewhere.[15,16]

Experimental Section

The chemicals used were all recrystallized from water prior to use. The water used was distilled twice in an all glass still, the final distillation being from alkaline permanganate. Saturated solutions were prepared at 20 °C and other solutions prepared from these by dilution. The spectra were run on Perkin-Elmer Model 457 in a thin film cell (path length $\sim 7\ \mu$) between KRS5 plates. The spectra were visually smoothed and weak sharp absorbances were removed by extrapolation of the librational band prior to digitization. The spectra were corrected for reflection losses and for change in total water concentration as previously reported.[7,15,16] The spectra were treated in two separate ways. First calculations were made of the integrated relative molar intensity, the band maximum, ν_m (where the bisector of equiabsorbance chords intersects the band), band width at half-height, $\omega_{1/2}$, and the asymmetry index, ν_{as} (difference between the band maximum and the center of the chord at half-band height). Secondly normalized band moments were determined.[17,18] Although it may be argued that the librational band is not well enough understood for band moments to be significant the first and second moments give similar information to that calculated directly from the band.

Results

In Table I are collected the results for each solute. The calculated absorbance plots are presented in the supplementary material (see paragraph at end of text regarding supplementary material). In all cases except the tetraalkylammonium nitrates the spectral variations were linear with concentration. For the tetraalkylammonium nitrates the changes increased more than linearly with concentration.

Discussion

The measurements of band intensity and band maximum reported here are highly reproducible—the uncertainty in intensity is $\sim \pm 1\%$ while for band maximum the reproducibility from run to run is $\pm 5\ cm^{-1}$ which is quite satisfactory for such a broad flat band. The shifts in band maximum are generally in agreement with calculations of normalized first moments. Due to the weighting given to the tail of the bands the shifts of first moment are, in the main, less negative than of the band maximum. The second moment is heavily dependent on the high- and low-frequency tail of the band and hence on the baseline absorbance. This is the weakest aspect of our observation and is reflected in variability and lack of reproducibility in the calculated moments.

The librational band has been assigned three main components the two of higher frequency being responsible for most the infrared intensity.[19,20] In addition these two bands appear to be strongly dependent on the degree of hydrogen bonding. As "complete" hydrogen bonding is replaced by "partial" hydrogen bonding the two bands move to lower frequency with the higher frequency band showing a greater shift than the lower frequency band.[20] Thus the behavior of this infrared band gives a fairly direct measure of structure making or structure breaking in the literal sense used by Franks.[21]

Urea can hydrogen bond to water through its four hydrogen atoms and the carbonyl oxygen. In addition the urea molecule is suited by symmetry to fit into the water network although its size is rather larger than that of water. The addition of urea causes an increase in the intensity of the librational band and moves the band maximum to lower frequency.[7] Similar changes are noted on addition of electrolytes.[15,16] The change in intensity may be associated with an increase in the dipole of the water molecule (affecting $d\mu/dQ$ for the vibration). The positive value of ν_{as} is attributable to an increase in intensity of the higher frequency component of the librational band. This band is associated with "complete" hydrogen bonding so the symmetry of the urea molecule is critical in the maintenance of the four hydrogen bond pattern. Increase in urea concentration shifts the whole band to lower frequency indicating that overall the degree of hydrogen bonding is decreasing but the participation of urea in a four hydrogen bond pattern is reflected in the increased intensity of the highest frequency band. The effect of urea may be both structure making and structure breaking. This is associated with previous findings.

In the series of solutes studied the effect of progressively blocking the ability of the urea molecule to hydrogen bond is examined. The replacement of one hydrogen by a methyl group causes no change in the band intensity, the shift to lower frequency is reduced but the asymmetry is shifted from the higher frequency side to the lower frequency side of the band. The addition of the methyl group also changes the symmetry of the urea molecule. When the addition of the one methyl group makes the formation of four hydrogen bonds to urea unlikely no intensity enhancement of the highest frequency band is noted. When the amine group is replaced by a methyl group in acetamide the effect noted for methylurea is enhanced. The intensity is unaffected but the shift of the band to lower frequency is negligible. This is best understood in terms of a balance between the polar part of the molecule tending to drive the band to lower frequency and the nonpolar part acting hydrophobically to drive the band to higher frequency as discussed below.

When both nitrogen atoms are blocked by the addition of methyl groups the solute behaves almost as though it has no effect on the water librations. It is certain that the two methyl groups have a hydrophobic influence on the water molecules but this is apparently balanced by the H bonding influence of the carbonyl group. The results obtained for solutions of thiourea clarify the influence of the carbonyl group on solution structure. Although hydrogen bonding is possible through the amine groups of thiourea, the results obtained are similar to *N,N'*-dimethylurea. Hence the reduction in hydrogen bonding by the replacement of C=O by C=S is similar to that when the amine groups are

TABLE I: Infrared Librational Band Characteristics[a]

	Concn, M	I_R	$\Delta\nu M$	ΔM_1	$\Delta W_{1/2}$	$\Delta(M_2)^{1/2}$	$\Delta\nu_{as}$
H_2O	55.2	1.00	685		455		−20
Urea	2	1.10	−30		−5		+16
	6	1.28	−45	−22	−25	0	+20
	10	1.44	−70	−36	−30	−5	+25
Methylurea	1	1.05	−5	0	−9	+2	−20
	2	1.11	−10	0	−15	+3	−18
	4	1.24	−15	0	−20	+6	−18
Ethylurea	1	1.05	0	−2	−5	1	−18
	2	1.09	0	0	−10	6	−18
	4	1.19	+5	−3	−15	7	−18
Propylurea	1	1.07	+15	0	−20	−1	−25
	2	1.09	+25	−2	−25	−3	−30
	4	1.19	+30	−7	−25	−5	−30
Butylurea	1	1.06	+15	+1	−30	−2	−30
	2	1.10	+25	−2	−35	−4	−30
	4	1.14	+30	−6	−45	−8	−35
N,N'-Dimethylurea	1	1.01	0	+3	−10	+1	−20
	2	1.03	0	+3	−5	+1	−20
	4	1.07	−5	+2	−10	+4	−20
N,N'-Diethylurea	1	1.00	+15	+6	0	+4	−18
	2	0.98	+15	+10	−5	+8	−18
	4	0.95	+15	+14	−5	+11	−18
Tetramethylurea	1	0.96	+15	+3	−50	+4	−20
	2	0.82	+20	+3	−60	+2	−15
	4	0.64	+25	+6	−65	+4	−15
Thiourea	0.5	1.01	0	−2	+5	0	−20
	1.0	1.05	0	−14	0	−22	−20
Methylthiourea	1	1.01	0		−10		−20
	2	0.98	−5		−15		−18
	4	0.96	−10		−20		−16
N,N'-dimethylthiourea	1	0.87	+5	−8	+5		−20
	2	0.82	−5	−15	0		−22
	4	0.75	−10	−23	−5		−23
Formamide	1	1.00	−10	−4	0	−3	−20
	2	0.96	+25	−6	+10	−6	−12
	4	0.92	+40	−14	+15	−15	−6
Acetamide	1	1.06	0	−4	0	+18	−20
	2	1.11	−5	+1	−5	0	−16
	4	1.23	−10	+2	0	+2	−16
Acetone	1	1.02	0				
	2	1.05	0				
	4	1.12	+5				
NH_4NO_3	1	1.02	−5	−5	+20	+1	−40
	2	1.03	−75	−12	+30	+1	−40
	4	1.06	−30	−23	+35	−2	−40
$(Me_4N)NO_3$	1	1.04	−10	−1	0	+1	−35
	2	1.07	−10	−6	−10	0	−35
	4	1.14	−20	−19	−20	−1	−40
$(Et_4N)NO_3$	1	1.06	−5	−4	−25	−2	−24
	2	1.12	−10	−11	−45	−4	−25
	3	1.21	−25	−22	−70	−5	−25
	4	1.37	−50	−44	−95	−10	−20
$(Pr_4N)NO_3$	1	1.10	−5	−4	−25	−2	−25
	1.5	1.15	−10	−8	−40	−1	−28
	2	1.20	−20	−17	−55	−3	−30
	2.8	1.40	−50	−37	−90	−0	−20
$(nBu_4N)NO_3$	0.5	1.05	0	−2	−20	−4	−25
	1.0	1.09	−5	−9	−35	−5	−25
	1.5	1.14	−15	−18	−50	−10	−22
	2.0	1.25	−35	−40	−60	−20	−22

[a] Concn is the concentration in mol dm^{-3}; I_R is integrated relative molar intensity of the band; $\Delta\nu M$ is shift in band maximum (cm^{-1}) from the value for water (line 1); ΔM_1 is the shift in the normalised first moment from the value for water; $\Delta W_{1/2}$ is the change in band half-width (cm^{-1}) from the value for water (line 1); $\Delta(M_2)^{1/2}$ is the change in the square root of the normalized second moment from the value for water; $\Delta\nu_{as}$ is the change in the band asymmetry index (cm^{-1}) from the value for water (line 1).

shielded by methyl substituents. For both solutes the symmetry is similar enough to that of a water molecule for no great amount of structural disturbance to occur. The influence of acetone on the water band is similar to that of dimethylurea except the smaller size of the acetone molecule produces less structural disturbance of the water structure

and the librational band moves slightly to higher frequency.

When the four hydrogen atoms in urea are replaced by methyl groups there is a dramatic change in the librational band. The intensity shows a pronounced decrease, an effect not previously observed in electrolyte solutions and the band maximum moves to higher frequency. The intensity decrease might be attributed to a decrease in the water molecule dipole but this is not likely. It is possible that the observed changes are due to the concentration of nonpolar aliphatic residues exerting a hydrophobic bonding influence. The relatively bulky molecules are interfering with the water structure and the carbonyl group cannot exert an appreciable influence due to steric interference. It is significant however that the band maximum moves to higher frequency as this indicates that the tendency to complete H bonding has been increased. A similar effect is noted with dimethylthiourea where the alkyl portion of the molecule is not as prominent but the loss of the hydrogen bonding through the carbonyl group lets the disruptive influence become effective. The shift of the band maximum to higher frequency in tetramethylurea is probably associated with the hydrophobic interaction as described later. The two methyl groups in *N,N'*-dimethylthiourea do not have sufficient hydrophobic influence to produce a shift in the band maximum.

The changes in spectra found for substituted ureas with larger alkyl groups than methyl further clarify the influence of the nonpolar portion of the solute. All of the monosubstituted ureas show similar intensity enhancement which indicates that it is the interaction between the polar portion of the urea molecule which is responsible for the increase in $(d\mu/dQ)$ over the band. The position of the band maximum shows a strong move to higher frequency as the alkyl chain length increases. The first moment of the band however shows essentially no movement indicating that the band mean is not changing. As expected ν_{as} becomes more negative as the ν_m moves to higher frequency. This indicates that the increasing alkyl chain length is increasing the tendency toward complete hydrogen bonding. Thus the cooperative effect of polar and nonpolar portions of the substituted ureas is to produce a structure enhancement. The effect of *N,N'*-diethylurea is similar to that of tetramethylurea. The intensity of the band is decreased indicating that the total degree of hydrogen bonding is diminished. The movement of the band to higher frequency indicates that the hydrogen bonding present tends to be complete hydrogen bonding. This demonstrates the difficulty in applying terms like structure making and structure breaking to aqueous solutions as the addition of *N,N'*-diethylurea both decreases the amount of hydrogen bonding (structure breaking) and increases the proportion of complete hydrogen bonding (structure making).

The series of symmetrical tetraalkylammonium salts provide solutes in which a progressively more strongly hydrophobic species can be examined in conjunction with ionic species. The results for the nitrate salts shown in Table I indicate that there is a regular change as the alkyl group is changed progressively through methyl, ethyl, propyl, and *n*-butyl. For similar concentrations of solute the intensity increases and the band maximum decreases in frequency with increasing chain length. The intensity increases for propyl and *n*-butyl alkyl groups are greater than observed for other electrolytes. The movement of the band to lower frequency characterizes a decrease in the extent of hydrogen bonding, in particular a decrease in the number of molecules having four hydrogen bonds. In terms of the structure of the water solvent there is no doubt that the tetraalkylammonium salts are acting as structure breakers. For the substituted urea solutes the hydrophobic interaction of the side chain was seen to give a progressively stronger structure making effect as the alkyl chain length increased. It would seem certain that the larger tetraalkylammonium cations have a powerful hydrophobic effect in spite of the cationic charge. In the absence of other charged or dipolar species this hydrophobic influence would promote structure in the solvent. The presence of the anion however provides alternate nuclei about which structuring can take place. In the resulting solution there is a restructuring of the solvent with anion–dipole bonding forming a basis for hydrogen bound species in which the presence of four and perhaps three hydrogen bonds to a given water molecule is not common. The increase in intensity observed can then be attributed in part to an increase in dipole moment of the water due to the ion–dipole interaction and in part to the increased amplitude of the vibration caused by the less complete hydrogen bonding.

The pattern of water–solute interactions developed above can be used to describe the results of other physicochemical experiments on tetraalkylammonium salts. It has been shown that the NMR reorientation time for water molecules is increased by a factor of 1.6–3 when tetraalkylammonium salts are added to water.[22] This was interpreted as indicating a structure making effect. The interpretation has been questioned as tetramethylammonium salts have a pronounced effect even though they are not structure making.[13] The results are in accord with the model we propose. The addition of tetraalkylammonium salt causes a reduction in the completely hydrogen bound water molecules. The hydrophobic influence then enhances the structure based on the hydrated anion. In the hydrated anionic structure the water molecule reorientation is restricted through the hydrophobic influence of the alkyl groups and, as expected, the reorientation time lengthens as the alkyl chain length increases.

Chemical shift of the water proton has been studied in aqueous solution and the trend of the data implies that the tetraalkyl salts are acting as structure breakers.[23] A retreatment of the data indicated that there may be a weak structure making influence.[13] The reduction in average number of hydrogen bonds coupled with a strengthening of the remaining hydrogen bonds give an admirable basis to these observations.

The structural changes we propose receive strong support from the x-ray diffraction studies of Narten and Lindenbaum.[24] These authors report that the average separation of water molecules is reduced and the number of nearest neighbors is also reduced on addition of R_4NX salts. The structure breaking required by the reduction in the number of molecules having four hydrogen bonds together with the promotion of an anion centered structure having enhanced strength but lower number density hydrogen bonds describes these diffraction results well.

Concluding Remarks

It has been possible in this study of the infrared librational band to describe the changes produced by enhancement of water structure, strengthening of hydrogen bond network with change of structure, and hydrophobic influence of alkyl side chains. This has enabled a cohesive de-

scription to be made of the nature of structure in solutions of urea, substituted ureas, and tetraalkylammonium nitrates. A range of other structure making and structure breaking effects is being studied in both electrolyte and nonelectrolyte solutions.

Acknowledgments. One of us R.F.A. acknowledges assistance from a Rural Credits Development Fund Fellowship during the course of which this work was commenced.

Supplementary Material Available: Plots of the peak maximum frequency of the librational bands of tetraalkylammonium nitrate solutions vs. concentration (Figure A), relative intensity of the librational bands vs. concentration (Figure B), and ir librational bands of NH_4NO_3 (Figure C), $(Me_4N)NO_3$, $(Et_4N)NO_3$, $(Pr_4N)NO_3$, and $(Bu_4N)NO_3$ (Figure D) solutions (4 pages). Ordering information is available on any current masthead page.

References and Notes

(1) O. D. Bonner and G. B. Woolsey, *J. Phys. Chem.*, **72**, 899 (1968).
(2) O. D. Bonner, *J. Phys. Chem.*, **72**, 2572 (1968).
(3) J. D. Worley and I. M. Klotz, *J. Chem. Phys.*, **45**, 2868 (1966).
(4) D. A. Armitage, M. J. Blandermer, M. J. Foster, N. H. Hidden, K. W. Morcom, M. C. R. Symons, and M. J. Wootten, *Trans. Faraday Soc.*, **64**, 1193 (1968).
(5) W. A. P. Luck, *Water: Compr. Treatise, 1973*, **2**, 235 (1973).
(6) G. E. Walrafen, *J. Chem. Phys.*, **44**, 1546 (1966).
(7) D. W. James and R. L. Frost, *J. Phys. Chem.*, **78**, 1754 (1974).
(8) M. Abu-Hamdiyyah, *J. Phys. Chem.*, **69**, 2720 (1965); J. F. Brandt, *J. Am. Chem. Soc.*, **86**, 4302 (1964).
(9) P. Mukerjee and A. Ray, *J. Phys. Chem.*, **67**, 190 (1963); M. J. Schick, *J. Phys. Chem.*, **68**, 3585 (1964); Y. Nozaki and C. Tanford, *J. Biol. Chem.*, **238**, 4074 (1963).
(10) J. A. Gordon and W. P. Jencks, *Biochemistry*, **2**, 47 (1963).
(11) J. A. Gordon and J. R. Warren, *J. Biol. Chem.*, **243**, 5663 (1968).
(12) P. R. Philip, G. Perron, and J. E. Desnoyers, *Can. J. Chem.*, **52**, 1709 (1967).
(13) W. Y. Wen, *J. Solution Chem.*, **2**, 253 (1973).
(14) G. E. Walrafen, *J. Chem. Phys.*, **55**, 768 (1971).
(15) D. W. James and R. F. Armishaw, *J. Phys. Chem.*, in press.
(16) D. W. James and R. F. Armishaw, *Aust. J. Chem.*, **28**, 1179 (1975). See also D. A. Draegert and D. Williams, *J. Chem. Phys.*, **48**, 401 (1968).
(17) R. G. Gordon, *J. Chem. Phys.*, **39**, 2788 (1963); **41**, 1819 (1964).
(18) R. N. Jones, K. S. Seshadri, N. B. W. Jonathan, and J. W. Hopkins, *Can. J. Chem.*, **41**, 750 (1963).
(19) G. E. Walrafen, *Water: Compr. Treatise, 1972*, **1** (1972).
(20) D. W. James, R. Irmer, and R. L. Frost, unpublished results.
(21) F. Franks in "Hydrogen Bonded Solvent Systems", A. K. Covington and D. Jones, Ed., Taylor and Francis, London, 1968, p 31.
(22) H. F. Hertz and M. D. Zeidler, *Ber. Bunserges. Phys. Chem.*, **68**, 821 (1964).
(23) H. G. Hertz and W. Spalthoff, *Z. Elektrochem.*, **63**, 1096 (1959).
(24) A. H. Narten and S. Lindenbaum, *J. Chem. Phys.*, **51**, 1108 (1969).

Proton Magnetic Resonance Line Shapes of Water and Ammonium Ions in Type-Y Zeolites

E. B. Whipple, P. J. Green, M. Ruta, and R. L. Bujalski*

Union Carbide Corporation, Central Scientific Laboratory, Tarrytown, New York 10591 *(Received November 24, 1975)*

Publication costs assisted by Union Carbide Corporation

Proton magnetic resonance line broadening mechanisms of adsorbed species in zeolites are analyzed using hydrated NH_4^+-Y^- as a model. The dominant mechanism originates from inhomogeneous magnetic fields inside the zeolite cavities due to bulk susceptibility effects, although this is partially narrowed by diffusion over interparticulate dimensions. Two methods for dealing with inhomogeneous broadening are shown to give practical methods for obtaining high resolution spectra of mobile species in zeolite cavities. Chemical exchange reactions among ammonium ions, water molecules, and lattice hydroxyl groups are then differentiated and discussed semiquantitatively. The lattice hydroxyl groups are shown to be strongly acidic, and apparently lead to structure degradation above ~16 per unit cell. Proton exchange between ammonium ions and water is shown to occur via deammoniation of NH_4^+, whose rate is measurable. In contrast to aqueous solutions, rapid quadrupole relaxation of ^{14}N in ammonium ions occurs inside zeolite cavities. The results in general provide a powerful means of observing structural, kinetic, and dynamic information about simple chemical processes inside zeolite cavities in comparison to aqueous solutions.

1. Introduction

The proton magnetic resonance lines of molecules adsorbed in most naturally occurring or synthetic zeolites are too broad to allow much useful information to be derived by straightforward observation of their high resolution spectra. This broadening can occur as the result of any combination of three sources: (1) relaxation effects; (2) inhomogeneous broadening; and (3) chemical exchange phenomena. Each of these contains potentially useful structural, dynamic, or kinetic information about molecular processes taking place inside the zeolite cavities, but it is often the case that so much information is present in so few resolvable line shapes that one is faced with a formidable problem in sorting it out. The present study addresses this aspect of the situation in a relatively simple system, a synthetic type-Y zeolite containing absorbed water and either sodium or ammonium cations.

2. Relaxation

Relaxation time measurements of water on fully hydrated, synthetic X zeolites have shown that nuclear dipole–dipole relaxation predominates below 300 K provided magnetic impurities are absent, and that the transverse relaxation time goes through a maximum of about 0.04 s, corresponding to a natural line width of ~8 Hz, near room temperature.[1] We have made ambient temperature measurements on a number of sodium- and ammonium-exchanged Y zeolites of similar high purity,[19] and obtain correspondingly long relaxation times. The line widths commonly observed in high resolution measurements on powdered samples are, on the other hand, of the order of 100 Hz or greater. One concludes, therefore, that in magnetically pure X or Y zeolites near ambient temperatures, relaxation processes make a minor contribution to the observed line shapes. This may not be true, if relatively impure natural or commercial materials are observed, or if the temperature is varied too far. In the case of commercial synthetic Y zeolites, at least some of the background impurities appear to be removable by forcing the ion exchange to very high levels.

3. Inhomogeneous Broadening

NMR lines in powdered solids are generally broadened as the result of bulk susceptibility differences between the particles and their surrounding medium.[2] This results both from the nonspherical shapes of the particles themselves and from the magnetization of neighboring particles. The total line broadening has been estimated[2] to be

$$\Delta H \simeq 3\chi_v H_0 \tag{1}$$

which, based on estimated susceptibilities, would lead to line widths of several hundred hertz at field strengths in the vicinity of 20 kG. Equation 1 also predicts a field-dependent line width, which prevents one from increasing the resolution of a multicomponent spectrum by the usual expedient of increasing the applied field strength.

4. Diffusional Narrowing

There are, however, several characteristics of the ^{1}H NMR line shapes that do not conform to those expected for an inhomogeneously broadened sample. In the first place, the line shapes are approximately Lorenzian rather than the Gaussian shape that one might expect for the envelope of an inhomogeneously broadened distribution. Secondly, while the line widths are field dependent, this dependence is not linear according to eq 1, but shows the behavior illustrated in Figure 1. A quadratic field dependence was observed in the proton resonance from adsorbed ethylene by Muha and Yates, who on this basis tentatively attributed the line broadening to incompletely averaged anisotropic shielding in spite of the fact that the magnitudes of the anisotropies required seem unreasonably large.[3] Thirdly, a characteristic of an inhomogeneously broadened line is the ability to "burn a hole" by saturating one part of the line with a strong radio-frequency field immediately prior to observing it in a fast sweep experiment.[4] Our attempts to carry out this experiment led, however, to a uniform saturation of the broader line. Finally, the observed line widths depend strongly on temperature, despite the fact that thermal relaxation processes make an insignificant contribution near ambient temperatures, and no thermally dependent terms appear in eq 1.

All these facts can be reconciled on the basis that the inhomogeneousy broadened distribution is partially narrowed by proton diffusion. Provided that the diffusion rate is fast

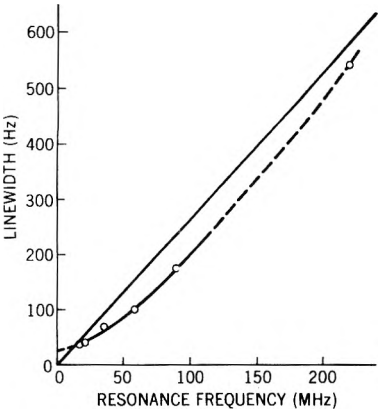

Figure 1. Field dependence of proton resonance line width of H_2O on Na-Y zeolite.

with respect to the inhomogeneously broadened line width, which in turn is large compared to the inverse relaxation time, one obtains an exchange narrowed, Lorenzian line shape whose width is approximated by

$$\Delta\nu_{1/2} = G_2\tau_d \qquad \left(\frac{\gamma\Delta H}{2} \gg G_2\tau_d \gg \frac{1}{T_2}\right) \tag{2}$$

where G_2 is the second moment of the unnarrowed line and τ_d is the correlation time for diffusion.[5] A quadratic field dependence occurs via the second moment term in eq 2. The "hole burning" will fail so long as diffusion is fast with respect to the time required to conduct the experiment. The temperature dependence results from the temperature dependence of the diffusion rate, which for activated diffusion has the exponential form

$$\tau_d = ke^{-\Delta H_d/RT} \tag{3}$$

where ΔH_d is the activation energy for diffusion.

The rather complicated temperature dependence of the H_2O line width in hydrated Na-Y, which is shown in Figure 2, is characterized by three main regions. Below 260 K, the line is strongly broadened by relaxation effects stemming from the lengthened correlation times for molecular rotation and short-range diffusion. This line broadening decreases very rapidly with increasing temperature, and is of no great consequence in the region above 280 K. From 280 to about 370 K, the inhomogeneously broadened line is narrowed by molecular diffusion. In the low temperature limit, this should approach a constant value equal to the width of the inhomogeneously broadened distribution in eq 1, which extrapolation indicates to be about 200 Hz in a magnetic field of 21 kG. This limit should be characterized by a linear field dependence. In the high temperature limit of this region, where extreme diffusional narrowing applies (eq 2), the line widths should be characterized by a quadratic field dependence and an exponential temperature dependence. Finally, in the region above 375 K, the line is anomalously broadened by increasing temperature. This is apparently the result of a reversible hydrolytic reaction

$$NaY + H_2O \rightleftharpoons HY + NaOH$$

which exchanges water protons with the lattice. Its temperature dependence is also exponential, but in the opposite direction from before. A least-squares fit of the experimental data above 320 K to a sum of exponentials yields an activation energy of 3.9 kcal/mol for the diffusion, which is slightly lower than that for liquid water (5.6 kcal/mol[6]), and intermediate

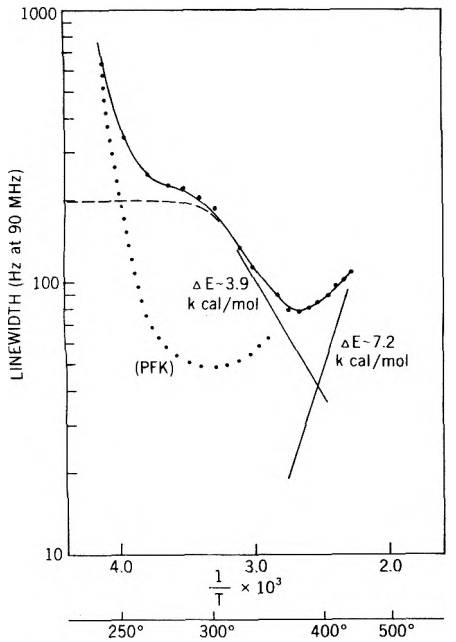

Figure 2. Temperature dependence of H_2O line width in hydrated Na-Y.

between the values (2.6 and 4.8 kcal/mol, respectively) for acid- and base-catalyzed proton exchange.[7] A similar activation energy, 3.5 kcal/mol, has been obtained by pulsed field gradient measurements on hydrated Na-Y.[8]

It is of considerable interest to gain some understanding of the physical dimensions over which this diffusional narrowing occurs. To make an order of magnitude estimate, one can assume the validity of eq 2 and estimate the second moment from the plateau line width of 200 Hz in Figure 2, obtaining for a Gaussian line shape

$$G_2(\nu) = 0.18(\Delta\nu_{1/2})^2 = 7200\ \text{Hz}^2$$

so that at ambient temperatures

$$\tau_d \simeq 180/7200 = 2.5 \times 10^{-2}\ \text{s}$$

For classical diffusion

$$D = \frac{1}{6}\frac{\langle r^2 \rangle}{\tau_d}$$

where D is the diffusion coefficient and $\langle r^2 \rangle$ is the mean square average distance over which the diffusive event occurs in time τ_d. Taking the value of $D \approx 10^{-5}$ cm^2/s from pulsed-field gradient measurements on hydrated zeolites,[8] one estimates

$$r \approx [6 \times 10^{-5} \times 2.5 \times 10^{-2}]^{1/2} \approx 1.2 \times 10^{-3}\ \text{cm}$$

which is larger than the particle dimensions. This would imply, as did the pulsed measurements, that interparticle diffusion is the principal line narrowing process in the ambient temperature region. From this, together with the overall Lorenzian line shape, we infer that intraparticle diffusion is already sufficiently fast to average the inhomogeneity within a single particle. We would expect, therefore, that the temperature dependent diffusional narrowing would disappear in a fine suspension wherein the particles are separated by a hydrophobic fluid. This behavior is shown in the dotted curve in Figure 2, where the line width variation of a powdered zeolite is compared to that in a PFK dispersion. The inhomogeneously broadened plateau drops to a value of ~41 Hz which shows no evidence of further narrowing as the temperature is increased, and as a result the two curves (both complicated by the high temperature hydrolysis) eventually merge.

5. Artificial Reduction of Line Widths

The inhomogeneous broadening in a two-phase system can generally be reduced by filling the voids between the particles with an inert fluid whose susceptibility more nearly matches that of the solid. As was shown in Figure 2, one thereby obtains a dramatic line narrowing when the zeolite sample is prepared in the form of a slurry in perfluorokerosene (PFK). Since PFK is a chemically inert, aprotic fluid whose molecules are too large to interfere directly with processes going on inside the zeolite cavities, the observed line narrowing without other perturbation of the spectrum can only be attributed to a bulk susceptibility effect. As a practical matter, however, the use of this technique seems limited. There is no assurance that the inhomogeneous broadening is completely eliminated, and when either working with dehydrated zeolites or at elevated temperatures, chemical reaction between the zeolite and PFK appears to take place.

A second, potentially more useful characteristic is the effect of sample spinning on the line widths. It has been pointed out elsewhere that the microscopic form of inhomogeneous broadening is similar to that of magnetic dipole–dipole interaction in solids, and should respond to sample rotation in the same way.[9] In particular, when the sample is spun rapidly compared to the unnarrowed line width about an axis at an angle, α, with respect to the magnetic field, the line should be narrowed by a factor[10] $\frac{1}{2}(3\cos^2\alpha - 1)$. We accordingly observe in Figure 3 that sample spinning[11] at selected angles with respect to the magnetic field leads to the predicted line width reduction, and in particular, that spinning at the "magic angle" of 54° 44′ eliminates the inhomogeneous broadening altogether. This experimental arrangement, which is illustrated in Figure 4, provides a generally useful means of obtaining high resolution spectra of mobile phases in zeolite cavities, as well as many other multiphase systems (surface adsorbed species, swollen polymers, pitch samples, gels, etc.) where inhomogeneous broadening presents a problem. To illustrate this point, the spectrum of ethyl alcohol in hydrated Na-Y is shown in Figure 5, where separate lines from the methyl and methylene protons are clearly resolved.

6. Chemical Exchange

Another potential source of line broadening is the limitation of the lifetimes of nuclei in a given spectroscopic environment due to chemical exchange reactions. This can lead to broadening, loss of hyperfine structure, coalescence, and eventual narrowing of multiple resonance lines as the exchange rate between two or more nuclear environments increases. The detailed line shape depends on the exchange rates and the nature of the spectrum in the absence of exchange. The latter should consist, in the case of NH_4^+-Y zeolites, of three separate signals: (1) a single, narrow line for protons in water; (2) a 1:1:1 triplet (due to ^{14}N, ^1H spin coupling) from the ammonium ions; and (3) a broad line from lattice hydroxyl groups which would be unobservable in ordinary high resolution experiments. A number of chemical reactions can occur which permute different combinations of these environments, and it is instructive to consider these reactions separately.

Exchange between Absorbed Species and the Lattice. The primary reactions of concern in this case are the protolysis of water

$$\text{H-Y} + \text{H}_2\text{O} \rightleftharpoons \text{H}_3\text{O}^+ + \text{Y}^- \qquad (1)$$

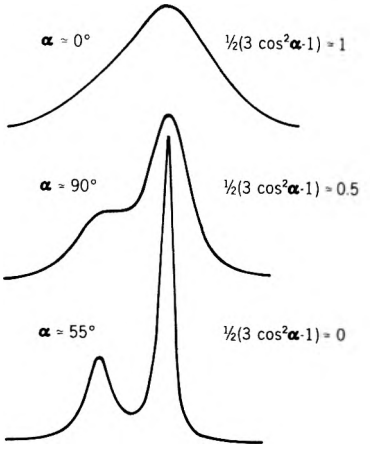

Figure 3. Effect of sample spinning on NH_4-Y.

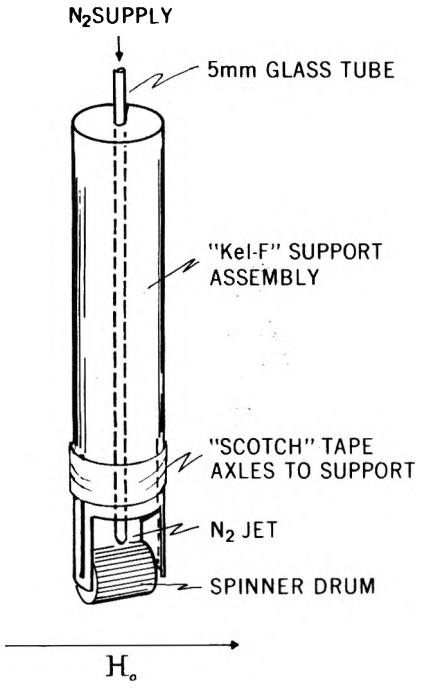

Figure 4. Sample spinner turbine.

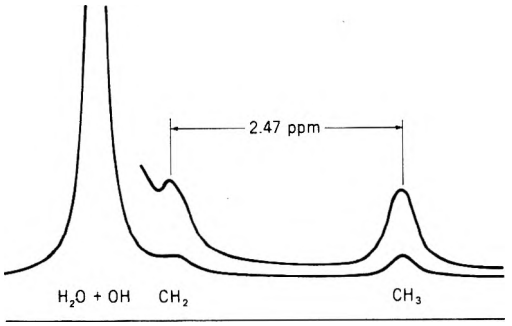

Figure 5. Proton magnetic resonance spectrum of ethyl alcohol adsorbed in hydrated Na-Y with "magic angle" spinning.

or its corresponding hydrolysis

$$H_2O + Y^- \rightleftharpoons H\text{-}Y + OH^- \quad (2)$$

and the deammoniation reaction

$$NH_4^+ + Y^- \rightleftharpoons NH_3 + H\text{-}Y \quad (3)$$

The equilibrium constants of reactions 1 and 2 are related by the ion product of water in the zeolite, while (2) and (3) are related by the decomposition product of ammonium hydroxide. Exchange between water molecules and lattice hydroxyl groups should generally lead to a broadening of the H_2O line, while that between ammonium ions and the lattice can also affect the ^{14}N, ^1H hyperfine structure in the ammonium ion resonance. In the limit of fast exchange, shifts in the center frequencies of either water and/or ammonium ions can also occur. Neither protonation of water nor deammoniation of ammonium would by itself change the overall symmetry of either resonance, but in concert, these reactions could serve to indirectly exchange protons between the two observed species, and thus cause coalescence if both reactions were fast. However, model line shape calculations show (Figure 6) that in this event the onset of coalescence precedes the collapse of hyperfine structure in the ammonium ion resonance.

Mutual Exchange between Adsorbed Species. In addition to indirect exchange via reactions 1–3, ammonium ions and water molecules can exchange protons directly

$$NH_4^+ + H_2O \rightleftharpoons H_3O^+ + NH_3 \quad (4)$$

and either species can undergo self-exchange

$$*HNH_3^+ + N'H_4^+ \rightleftharpoons NH_4^+ + *HN'H_3^+ \quad (5)$$

$$H*OH + H_2O' \rightleftharpoons H_2O + H*O'H \quad (6)$$

Reaction 6 does not cause immediately observable effects on the water spectrum but is presumably fast. Reaction 5 is observable through its effect on the ^{14}N, ^1H hyperfine splitting in ammonium ion, and reaction 4 tends to coalesce the water and ammonium resonances. These reactions have been studied in aqueous solution,[12] and found to be slow unless catalyzed by bases. The actual reactions of concern are, therefore

$$*HNH_3^+ + N'H_3 \rightleftharpoons NH_3 + *HN'H_3^+ \quad (7)$$

and

$$NH_3 + H_2O \rightleftharpoons NH_4^+ + OH^- \quad (8)$$

Both are intrinsically fast, so that one must go to fairly high acidity (pH <2) to observe separate ammonium ion and water resonances in aqueous solution. Moreover, the self-exchange rate between ammonium ions in aqueous solutions exceeds their cross exchange rate with water, so that the loss of hyperfine structure (pH <1.5) precedes the coalescence (pH ~2.5). This is in opposite order than the indirect exchange via reactions 1–3, and on this basis the direct and indirect exchange processes are distinguishable, in principle.

Characteristics of Observed Resonance Pattern. A typical pattern for the proton resonance of a fully hydrated NH_4^+–Y^- zeolite at room temperature is shown in Figure 7. The spectrum (90 MHz) consists of two lines separated by ~2 ppm, with the water line at higher field. The width of the NH_4^+ band (~88 Hz) is less than the envelope of the ^{14}N, ^1H hyperfine splitting pattern (1:1:1 triplet, J_{NH} = 51 Hz[12]) in the ammonium ion, so that this splitting must be dynamically averaged. Also, partial coalescence of the water and ammonium ion resonances is indicated by the fact that the observed spectrum (solid curve) is not the sum of two symmetrical bands centered at the separate frequencies of each (broken curve), but an added filling of the intermediate region occurs. Additional, very direct evidence of cross exchange is obtained

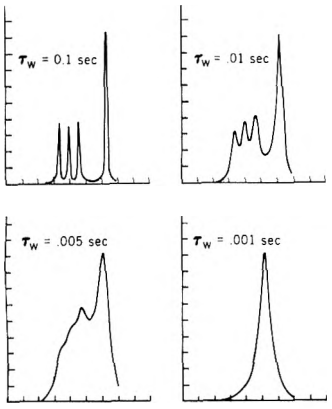

Figure 6. Calculated spectra of hydrated NH_4^+-Y^- undergoing cross exchange between NH_4^+ ions and H_2O molecules.

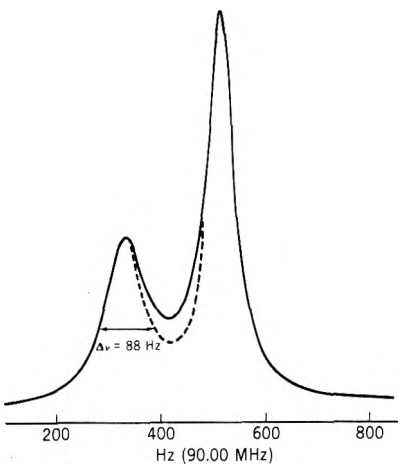

Figure 7. Proton magnetic resonance spectrum of hydrated NH_4^+-Y^- zeolite with "magic angle" spinning.

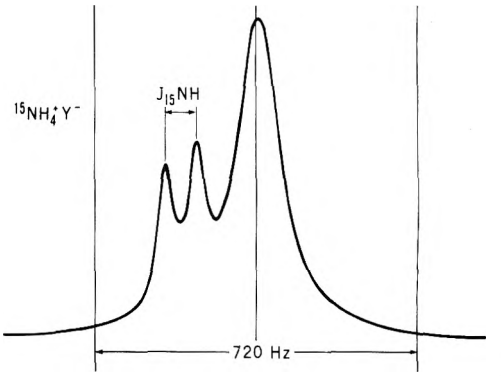

Figure 8. ^1H NMR spectrum (90 MHz) of hydrated $^{15}NH_4^+$-Y^- zeolite.

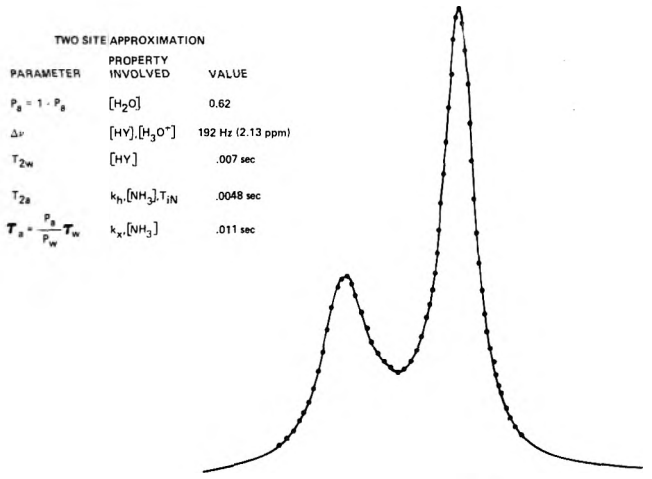

Figure 9. Observed and simulated spectrum of NH_4^+-Y^- (Figure 7) using five parameters.

from magnetization transfer experiments,[13] whereby it is observed that saturation of either resonance greatly diminishes the intensity of the other.

The absence of ^{14}N, ^1H hyperfine structure and the advent of cross exchange together suggest the action of base-catalyzed exchange reactions 7 and 8. However, the electric quadrupole moment of ^{14}N provides an alternate means of averaging out the hyperfine splitting by relaxation processes. While the high symmetry of its molecular environment precludes fast ^{14}N quadrupole relaxation in aqueous ammonium salt solutions, this situation does not necessarily hold in the internal fields inside zeolite cavities. The spectrum of an $^{15}NH_4^+$ exchanged zeolite, in which electric quadrupole relaxation cannot be effective ($I_{^{15}N} = \frac{1}{2}$), indeed shows that the hyperfine splitting is not averaged by chemical exchange (Figure 8). Hence, one concludes that the base-catalyzed mechanism is not responsible for the cross exchange, but rather a combination of reactions 3 and 1. One also determines that quadrupole relaxation is in fact much more effective in zeolite cavities than in aqueous solution. The T_d symmetry of the ammonium ion would ordinarily preclude electric quadrupole relaxation as an effective mechanism. However, local distortions of the electric fields about $^{14}NH_4^+$ evidently permit this process to operate even in aqueous solutions, as evidenced by the fact that no nuclear Overhauser effect is observed from protons on the ^{14}N resonance, as contrasted with ^{15}N (spin = $\frac{1}{2}$) in ammonium salt solutions.[14] One cannot immediately conclude that the local fields in zeolite cavities are stronger than in aqueous solutions, however, since the quadrupole relaxation rate also depends on the correlation time for molecular reorientation, which is also presumably longer in the intracrystalline fluid.

Since the ^{14}N hyperfine splittings are independently averaged, one can simplify the kinetic problem to one involving three magnetic environments differing only in chemical shifts and relaxation times, and treat the line shapes in terms of a classical formalism based on the Bloch equation.[15] Five parameters are involved in the simulation, each of which yields complementary information about the rate processes. These are described, and the results of a typical simulation shown, in Figure 9.

Effect of Lattice Protons on Exchange Rates. Experimental results from line shape simulations in a series of partially deammoniated NH_4^+-Y^- zeolites are summarized in Table I. The result of the various heat treatments is to thermally decompose ammonium ions to produce lattice hydroxyl groups and gaseous ammonia, the extent to which this has occurred being measured by chemical analysis of the cation deficiency, D. Samples were subsequently reequilibrated over saturated $CaCl_2$ solution in a closed desiccator, and their NMR spectra measured either in PFK suspension or by "magic angle" spinning of the solid. At low cation deficiency either method gives comparable results.

Since the ammonium ion content is known from the chemical analysis, the relative proton populations on water

TABLE I: NMR and Analytical Data on Partially Deammoniated NH_4-Y Zeolites[a]

	Original material	100 °C in wet N_2 (PFK)	SBVA 60 °C (PFK)	100 °C in dry N_2 (PFK)	SBVA 120 °C (PFK)	VA 200 °C (S)	VA 250 °C (S)	VA 300°C (S)
Analysis no.								
N/Al		0.786	0.72	0.67	0.62	0.39	0.22	0.045
$[NH_4^+]$ = N/Al [Al]	49.8	46.5	42.6	39.6	36.7	23.2	12.8	2.7
D = [Al] − $[Na^+]$ − $[NH_4^+]$	1.0	4.3	8.2	11.2	14.1	27.6	38.0	48.1
Pa	0.375	0.355	0.325	(0.325)	0.29	0.195		
$[H_2O]$ = 2(1 − Pa)/Pa $[NH_4^+]$	166.0	169.0	177.0	(164.5)	180	192		
$[NH_4^+]$ + $[H_2O]$	216.0	215.5	219.6	(204.1)	216.7	215.2		
$T_{2w} \times 10^3$		5.2	(3.5)	3.0	2.5	1.0		
$T_{2a} \times 10^3$		4.8	5.2	5.0	5.0	4.5		
$\tau_a \times 10^3$		14.5	13.0	(9.5)	11.0	9.0		
$\nu_w - \nu_a$		−196	−184	(−184)	−172	−160		

[a] Iron free, [Al] = 59.2, $[Na^+]$ = 8.4 per unit cell.

and ammonium ion can be used to calculate the total amount of water in the zeolite. These values are given in row 6 of Table I. From these data it appears that the total hydration increases only by the extent to which ammonium ions are removed; i.e., the population of water molecules plus ammonium ions (row 7) remains approximately constant at about 216 per unit cell. The same degree of hydration is also obtained by chemical analysis, demonstrating that all the water and ammonium ions are observed in the NMR measurements. The amount of adsorbed water is only ~⅔ of capacity, however.

The transverse relaxation times of ammonium ions do not appear to be substantially altered by deammoniation, while those of water are progressively shortened. Hence, exchange of lattice hydroxyl groups occurs only with water. Since the chemical shift of water (assuming the ammonium ion shift remains constant) also changes, reaction 1 appears to occur in the fast exchange limit. In this extreme, the H_2O relaxation time is given by[16]

$$\frac{1}{T_{2'w}} = \frac{1-x}{T_{2w}} + \frac{x}{T_{2l}} = \frac{1}{T_{2w}} + \frac{x}{T_{2l}} \qquad (9)$$

where T_{2w} is the relaxation time for water moeecules, $T_{2l} \ll T_{2w}$ that for lattice hydroxyl groups, and x is the proton fraction on the lattice, given in the absence of ionization by

$$x = \frac{[H\text{-}Y]}{2[H_2O] + [H\text{-}Y]} \simeq \frac{D}{2W_0 + 3D} \qquad (10)$$

The latter substitution makes use of the observation that each deammoniation adds one water molecule to the number, W_0, originally present in hydrated NH_4^+-Y. Combining (9) and (10), one obtains

$$\frac{1}{T_{2'w}} = \frac{1}{T_{2w}} + \frac{T_{2l}^{-1}D}{2W + 3D} \qquad (11)$$

The chemical shift of water in the fast exchange limit is also equal to the weighted average,[15] so that

$$\delta_W = \delta_{H_2O} + \frac{(\delta_{H\text{-}Y} - \delta_{H_2O})}{2W + 3D} D \qquad (12)$$

and one might therefore expect the change in chemical shift to parallel that in line width. The actual variations of both parameters with D are shown in Figure 10, where it is clear that a linear relation between the two is not observed. Both parameters show pronounced curvature, the line width tending to increase more rapidly with increasing cation deficiency (concave upward), while the chemical shift increases less rapidly (concave downward). All of these deviations can be explained on the basis that the lattice hydroxyl groups undergo substantial ionization which is suppressed at higher cation deficiencies. A significant acidity of the lattice protons is evidenced independently by the suppression of cross exchange between water and ammonium ions at cation deficiencies as small as D = 1 per unit cell, since coalescence of these lines is known to occur in aqueous solution unless the pH is less than two; since the zeolite unit cell is (24.8 Å)^3 in size, a hydrogen ion concentration of 10^{-2} m would correspond to 0.1 hydronium ions per unit cell, or 10% ionization as a lower limit. Equations 11 and 12 must be modified, therefore, to include the effect of ionization.

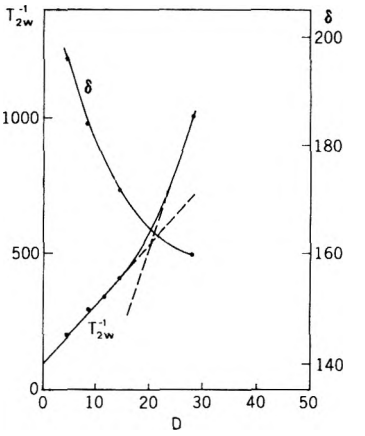

Figure 10. Chemical shift and relaxation time of water on deammoniated NH_4-Y zeolites.

The concentration terms in reaction 1 may be written

$$\underset{\text{H-Y}}{D(1-\alpha)} + \underset{}{W - \alpha D} \rightleftharpoons \underset{}{\alpha D} + \underset{\text{Y}^-}{M + \alpha D = A - D(1-\alpha)}$$

where D = cation deficiency (per unit cell), A = number of lattice aluminum, $M = A - D$ = number of cations (Na^+, NH_4^+), W = water of hydration, α = degree of ionization of H-Y ($\alpha < 1$), and $N = 2W + D$ = number of exchanging protons (excluding NH_4^+). Assuming that the transverse relaxation times for protons on hydronium ions are comparable to those on water (and, for that matter, ammonium ions), eq 11 is simply modified to read

$$\frac{1}{T_2'} = \frac{1}{T_{2w}} + \frac{(1-\alpha)D}{T_{2l}(2W_0 + 3D)} \qquad (11')$$

By setting $\delta_{H_2O} = 0$ as a reference point, the chemical shift becomes

$$\langle\delta\rangle = \frac{3\alpha D}{2W_0 + 3D}\delta_{H_3O^+} + \frac{D(1-\alpha)}{2W_0 + 3D}\delta_{H\text{-}Y}$$

While hydronium ions should not have much effect on the relaxation time, they are the predominant influence on the chemical shift in aqueous acids. Hence, if one assumes that $\delta_{H_3O^+} \gg \delta_{H\text{-}Y}$, eq 12 becomes, approximately

$$\langle\delta\rangle = \frac{3\alpha\delta_{H_3O^+}}{2W_0 + 3D}D \qquad (12')$$

The curvature in Figure 10 is therefore attributed primarily to a decrease in the degree of dissociation, α, as the concentration of acidic sites increases, and this affects the relaxation time and chemical shift in opposite ways.

One can use either eq 11′ or 12′ to estimate the degree of ionization. The rigid lattice relaxation time of hydroxyl groups on NH_4^+-Y has been measured to be 42 μs,[17] which, taken together with the limiting slope and intercept ($T_{2w}^{-1} \simeq 100\ s^{-1}$) at $D \to 0$ in Figure 10, yields a value of $\alpha = 0.7$. A smaller value of $\alpha \simeq 0.4$ is obtained less reliably from the chemical shifts by estimating, on the basis of aqueous solution results, a value of $\delta_{H_3O^+} = 10$ ppm.[18] Either result implies that hydrogen-Y zeolite is a strong acid ($K_w \sim 13.7$).

Ionization is strongly suppressed at high cation deficiencies in spite of the buffer action one might normally expect from the anionic sites. This is accompanied by the broadening of the x-ray powder patterns, indicating that degradation of the framework occurs at cation deficiencies greater than ~16 per unit cell.

The cross exchange reaction between water and ammonium ions increases slightly with the cation deficiency, and hence is clearly not due to a base-catalyzed reaction. This confirms the conclusion reached on the basis of the $^{15}NH_4^+$ experiment in Figure 6; namely, that the mechanism involved is deammoniation coupled with fast exchange of the products with water. It is still not obvious why the slow step in this sequence, namely

$$NH_4^+ + Y^- \rightarrow NH_3 + H\text{-}Y$$

should be accelerated by a process which removes, to the extent $(1 - \alpha)D$, acceptor sites from the lattice. A clue to this question is found in the observation that partial dehydration of the zeolite by evacuation at room temperature also enhances the cross exchange between water and ammonium ions to the extent where coalescence of their NMR signals occurs. Removal of water therefore appears to accelerate the deammoniation step, as one might reasonably expect. Since the total water available in the partially decationized NH_4^+-Y^- samples in Table I is approximately $W_0 + D$, and decationization produces hydrogen ions to the extent αD, then the effective hydration of ammonium ions will decrease with increasing D provided $n\alpha > 1 + W_0/A \simeq 4.3$ where n is the hydration number of the proton. One possible explanation of the increased cross exchange rate is, therefore, that the hydronium ion is more strongly and extensively hydrated than the ammonium ion. This would require again that α be in the range of strong acids ($\alpha \to 1$), since this has the dual effect of effectively dehydrating the system and maintaining the number of lattice acceptor sites. These observations exemplify the difficulty in separating the dehydration and deammoniation steps in ammonium-exchanged zeolites, since the removal of water itself tends to displace reaction 3 to the right. Indeed, simple room temperature evacuation of NH_4^+-Y^- zeolites produces cation deficiencies of one to two atoms per unit cell. Direct evidence for the high temperature hydrolysis of Na-Y was observed in Figure 2, and the deammoniation reaction 3 is the counterpart of this reaction in NH_4^+-Y^- at room temperature.

Acknowledgment. We thank Dr. Jacob Schaefer for his detailed drawings of sample spinner turbine and comments on its use.

References and Notes

(1) H. A. Resing and J. K. Thompson, *J. Chem. Phys.*, **46**, 2876 (1967).
(2) L. E. Drain, *Proc. Phys. Soc.*, **80**, 1380 (1962).
(3) G. M. Muha and D. J. C. Yates, *J. Chem. Phys.*, **49**, 5073 (1968).
(4) N. Bloembergen, E. M. Purcell, and R. V. Pound, *Phys. Rev.*, **73**, 679 (1948).
(5) A. Abragam, "The Principles of Nuclear Magnetism", Oxford University Press, London, 1961, Chapter X.
(6) G. E. Walrafen, *J. Chem. Phys.*, **44**, 1546 (1966).
(7) A. Lowenstein and A. Szoke, *J. Am. Chem. Soc.*, **84**, 1151 (1962).
(8) E. Reidel, J. Karger, and H. Winkler, *Z. Phys. Chem. (Leipzig)*, **252**, 161 (1973).
(9) D. Doskocilova and B. Schneider, *Macromolecules*, **5**, 125 (1972).
(10) E. R. Andrew, A. Bradbury, and R. G. Eades, *Nature (London)*, **183**, 1802 (1959).
(11) E. D. Stejskal, J. Schaefer, J. M. S. Henis, and M. K. Tripodi, *J. Chem. Phys.*, **61**, 2351 (1974).
(12) H. M. McConnell and D. D. Thompson, *J. Chem. Phys.*, **31**, 85 (1959).
(13) R. A. Hoffman, B. Gestblom, and S. Forsén, *J. Chem. Phys.*, **40**, 3734 (1964).
(14) E. W. Randall, in "Nitrogen NMR", M. Witanowski and G. A. Webb, Ed., Plenum Press, New York, N.Y., 1973, p 64.
(15) H. M. McConnell, *J. Chem. Phys.*, **28**, 430 (1958).
(16) H. S. Gutowsky, D. W. McCall, and C. P. Slichter, *J. Chem. Phys.*, **21**, 279 (1953).
(17) M. M. Mestdagh, W. E. Stone, and J. J. Fripiat, *J. Phys. Chem.*, **76**, 1220 (1972).
(18) G. C. Hood, O. Redlich, and C. A. Reilly, *J. Chem. Phys.*, **22**, 2067 (1954).
(19) The zeolite samples used in this study were specially prepared from reagent grade materials in all-glass systems to eliminate complications from magnetic impurities. The unit-cell composition according to chemical analysis is $M_{56}(AlO_2)_{56}(SiO_2)_{133}$. R. J. Bishop and G. W. Skeels provided the source materials for this study.

Longitudinal Relaxation in Spin 7/2 Systems. Frequency Dependence of Lanthanum-139 Relaxation Times in Protein Solutions as a Method of Studying Macromolecular Dynamics

Jacques Reuben* and Zeev Luz

Isotope Department, Weizmann Institute of Science, Rehovot, Israel *(Received October 9, 1975)*

A matrix for the longitudinal relaxation in spin 7/2 systems is derived and solved numerically. The numerical solution is approximated by an analytical expression which is used in the interpretation of lanthanum-139 relaxation times in dilute solutions of bovine serum albumin (BSA). The protein induces frequency dependent enhancements in the ^{139}La relaxation rate through the rapid exchange of La^{3+} between its aquo and BSA complexes. The La^{3+} ions associate with the free carboxylates of the protein and as a result the quadrupole coupling constant of ^{139}La is increased. In the BSA complex the interaction between the electric field gradient on the ^{139}La nucleus and the quadrupole moment is modulated by the isotropic rotational motion of the protein molecule which is characterized by a correlation time $\tau_c = 3.7 \times 10^{-8}$ s. The dissociation constant of the La^{3+}–BSA complex is $K_D = 0.46$ M and its mean lifetime is bracketted: 3.7×10^{-8} s $< \tau_M < 2.1 \times 10^{-6}$ s.

Introduction

It has recently been suggested that nuclear relaxation rates of lanthanum-139 can be used to study the molecular dynamics of proteins in solution.[1] In this communication we present results of the application of the method to aqueous solutions of bovine serum albumin (BSA) and provide a detailed analysis of the ^{139}La longitudinal relaxation times in terms of the La^{3+}–protein binding equilibrium and the rotational diffusion of the macromolecular complex.

Lanthanum-139 (natural abundance 99.9%) is a nucleus of spin $I = 7/2$. In diamagnetic systems its dominant nuclear relaxation mechanism is the modulation of the nuclear quadrupole interaction by molecular motion. In solutions of La^{3+} salts where the cation is symmetrically solvated by the solvent molecules the relaxation rate is relatively slow because of the small quadrupole interaction and also the short correlation times modulating the quadrupole interaction in these systems. Upon complex formation, e.g., ion pairing or binding to proteins, the asymmetric environment of the La^{3+} ions gives rise to an increase in the quadrupole coupling constant and usually also to longer correlation times. As a result there is a considerable increase in the ^{139}La nuclear relaxation rate.[1,2] Thus by studying the effect of complexing agents on the ^{139}La relaxation rate and comparison with theoretical prediction, information on both the binding equilibria of the La^{3+} ions as well as on the molecular dynamics of their complexes may be obtained.

In the theoretical section below we derive expressions for the longitudinal relaxation rate of a spin $I = 7/2$ system by modulation of the quadrupole interaction. It is shown that the longitudinal relaxation rate can be expressed (to a good approximation) in terms of a single exponent over the whole range of the relaxation theory and an approximate analytical expression is derived for T_1 in a convenient form. This expression is then used in the analysis of the frequency dependence of the ^{139}La relaxation rates in BSA solutions. The binding sites for the La^{3+} ions are believed to be free carboxylates of the BSA molecules. In order to obtain an estimate for their number as well as for the value of the quadrupole coupling constant, the effect of acetate ions on the ^{139}La relaxation rates was studied.

Relaxation Theory for Spin 7/2 Systems

In this section we derive expressions for the longitudinal relaxation of a nucleus of spin $I = 7/2$ by modulation of the quadrupole interaction using Redfield's theory. The corresponding derivation of the transverse relaxation (for the equivalent case of the zero field splitting interaction) was discussed previously and used in the interpretation of electron spin resonance spectra of Gd^{3+} complexes in solution.[3-5]

The quadrupole Hamiltonian can be written as a direct product of the irreducible second rank tensor operators, T^{2p}, of the spin part and F^{2p}, of the spatial part:

$$H_Q = \sum_{p=-2}^{2} (-)^p F^{2p} T^{2-p} \tag{1}$$

The components of the tensors in their corresponding principal coordinate systems [laboratory fixed for T^{2p} and molecule fixed (F'^{2p}) for F^{2p}] are summarized in Table I where

$$A = \frac{e^2qQ}{4I(2I-1)} = \frac{1}{84} e^2qQ \qquad (\text{for } I = 7/2) \tag{2}$$

and η is the asymmetry parameter of the quadrupole interaction. The longitudinal relaxation behavior of the spin system is obtained from the so-called relaxation matrix, the elements of which in the basis of the M_I spin state a,b are

$$R_{aabb} = 2J_{abab}/\hbar^2 \qquad a \neq b \tag{3a}$$

$$P_{aaaa} = -\sum_{b \neq a} R_{aabb} \tag{3b}$$

The spectral densities for rotational diffusion are

$$J_{abab} = \frac{1}{5} j[(a-b)\omega_0] \sum_p |\langle a|T^{2-p}|b\rangle|^2 \sum_q (F'^{2q}) \tag{4}$$

$$= \frac{\Delta^2}{5} j[(a-b)\omega_0] \sum_p |\langle a|T^{2-p}|b\rangle|^2 \tag{5}$$

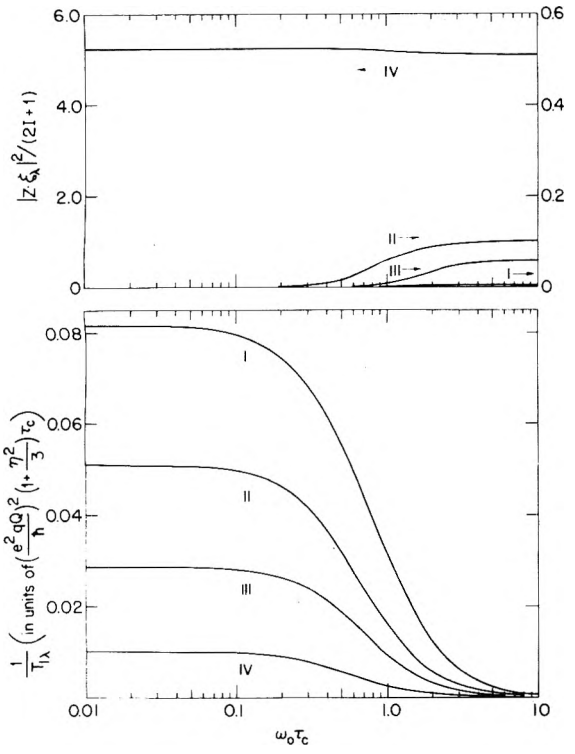

Figure 1. Plots of the longitudinal relaxation rates, $1/T_{1\lambda}$, in units of $(e^2qQ/\hbar)^2[1 + (\eta^2/3)]\tau_c$, and of the corresponding amplitudes, as function of $\omega_0\tau_c$ for $I = 7/2$. The plots were calculated from the relaxation matrix as explained in the text. Note that the amplitudes for lines I, II, and III are plotted on an expanded vertical scale.

where

$$\Delta^2 = 6A^2\left(1 + \frac{\eta^2}{3}\right) = \frac{1}{1176}(e^2qQ)^2\left(1 + \frac{\eta^2}{3}\right) \qquad (6)$$

$$j[(a-b)\omega_0] = \frac{\tau_c}{1 + [(a-b)\omega_0]^2\tau_c{}^2},$$

and ω_0 and τ_c are respectively the Larmor frequency and the correlation time for the rotational diffusion. With these definitions relaxation matrix I is derived where

$$A = 21j(\omega_0) \qquad \alpha = 7j(2\omega_0)$$
$$B = 16j(\omega_0) \qquad \beta = 15j(2\omega_0)$$
$$C = 5j(\omega_0) \qquad \gamma = 20j(2\omega_0)$$

The decay of the longitudinal magnetization consists of a superposition of a number of exponentially decaying functions, the relaxation rates of which, $1/T_{1\lambda}$, are the eigenvalues of the relaxation matrix, and their amplitudes are proportional to

$$|\mathbf{Z}\cdot\xi_\lambda|^2/(2I+1) \qquad (7)$$

TABLE I

p	$F^{\prime 2p}$	T^{2p}
0	$\sqrt{6}A$	$\frac{1}{\sqrt{6}}[3I_z{}^2 - I(I+1)]$
±1	0	$\mp\frac{1}{2}(I_\pm I_z + I_z I_\pm)$
±2	ηA	$\frac{1}{2}(I_\pm)^2$

where ξ_λ is the eigenvector corresponding to the eigenvalue $1/T_{1\lambda}$, and $\mathbf{Z}$ is a vector with components $\langle a|M_z|a\rangle$. In the present case the longitudinal relaxation is given by four decaying functions; the amplitudes of the four other eigenvalues vanish. This can be seen by noting that the 8×8 relaxation matrix can be transformed into two uncoupled matrices (II) corresponding to the basis $[M_I + (-M_I)]$ and $[M_I - (-M_I)]$, where the upper and lower sign correspond to the symmetric and antisymmetric basis functions, respectively. The required relaxation times and amplitudes can be obtained directly by diagonalizing the 4×4 matrix of the antisymmetric basis set.

$$\frac{24\Delta^2}{\hbar^2}\times\begin{vmatrix} A+\alpha & -A & -\alpha & 0 \\ -A & A+B+\beta & -B & -\beta \\ -\alpha & -B & B+C+\alpha+\gamma & -C\mp\gamma \\ 0 & -\beta & -C\mp\gamma & C+\beta+\gamma \end{vmatrix} \qquad \text{(II)}$$

The results for the various $1/T_{1\lambda}$'s and the corresponding amplitudes are plotted in Figure 1 as functions of the parameter $\omega_0\tau_c$. It is seen that three of these functions have very small amplitudes and are negligible over the whole $\omega_0\tau_c$ range. Thus in practice we expect the magnetization to decay with a single exponent, corresponding to line IV in Figure 1. There is no analytical expression for this curve (except when $\omega_0\tau_c \ll 1$) but it is almost identical with the "average longitudinal relaxation rate" $\langle 1/T_1\rangle$ defined by McLachlan[6] and for which an analytical expression does exist:

$$\left\langle\frac{1}{T_1}\right\rangle = \sum_\lambda \frac{3|\mathbf{Z}\cdot\xi_\lambda|^2}{I(I+1)(2I+1)}\frac{1}{T_{1\lambda}} = \frac{2}{50}\Delta^2[4I(I+1)-3][j(\omega_0) + 4j(2\omega_0)] = \frac{1}{490}\left[\frac{1}{1+(\omega_0\tau_c)^2} + \frac{4}{1+(2\omega_0\tau_c)^2}\right] \times \left(\frac{e^2qQ}{\hbar}\right)^2\left(1+\frac{\eta^2}{3}\right)\tau_c = \frac{12}{5}\left[\frac{1}{1+(\omega_0\tau_c)^2} + \frac{4}{1+(2\omega_0\tau_c)^2}\right]\left(\frac{\Delta}{\hbar}\right)^2\tau_c \qquad (8)$$

This function is plotted in the lower part of Figure 2. As can be seen it is practically identical with line IV of Figure 1.

$$\frac{24\Delta^2}{\hbar^2}\times\begin{vmatrix} A+\alpha & -A & -\alpha & & & & & \\ -A & A+B+\beta & -B & -\beta & & & & \\ -\alpha & -B & B+C+\alpha+\gamma & -C & -\gamma & & & \\ & -\beta & -C & C+\beta+\gamma & 0 & -\gamma & & \\ & & -\gamma & 0 & C+\beta+\gamma & -C & -\beta & \\ & & & -\gamma & -C & B+C+\alpha+\gamma & -B & -\alpha \\ & & & & \beta & -B & A+B+\beta & -A \\ & & & & & -\alpha & -A & A+\alpha \end{vmatrix} \qquad \text{(I)}$$

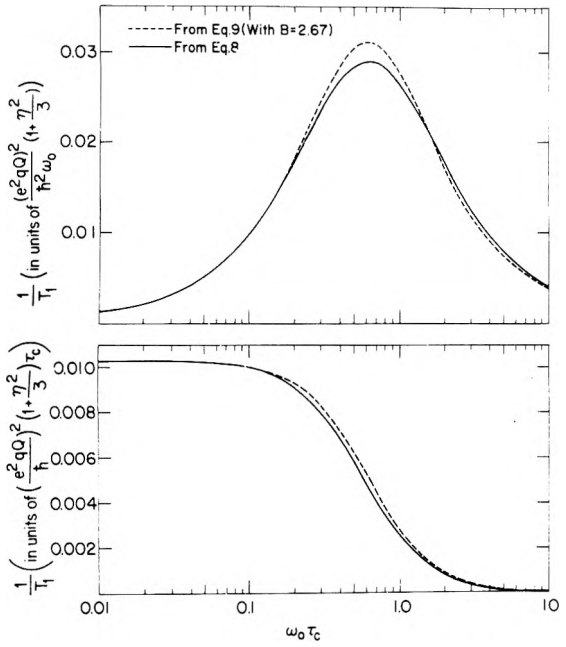

Figure 2. Bottom: as in Figure 1 for the average $\langle 1/T_1 \rangle$ (eq 8) and the "best fit" equation (eq 9). Top: $1/T_1$ from eq 8 and 9 in units of $(e^2qQ/\hbar)^2[1 + (\eta^2/3)]/\omega_0$.

For practical application of relaxation results it is often convenient to express the frequency dependence of the relaxation rate in terms of a single dispersion step. In our analysis we have used the approximate equation:

$$\frac{1}{T_1} = \frac{1}{490}\frac{5}{1 + B(\omega_0\tau_c)^2}\left(\frac{e^2qQ}{\hbar}\right)^2\left(1 + \frac{\eta^2}{3}\right)\tau_c$$

$$= 12\left(\frac{\Delta}{\hbar}\right)^2\frac{\tau}{1 + B(\omega_0\tau_c)^2} = \frac{C\tau_c}{1 + B(\omega_0\tau_c)^2} \quad (9)$$

with $B = 2.67$, where the value of B was obtained by best fitting eq 9 to eq 8 in the region $0.1 < \omega_0\tau_c < 2.0$. This function is compared with that calculated from eq 8 in Figure 2, where the similarity of both curves is clearly demonstrated. Note also that all of the three functions (i.e., line IV and eq 8 and 9) approach the classical expression for quadrupole relaxation in the limit $\omega_0\tau_c \to 0$:[7]

$$\frac{1}{T_1} = \frac{1}{98}\left(\frac{e^2qQ}{\hbar}\right)^2\left(1 + \frac{\eta^2}{3}\right)\tau_c = C\tau_c \quad (10)$$

Finally we note that the representation of the relaxation rate in units of $(e^2qQ/\hbar)^2[1 + (\eta^2/3)]\tau_c$ (lower part of Figure 2) is convenient for studies of the frequency dependence (dispersion behavior) at fixed correlation times (fixed temperatures). For studies at fixed frequency but varying temperatures, where a T_1 minimum is often sought, it is more convenient to plot $1/T_1$ in units which are independent of τ_c. This we do in the upper part of Figure 2 for the functions corresponding to eq 8 and 9. Both curves predict a T_1 minimum at $\omega_0\tau_c \simeq 0.62$ and at this point the predicted values of $1/T_1$ for the two curves differ by approximately 10%, corresponding to about 3% difference in e^2qQ/h.

The expressions derived above for the quadrupole relaxation of a nuclear spin $I = 7/2$ are, of course, also applicable for electron spin relaxation by modulation of the quadratic zero fluid splitting interaction for $S = 7/2$, e.g., Gd^{3+}.

Experimental Section

Relaxation times were measured at the ambient probe temperature of 23 ± 2 °C with a Bruker 322S pulsed NMR spectrometer as previously described.[1,2] Most of the measurements were done with a constant $LaCl_3$ concentration of 0.4 M with the BSA concentration varying up to 3.75 mg/ml. Crystallized and lyophilized BSA was a product of Sigma Chemical Co. Its concentration was determined from the absorbance at 280 mμ using 0.66 as the absorbance of 1 mg ml^{-1} cm^{-1} and a molecular weight of 69 000.[8] Treatment of the BSA stock solutions with Chelex (Bio-Rad Labs.), which effectively removes metal ions from the solution, did not affect the results and therefore most of the experiments were carried out using the untreated protein. All solutions were freshly prepared before each run and were made in 50 mM MES[9] buffer at pH 6.2. The presence of the buffer did not alter the T_1 values of ^{139}La.

Results and Discussion

The effect of added BSA on the longitudinal relaxation of ^{139}La was measured in the frequency range 4.2–8.4 MHz. Typical results are shown in Figure 3. The quantity plotted, $1/T_{1p}$, is defined as

$$1/T_{1p} = 1/T_1 - 1/T_1^0 \quad (11)$$

where $1/T_1^0$ is the relaxation rate in the absence of protein. Measurements were also done at a constant BSA concentration and varying $LaCl_3$ concentrations at 8.4 MHz. The T_{1p} values are presented in Figure 4. There are three important features on the basis of which we interpret the results in terms of the binding equilibrium and the dynamics of the La^{3+}–protein complex. (i) At constant $LaCl_3$ concentration the relaxation rate is linear with the BSA concentration. (ii) At constant BSA concentration the relaxation *time*, T_{1p}, is linear with the $LaCl_3$ concentration with a nonzero intercept. (iii) The relaxation rate, $1/T_{1p}$, depends strongly on the frequency, whereas in the absence of BSA, $1/T_1^0$ is frequency independent.[1] These features indicate that the La^{3+} ions are partly complexed to the protein molecules, where their relaxation rate is significantly enhanced, and that there is fast exchange between the solvated and complexed forms. Under these conditions, $1/T_{1p}$ is given by

$$\frac{1}{T_{1p}} = \frac{P_M}{T_{1b}} = \frac{n[P_t]}{K_D + [M_t]}\frac{1}{T_{1b}} \quad (12)$$

where T_{1b} is the relaxation time in the bound state, P_M is the fraction of bound La^{3+} ions, $P_M = [M_b]/[M_t]$, $[P_t]$ is the total protein concentration, n is the number of binding sites per protein molecule, and K_D is the dissociation constant:

$$K_D = \frac{[M_f](n[P_t] - [M_b])}{[M_b]} \approx \frac{[M_t](n[P_t] - [M_b])}{[M_b]} \quad (13)$$

and we have assumed that the complexing sites are independent. In eq 13 we have used the fact that in all solutions studied the concentration of protein binding sites was much less than the concentration of $LaCl_3$, thus $[M_f] \sim [M_t]$. Equation 12 shows that $1/T_{1p}$ should be linear with total protein concentration but that the dependence on the La^{3+} concentration depends on the magnitude of K_D. If the dissociation constant is small (strong complexing), $1/T_{1p}$ is inversely proportional to $[M_t]$, $1/T_{1p} = n[P_t]/(T_{1b}[M_t])$; whereas when K_D is large (weak complexing) $1/T_{1p} = n[P_t]/(T_{1b}K_D)$, i.e., independent of $[M_t]$. In both these extreme cases the parameters of interest K_D, n, and $1/T_{1b}$ cannot be extracted separately from the experimental results. However, when $K_D \sim [M_f]$, K_D may be obtained by a suitable plot of eq 12:

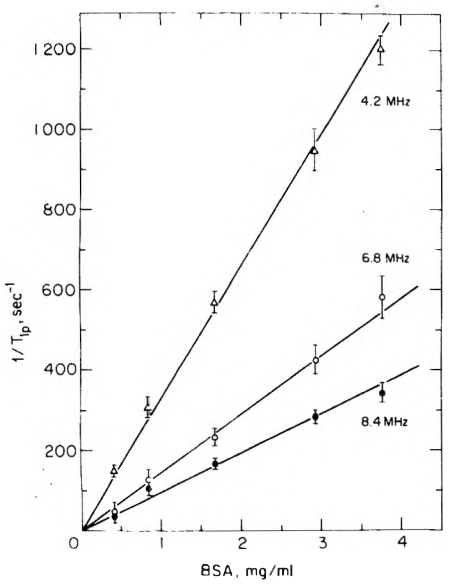

Figure 3. The increment in the longitudinal relaxation rate, $1/T_{1p}$, of ^{139}La in 0.4 M solutions of $LaCl_3$ as a function of BSA concentration at different resonance frequencies.

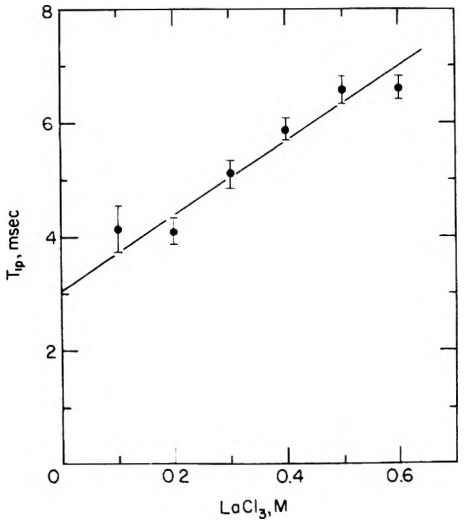

Figure 4. The relaxation time, T_{1p}, of ^{139}La as a function of the $LaCl_3$ concentration in solutions containing a constant concentration (1.11 mg/ml) of BSA.

$$T_{1p} = \frac{K_D T_{1b}}{n[P_t]} + \frac{[M_t]T_{1b}}{n[P_t]} \tag{14}$$

From the plot on Figure 4, we obtain $K_D = 0.46$ M, $n/T_{1b} = 9.4 \times 10^6$ s^{-1}. It is clear from the relatively large apparent dissociation constant of the La^{3+}–BSA complex that the binding is nonspecific. For the specific binding of another member of the lanthanide series, Gd^{3+}, a dissociation constant of the order of 10^{-4} M has been reported.[10] The most likely locale for the binding of La^{3+} to BSA is the ionized carboxyl groups. Bovine serum albumin has about 100 free carboxyl groups, and it has been shown that virtually all of them interact with metal ions.[11-14] The apparent dissociation constant obtained in the present work is for relatively high saturation of the protein binding sites due to the high $LaCl_3$ concentrations employed. For the related case of the Co^{2+}–BSA complex it was found that the dissociation constant increased with increasing saturation of the binding sites[14] as would be expected for the interaction of cations with negatively charged spherical macromolecules with the net charge spread uniformly over their surface.[15]

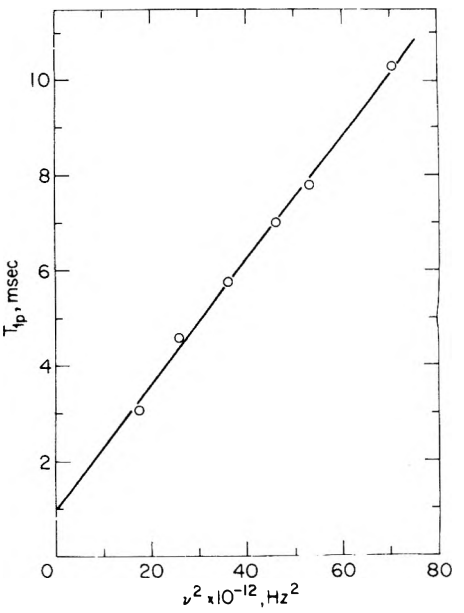

Figure 5. The relaxation time, T_{1p}, of ^{139}La in 0.4 M solutions of $LaCl_3$ and 1 mg/ml of BSA as a function of the square of the resonance frequency.

We next consider the frequency dependence of $1/T_{1p}$, which reflects the fact that the longitudinal relaxation in the bound state falls in the dispersion region $\omega_0\tau_c > 1$. Substituting eq 9 into eq 12 and inverting gives

$$T_{1p} = \frac{2.67\omega_0^2\tau_c}{P_M C} + \frac{1}{P_M C \tau_c} \tag{15}$$

Thus a plot of the inverse slopes of lines such as those given in Figure 3 vs. ω_0^2 should be linear and from its slope and intercept the correlation time, τ_c, can be obtained. Such a plot is shown in Figure 5. It is almost perfectly linear with intercept and slope of 0.93×10^{-3} s and 3.3×10^{-18} s^3, respectively, from which $\tau_c = 3.7 \times 10^{-8}$ s is calculated. This value is in excellent agreement with the correlation time for the isotropic rotation of BSA obtained by other methods: 4.0×10^{-8} from deuterium quadrupole relaxation[16] and 4.17×10^{-8} s from fluorescence polarization.[17] Thus the correlation time, τ_c, found for the La^{3+}–BSA complex can be identified with the rotational tumbling time, τ_R, of the protein. Since the correlation time for quadrupole relaxation is in general the sum of two contributions[18]

$$\frac{1}{\tau_c} = \frac{1}{\tau_R} + \frac{1}{\tau_M} \tag{16}$$

where τ_M is the mean lifetime of the La^{3+}–protein complex, the above value of τ_c places a lower limit of 3.7×10^{-8} s for τ_M. We show below that τ_M can also be given an upper limit based on the fast exchange condition for the La^{3+} ions.

In order to obtain more information on the La^{3+}–protein complex we need to separate the ratio n/T_{1b} into its constituents. These quantities appear always in this form in the relaxation experiments and cannot be separated without further assumptions. As indicated above, the most likely site for the association of the lanthanum ions with BSA are the free carboxylates on the protein molecule. It has been found, e.g., that the spectral changes produced by BSA in the absorption

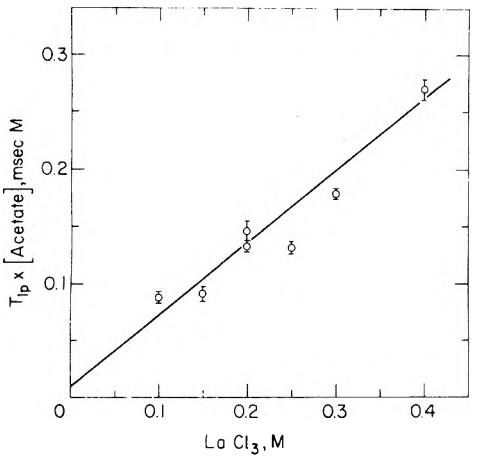

Figure 6. The product of the relaxation time, T_{1p}, of ^{139}La and the acetate concentration as a function of the $LaCl_3$ concentration.

spectrum of Nd^{3+} are reproduced by a variety of simple carboxylates.[19] We therefore make the assumption that the quadrupole interaction of ^{139}La in the protein complex is similar to that in its complexes with simple carboxylates and proceed to determine its value in the case of the acetate complex. Relaxation times of ^{139}La in solutions containing 10 or 20 mM lithium acetate with $LaCl_3$ concentrations ranging from 0.1 to 0.4 M were measured at 8.4 MHz. The results of T_{1p} are plotted vs. the $LaCl_3$ concentration in Figure 6 and the same analysis as that described for the protein case was applied (cf. eq 14). Since in this case $n = 1$, the dissociation constant and $1/T_{1b}$ (acetate) can be directly obtained: K_D = 14 mM, $1/T_{1b} = 1580\ s^{-1}$. The result for K_D, although subject to large uncertainty due to the small intercept, may be compared with the values 8.55 and 27.4 mM reported for the monoacetato complex of La^{3+} at ionic strength of 0.1 and 2.0 M, respectively.[20,21] Using eq 9 we can now estimate the quadrupole coupling constant for the acetato complex by assuming a value for τ_c. With $\tau_c = 7 \times 10^{-11}$, a value previously determined for small lanthanide complexes,[10] we obtain $e^2qQ/h = 7.5$ MHz. Inserting this value and that of τ_c determined above for the BSA–La^{3+} complex in eq 9 the relaxation rate $1/T_{1b}$ for the latter complex at 8.4 MHz is calculated to be $7.63 \times 10^4\ s^{-1}$ and comparison with the experimental value for n/T_{1b} at the same frequency gives $n = 124$, in good agreement with the number of free carboxyl groups determined by independent methods.[11,13] It thus seems that all of the free carboxyl groups in the BSA molecule are available for La^{3+} binding.

Finally, we note that the assumption of fast exchange sets an upper limit for $\tau_M \leq T_{1b}$. Taking the value of T_{1b} extrapolated to zero frequency gives 2.1×10^{-6} s. Thus the mean lifetime of the La^{3+}–BSA complex is bracketted $3.7 \times 10^{-8} < \tau_M < 2.1 \times 10^{-6}$ s.

The present results indicate that the trivalent lanthanum cations associate weakly with virtually all of the free carboxylates of bovine serum albumin. This interaction appears to be nonselective and it is therefore likely that such La^{3+} binding will be general to all proteins. Complex formation with the protein has a twofold effect on the ^{139}La nucleus: the quadrupole coupling constant increases and the rotational diffusion rate slows down, thereby bringing the system into the region where $\omega_0\tau_c \geq 1$. As a result the longitudinal relaxation rate of ^{139}La increases and becomes frequency dependent. The frequency dependence can thus be used as a method of determining rotational correlation times of La^{3+}–protein complexes. Lanthanides are now used as spectroscopic probes in studies of biological macromolecules[22] and often the rotational correlation time is an essential parameter for the data interpretation.

The expression for the longitudinal relaxation behavior of a spin 7/2 system derived in this paper can, of course, be used for other $I = 7/2$ nuclei, among which one finds calcium-43, scandium-45, and cesium-133. The same theory also applies to the electron spin relaxation by modulation of the quadratic zero-field splitting interaction in $S = 7/2$ systems, e.g., gadolinium(III) complexes.

Acknowledgments. The technical assistance of Naomi Baumann and the help of Amikam Reuveni with some of the computations are gratefully acknowledged. This work was supported in part by a grant from the United States–Israel Binational Science Foundation.

References and Notes

(1) J. Reuben, *J. Am. Chem. Soc.*, **97**, 3823 (1975).
(2) J. Reuben, *J. Phys. Chem.*, **79**, 2154 (1975).
(3) A. Hudson and J. W. E. Lewis, *Trans. Faraday Soc.*, **66**, 1297 (1970).
(4) R. Poupko, A. Baram, and Z. Luz, *Mol. Phys.*, **27**, 1345 (1974).
(5) J. Reuben, *J. Phys. Chem.*, **75**, 3164 (1971).
(6) A. D. McLachlan, *Proc. Roy. Soc. London, Ser. A*, **280**, 27 (1964).
(7) A. Abragam, "The Principles of Nuclear Magnetism", Oxford University Press, London, 1961.
(8) E. J. Cohn, W. L. Hughes, Jr., and J. H. Weare, *J. Am. Chem. Soc.*, **69**, 1753 (1947).
(9) MES is 2[*N*-morpholino]ethanesulfonic acid. It was neutralized to pH 6.2 with tetramethylammonium hydroxide.
(10) J. Reuben, *Biochemistry*, **10**, 2834 (1971).
(11) F. R. N. Gurd and G. R. Murray, Jr., *J. Am. Chem. Soc.*, **76**, 187 (1954).
(12) M. S. N. Rao and H. Lal, *J. Am. Chem. Soc.*, **76**, 4867 (1954).
(13) H. Lal and M. S. N. Rao, *J. Am. Chem. Soc.*, **79**, 3050 (1957).
(14) M. S. N. Rao and H. Lal, *J. Am. Chem. Soc.*, **80**, 3226 (1958).
(15) G. Scatchard, *Ann. N.Y. Acad. Sci.*, **51**, 660 (1949).
(16) J. Andrasko and S. Forsén, *Chem. Scripta*, **6**, 163 (1974).
(17) P. Wahl, *C. R. Acad. Sci., Ser. D*, **263**, 1525 (1966).
(18) A. G. Marshall, *J. Chem. Phys.*, **52**, 2527 (1970).
(19) E. R. Birnbaum, J. E. Gomez, and D. W. Darnall, *J. Am. Chem. Soc.*, **92**, 5287 (1970).
(20) R. S. Kolat and J. E. Powell, *Inorg. Chem.*, **1**, 293 (1962).
(21) A. Sonesson, *Acta Chem. Scand.*, **12**, 165 (1958).
(22) For recent reviews cf. J. Reuben, *Naturwissenschaften*, **62**, 172 (1975); E. Nieboer, *Structure Bonding*, **22**, 1 (1975).

Electron Paramagnetic Resonance Spectrum of a Sea Shell. *Mytilus edulis*

Stuart C. Blanchard and N. Dennis Chasteen*

Department of Chemistry, University of New Hampshire, Durham, New Hampshire 03824 *(Received January 26, 1976)*

Publication costs assisted by the University of New Hampshire

The EPR spectra of the periostracum, the calcitic prismatic region, and the aragonitic nacre of the shell of the three layer bivalue *Mytilus edulis* were investigated. The organic periostracum exhibits a $g = 4.3$ signal due to high-spin Fe^{3+} in a low symmetry coordination environment and a $g = 2.0044 \pm 0.0002$ signal presumably due to a semiquinone or quinone radical. However, the Fe^{3+} signal can account for only a small fraction of the approximately 0.1% total iron by weight, in this tissue. The prismatic region exhibits a weak Fe^{3+} signal at $g = 4.3$ and strong Mn(II) lines arising from manganese substituted for calcium in the calcite lattice of the shell. Examination of the Mn(II) spectrum of an oriented section of the prismatic region reveals a high degree of structural organization with the principal axis of the zero field tensor paralleling the iridescent cross sectional striations (long axis of the prisms) which correspond to the c axis of the shell. Organic material remaining after decalcification of the prismatic region with HCl displays a radical signal, $g = 2.0022 \pm 0.0002$. The nacre exhibits the $g = 4.3$ Fe^{3+} signal and a doubled $g = 2.0044 \pm 0.0002$ radical signal. Oriented sections of the nacre have a very weak but anisotropic Mn(II) signal of unknown origin. The concentration of Mn(II) in the calcite of the prismatic region, as determined by EPR, correlates positively with the position of the animal above low tide. These results suggest that EPR might be useful in investigations of calcified tissue, particularly the exoskeletons of marine animals.

Introduction

The electron paramagnetic resonance (EPR) spectra of transition metal ions doped into synthetic minerals have been extensively investigated over the years;[1] these studies have been valuable in establishing crystal field effects on the electronic structure of metal ions in various ligand environments. However, the spectra of paramagnetic species naturally occurring in mineralized tissue have received little attention. In particular, the spectra due to radicals and transition metal ions found in the exoskeletons of marine organisms have not been examined. We have become interested in the possibility of using EPR spectroscopy to obtain information concerning the oxidation states and coordination environments of trace paramagnetic transition metals in calcified tissue.[2,3] It is not known whether these impurities occur in unusual environments or occupy specific lattice sites which possess symmetry relative to the external morphology or growth characteristics of marine shells. If they do, conceivably these paramagnetic metal ions could serve as probes of the microstructure of sea shells and other calcified tissue.

Metal ion speciation is an important aspect of modern analytical chemistry. The application of EPR to examine mineralized tissue could be of use in investigations of biomineralization processes and of biogeochemical cycling of trace elements as well as in other fields. We report here a model study of the EPR spectra of the shell of the edible blue mussel, *Mytilus edulis*.

Sea shells are composed of 97–99% $CaCO_3$ (calcite, aragonite, or vaterite) with lesser amounts of $MgCO_3$, $(Al,Fe)_2O_3$, SiO_2, $Ca_3P_2O_8$, $CaSO_4$, protein, and mucopolysaccharides.[4–6] In addition to these major and minor constituents, trace amounts of Sn, Mo, Mn, Cd, Ti, B, Pb, Au, Ag, Ni, Co, Bi, Cu, Sr, Rb, and As have also been found in varying amounts.[7,8]

Investigations of the structure of mollusk shells often reveal a highly ordered arrangement of organic and mineral components.[4] Tiny crystals are separated from one another by an organic matrix consisting of a protein with a keratin type structure and mucopolysaccharide which serves as a cement. It is generally believed that the organic matrix provides sites of nucleation for $CaCO_3$ crystals and dictates the type of crystalline polymorph that forms.[5,9]

The blue mussel is an example of a typical three-layer bivalve mollusk (Figure 1).[10] The outer layer of the shell or periostracum is largely composed of quinone tanned protein. The deep blue crystalline layer just beneath the periostracum is the prismatic region which contains unique anvil-like prisms of calcite.[10] Finally, the inner pearl-like nacreous layer consists of aragonite crystals arranged in neatly packed horizontal rows. In the crystalline portions of the shell, the individual crystallites are surrounded by matrix protein.[10] Biomineralization activity is centered in the extrapallial fluid and the mantle (Figure 1).[4] We have examined in some detail, the spectra of the individual components of the shell of *Mytilus*.

Experimental Section

EPR spectra were measured on a Varian E-9 spectrometer operating at X-band and 100-kHz magnetic field modulation. Oriented specimens were mounted on a quartz rod attached to a goniometer. A rectangular dual cavity was employed with Varian strong pitch, $g = 2.0028$, as a reference.

Samples of fresh Mytilus were collected on May 15, 1975, from five levels above low tide on the beach near Odiorne State Park, N.H., and labeled NR01–NR05. They were frozen until needed.

Single shells for Mn and Fe atomic absorption analysis were cleaned in 2.5% NaOH to remove the periostracum as previously described.[3] The periostracum was prepared for atomic absorption analysis by dissolving about 0.1 g in several milliliters of concentrated nitric acid with gentle heating. The solution was diluted to 25.0 ml with 1 N HCl. A 5.0-ml aliquot was removed and diluted to 25 ml with 1 N HCl for analysis. A Varian Techtron Model AA-3 spectrometer modified with AA-5 electronics was used for the atomic absorption analysis. Wavelengths (and slit widths) employed were 279.68 nm (100

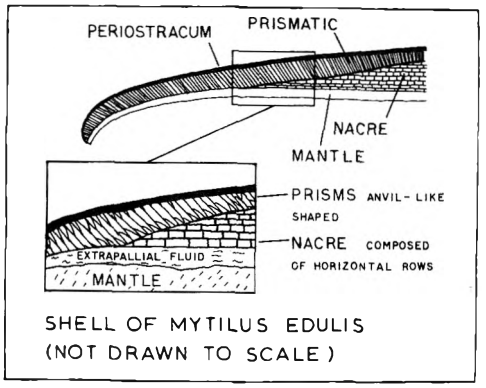

Figure 1. Schematic diagram of the shell structure, extrapallial fluid, and mantle for the edible blue mussel, *Mytilus edulis*.

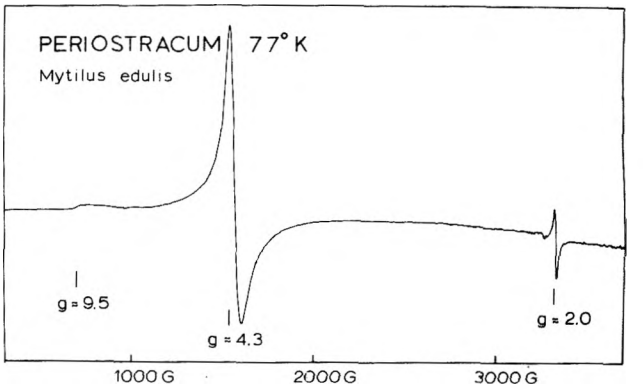

Figure 2. Liquid nitrogen temperature EPR spectrum of the periostracum of *Mytilus*.

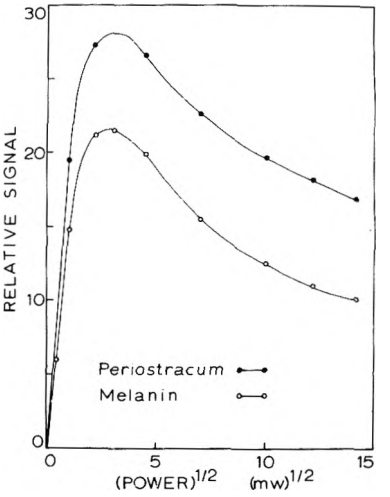

Figure 3. Room-temperature power saturation curves for the g = 2.0044 ± 0.0002 peak of the periostracum and the free radical melanin.

μ) and 248.33 nm (50 μ) for Mn and Fe, respectively. Additional details are given elsewhere.[3]

The prismatic and nacreous layers were separated by scraping or breaking off pieces from the shell. A particularly large specimen was used to obtain samples for the orientation studies. Sufficient quantities of periostracum for EPR and metal analyses were removed from about 12 shells by scraping and were dried for 10 min at 50 °C.

The mineral form of the calcium carbonate in several powdered samples was determined by x-ray diffraction on either a General Electric Model BR1 or a North American Phillips unit both using Cu Kα radiation.

Results and Discussion

A. *Periostracum.* The EPR spectrum of the organic periostracum at 77 K is shown in Figure 2. Two principal resonances occurring at g = 4.3 and g = 2.0 are observed. The sharp resonance near g = 2.0 is probably due to an organic radical since the room-temperature power saturation behavior is similar to that of other radicals such as melanin found in hair (Figure 3). The g value for the radical is 2.0044 ± 0.0002 with a peak-to-peak line width σ = 6.9 ± 0.2. For an older sample, g = 2.0047 with σ = 6.7 G was observed. Resonance lines with g values of 2.0046 were also observed for the periostracum of the Atlantic Ribbed Mussel *Vossella demissa* (σ = 9.2 G) and the Razor Clam, *Solen Viridis* (σ = 10.1 G). Quinone and semiquinone radicals which exhibit EPR signals are frequently associated with various pigments in living systems[11] and typically have g values in the range 2.0040 to 2.0050.[12] The values for the periostracum of various species are consistent with the belief that this material is composed in part of quinone tanned proteins.[13]

The resonance line near g = 4.3 (Figure 2) with σ = 70 G and the associated line at g = 9.5 are characteristic of high spin Fe^{3+} in a completely rhombic enivronment.[14,15] These signals are frequently observed with non-heme iron proteins.[14-16] At room temperature, the spin–lattice relaxation time, T_1, is considerably shorter and the iron signal is only 1/22 as intense as that at 77 K (Figure 2).

The iron signal can be adequately described by the S = 5/2 spin Hamiltonian

$$\mathcal{H} = D\left[S_z^2 - \frac{1}{3}S(S+1)\right] + E(S_x^2 - S_y^2) + g\beta\vec{H}\cdot\vec{S} \qquad (1)$$

in which D and E are the axial and rhombic components, respectively, of the zero field. In the situation giving rise to the g = 4.3 resonance E/D = 1/3.[14]

The total iron content of the periostracum was determined by atomic absorption to be 12 500 ppm. The high concentration of iron in the periostracum is probably indicative of an important role of iron in this tissue which has not been noted previously.[13,17] A semiquantitative determination of the spin concentration from the EPR spectrum indicates that the signal in Figure 2 accounts for less than 10% of the total iron in the sample, the remaining iron being EPR silent at 77 K. The lack of an EPR signal might be attributed to an unusual structure consisting of exchanged coupled Fe^{3+} ions or possibly Fe^{2+} ions which are difficult to observe by EPR.[1]

The intensity of the g = 4.3 resonance changes very little when the periostracum is soaked in six changes of 1% (w/v) *o*-phenanthroline, pH 4.5, over several days until no more of the reddish iron o-phenathroline complex is observed. Apparently, the iron responsible for the EPR signal binds tenaciously. However, the total iron content of the periostracum is significantly reduced to only 707 ppm, or 5.7% of the original value of 12 500 ppm. This indicates that the EPR silent iron is bound relatively weakly. Additional studies are clearly indicated.

B. *The Prismatic Region.* At 77 K, a g = 4.3 iron signal is also observed with the prismatic region although it is much less intense than observed for the periostracum. The iron content for this portion of the shell is typically only 20 to 50 ppm. In this case, the iron is probably coordinated to the matrix protein of the shell.

A singlet EPR signal was observed at $g = 2.0022 \pm 0.0002$ with $\sigma = 10.5$ G for the organic material obtained from a HCl decalcified section of the prismatic layer. The origin of this signal is not known; however, it is likely due to a free radical.

The $g = 2$ region of the spectrum of a powdered sample of the prismatic region is shown in Figure 4. The spectrum is typical of Mn^{2+} in carbonate minerals.[18] The prismatic region contains typically 10 ppm Mn. The six main lines arise from the coupling of the electron magnetic moment, $S = 5/2$, with the manganese nuclear moment, $I = 5/2$, for the $M_S = -1/2 \leftrightarrow +1/2$ transitions. The other transitions such as $M_S = +1/2 \leftrightarrow -3/2$ are very anisotropic and often difficult to observe with powdered samples. The weaker pairs of lines between the main lines are the so-called forbidden lines in which both electron and nuclear spin states change, i.e., $\Delta M_S = 1$ and $\Delta M_I = 1$ (strong field notation).[19]

As we shall see, the EPR data are consistent with Mn(II) substituted for Ca(II) in the calcite lattice of the prismatic region. Figure 5 shows the metal site of trigonal symmetry in the rhombohedral unit cell of calcite. The threefold axis is coincident with the crystallographic c axis.

The axially symmetric spin Hamiltonian without quartic terms in the electron spin is given by

$$\mathcal{H} = g_{\parallel}\beta H_z S_z + g_{\perp}\beta(H_x S_x + H_y S_y) + AS_z I_z + B(S_x I_x + S_y I_y) + D\left[S_z^2 - \frac{1}{3}S(S+1)\right] \quad (2)$$

where A and B are the parallel and perpendicular hyperfine constants, respectively.

The general equation for the resonance fields of allowed transitions in a strong magnetic field using perturbation theory to second order is given in the classic paper by Bleany.[20] Hurd et al.[21] have expanded this general equation by including a d' term required in the interpretation of spectra exhibiting large axial crystalline-field effects, and also include fourth-order terms. However, they omit the important third-order term later given by Bleany and Rubins.[22] The third-order term is given as the energy of the spin state. From the energy, we have evaluated the third-order contribution to the resonance field for the $M_S \rightarrow M_S - 1$ transition. When simplified, the result is in agreement with the third-order term given by Tsay et al.[23] for the $M_S = 1/2 \rightarrow -1/2$ transition. There has been some question as to the correctness of various terms in the equation for the resonance fields.[24]

The general equation, which we believe to be correct, including third-order terms is given below. The following conventions apply. (1) A, B, and D are defined to have negative values[19] and are expressed in gauss. Thus the $M_I = -5/2$ line for the Mn(II) spectrum is the low field line. (2) D has been substituted for $D/2$ in the terms taken from Hurd et al.[21] to be consistent with the nomenclature of later papers.

$$\begin{aligned} H(\theta) = H_0 &+ D(M_S - 1/2)[3(g_{\parallel}^2/g^2)\cos^2\theta - 1] \\ &+ (Dg_{\perp}g_{\parallel}\sin\theta\cos\theta/g^2)^2(1/2H_0)\{4S(S+1) \\ &- 24M_S(M_S-1) - 9\} - (Dg_{\perp}^2\sin^2\theta/g^2)(1/8H_0)\{2S(S+1) \\ &- 6M_S(M_S-1) - 3\} - d\{140M_S^3 - 210M_S^2 \\ &+ [190 - 60S(S+1)]M_S + 30S(S+1) \\ &- 60\}[35(g_{\parallel}\cos\theta/g)^4 - 30(g_{\parallel}\cos\theta/g)^2 + 3] + KM_I \\ &- [B^2(A^2+K^2)/K^2](1/4H_0)[I(I+1) - M_I^2 \\ &+ M_I(2M_S^2 - 1)] - (D^2AM_I)(1/8H_0^2)\{[6M_S(M_S-1) \\ &- 2S(S+1) + 3]\sin^4\theta + [3M_S(M_S-1) - 2S(S+1) \\ &- [S(S+1)]^2/[M_S(M_S-1)]]\sin^2 2\theta\} \end{aligned} \quad (3)$$

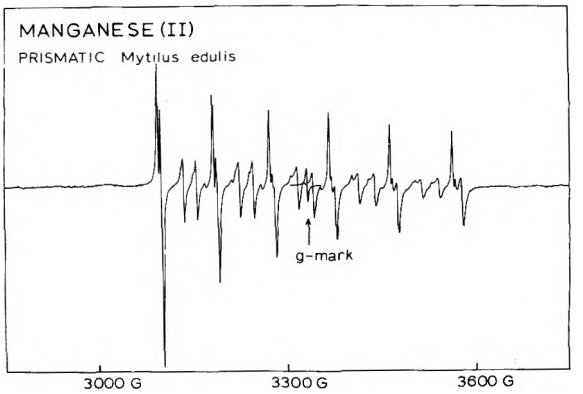

Figure 4. Room-temperature EPR spectrum of the $g = 2$ region for the powdered prismatic region of *Mytilus edulis*. At liquid nitrogen temperature a $g = 4.3$ resonance is observed.

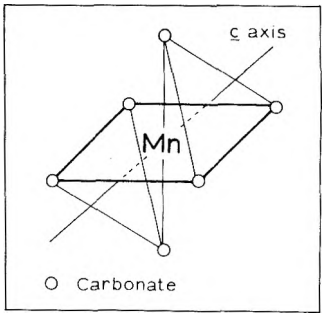

Figure 5. The Mn(II) site in a calcite lattice. O denotes oxygen atoms from different carbonate anions.

where

$$\begin{aligned} A' &= Ag_{\parallel}\beta \\ B' &= Bg_{\perp}\beta \\ K' &= 1/g[(A'g_{\parallel}\cos\theta)^2 + (B'g_{\perp}\sin\theta)^2]^{1/2} \\ K &= K'/g\beta \\ g &= [(g_{\parallel}\cos\theta)^2 + (g_{\perp}\sin\theta)^2]^{1/2} \\ \nu &= g_{\mathrm{mark}}\beta H_{\mathrm{mark}}/h \\ H_0 &= h\nu/g\beta \end{aligned} \quad (4)$$

Here h is Plank's constant and θ is the angle between the symmetry axis and the applied magnetic field.

Equation 3 is applicable to oriented samples. For powders, D can be obtained from the doubling of the $M_S = -1/2 \leftrightarrow 1/2$ hyperfine lines due to second and higher order terms in the perturbation equations. These lines are isotropic to first order. The complicated general equations describing these effects[22] can be reduced to

$$\delta H = (50D^2/9H_0)[1 - (55aM_I/9H_0] \quad (5)$$

for the Mn(II), $S = 5/2$, system under consideration. Here a is the hyperfine splitting measured from the powder spectrum. a and D are expressed in gauss and are taken to be negative.[19] The value of δH is usually taken from the $M_I = 5/2$ (high-field line) where the splitting of the doublet is maximum.

The spectrum in Figure 4 is characterized by $g = 2.0006 \pm 0.0002$, $a = -93.8 \pm 0.2$ G, and $D = -86.3 \pm 0.2$ G[25] from eq 5. These values are in reasonable agreement with those published for Mn(II) in calcite.[21]

We were particularly interested in establishing whether the

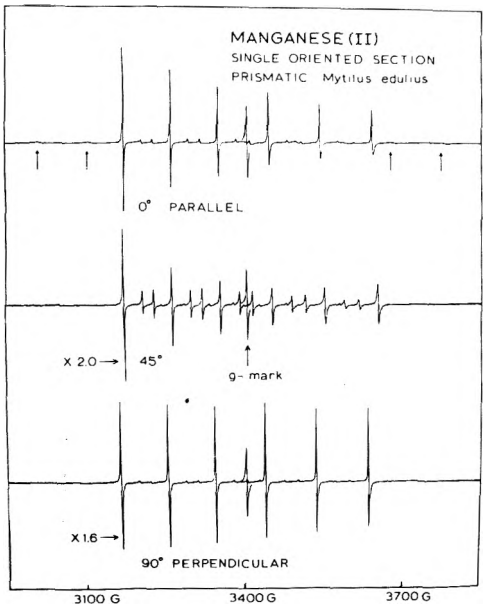

Figure 6. The Mn(II) spectrum at three angles for a single oriented section of the prismatic region of *Mytilus*.

Mn(II) EPR spectrum could be used to establish the degree of order of the individual crystallites of the shell. The long dimensions of the prisms in the prismatic layer are oriented with varying angles relative to the shell surface depending on the section of the shell (see Figure 1).[10] Because of the difficulty in doing electron microscopy and EPR spectroscopy on the same shell section, we attempted to estimate the orientation of the prisms from the shell color. Careful examination of the prismatic region of a shell from a large animal revealed iridescent striations which varied in angle with the shell surface in the same way as the long axis of the prisms in Figure 1. A section of the shell in which the striations made an angle of about 45° with the shell surface was chosen to search for any anisotropy in the EPR spectrum.

The shell section was mounted on a quartz rod such that the striations made an angle θ with the magnetic field vector. The spectrum as a function of angle is shown in Figure 6. The six main $M_S = -1/2 \leftrightarrow +1/2$ transitions are evident. The variation in the intensities of the forbidden lines with angle are similar to those found for Mn(II) in calcite.[19] Note that the forbidden lines gain intensity at the expense of the allowed lines. At certain orientations, other transitions which are very anisotropic such as $M_S = +1/2 \leftrightarrow -3/2$ can be seen (arrows in Figure 6). Unfortunately, these transitions could not be observed over a sufficiently large range of angles to permit their close examination.

The positions of the $M_I = 5/2$ line varies by about 16 G over the range of angles due to second- and third-order terms in D. The observed and computer calculated line positions using eq 3 are shown in Figure 7. In the calculation, we assume that the direction of the shell striations and the principal axis of the magnetic tensor (c crystallographic axis) are coincident. The calculation is for the parameters $g_\parallel = 1.9998 \pm 0.0002$, $g_\perp = 2.0004 \pm 0.0002$, $A = -94.1 \pm 0.2$ G, $B = -94.0 \pm 0.2$ G, and $D = -80.0 \pm 0.2$ G which were obtained from the spectrum to give the best overall fit to the observed line positions.

Travis[10] found through a lengthy electron microscopic and diffraction study that the c axis of the calcite crystallites paralled the long dimensions of the prisms in which they were located. She estimated that the prismatic region was composed of nearly 100% highly ordered crystalline calcite. The

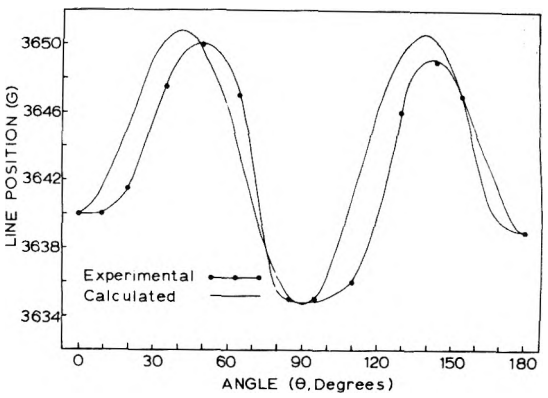

Figure 7. Variation in line position for the $M_I = +5/2$ Mn(II) line of the single oriented section of the prismatic region.

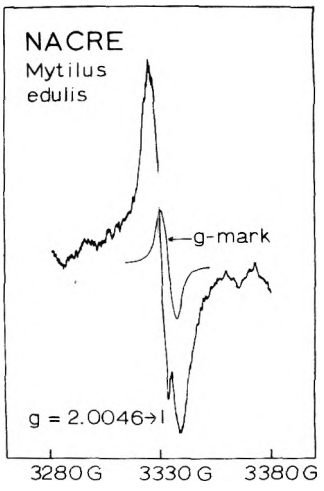

Figure 8. EPR spectrum showing the splitting of the $g = 2.0$ peak for the nacre.

good agreement between the observed and theoretical line positions (Figure 7) and the sharpness of the spectrum (Figure 6) are in accord with this.

Not all shells exhibit such a high degree of order as *Mytilus*. The common barnacle, *Balanus balanoides*, of which practically nothing is known about its shell structure, has been examined by EPR in a similar fashion.[26] The EPR spectrum indicates that only about 75% of the calcite microcrystallites possess any degree of order; the rest of the shell consists of polycrystalline substance in which much of the Mn(II) is in sites of low symmetry. In this case, the crystallographic c axis of the ordered calcite crystallites is normal to the shell surface.

C. *The Nacre.* The only clearly observed resonance for powdered samples of the nacreous layer was a relatively sharp line ($\sigma = 10$ G) at $g = 2.0044 \pm 0.0002$ shown in Figure 8. The doubling of the line suggests that two radical species are present. This resonance may be closely related to the $g = 2.0044$ radical observed for the periostracum. At liquid nitrogen temperature, a weak Fe(III) signal becomes visible at $g = 4.3$.

No Mn(II) spectrum was observed for the powdered nacreous layer at room temperature or liquid nitrogen temperature although the sample contained about 8 ppm Mn by atomic absorption spectroscopy. However, when an oriented section of the nacre is placed in the cavity, a weak anisotropic Mn(II) signal is observed (Figure 9). (The sloping baseline is due to Fe_2O_3, $g = 2.1$, trapped between the growth layers of the shell.) The EPR parameters $g = 2.0026$, $a = -95$ G, and

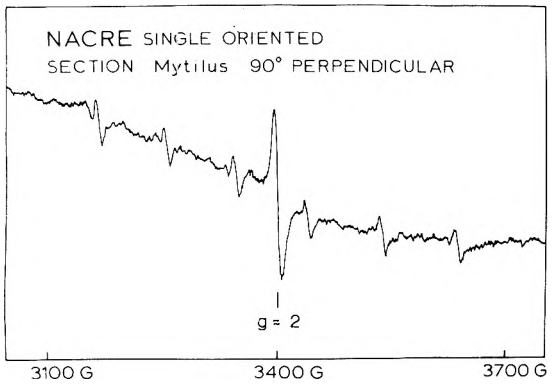

Figure 9. The EPR spectrum for a single oriented section of the nacre of *Mytilus*. The normal to the shell surface is perpendicular to the magnetic field vector.

$D = -80$ G are comparable to those for Mn(II) in various carbonate minerals.[18] We were not able to locate a perfect symmetry axis such that rotation about this axis produced an invariant spectrum, although the principal axis of the zero-field tensor appears to be roughly perpendicular to the underside of the shell. The metal site could have rhombic symmetry.

The nacre was shown by x-ray diffraction to be aragonite with no detectable calcite; thus the Mn spectrum is not due to Mn(II) in calcite (or calcite impurities in aragonite). However, the signal is not likely due to Mn(II) substituted for Ca(II) in aragonite either, since the signal is quite different from that which we have observed with aragonitic shells.[27] Its origin remains obscure.

When a powdered sample of the nacre is heated for 1 h at 600 °C above the transition temperature (520 °C) from aragonite to calcite, strong Mn(II) signals similar to those for the prismatic region were observed (Figure 4). X-ray diffraction confirmed the transition to calcite. It is not clear why most of the Mn(II) exhibits no EPR spectrum in the nacre of the unheated shell. Experiments at liquid helium temperature may prove useful.

D. *Correlation of the EPR Spectrum with Tidal Position.* The trace metal ion composition of marine shells is sometimes found to correlate with their environment.[28] Table I shows the results for the metal analysis for the prismatic region of *Mytilus* for five animals collected at different positions above low tide.

The concentration of Mn(II) substituted for Ca(II) in calcite (Table I) was determined by comparison with a standard sample and using the formula

$$\mathrm{Mn(II)_u} = \mathrm{Mn(II)_k}\frac{S_u}{\text{slope } (G_u W t_u)}\left(\frac{\sigma_u^2}{\sigma_k}\right) \qquad (6)$$

where S_u is the peak-to-peak first-derivative signal height of the unknown, G_u is the instrument gain setting, Wt_u is the weight of the unknown in the sample tubes, and slope is the slope of the plot of the signal height divided by the instrument gain vs. sample weight for the known sample. The known sample was a barnacle (RN002) with $\sigma_k = 8.30 \pm 0.02$ G for the $M_I = -5/2$ low-field line.[3] For the prismatic region of *Mytilus*, $\sigma_u = 7.68 \pm 0.02$ (Figure 4). Equation 6 assumes the same line shape function for both samples, which is reasonable. Precautions required in this type of analysis are detailed elsewhere.[3]

There appears to be no relationship between the *total Mn* by AA and the position of the animal in the intertidal zone (Table I). However, there is a strong positive correlation (coeff

TABLE I: Metal Content of Prismatic Region[a]

Sample	Height[b]	AA ppm Fe	AA[c] ppm Mn	EPR[d] ppm Mn(II)
NR01	0.0	19.4	8.6	4.7
NR02	0.5	42.2	10.6	4.1
NR03	1.0	59.3	12.0	8.2
NR04	1.5	47.3	11.5	7.8
NR05	2.0	27.4	10.6	11.1

[a] Error in values estimated to be ±3%. [b] Approximate height above low tide in meters. [c] Total manganese by atomic absorption spectroscopy (method of standard additions). [d] Based on the EPR signal vs. weight curve for reference sample RN002 with line width correction. Mn(II) substituted for Ca(II) in calcite. See ref 3.

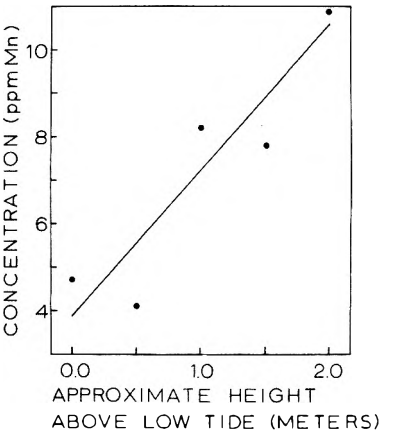

Figure 10. Correlation of the concentration of Mn(II) in calcite of the prismatic region of *Mytilus* against the height of the animal above low tide (0.0). The linear regression line is shown.

0.916), albeit on a limited number of samples, between the *Mn(II) substituted for Ca(II)* in calcite and the tidal position (see Table I and Figure 10). Interestingly, a similar correlation has been observed for the *total Mn* in barnacle shells.[3,28]

It would appear that EPR might be useful in investigating environmental influences on the accumulation of manganese in different structural components of marine shells.

Conclusion

The results presented here suggest that EPR spectroscopy can be profitably used to examine certain trace elements and radicals in calcified tissue and to obtain information concerning structural organization. EPR might be employed in organic fractionation studies to help identify which components of the periostracum or organic matrix are responsible for the observed radical signals.

Biomineralized tissue can provide unusual metal ion environments in which to study crystal field effects on transition metal ions. For example, the Ca(II) ion in aragonite is nine coordinate.[29] Marine animals appear to be one of the few sources of this thermodynamically unstable form of $CaCO_3$. Surprisingly, a study of Mn(II) doped in aragonite has never been reported. We find that aragonitic shells exhibit a very unusual Mn(II) spectrum in which the forbidden lines are more intense than the allowed lines at X-band frequencies.[27]

Acknowledgment. The authors wish to thank the National Science Foundation, Grant No. NSF MPS 75-03474, and the University of New Hampshire Central University fund for support of this research.

References and Notes

(1) For review see H. A. Kuska and M. T. Rogers in "Radical Ions", K. T. Kaiser and L. Levan, Ed., Wiley, New York, N.Y., 1968, pp 579–745; and B. A. Goodman and J. D. Raynor, *Adv. Inorg. Chem. Radiochem.*, **13**, 135 (1970).
(2) B. A. Burgess, N. D. Chasteen, and H. E. Gaudette, *Environ. Geol.*, **1**, 171 (1975–1976).
(3) S. C. Blanchard and N. D. Chasteen, *Anal. Chim. Acta*, **82**, 113 (1976).
(4) K. M. Wilbur in Physiology of Mollusca", Vol. 2, K. M. Wilbur and C. M. Yong, Ed., Academic Press, New York, N.Y., 1964, p 243.
(5) K. M. Wilbur and K. Simkiss, *Compre. Biochem.*, **26A**, 229 (1968).
(6) E. T. Degens, D. W. Spencer, and R. H. Parker, *Comp. Biophys. Biochem. Physiol.*, **20**, 553 (1967).
(7) R. R. Brooks and M. G. Rumsby, *Limnol. Oceanogr.*, **10**, 521 (1965).
(8) P. Tasch, "Paleobiology of the Invertebrates", Wiley, New York, N.Y., 1973, pp 312, 881.
(9) S. Weiner and L. Hood, *Science*, **190**, 987 (1975).
(10) D. F. Travis, *J. Ultrastruct. Res.*, **23**, 183 (1968).
(11) A. E. Needham, "The Significance of Zoochromes" in "Zoophysiology and Ecology", Vol. 3, Springer Verlag, New York, N.Y., 1974.
(12) M. Adams, M. S. Blois, Jr., and R. H. Sands, *J. Chem. Phys.*, **28**, 774 (1958).
(13) R. E. Hillman, *Science*, **134**, 1754 (1961).
(14) H. H. Wickman, M. P. Klein, and D. A. Shirley, *J. Chem. Phys.*, **42**, 2113 (1965).
(15) W. T. Oosterhius, *Struct. Bonding (Berlin)*, **20**, 59 (1974).
(16) J. Peisach and W. E. Blumberg, "Metalloproteins as Studied by Electron Paramagnetic Resonance" in "Electron Spin Resonance of Metal Complexes", T. F. Yen, Ed., Plenum Press, New York, N.Y., 1969, p 72.
(17) V. R. Meenakshi, P. E. Hare, N. Watabe, and K. M. Wilbur, *Comp. Biochem. Physiol.*, **29**, 611 (1969).
(18) T. R. Wildeman, *Chem. Geo.*, **5**, 167 (1969).
(19) P. A. Narayana, *J. Chem. Phys.*, **55**, 4283 (1971).
(20) B. Bleany, *Phil. Mag.*, **42**, 441 (1951).
(21) F. K. Hurd, M. Sachs, and W. D. Hershberger, *Phys. Rev.*, **93**, 373 (1954).
(22) B. Bleany and R. S. Rubins, *Proc. Phys. Soc. (London)*, **77**, 103 (1961); corrigendum, **78**, 778 (1961).
(23) F. Tsay, S. L. Manatt, and S. I. Chan, *Chem. Phys. Lett.*, **17**, 223 (1972).
(24) H. W. de Wijn and R. F. van Balderen, *J. Chem. Phys.*, **46**, 1381 (1967).
(25) The stated errors reflect only the uncertainty in the magnetic field measurements due to the line widths. They do not take into account any systematic error due to the possible noncoincidence of the principal resonance fields and the experimental line positions due to "powder effects".
(26) S. C. Blanchard and N. D. Chasteen, manuscript in preparation.
(27) L. K. White, A. Szabo, and N. D. Chasteen, work in progress.
(28) See, for example, O. H. Pilkey and R. C. Harriss, *Limnol. Oceanogr.*, **11**, 381 (1960); C. M. Gordon, R. A. Carr, and R. E. Larson, *ibid.*, **15**, 461 (1970).
(29) J. P. R. de Villiers, *Am. Mineral.*, **56**, 758 (1971).

Lattice Vibrations of Quinhydrone and the Intermolecular Potential in the Crystal

Kunio Fukushima* and Masataka Sakurada

Department of Chemistry, Faculty of Science, Shizuoka University, 836, Oya, Shizuoka, Japan

(Received December 23, 1975)

Infrared spectra of quinhydrone, quinhydrone-d_2, and phenoquinone were measured in the region of 4000–30 cm^{-1}. On the basis of the observed vibrational frequencies, the intermolecular potential in the quinhydrone crystal was investigated by carrying out calculation of the optically active lattice vibrations.

The crystal structure of quinhydrone has been studied by Matsuda et al. [1] and also by Sakurai.[2] According to their studies, each hydroquinone molecule in the crystal is connected to two quinone molecules by hydrogen bonds, and the perpendicular projection of the hydroquinone molecule on the neighboring quinone molecule seems to indicate that the interaction of the two kinds of molecules by charge transfer force is not so strong as other charge transfer complexes, for example, the hexamethylbenzene–chloranil complex. Lattice vibrations of the crystal are expected to reflect sensitively the strength of interactions due to the charge transfer force. Spectroscopic investigations of quinhydrone in the lower frequency region have not yet been made, although those in the higher frequency region have been carried out.[3,4] Therefore, in the present investigation vibrational spectra of quinhydrone in the lower frequency region were observed and the interaction of the hydroquinone molecule with quinone molecules in the crystal was studied by carrying out calculation of the optically active vibrations on the basis of the experimental results.

Experimental Section

Quinhydrone crystal was prepared by slow evaporation of an acetone solution containing an equimolecular mixture of hydroquinone (prepared by recrystallization of hydroquinone (grade G.R., Wako Pure Chemicals Co. Ltd.)) and *p*-benzoquinone (grade G.R., Wako Pure Chemicals Co. Ltd.) at room temperature. The crystal melted at 167–168 °C. Phenoquinone crystal was prepared in a similar way from a petroleum solution containing phenol (grade G.R., Wako Pure Chemicals Co. Ltd.) and *p*-benzoquinone in molar ratio of 2 to 1. The crystal melted at 70–71 °C. Quinhydrone-d_2 was prepared by dropping 1 cm^3 of a cooled heavy water solution containing 0.1875 g of sodium periodate slowly into 1.5 cm^3 of a cooled heavy water solution containing 0.38 g of hydroquinone-d_2 and then drying the generated precipitate.

Infrared spectra of crystal samples in a Nujol mull and of phenoquinone in solution were measured. A Hitachi EPI-G3 infrared spectrophotometer was used for the measurements in the region of 4000–400 cm^{-1}, and a Hitachi FIS-3 far-infrared spectrometer for the region of 400–30 cm^{-1}. Spectra of solutions were measured using KBr window cells of 0.1 mm thickness and polyethylene cells of 0.5 mm thickness. The results of measurements are shown in Tables I and II.

Calculation of Optically Active Lattice Vibrations

Quinhydrone crystal formed by slow evaporation of an acetone solution containing hydroquinone and *p*-benzoquinone in a molar ratio of 1:1 is monoclinic.[1,2] The crystal structure has been analyzed as belonging to the space group $P2_1/c$.[1,2] Two chemical units of $C_6H_6O_2 \cdot C_6H_4O_2$ belong to each lattice point of the unit cell of the crystal. Constellation of the two

TABLE I: Infrared Bands of Quinhydrone (QH), Quinhydrone-d_2 (QH-d_2), Quinone (Q), Hydroquinone (HQ), and Hydroquinone-d_2 (HQ-d_2) in Nujol Mull

QH	QH-d_2	Q	HQ	HQ-d_2	Assignment
3226(s)	2402(s)		3182(s)	2429(s)	OH(OD) str
	2356(sh)				
3056(vw)[a]					
3031(vw)[a]					
2964(vw)[a]					
1656(sh)	1656(sh)	1676(sh)			
1629(vs)	1625(vs)	1655(s)			C=O str
1587(m)	1587(m)	1588(m)			
1578(sh)	1578(sh)				
1561(sh)	1566(sh)				
1546(sh)	1539(sh)				
1513(sh)	1507(s)		1511(s)	1502(s)	
1478(m)[a]	1476(sh)				
1460(sh)[a]	1080(sh)		1474(s)	1030(m)	OH(OD) bend
1374(s)	1368(m)		1362(w)	1367(w)	
1363(s)		1363(s)			
1350(sh)	1354(sh)		1350(m)	1353(w)	
1333(vw)	1341(sh)	1339(m)			
1319(s)	1321(m)	1308(s)			
1300(sh)	1300(m)		1310(w)	1309(vw)	
			1290(vw)	1287(w)	
1260(s)	1257(s)		1257(m)	1260(m)	
1246(sh)	1246(sh)		1240(m)	1232(s)	
			1220(sh)	1210(sh)	
1207(s)	981(s)		1205(s)	989(m)	
			1190(s)	969(m)	
1104(m)	1109(m)		1096(m)	1106(m)	
1088(s)	1090(m)	1084(s)			
		1072(sh)			
1010(w)	1012(sh)		1005(w)	1005(w)	
979(w)	[c]				
948(m)	948(m)	942(m)			
932(sh)	932(sh)		938(w)	940(sh)	
			918(w)	919(w)	
			890(w)	890(vw)	
877(s)	875(s)	896(m)			
833(m)	832(m)		826(m)	830(m)	
				822(m)	
761(m)	752(m)		758(s)	748(s)	
757(sh)		744(w)			
684(m)	500(m)				C-OH(C-OD)
			613(m)	440(w)	tors
528(m)	530(m)	521(w)			
515(vw)	515(vw)		517(m)	512(m)	
447(m)	448(m)				
		414(m)			
			409(w)	400(w)	
386(m)	373(m)		387(m)	387(m)	
			374(sh)	373(sh)	
				360(w)	
349(w)	349(w)				
			211(s)	210(s)	
192(w)	190(w)		192(s)	191(m)	
153(s)	148(s)		154(m)	151(m)	
129(m)	128(m)		122(m)	122(m)	
106(s)	103(s)	116(s)[b]	100(sh)	100(sh)	
		109(sh)[b]			
87(sh)	87(sh)		84(w)	84(w)	
77(sh)	76(sh)		76(w)	74(w)	
			61(vw)	61(vw)	
			54(vw)	54(vw)	

[a] Hexachlorobutadiene mull. [b] Corresponding band of benzene solution is observed at 110 cm^{-1}. [c] This band is overlapped by the band at 981 cm^{-1}.

TABLE II: Infrared Bands of Phenoquinone (PQ) in Nujol Mull and in Solution

Crystal	Solution		
	3612(m)	OH str (free)	
3265(s)[a]	3439(m)	OH str (bonded)	
3074(vw)	3037(w)		
3024(vw)			
	1671(sh)	C=O str (free)	Q[c]
1638(vs)	1657(vs)	C=O str (bonded)	Q
1603(m)	1605(sh)		
1587(s)	1596(s)		Q
1500(w)	1499(m)		
1470(s)	1469(m)		
1397(vw)[a]	1383(vw)		
1371(m)[a]	1355(w)		Q
1359(m)[a]	1340(w)		Q
1319(m)	1301(m)		Q
1265(m)	1258(m)[b]		
1220(s)	1214(m)		
1170(w)	1178(m)		
1159(m)	1150(w)		
1113(sh)			
1087(m)			
1069(m)	1067(m)		Q
1021(w)	1022(vw)		
943(w)	942(w)		Q
927(sh)			
892(sh)			
880(m)	882(s)		Q
834(w)	830(w)[b]		
826(sh)			
814(m)	813(m)[b]		
764(sh)			
761(s)	753(s)[b]		
691(m)	687(m)		
662(m)		C–OH tors	
530(vw)	526(vw)[b]		
512(m)	501(w)		Q
454(m)			
414(m)	403(w)		Q
	400(s,br)[b]		
343(w)			
248(w)			
148(s)			
134(s)			
104(m)	110(m)[b]		Q
86(w)			

[a] Hexachlorobutadiene mull. [b] Benzene solution. [c] Q = quinone.

chemical units (couple of I HQ–I Q and that of II HQ–II Q) is shown in Figure 1.

The number of optically active lattice vibrations of each symmetry species for this crystal structure, which were obtained by a factor group analysis, are shown in Table III. In this table, N, T, T', R', and n represent, respectively, total degrees of freedom, translational motion of the two units as a whole, translational vibrations, rotational vibrations, and internal vibrations for each set of the two chemical units. The optically active lattice vibrations were treated by the method developed by Shimanouchi et al.[5] Expressing a lattice point in the above mentioned $P2_1/c$ lattice by (i,j,k), the Cartesian symmetry coordinate vector, $(X_s)^{i,j,k}_{\text{Bravais}}$, and the internal symmetry coordinate vector, $(R_s)^{i,j,k}_{\text{Bravais}}$, which both belong to

TABLE III: Results of the Factor Group Analysis ($2C_6H_6O_2 \cdot C_6H_4O_2$ per Bravais Cell; Factor Group, C_{2h}^5)

	N	T	T'	R'	n
A_g	39	0	3	3	33
A_u	39	1	2	3	33
B_g	39	0	3	3	33
B_u	39	2	1	3	33

TABLE IV: Force Constants of Quinhydrone (mdyn/Å)[a]

K(C1—C2)HQ	4.000	t(C–O)HQ	0.110 mdyn Å
K(C2–C3)HQ	4.750	t(C1–C2)Q	0.100 mdyn Å
K(C3–C4)HQ	5.500	t(C2–C3)Q	0.300 mdyn Å
K(C–O)HQ	5.500	t(C3–C4)Q	0.100 mdyn Å
K(C–H)HQ	4.100	F(C1–C2–C3)HQ	0.370
K(O–H)HQ	5.000	F(C2–C3–C4)HQ	0.350
K(C1–C2)Q	5.000	F(C6–C1–C2)HQ	0.350
K(C2–C3)Q	5.500	F(O–C1–C2)HQ	0.660
K(C3–C4)Q	3.600	F(O–C1–C6)HQ	0.350
K(C=O)Q	6.800	F(H–C1–C2HQ	0.700
K(C–H)Q	4.150	F(H–C2–C4)HQ	0.630
K(H···O)	0.392	F(H–C2–C3)HQ	0.580
K(H···H)	0.028	F(H–C3–C2)HQ	0.580
H(C1–C2–C3)HQ	0.430	F(C–O–H)HQ	0.600
H(C2–C3–C4)HQ	0.350	F(C1–C2–C3)Q	0.350
H(C6–C1–C2)HQ	0.350	F(C2–C3–C4)Q	0.350
H(O–C1–C2)HQ	0.450	F(C6–C1–C2)Q	0.300
H(O–C1–C6)HQ	0.400	F(O=C–C)Q	0.400
F(H–C–C)HQ	0.190	F(H–C2–C1)Q	0.640
H(C–O–H)HQ	0.640	F(H–C2–C3)Q	0.700
H(C1–C2–C3)Q	0.350	F(H–C3–C2)Q	0.700
H(C2–C3–C4)Q	0.350	F(H–C3–C4)Q	0.540
H(C6–C1–C2)Q	0.500	f(HQ···HQ)	0.001
H(O=C–C)Q	0.480	f(Q···Q)	0.001
H(H–C–C)Q	0.255	f(HQ···Q)	0.005
L(O–H···O)1	0.050	K_x(HQ)	0.000 mdyn Å
L(O–H···O)2	0.070	K_y(HQ)	0.001 mdyn Å
π(C·COC)HQ	0.500 mdyn Å	K_z(HQ)	0.001 mdyn Å
π(C·CHC)HQ	0.370 mdyn Å	K_x(Q)	0.000 mdyn Å
π(C·COC)Q	0.460 mdyn Å	K_y(Q)	0.001 mdyn Å
π(C·CHC)Q	0.430 mdyn Å	K_z(Q)	0.001 mdyn Å
t(C–C)HQ	0.055 mdyn Å		

[a] K's, H's and F's are bond stretching force constants, angle bending force constants, and repulsive force constants, the definition of which are described in ref 16. t's are internal rotation vibration force constants, and π's are out-of-plane bending force constants. The carbon atom–carbon atom bonds of hydroquinone, C1–C2 (C4–C5), C2–C3 (C5–C6) and C3–C4 (C6–C1), correspond to the bond lengths 1.416, 1.407, and 1.335 Å in ref 1, respectively. In the same way the carbon atom–carbon atom bonds of p-benzoquinone C1–C2 (C4–C5), C2–C3 (C5–C6), and C3–C4 (C6–C1), correspond to the bond lengths 1.447, 1.335, and 1.482 Å in ref 1, respectively. L(O–H···O)1 is the force constant for linear bending in the plane formed by C–O–H group and O atom in C=O group, which are connected by a hydrogen bond, while L(O–H···O)2 is that for linear bending out-of-plane.

TABLE V: Observed and Calculated Frequencies and Potential Energy Distributions of A_u and B_u Optically Active Vibrations of Quinhydrone [a]

ν_{obsd}	ν_{calcd}		
QH	QH	QH-d_2	Potential energy distributions
			A_u Vibrations
3226	3207		OH str (93)
3056	3080	3080	CH str (95)
	3049	3049	CH str HQ(95)
3031			
	3030	3049	CH str Q(100)
2964	3011	3011	CH str HQ(101)
2356		2322	OD str (94)
1656	1672	1650	CC str HQ(39), COH bend (21)
1629	1649	1646	C=O str Q(23), CC str Q(22)
1587	1584	1584	CC str Q(82)
1578	1550	1524	C-O str HQ(22), CC str HQ(22)
1478	1450		COH bend(46), CC str HQ(22)
1363	1364	1364	CCH bend Q(59)
1319	1325	1325	C=O str Q(23), CCH bend Q(20)
1260	1252	1286	C-O str HQ(35), CCH bend HQ(19)
1207	1222	1246	CC str HQ(37), CCH bend HQ(23)
	1187	1187	CC str Q(31), CCH bend Q(14)
1104	1102	1124	CC str HQ(26), CCH bend HQ(20)
1088	1068	1068	CH out-of-plane Q(75)
1080		1047	COD bend (49), CC str HQ(17)
948	955	954	CC str Q(24), CCH bend Q(17)
	946	945	CCH bend HQ(25), CC str HQ(21)
932			
	923	922	CH out-of-plane HQ(90)
877	879	878	CH out-of-plane Q(65)
833	841	840	CH out-of-plane HQ(64)
761	742	742	C-O tors HQ(20), CCC bend Q(19)
	716	706	C-O tors HQ(22), CCC bend HQ(15)
684	681		C-O tors HQ(48), O-H···O in-plane bend (42)
528	520	525	C-O out-of-plane HQ(49), C=O out-of-plane Q(28)
515	495	515	C=O out-of-plane Q(54), C-O out-of-plane HQ(26)
		475	C-O tors HQ(24), O-D···O in-plane bend (22)
447	441	437	OCC bend Q(23), H···O str (19),
386	373	359	OCC bend HQ(47)
349	351	351	C-C tors Q(59), CH out-of-plane Q(12)
192	215	215	HQ···Q str (62)
192	195	194	C-C tors HQ(56)
153	158	158	H···O str (36), H···H str (24)
129	128	128	H···H str (46), Q···Q str (32)
106	108	108	C-C tors Q(57)
87	91	90	C-C tors HQ(47)
77	75	73	H···O str(21), Q···Q str(16)
	35	35	H···H str(45)
			B_u Vibrations
3226	3207		OH str HQ(93)
	3080	3080	CH str Q(94)
3056			
	3050	3050	CH str HQ(95)
3031	3027	3027	CH str Q(100)
2964	3007	3007	CH str HQ(100)
		2322	OD str (94)
1656	1671	1647	CC str HQ(40), COH bend (21)
1629	1647	1646	C=O str Q(23), CC str Q(22)
1587	1584	1584	CC str Q(82)
1546	1549	1523	C-O str HQ(23), CC str HQ(22)

TABLE V (*continued*)

ν_{obsd}	ν_{calcd}		
QH	QH	QH-d_2	Potential energy distributions
1460	1448		COH bend (47), CC str HQ(21)
1374	1367	1367	CCH bend Q(64)
1319	1325	1325	C=O str Q(26), CCH bend Q(23)
1260	1251	1286	C–O str HQ(33), CCH bend HQ(22)
1207	1222	1247	CC str HQ(32), CCH bend HQ(22)
	1194	1194	CC str Q(33), CCH bend Q(13)
1104	1107	1128	CC str HQ(28), CCH bend HQ(18)
1088	1073	1073	CH out-of-plane Q(74)
		1046	COD bend (51), CC str HQ(16)
948	951	951	CC str Q(25), CCH bend Q(19)
	943	941	CCH bend HQ(26), CC str HQ(22)
932			
	925	925	CH out-of-plane HQ(86)
877	881	880	CH out-of-plane Q(57)
833	836	835	CH out-of-plane HQ(56)
761	740	740	C=O str Q(20), CCC bend Q(19)
	714	705	C–O tors HQ(21), CCC bend HQ(15)
684	682		C–O tors HQ(48), O–H···O in-plane bend(42)
528	524	527	C–O out-of-plane HQ(48), C=O out-of-plane Q(29)
		513	C–O out-of-plane Q(42), C–O tors HQ(23)
515	487	471	C=O out-of-plane Q(53), C–O out-of-plane HQ(27)
447	440	436	OCC bend Q(23), H···O str (20)
386	372	361	OCC bend HQ(45)
349	359	355	C–C tors Q(51), CH out-of-plane Q(12)
	213	213	HQ···Q str (64)
192	204	203	C–C tors HQ(51)
	139	138	H···O str(45), Q···Q str(7)
106	104	104	C–C tors Q(51)
87	87	86	C–C tors HQ(45)
77	68	67	H···H str (42), Q···Q str (25)
	55	54	Q···Q str (24), O–H···O out-of-plane bend (17)

[a] The potential energy distributions are those of QH except for those of the vibrations calculated to be at 2322, 1047, and 475 cm^{-1} of QH-d_2. Abbreviations: str = stretching; bend = bending; tors = torsion (internal rotation).

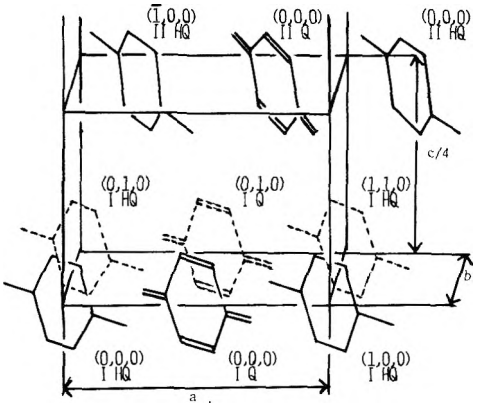

Figure 1. A part of quinhydrone crystal lattice: *a*, *b*, *c*, lattice parameters; I, chemical unit I; II, chemical unit II; (*i,j,k*), Bravais cell number; HQ, hydroquinone; Q, quinone.

the Bravais cell, (i,j,k), are related to the optically active Cartesian coordinate vector, X_{op}, and the optically active internal symmetry coordinate vector, R_{op}, by the following relation:

$$X_{op} = \lim (n_1 n_2 n_3)^{-1/2} \sum_{i=0}^{n_1} \sum_{j=0}^{n_2} \sum_{k=0}^{n_3} (X_s)^{i,j,k}_{\text{Bravais}}$$

$$R_{op} = \lim (n_1 n_2 n_3)^{-1/2} \sum_{i=0}^{n_1} \sum_{j=0}^{n_2} \sum_{k=0}^{n_3} (R_s)^{i,j,k}_{\text{Bravais}}$$

$$R_{op} = B_{op} X_{op},$$

$$F_{op} = F_{000} + F_{100} + \bar{F}_{100} + F_{010} + \bar{F}_{010} + F_{001} + \bar{F}_{001} + \ldots$$

Here, F_{000} is the potential energy matrix associated with a Bravais cell and F_{100}, F_{010}, F_{001}, $\cdots$ are the interaction potential energy matrices between the Bravais cell and other Bravais cells surrounding it. X_{op} and R_{op} are expressed in terms of the coordinate vectors, X^{I}_{op}, $X^{I'}_{op}$, X^{II}_{op}, $X^{II'}_{op}$, R^{I}_{op}, $R^{I'}_{op}$,

R_{op}^{II}, and $R_{op}^{II'}$, where I and II represent the two chemical units in a Bravais cell. X_{op}^{I}, X_{op}^{II}, R_{op}^{I}, and R_{op}^{II} are changed into $-X_{op}^{I'}$, $-X_{op}^{II'}$, $R_{op}^{I'}$, and $R_{op}^{II'}$, respectively, by the symmetry operation of inversion.

$$X_{op} = (X_{op}^{I} - X_{op}^{I'} - X_{op}^{II} + X_{op}^{II'})/2 \quad (A_g \text{ species})$$

$$X_{op} = (X_{op}^{I} + X_{op}^{I'} - X_{op}^{II} - X_{op}^{II'})/2 \quad (A_u \text{ species})$$

$$X_{op} = (X_{op}^{I} - X_{op}^{I'} + X_{op}^{II} - X_{op}^{II'})/2 \quad (B_g \text{ species})$$

$$X_{op} = (X_{op}^{I} + X_{op}^{I'} + X_{op}^{II} + X_{op}^{II'})/2 \quad (B_u \text{ species})$$

$$R_{op} = (R_{op}^{I} + R_{op}^{I'} + R_{op}^{II} + R_{op}^{II'})/2 \quad (A_g \text{ species})$$

$$R_{op} = (R_{op}^{I} - R_{op}^{I'} + R_{op}^{II} - R_{op}^{II'})/2 \quad (A_u \text{ species})$$

$$R_{op} = (R_{op}^{I} + R_{op}^{I'} - R_{op}^{II} - R_{op}^{II'})/2 \quad (B_g \text{ species})$$

$$R_{op} = (R_{op}^{I} - R_{op}^{I'} - R_{op}^{II} + R_{op}^{II'})/2 \quad (B_u \text{ species})$$

Lattice vibration frequencies were obtained by solving the secular equation, $|M^{-1}F_{xs} - \lambda E| = 0$, where $F_{xs} = \vec{B}_{op}F_{op}B_{op}$ and M^{-1} is a diagonal matrix consisting of inverse atomic masses. The following potential was assumed for the crystal:

$$V = V_{C_6H_6O_2} + V_{C_6H_4O_2} + V_{inter}$$

Here, $V_{C_6H_6O_2}$ and $V_{C_6H_4O_2}$ represent the modified Urey–Bradley force field for hydroquinone and *p*-benzoquinone, respectively, and V_{inter} represents intermolecular potential for hydroquinone–*p*-benzoquinone, hydroquinone–hydroquinone, and *p*-benzoquinone–*p*-benzoquinone interactions. V_{inter} is expressed as:

$$\begin{aligned}2V_{inter} = {} & \sum K(\text{H}\cdots\text{O})\Delta q_i(\text{H}\cdots\text{O})^2 + \sum K(\text{H}\cdots\text{H})\Delta q_i(\text{H}\cdots\text{H})^2 \\ & + \sum f_i(\text{HQ}\cdots\text{Q})\Delta R_i(\text{HQ}\cdots\text{Q})^2 \\ & + \sum f_i(\text{HQ}\cdots\text{HQ})\Delta R_i(\text{HQ}\cdots\text{HQ})^2 \\ & + \sum f_i(\text{Q}\cdots\text{Q})\Delta R_i(\text{Q}\cdots\text{Q})^2 + \sum K_x(\text{HQ})\Delta\theta_{i,x}^{HQ^2} \\ & + \sum K_y(\text{HQ})\Delta\theta_{i,y}^{HQ^2} + \sum K_z(\text{HQ})\Delta\theta_{i,z}^{HQ^2} + \sum K_x(\text{Q})\Delta\theta_{i,x}^{Q^2} \\ & + \sum K_y(\text{Q})\Delta\theta_{i,y}^{Q^2} + \sum K_z(\text{Q})\Delta\theta_{i,z}^{Q^2} + \sum L(\text{O–H}\cdots\text{O})1\Delta\psi_{1i}^2 \\ & + \sum L(\text{O–H}\cdots\text{O})2\Delta\psi_{2i}^2\end{aligned}$$

where the symbols HQ and Q represent hydroquinone and quinone, respectively, *R*'s represent distances between centers of gravity of molecules, θ's represent rotation angles around the centers of gravity, and ψ's represent linear bending angles of the O–H···O hydrogen bond. The atom–atom or molecule–molecule interactions taken into account are as follows: O···H hydrogen bond interactions; the intermolecular hydrogen atom–hydrogen atom pair interactions with the nearest distance in I and II; HQ···Q interactions in the direction parallel to the axis, *a*; HQ···HQ and Q···Q interactions in the direction parallel to the axis, *b* (Figure 1). The final set of force constant values, calculated frequencies, and potential energy distributions are shown in Tables IV and V. In these tables, abbreviations QH, HQ, and Q were used for quinhydrone, hydroquinone, and quinone, respectively. The potential energy distributions are expressed using the names of coordinates without showing the detailed forms of the coordinates, because description of the detailed forms would require a large space and is not essential for description of the nature of the calculated frequencies.

Discussion

Intramolecular Vibrations. As shown in Tables I and V, the bands of quinhydrone, which are due to intramolecular vibrations, have frequencies close to those of component molecules hydroquinone and p-benzoquinone. However, the bands of quinhydrone at 877 cm^{-1} (CH out-of-plane bending, Q), 761 cm^{-1} (CCC bending, Q), and 447 cm^{-1} (C=O in-plane bending, Q) have frequencies different from those of component molecule quinone, which are at 896, 744, and 414 cm^{-1}.[4-15] In particular, the considerable frequency difference of CH out-of-plane bending vibration suggests that the intermolecular force between hydroquinone and *p*-benzoquinone is not so weak in quinhydrone, and that the contribution of force other than hydrogen bonding is considerable between the two component molecules.

Intermolecular Vibrations. Among the vibrations, only A_u and B_u vibrations are infrared active. Therefore, they correspond to the observed infrared bands.

A_u Vibrations. There exists a contribution of the hydrogen bond stretching mode to the vibration calculated to be at 441 cm^{-1}. However, the vibration is primarily a skeletal deformation. The vibrations in which the contribution of intermolecular vibrational modes is striking have lower calculated frequencies. Of these, the vibration calculated to be at 215 cm^{-1} is the lattice vibration in which the hydroquinone molecule and the *p*-benzoquinone molecule oscillate about each other, as shown in the potential energy distribution of the vibration (Table V). In this vibration, the effect of charge transfer force is predominant, while contribution of the hydrogen bond stretching mode is not eminent. This vibration corresponds to the band at 192 cm^{-1}. On the other hand, the potential energy distribution of the vibration calculated at 158 cm^{-1}, along with the following experimental facts regarding phenoquinone and quinhydrone-d_2, show that the band at 153 cm^{-1} is primarily due to the hydrogen bond stretching mode. In phenoquinone, where the bonding of *p*-benzoquinone with phenol somewhat resembles that in quinhydrone, bands appear at 343, 248, 148, 134, 104, and 86 cm^{-1} in the lower frequency region. Only the band at 104 cm^{-1} remains in the solution spectra as shown in Table II. Therefore, the five vanishing bands are due to intermolecular vibrational modes. Moreover, the strong band of quinhydrone at 153 cm^{-1} shifts to lower frequency by 5 cm^{-1} on deuteration (Table I) and is considered to be due to the hydrogen bond stretching mode. The resemblance of the frequency value of the band at 148 cm^{-1} of phenoquinone with that of the band of quinhydrone at 153 cm^{-1} seems to suggest the above assignment of the band at 153 cm^{-1} is reliable. The fact that the frequency of the band at 192 cm^{-1} (calcd 215 cm^{-1}) is higher than that at 153 cm^{-1} (calcd 158 cm^{-1}), where the hydrogen bond stretching mode contributes to a considerable extent, suggests that the charge transfer force between hydroquinone and *p*-benzoquinone is considerably strong in this crystal. The vibrations calculated at 195 and 108 cm^{-1} are contributed mainly by intramolecular vibrational modes and are not affected much by the charge transfer force. The vibration calculated at 75 cm^{-1} is affected both by hydrogen bonding and the charge transfer force.

B_u Vibrations. The vibrations calculated at 213, 204, and 139 cm^{-1} have potential energy distributions similar to the corresponding A_u vibrations at 215, 195, and 158 cm^{-1}, respectively. The vibrations calculated at 104 and 87 cm^{-1} are intramolecular vibrations, while the vibrations having frequencies smaller than those are contributed by charge transfer force.

Intermolecular Potential. As shown in Table IV, the relatively large force constant value of 0.392 was obtained for K(H···O). Therefore, it is true that considerably strong hydrogen bond interaction exists in quinhydrone. At the same time, the force constant K(H···H), which is expected to increase corresponding to the interaction due to charge transfer force between hydroquinone and *p*-benzoquinone, has the

considerable value of 0.028. Moreover, the force constant, f(HQ···Q), which also depends on the hydroquinone–p-benzoquinone interaction, has the nonnegligible value of 0.005. These force constant values also seem to indicate considerably strong interactions due to charge transfer force in quinhydrone.

Appendix

Quinhydrone forms both monoclinic crystal and triclinic crystal.[1,2,17] The quinhydrone crystals examined in the present study were prepared according to the method described in papers[1,2] in which the crystal structure of monoclinic quinhydrone was studied. They were long prisms, corresponding to those described in the appendix in ref 17 and were different from flat parallelepiped crystals of triclinic quinhydrone which are also described in the appendix.

References and Notes

(1) H. Matsuda, K. Osaki, and I. Nitta, *Bull. Chem. Soc. Jpn.*, **31**, 611 (1958).
(2) T. Sakurai, *Acta Crystallogr., Sect. B*, **24**, 403 (1968).
(3) K. Kotera, *Yakugaku Zasshi*, **80**, 655 (1960).
(4) M. A. Slifkin and R. H. Walmsley, *Spectrochim. Acta, Part A*, **26**, 1237 (1970).
(5) T. Shimanouchi, M. Tsuboi, and T. Miyazawa, *J. Chem. Phys.*, **35**, 1597 (1961).
(6) R. D. Kross, V. A. Fassel, and M. Margoshes, *J. Am. Chem. Soc.*, **78**, 1332 (1956).
(7) T. Anno and A. Sado, *Bull. Chem. Soc. Jpn.*, **31**, 734 (1958).
(8) J. F. Bagli, *J. Am. Chem. Soc.*, **84**, 177 (1962).
(9) M. Davies and F. E. Prichard, *Trans. Faraday Soc.*, **59**, 1248 (1963).
(10) H. Stemmreich and T. H. Teixeira Sans, *J. Chem. Phys.*, **42**, 920 (1965).
(11) E. Charney and E. D. Becker, *J. Chem. Phys.*, **42**, 910 (1965).
(12) H. Ziffer, E. Charney, and E. D. Becker, *J. Chem. Phys.*, **42**, 914 (1965).
(13) T. Anno, *J. Chem. Phys.*, **42**, 932 (1965).
(14) E. D. Becker, E. Charney, and T. Anno, *J. Chem. Phys.*, **42**, 942 (1965).
(15) B. Lunelli and C. Pecile, *Spectrochim. Acta, Part A*, **29**, 1989 (1972).
(16) T. Shimanouchi, *J. Chem. Phys.*, **17**, 245 (1949).
(17) T. Sakurai, *Acta Crystallogr.*, **19**, 320 (1965).

Crystal-Field Calculations with Trigonal Bipyramidal Symmetry Potential. 1. Weak Crystal Field for $d^{3,7}$ Configurations

F. Gómez Beltrán and F. Palacio*

Inorganic Chemistry Department, University of Zaragoza, Zaragoza, Spain

(Received August 13, 1975)

Publication costs assisted by the Inorganic Chemistry Department, University of Zaragoza

Trigonal bipyramidal crystal-field energy matrices for a $d^{3,7}$ configuration in the limit of zero spin–orbit perturbation in a weak field scheme are given. Racah algebra has been used for calculating them. The appropiate weak-field basis eigenfunctions as well as the necessary reduced matrix elements for tensor $\hat{C}^{(k)}$ (k = 0, 2, 4) and rotation matrix $D^{(J)}(\alpha, \beta, \gamma)$, for J = 5, are also given. All crystal field matrices here calculated are shown to be consistent with the strong field ones previously published.

Introduction

Crystal field calculations have been carried out in more than one representation for most of the d^n configurations, although most of the energy matrices published have been obtained from potentials corresponding to symmetrical[1] or distorted[2] octahedra. Among the noncubic potentials, the trigonal bypramidal symmetry is the one to which most attention has been paid. Thus, calculations for the $d^{1,9}$ configurations, with and without spin–orbit coupling,[3,4] for the $d^{2,8}$ configurations, either in weak[3a,b] or in strong field[5] representations even including spin–orbit coupling perturbation,[6] and for the $d^{3,7}$ configurations in strong field representation[7] have been performed. Moreover, Norgett, Thornley, and Venanzi[8] and Wood[9] have worked out level diagrams for the $d^{2,3,6,7,8}$ configurations, but these diagrams are not complete although they are well suited for the discussion of the spectroscopic data of these authors. Nevertheless, in order to treat the general case it is convenient to have explicit expressions for the complete energy matrices since the general energy level diagrams are five dimensional. Besides, because at present Co(II) high-spin complexes of bipyramidal trigonal symmetry are sufficiently well established[9,10] we feel that knowledge of the explicit forms for the energy matrices would be useful. The purpose of the present paper is to give these matrices, diagonalizing in the weak field representation a Hamiltonian comprised of the interelectronic repulsion and crystal field terms, namely

$$H = \sum_{i>j} \frac{e^2}{r_{ij}} + V_{CF} \tag{1}$$

A "free atom" type representation[11] including spin–orbit coupling will be treated in a later paper.

Theoretical Treatment

The crystal field potential has the well-known general form

$$V_{CF} = \sum_{kq} \sqrt{\frac{4\pi}{2k+1}} \sum_i Z_i \frac{r_{i>}^k}{r_{i>}^{k+1}} Y_{kq}^*(\theta_i, \phi_i)\, C_q^{(k)}(\theta, \phi) \tag{2}$$

which in our particular case reduces to

* Address correspondence to this author at the Fundamental Physics Department, Sciences Faculty, University of Zaragoza, Zaragoza, Spain.

$$V_{D_{3h}} = \left[\frac{3q_1}{r_{1>}} + \frac{2q_2}{r_{2>}}\right] C_0^{(0)}(\theta, \phi) + \left[-\frac{3}{2} q_1 \frac{r_{1>}^2}{r_{1>}^3} + 2q_2 \frac{r_{2>}^2}{r_{2>}^3}\right] C_0^{(2)}(\theta, \phi) + \left[\frac{9}{8} q_1 \frac{r_{1>}^4}{r_{1>}^5} + 2q_2 \frac{r_{2>}^4}{r_{2>}^5}\right] C_0^{(4)}(\theta, \phi) \quad (3)$$

where three charges (q_1) are located on the XY plane at distances r_1 and two (q_2) on the Z axis at r_2 from the central ion. The $C_q^{(k)}(\theta, \phi)$ are also named Racah's rationalized spherical harmonics,

$$C_q^{(k)}(\theta, \phi) = \sqrt{\frac{4\pi}{2k+1}}\, Y_{kq}(\theta, \phi) \quad (4)$$

In a weak field representation, at the zero spin–orbit interaction limit, the eigenstates are described by $|\alpha SL\Gamma\gamma a\rangle$ where α distinguishes between terms with equal S and L; Γ characterizes the irreducible representation in the group D_{3h}; γ distinguishes the different degenerate states contained in Γ, if there are any, and a is any set of quantum numbers distinguishing states with equal S and Γ. These states are calculable as functions of those of the free ion, because, in general, any G puntual group is a subgroup of the three-dimensional proper rotation group SO(3). Therefore any $D^{(J)}$ (SO(3)) representation of SO(3) will subduce another $D^{(J)}$ (G) of the group G, which, in general, will be reduced according to

$$D^{(J)}(\mathrm{G}) = \sum_i a_i^{(J)} \Gamma_i \quad (5)$$

where $a_i^{(J)}$ expresses the number of times that the irreducible representation Γ occurs. So, our states $|\alpha SL\Gamma\gamma a\rangle$ [12] will be a projection of those of the free ion $|\alpha SLM_L\rangle$ on the D_{3h} group

$$|\alpha SL\Gamma\gamma a\rangle = \sum_{M_L} |\alpha SLM_L\rangle \langle \alpha SLM_L|\alpha SL\Gamma\gamma a\rangle \quad (6)$$

The expansion coefficients $\langle \alpha SLM_L|\alpha SL\Gamma\gamma a\rangle$ can be determined by König and Kremer's method:[13]

$$\sum_a \langle \alpha LM'_L|\alpha L\Gamma\gamma' a\rangle \langle \alpha L\Gamma\gamma a|\alpha LM_L\rangle = \frac{d_\Gamma}{g} \sum_R D^{\Gamma}_{\gamma'\gamma}(R)^* D^{(L)}_{M'_L M_L}(R) \quad (7)$$

where d_Γ is the dimension of the irreducible representation Γ and g the dimension of the G group to which Γ belongs. The matrices $D^{\Gamma}_{\gamma'\gamma}(R)$ are straightforward[14] and the $D^{(L)}_{M'_L M_L}(R)$ can be obtained from the $D^{(J)}_{M'M}(\alpha, \beta, \gamma)$, for J integer, through the following Eulerian rotations[6] $C_3(Z) \rightarrow \alpha = 2\pi/3, \beta, \gamma = 0$; $C_2(x) \rightarrow \alpha = 0, \beta, \gamma = \pi$; $\sigma_v(x, y) = C_2(y) \rightarrow \alpha, \gamma = 0, \beta = \pi$; $\sigma_h(x, y) = C_2(Z) \rightarrow \alpha = \pi, \beta, \gamma = 0$; and $S_3(Z) = C_{6/5}(Z) \rightarrow \alpha = 5\pi/3, \beta, \gamma = 0$.

In this paper rotation matrices with $J = 0, 1, 2, 3, 4$, and 5 have been used. Rotation matrices for $J \leq 4$ are known[15] and in Appendix I (available as supplementary material; see paragraph at end of text regarding supplementary material) the explicit expression for the $J = 5$ rotation matrix is given.

The eigenfunctions obtained in the basis $\{\alpha SL\Gamma\gamma a\}$ are given in Table I (supplementary material) as functions of the free ion $|\alpha SLM_L\rangle$. In turn these free ion functions can be expressed as appropriate antisymmetrized combinations of monoelectronic function products, using the fractional parentage coefficients defined and calculated by Racah,[16] i.e.:

$$|\mathrm{d}^3\alpha SL\rangle = \sum_{\bar\alpha \bar S \bar L} \langle \mathrm{d}^2(\bar\alpha \bar S \bar L)\mathrm{d}\alpha SL\}\, \mathrm{d}^3\alpha SL)|\, \mathrm{d}^2(\bar\alpha \bar S \bar L)\mathrm{d}\alpha SL\rangle \quad (8)$$

It is convenient to note that the crystal field eigenfunctions we have stated in Table I are equally adequate for calculating the effects of the interelectronic repulsion term in the free ion, since the interelectronic repulsion potential commutes with any symmetry operator of the group D_{3h} (in general, it commutes with the symmetry operators of any of the 32 puntual groups that can represent a crystal field symmetry).

Calculation of the Crystal Field Matrices

To calculate the complete matrices of a Hamiltonian such as that expressed in (1) we only have to add the free ion interelectronic repulsion matrix

$$\langle \mathrm{d}^3\alpha SL\Gamma\gamma a \left| \sum_{i>j} \frac{1}{r_{ij}} \right| \mathrm{d}^3\alpha' S'L'\Gamma'\gamma' a'\rangle = \delta_{\Gamma\Gamma'}\delta_{\gamma\gamma'}\delta_{aa'}\delta_{LL'}\delta_{SS'} \langle \mathrm{d}^3\alpha SL \left| \sum_{i>j} \frac{1}{r_{ij}} \right| \mathrm{d}^3\alpha' SL\rangle \quad (9)$$

to that of the crystal field. The calculation of this last matrix is not difficult using tensorial operator techniques:

$$\langle \mathrm{d}^3\alpha SL\Gamma\gamma a|\, V_{D_{3h}} |\mathrm{d}^3\alpha' S'L'\Gamma'\gamma' a'\rangle = \delta_{\Gamma\Gamma'}\delta_{\gamma\gamma'}\delta_{aa'}\delta_{SS'} \times \sum_{M_L M'_L} \langle \alpha SL\Gamma\gamma a|\alpha SLM_L\rangle \langle \alpha' S'L'M'_L|\alpha' S'L'\Gamma'\gamma' a'\rangle \times (-1)^{L-M_L} \sum_{k=0,2,4} h_{k0}(3\mathrm{d}; 3\mathrm{d}) \times \begin{pmatrix} L & k & L' \\ -M_L & 0 & M'_L \end{pmatrix} \langle \mathrm{d}^3\alpha SL||\hat C^{(k)}||\mathrm{d}^3\alpha' S'L'\rangle \quad (10)$$

where $h_{k0}(3\mathrm{d}; 3\mathrm{d})$ has the following values, according to whether $k = 0$, 2, or 4:

$k = 0$

$$h_{00}(3\mathrm{d}; 3\mathrm{d}) = 3q_1 G_1^{(0)}(3\mathrm{d}; 3\mathrm{d}) + 2q_2 G_2^{(0)}(3\mathrm{d}; 3\mathrm{d}) \quad (11)$$

$k = 2$

$$h_{20}(3\mathrm{d}; 3\mathrm{d}) = -\frac{3}{2} q_1 G_1^{(2)}(3\mathrm{d}; 3\mathrm{d}) + 2q_2 G_2^{(2)}(3\mathrm{d}; 3\mathrm{d}) \quad (12)$$

$k = 4$

$$h_{40}(3\mathrm{d}; 3\mathrm{d}) = \frac{9}{8} q_1 G_1^{(4)}(3\mathrm{d}; 3\mathrm{d}) + 2q_2 G_2^{(4)}(3\mathrm{d}; 3\mathrm{d}) \quad (13)$$

and $G_i^{(k)}(3\mathrm{d}; 3\mathrm{d})$ is given by the general expression[17]

$$G_i^{(k)}(nl; n'l') = \int_0^\infty R_{nl} \frac{r_{i>}^k}{r_{i>}^{k+1}} R_{n'l'} r^2\, \mathrm{d}r \quad (14)$$

The form of the reduced matrix element is

$$\langle \mathrm{d}^3\alpha SL||\hat C^{(k)}||\mathrm{d}^3\alpha' S'L'\rangle = \delta_{SS'} 15 \sqrt{(2L+1)(2L'+1)} \times \begin{pmatrix} 2 & k & 2 \\ 0 & 0 & 0 \end{pmatrix} \sum_{\substack{\bar\alpha \bar S \bar L \\ \bar\alpha' \bar S' \bar L'}} (-1)^{L_1+k+L} \langle \mathrm{d}^3\alpha SL\, \{\mathrm{d}^2(\bar\alpha \bar S \bar L)\mathrm{d}\alpha SL\rangle \times \langle \mathrm{d}^2(\bar\alpha' \bar S' \bar L')\mathrm{d}\alpha' S'L'\}\mathrm{d}^3\alpha' S'L'\rangle \begin{Bmatrix} L_1 & 2 & L \\ k & L' & 2 \end{Bmatrix} \times \delta_{\bar\alpha\bar\alpha'}\delta_{\bar S\bar S'}\delta_{\bar L\bar L'} \quad (15)$$

However, considering the definition of unitary tensor[18] and the relation

$$\langle \mathrm{d}^3\alpha SL||\hat C^{(k)}||\mathrm{d}^3\alpha' S'L'\rangle = 5 \begin{pmatrix} 2 & k & 2 \\ 0 & 0 & 0 \end{pmatrix} \langle \mathrm{d}^3\alpha SL||\hat U^{(k)}||\mathrm{d}^3\alpha' S'L'\rangle \quad (16)$$

Nielson and Koster's tables[19] can be used.

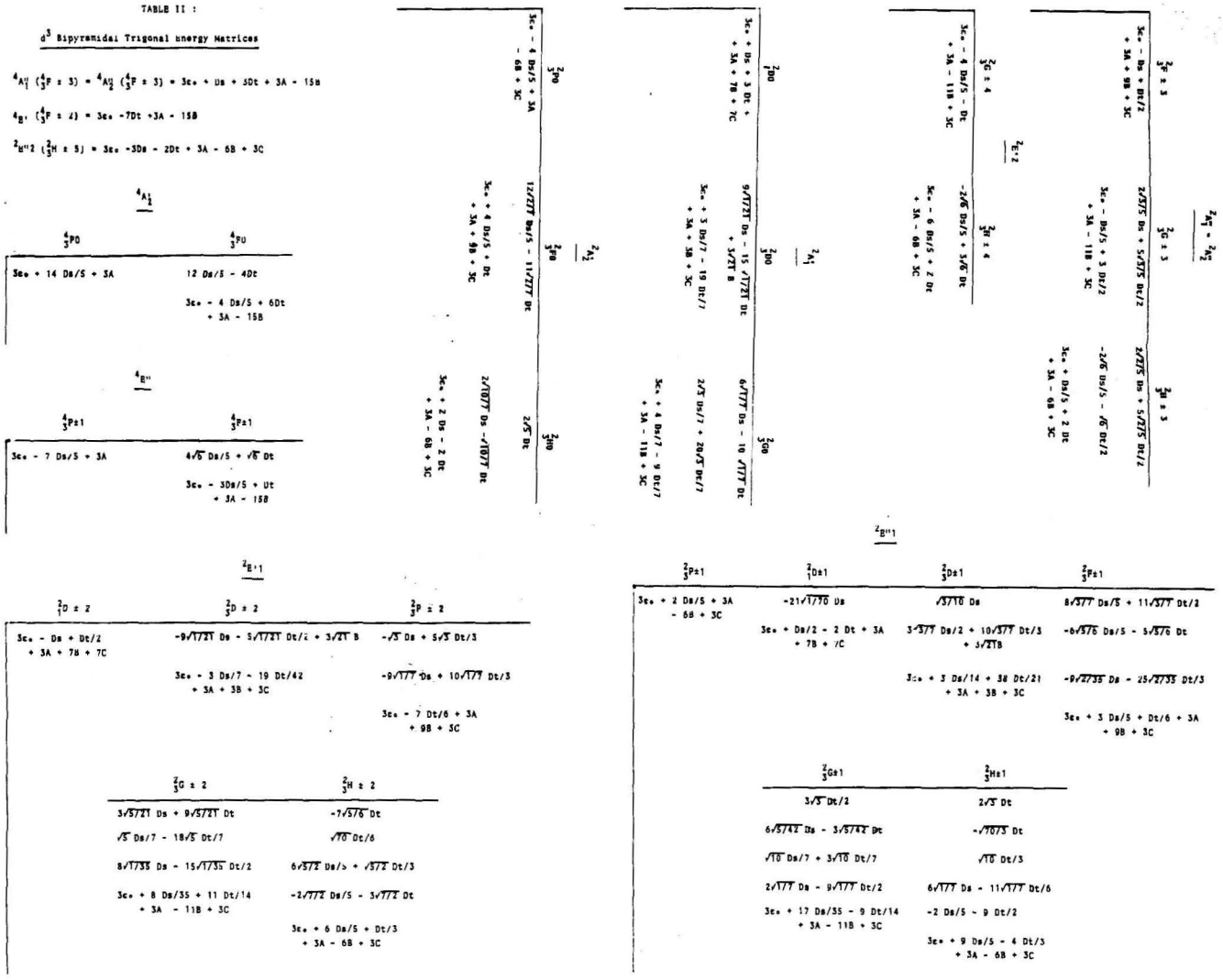

In Appendix II (supplementary material) the $\langle d^3\alpha SL||\hat{C}^{(k)}||d^3\alpha'S'L'\rangle$ coefficients are given. In Table II we give the complete matrices (expression 9 and expression 10) for the d^3 configuration in the $\{\alpha SL\Gamma\gamma a\}$ basis as function of Racah's parameters A, B, and C[20] and the ϵ_0, Ds, and Dt crystal field parameters.

We remark that this ϵ_0, Ds, and Dt crystal field parameters[7,10] and our h_{k0} ($k = 0, 2, 4$) ones are simply related by

$$h_{00} = \epsilon_0 \quad h_{20} = 7Ds \quad h_{40} = 21Dt \tag{17}$$

Also, there is a simple relation between our h_{k0} ($k = 0, 2, 4$) parameters and those used by Becker and co-workers:[21]

$$h_{20} = 7Db/2 \quad h_{40} = 75Dq/4 \tag{18}$$

The energy matrices for the d^7 configuration can be obtained from those of Table II (miniprint; see paragraph at end of text regarding supplementary material) by changing the sign of the ϵ_0, Ds, and Dt parameters.

Check of the Energy Matrices with Those of Strong Field

The weak field matrices of Table II have been checked with the corresponding strong field ones.[7] As they are related to one another by a similarity transformation, the trace should be conserved for each matrix. Besides, considering that the Hamiltonian used in both cases is the same, a complete diagonalization of each matrix, with the same values of the parameters, will, in turn, give the same energy eigenvalues. Every matrix given in Table II fulfilled the checking procedures.[22]

Acknowledgments. The authors are very much indebted to Professor D. Gonzalez for his helpful discussions and to Professor T. M. Dunn and R. Alcalá for the critical reading of the paper. One of us (F.P.) acknowledges gratefully a fellowship from the Ministerio de Educación y Ciencia.

Supplementary and Miniprint Material Available: Table I ($d^{3,7}$ eigenfunctions) and two Appendices (rotation matrix $D^5_{M'M}(\alpha, \beta, \gamma)$ and reduced C^k ($k = 0, 2, 4$) tensor matrix elements) (10 pages) and full-size photocopies of Table II (5 pages). Ordering information is available on any current masthead page.

References and Notes

(1) See, for example, (a) A. D. Liehr, *J. Phys. Chem.*, **64**, 43 (1960); (b) C. J. Ballhausen, *K. Dan. Vidensk. Selsk., Mat. Fys. Medd.*, **29**, no. 4 (1954); (c) *ibid.*, no. 8 (1955); (d) Y. Tanabe and S. Sugano, *J. Phys. Soc. Jpn.*, **9**, 753 (1954); (e) A. D. Liehr and C. J. Ballhausen, *Ann. Phys.*, **6**, 134 (1959); (f) R. N. Euwema, *J. Chem. Phys*, **42**, 892 (1965); (g) J. C. Eisenstein, *ibid.*, **34**, 310 (1961); (h) *ibid.*, **34**, 1628 (1961) (erratum, *ibid.*, **35**, 2246 (1961)); (i) W. A. Runciman and K. A. Schroeder, *Proc. R. Soc. London, Ser. A*, **265**, 489 (1962); (j) J. Ferguson, *Aust. J. Chem.*, **23**, 635 (1970); (k) H. A. Weakliem, *J. Chem. Phys.*, **36**, 2117 (1962); (l) J. Ferguson, H. J. Guggenheim, and E. R. Krausz, *Aust. J. Chem.*, **22**, 1809 (1969); (m) K. A.

Schroeder, *J. Chem. Phys.*, **37**, 2553 (1962); (n) T. M. Dunn and W.-K. Li, *ibid.*, **47**, 3783 (1967) (erratum, *ibid.*, **53**, 2132 (1970); E. R. Krausz, *ibid.*, **53**, 2131 (1970)); (o) W.-K. Li, *Spectrochim. Acta, Part A*, **24**, 1573 (1968); (p) K. A. Schroeder, *J. Chem. Phys.*, **37**, 1587 (1962).
(2) (a) J. Otsuka, *J. Phys. Soc. Jpn.*, **21**, 596 (1966) (erratum, *ibid.*, **21**, 1229 (1966)); (b) H. Kammer, *Acta Chim. Acad. Scient. Hung.*, **66**, 189 (1970); (c) A. B. P. Lever and B. R. Hollebone, *J. Am. Chem. Soc.*, **94**, 1816 (1972); (d) G. Maki, *J. Chem. Phys.*, **28**, 651 (1958); (e) R. F. Fenske, D. S. Martin, Jr., and K. Ruedenberg, *inorg. Chem.*, **1**, 441 (1962); (f) M. Flato, *J. Mol. Spectrosc.*, **17**, 300 (1965); (g) J. R. Perumareddi, *Z. Naturforsch. A*, **27**, 1820 (1972); (h) *J. Phys. Chem.*, **76**, 3401 (1972); (i) H. U. Rahman and W. A. Runciman, *J. Phys. C*, **4**, 1576 (1971); (j) J. R. Perumareddi, *Z. Naturforsch. A*, **28**, 1247 (1973); (k) *J. Phys. Chem.*, **71**, 3144 (1967); (l) *Coord. Chem. Rev.*, **4**, 73 (1969); (m) H. U. Rahman, *Physica*, **53**, 256 (1971); (n) J. R. Perumareddi, *J. Phys. Chem.*, **78**, 2678 (1974).
(3) (a) M. Ciampolini, *Inorg. Chem.*, **5**, 35 (1966); (b) R. Polak and V. Cerny, *J. Phys. Chem. Solids*, **29**, 945 (1968); (c) S. T. Spees, Jr., J. R. Perumareddi, and A. W. Adamson, *J. Phys. Chem.*, **72**, 1822 (1968).
(4) C. A. L. Becker, D. W. Meek, and T. M. Dunn, *J. Phys. Chem.*, **72**, 3588 (1968).
(5) M. N. S. Murthy, A. P. B. Sinha, and A. S. Apte, *Indian J. Pure Appl. Phys.*, **8**, 473 (1970).
(6) C. A. L. Becker, D. W. Meek, and T. M. Dunn, *J. Phys. Chem.*, **74**, 1568 (1970).
(7) J. A. Varga and C. A. L. Becker, *J. Phys. Chem.*, **76**, 2907 (1972).
(8) M. J. Norgett, J. H. M. Thornley, and L. M. Venanzi, *J. Chem. Soc. A*, 540 (1967).
(9) J. S. Wood, *Inorg. Chem.*, **7**, 852 (1968).
(10) (a) M. Ciampolini and I. Bertini, *J. Chem. Soc. A*, 2241 (1968); (b) J. S. Wood, *Prog. Inorg. Chem.*, **16**, 227 (1972); (c) R. Morassi, I. Bertini, and L. Sacconi, *Coord. Chem. Rev.*, **11**, 343 (1973).
(11) We are giving J. Ferguson's meaning (J. Ferguson, *Prog. Inorg. Chem.*, **12**, 159 (1970)) to the "free atom" type representation, so these matrices will be obtained by complete diagonalization of the hamiltonian $H = H_{re} + H_{so} + V_{CF}$.
(12) We are including the quantum number S in the states characterization to distinguish between different orthogonal functions, however, because S is a motion constant in a crystal field, it will not deal with the expansion coefficients of the functions nor with the matrix elements.
(13) E. König and S. Kremer, *Teor. Chim. Acta*, 32, 27 (1973).
(14) F. A. Cotton, "Chemical Applications of Group Theory", Wiley, New York, N.Y., 1971.
(15) Of course $D^0(\alpha, \beta, \gamma) = 1$ and it is invariant to any rotation. (a) The $J = 1$ matrix has been published by M. Tinkham, "Group Theory and Quantum Mechanics", McGraw-Hill, New York, N.Y., 1964 Chapter 5; (b) The $J = 2$ matrix has been given in ref 4. (c) The $J = 3$ and $J = 4$ matrices have been shown in ref 6.
(16) G. Racah, *Phys. Rev.*, **63**, 367 (1943).
(17) C. J. Ballhausen and E. M. Ancmon, *K. Dan. Vidensk. Selsk., Mat. Fys. Medd.*, **31**, no. 9 (1958).
(18) U. Fano and G. Racah, "Irreducible Tensorial Sets", Academic Press, New York, N.Y., 1959, p 94.
(19) C. W. Nielson and G. F. Koster, "Spectroscopic Coefficients for the p^n, d^n, and f^n Configurations", MIT Press, Boston, Mass., 1963.
(20) G. Racah, *Phys. Rev.*, **62**, 438 (1942).
(21) See ref 4 and 6; however, these authors do not consider the crystal field spherically symmetric term, ϵ_0, because it is the same amount for all levels.
(22) We noted a misprint in the $^2E''$ matrix of ref 7. The $\langle \psi_{25}{}^2E'' | V_{D_{3h}} + H_{re} | \psi_{25}{}^2E'' \rangle$ matrix element should be $3\epsilon_0 - 3Ds - 2Dt + 3A + 3B + 3C - E$.

Experimental Study of the Temperature Dependence of Multicomponent Isothermal Diffusion Coefficients

Robert G. Mortimer* and Biram C. Hicks

Department of Chemistry, Southwestern at Memphis, Memphis, Tennessee 38112 *(Received October 3, 1975)*

Publication costs assisted by Southwestern at Memphis

Multicomponent diffusion coefficients for the system 2,2-dichloropropane–1,1,1-trichloroethane–carbon tetrachloride were measured at temperatures ranging from 25 to 45 °C, using a rotating diaphragm cell technique. Onsager diffusion coefficients were deduced from the data, and were interpreted in terms of a transition-state model theory, which had previously been tested by comparison with measurements at 25 °C. Free energy, enthalpy, and entropy changes of activation were calculated, and found to be equal to 4.9 ± 0.5 kcal mol^{-1}, 2.5 ± 0.4 kcal mol^{-1}, and −7.8 ± 2.0 cal deg^{-1} mol^{-1}. The composition dependence of the Onsager diffusion coefficients was also studied at 40 °C, and was found to indicate the same predominant molecular process of diffusion, exchange in position of two adjacent molecules, as was indicated at 25 °C.

Introduction

Isothermal multicomponent diffusion coefficients have been measured in a variety of liquid systems.[1-5] Such measurements have been reported not only for their inherent interest, but also as tests of model theories of diffusion.[4,6-8] All of the reported measurements, which include measurements on thermodynamically ideal as well as nonideal systems, were made to determine the magnitude of diffusion coefficients and their composition dependence at a single temperature. No studies of the temperature dependence of multicomponent diffusion coefficients seem to be in the literature. The measurements which we now report were undertaken to determine the temperature dependence of the multicomponent diffusion coefficients for a thermodynamically ideal system studied previously[1] and to use these results to test further a model theory of isothermal multicomponent liquid diffusion.[6]

Theory

The liquid diffusion theory of Mortimer and Clark[6] is a transition state theory, based on the assumption that diffusing molecules move from equilibrium positions in a disordered solidlike lattice (quasilattice), through transition states, to new equilibrium positions. It includes not only motions of single molecules, but also correlated motions of pairs of molecules. The predictions of the theory may be summarized by equations for the Onsager diffusion coefficients, L_{ij}

$$L_{ii} = ax_i + bx_i^2 \qquad (1a)$$

$$L_{ij} = bx_i x_j \qquad (i \neq j) \tag{1b}$$

These coefficients occur in the phenomenological relations

$$\mathbf{J}_i = -\sum_{j=1}^{n} L_{ij} \nabla \mu_j \tag{2}$$

where n is the number of chemical components in the system, $\mathbf{J}_i$ is the diffusion flux of component i in the coordinate frame in which the local center of mass is stationary, and μ_j is the chemical potential of component j. A subset of these coefficients is the appropriate set of coefficients for the properly chosen linearly independent forces and fluxes for this coordinate frame.[9] The mole fractions of components i and j are x_i and x_j, and the parameters a and b are

$$a = \frac{c}{Nh} \sum_{\nu} \mathcal{K}_\nu \exp(-\Delta G^\circ_\nu{}^{\ddagger}/RT) z_{\alpha\nu}{}^2 + \frac{c}{Nh} \sum_{\gamma} \mathcal{K}_\gamma \exp(-\Delta G^\circ_\gamma{}^{\ddagger}/RT)(z_{\alpha\gamma}{}^2 + z_{\beta\gamma}{}^2) \tag{3}$$

$$b = \frac{c}{Nh} \sum_{\gamma} \mathcal{K}_\gamma \exp(-\Delta G^\circ_\gamma{}^{\ddagger}/RT) z_{\alpha\gamma} z_{\beta\gamma} \tag{4}$$

Here N is Avogadro's number, h is Planck's constant, c is the total concentration, and ν and γ are indices representing distinct diffusive processes, with ν denoting single-particle processes and γ denoting processes consisting of motions of pairs of particles. The quantity $z_{\alpha\gamma}$ is the projection on the direction of macroscopic diffusion of the displacement of particle α in process γ. In a two-particle process, one particle is arbitrarily called α and the other is called β. The standard state Gibbs free energy change of activation for process γ is called $\Delta G^\circ_\gamma{}^{\ddagger}$, and $\mathcal{K}_\nu$ is a generalized "transmission coefficient," equal to the probability that process ν will be completed once it is begun.

Previously reported measurements[1] tested the agreement of eq 1 with data collected at 25 °C and at various compositions for the system: 2,2-dichloropropane (component 1), 1,1,1-trichloroethane (component 2), and carbon tetrachloride (component 3). Three tests were made: (I) The experimental composition dependence of L_{11} and L_{22} was compared with eq 1a. (II) The experimental composition dependence of L_{12} and L_{21} was compared with eq 1b. (III) The equality of the values of the parameter b from the diagonal and off-diagonal coefficients was tested. All of these tests verified the theoretical predictions within experimental error, and it was also possible to determine that the predominant diffusive process was the exchange in position of two adjacent molecules.

Measurements

Measurements were undertaken on the same system as in ref 1, both at varying temperature with fixed composition and at a different fixed temperature with varying composition, using the same rotating diaphragm cell with horizontal axis as in ref 1. The body of the cell was a glass tube of 25 mm diameter with a fine porosity sintered glass disk of thickness 2 mm fused into it, obtained from the Kontes Glass Co.

Toor[10] found that a diaphragm cell with vertical diaphragm is subject to serious error from convection if the two solutions are not of equal density. However, Toor's analysis does not apply to a rotating diaphragm cell, in which a given element of the disk is sometimes at the top of the cell and sometimes at the bottom, thus having a hydrostatic force of continually reversing direction acting on the fluid in it, instead of the force of fixed direction acting in Toor's cell. The oscillatory convective flow through our disk will be unimportant if the maximum displacement during a half-period of rotation (about 0.5 s) is small compared with the pore length, which cannot be less than the disk thickness.

The maximum convective displacement (at the edge of the disk) was estimated in two ways. First, the hydraulic conductivity of a similar tube was measured and found to be 1.10×10^{-7} cm^2 s g^{-1}. Using the maximum density difference in any of our subexperiments, 0.0867 g cm^{-3}, and the assumption that the total pore area was half the disk area and the average pore length was 4 mm, a maximum displacement estimate of 3×10^{-5} cm was obtained for a half-period of rotation. A different estimate of 5×10^{-4} cm was obtained by using Poiseuille's equation and an average pore radius of 5 μm. Either estimate indicates that the convective flow contributes only to the stirring of the boundary layer near the diaphragm and constitutes a negligible source of error.

Furthermore, the actual density differences were in different directions with respect to the concentration gradients of component 1 or component 2 in different subexperiments, and ranged from 0.0011 g cm^{-3} to 0.0867 g cm^{-3}. Any important contribution to transport by convection would have produced an inconsistency of results which was not observed.

The procedure for the measurements was the same as in ref 1, except that it was impossible to maintain room temperature at the temperature of the experiments. It was found necessary to keep all solutions and the cell at the temperature of the experiment during all filling operations in order to avoid the formation of bubbles during the runs. The cell constant was redetermined and found to be unchanged from its previously determined value of 0.6492 ± 0.0063. All runs were of 18 h duration, as before, but duplicate runs instead of the triplicate runs of ref 1 were made. Final mole fractions were determined by the same gas chromatographic technique as in ref 1. The only important sources of experimental uncertainty were assumed to be the uncertainty in the cell constant and the uncertainties in the final mole fractions. At least five determinations of the final mole fractions were made for each solution, and the ten or more determinations from each pair of duplicate runs were treated as a single statistical sample, since the agreement between duplicate runs was at least as good as the agreement between different determinations from the same diffusion run. Expected errors were calculated at the 95% confidence level, and were propagated through the entire calculation, resulting in the expected errors which are reported at the 95% confidence level for all calculated quantities.

The most difficult part of the data reduction was the calculation of the diffusion coefficients, D_{ij}, which were calculated from the initial and final concentrations. Since there are four independent diffusion coefficients and only two independent mole fractions or concentrations in a three-component mixture, two subexperiments at the same average composition but with different initial concentration differences between the two sides of the cell must be carried out in order to compute the D_{ij}'s for a single composition (which is always taken to be the average composition). If a regression technique[11] is to be used, the data from more than two subexperiments can be used, with a probable reduction of the expected error.

Approximate values of the diffusion coefficients were obtained using the linearized equations of Burchard and Toor.[3] These were used as initial estimates in an iterative procedure to find accurate numerical values as follows: Burchard and Toor's eq 17 was rewritten in the form

$$f_i = 0 \qquad (i = 1, 2, 3, 4) \tag{5}$$

where the four f functions arising from the pair of subexpe-

riments are complicated functions of the initial and final concentration differences, the four diffusion coefficients, the cell constant, and the length of the runs.[3] The values of the D_{ij}'s satisfying eq 5 were found by a vector version of Newton's method,[12] using the initial estimates as a starting point for iteration. In spite of the closeness of these values to the actual roots, the convergence was usually oscillatory, slow, and uncertain. Since a fairly slow computer was being used, the procedure was modified to use Aitken's Δ^2 process,[13] which assigns the value

$$\xi = (x_1x_3 - x_2^2)/(x_3 - 2x_2 + x_1) \quad (6)$$

to the next estimate of a root if x_1, x_2, and x_3 are three successive estimates obtained by some procedure (in our case by Newton's method). In most of our cases, the convergence was then extremely rapid, but one or two experiments remained for which the convergence was oscillatory and very slow. In these cases it proved necessary to experiment with the initial estimates taken for the roots (by taking values produced by various numbers of ordinary Newton iterations as initial estimates) before satisfactory convergence in a reasonable length of time was obtained. In most of the experiments, the final accurate values of the roots were well within experimental error of the initial estimates found by the linearized equations of Burchard and Toor, but in a few cases were different by an amount approximately equal to the expected experimental error.

Since the error propagation was accomplished by multiple repetitions of each stage of the calculations with suitable incremented or decremented values of experimentally uncertain quantities, and since the method of Burchard and Toor was fairly accurate, the error propagation in this part of the calculation was done by the method of Burchard and Toor. The remainder of the data reduction was performed just as in ref 1.

Experiments at Various Temperatures. This first set of experiments used the same nominal initial compositions as experiment II of ref 1. The average mole fraction of 2,2-dichloropropane (component 1) was $\bar{x}_1 = 0.101$, and the average mole fraction of 1,1,1-trichloroethane (component 2) was $\bar{x}_2 = 0.152$. Experiments were conducted at intervals of 5 °C, ranging from 30 to 45 °C. At each temperature, two subexperiments were done, one with initial mole fraction differences $\Delta x_1 = +0.109$ and $\Delta x_2 = +0.115$, and one with initial mole fraction differences $\Delta x_1 = -0.067$ and $\Delta x_2 = +0.231$.

Table I shows the measured diffusion coefficients from the first set of experiments. These coefficients are identified with those in the volume-fixed coordinate frame, since the average molal volumes changed only slightly during an experimental run. Equations of Miller[14] were used to compute the proper linearly independent Onsager diffusion coefficients in the volume frame, and eq 11 of ref 1 and its analogues were used to compute the proper linearly independent Onsager diffusion coefficients in the center-of-mass frame. These coefficients are shown in Table II. The Onsager reciprocal relation

$$L_{12} = L_{21} \quad (7)$$

is obeyed within experimental error at all temperatures. However, at the composition chosen, the magnitude of the off-diagonal coefficients is so small that the coefficients are roughly the same size as their uncertainties. The values of the coefficients at 25 °C are recalculated from ref 1.

Figure 1 shows a plot of the natural logarithm of L_{22} vs. the reciprocal of the absolute temperature. The apparent curvature is smaller than the experimental uncertainties, so that no deviation from the temperature dependence predicted by eq 3 and eq 4 is indicated, if only a single diffusive process is involved. The line in the figure is the least-squares line, and has the slope $(-1.16 \pm 0.15) \times 10^3$ K. The plot of ln (L_{11}) is similar except for having slightly larger deviations from its least-squares line, which has a slope of $(-1.32 \pm 0.36) \times 10^3$ K.

Experiments at Various Compositions at 40 °C. A second set of experiments was conducted to study the composition dependence of the Onsager diffusion coefficients at 40 °C, in order to determine whether the agreement between theory and experiment at 25 °C[1] could be duplicated at a second temperature, and to see if the relationship between the parameters a and b in eq 1 would indicate the predominance of the same molecular diffusion process as at 25 °C.

TABLE I: Diffusion Coefficients ($cm^2\ s^{-1}$) for $\bar{x}_1 = 0.101$, $\bar{x}_2 = 0.152$

	$D_{11} \times 10^5$	$D_{21} \times 10^5$	$D_{12} \times 10^5$	$D_{22} \times 10^5$
Expt 1 25 °C	1.38 ± 0.07	−0.03 ± 0.04	−0.05 ± 0.03	1.41 ± 0.02
Expt 2 30 °C	1.54 ± 0.08	0.08 ± 0.08	0.00 ± 0.04	1.55 ± 0.04
Expt 3 35 °C	1.64 ± 0.08	0.03 ± 0.08	−0.07 ± 0.04	1.66 ± 0.04
Expt 4 40 °C	1.75 ± 0.07	−0.06 ± 0.07	−0.01 ± 0.04	1.81 ± 0.04
Expt 5 45 °C	2.05 ± 0.11	0.11 ± 0.13	0.05 ± 0.05	2.02 ± 0.05

TABLE II: Mass Frame Onsager Coefficients ($mol^2\ cm^{-1}\ s^{-2}\ cal^{-1}$)

	$L_{11} \times 10^{11}$	$L_{21} \times 10^{11}$	$L_{12} \times 10^{11}$	$L_{22} \times 10^{11}$
Expt 1 25 °C	2.27 ± 0.13	−0.28 ± 0.08	−0.37 ± 0.09	3.29 ± 0.07
Expt 2 30 °C	2.48 ± 0.15	−0.12 ± 0.16	−0.26 ± 0.12	3.46 ± 0.13
Expt 3 35 °C	2.58 ± 0.15	−0.31 ± 0.15	−0.43 ± 0.12	3.65 ± 0.13
Expt 4 40 °C	2.70 ± 0.12	−0.37 ± 0.12	−0.47 ± 0.11	3.88 ± 0.12
Expt 5 45 °C	3.08 ± 0.19	−0.13 ± 0.22	−0.32 ± 0.16	4.21 ± 0.16

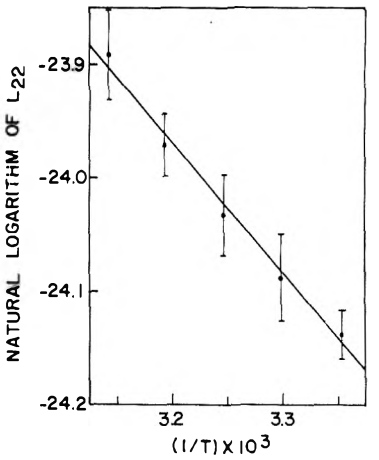

Figure 1. The logarithm of a diagonal Onsager diffusion coefficient, L_{22} ($mol^2\ cm^{-1}\ s^{-1}\ cal^{-1}$), vs. reciprocal temperature.

TABLE III: Average Mole Fractions ($\bar{x}_i$) and Initial Mole Fraction Differences (Δx_i)

Expt No.	$\bar{x}_1$	Δx_1	$\bar{x}_2$	Δx_2
4-1	0.1010	+0.1093	0.1522	+0.1145
4-2	0.1009	−0.0675	0.1524	+0.2310
6-1	0.2381	+0.0790	0.7002	−0.1559
6-2	0.2381	+0.0848	0.7002	−0.0013
7-1	0.1915	−0.1656	0.4569	+0.1211
7-2	0.1915	+0.1346	0.4569	+0.0486

TABLE IV: Diffusion Coefficients ($cm^2\ s^{-1}$) at 40 °C

$D_{11} \times 10^5$	$D_{21} \times 10^5$	$D_{12} \times 10^5$	$D_{22} \times 10^5$
Expt 4 ($\bar{x}_1 = 0.101, \bar{x}_2 = 0.152$)			
1.75 ± 0.07	−0.06 ± 0.07	−0.01 ± 0.04	1.81 ± 0.04
Expt 6 ($\bar{x}_1 = 0.2381, \bar{x}_2 = 0.7002$)			
1.75 ± 0.13	0.02 ± 0.25	−0.11 ± 0.09	1.88 ± 0.18
Expt 7 ($\bar{x}_1 = 0.1915, \bar{x}_2 = 0.4569$)			
1.79 ± 0.05	−0.12 ± 0.09	−0.05 ± 0.08	1.74 ± 0.15

TABLE V: Mass Frame Onsager Coefficients ($mol^2\ cm^{-1}\ s^{-2}\ cal^{-1}$) at 40 °C

$L_{11} \times 10^{11}$	$L_{21} \times 10^{11}$	$L_{12} \times 10^{11}$	$L_{22} \times 10^{11}$
Expt 4 ($\bar{x}_1 = 0.101, \bar{x}_2 = 0.152$)			
2.54 ± 0.12	−0.54 ± 0.12	−0.63 ± 0.11	3.74 ± 0.12
Expt 6 ($\bar{x}_1 = 0.2381, \bar{x}_2 = 0.7002$)			
5.74 ±0.83	−4.12 ± 1.74	−4.46 ± 1.10	5.27 ± 2.31
Expt 7 ($\bar{x}_1 = 0.1915, \bar{x}_2 = 0.4569$)			
4.83 ± 0.30	−2.08 ± 0.58	−2.14 ± 0.53	7.29 ± 1.02

The average compositions and initial mole fraction differences are shown in Table III. Three different compositions were studied, including the composition already studied at 40 °C in the first set of experiments (experiment 4).

Table IV shows the diffusion coefficients measured at 40 °C, and Table V shows the center-of-mass frame Onsager diffusion coefficients computed from them. Again, the Onsager reciprocal relation is obeyed at the 95% confidence level at each composition.

Figure 2 shows the diagonal Onsager diffusion coefficients, L_{11} and L_{22}, as a function of mole fraction, with both coefficients plotted on the same graph. The curve shown is the least-squares parabola of zero intercept. All of the points lie within experimental error of the curve except the value of L_{11} from experiment 4. The values of the parameters a and b which are obtained from the least-squares fit are

$$a = (31.65 \pm 4.91) \times 10^{-11}\ mol^2\ cm^{-1}\ s^{-1}\ cal^{-1} \quad (8a)$$

$$-b = (34.40 \pm 3.61) \times 10^{-11}\ mol^2\ cm^{-1}\ s^{-1}\ cal^{-1} \quad (8b)$$

The uncertainties here were obtained by considering the expected errors in the six coefficients used in Figure 2 as a statistical sample. If the residuals from the least-squares fit were used as a sample, the expected errors would be smaller. The correlation coefficient of the least-squares fit was 0.9985.

Figure 3 shows L_{12} and L_{21} as a function of x_1x_2, the product of the two mole fractions. The broken line shown is the line with zero intercept and slope equal to $-b$ from eq 8b. The solid line is the least-squares line of zero slope determined by the six data points on the graph. The difference between the two lines is approximately the same size as the expected experimental errors in the L_{12}'s and L_{21}'s, and satisfactory agreement would be obtained if the slope of the broken line were lowered by its expected error.

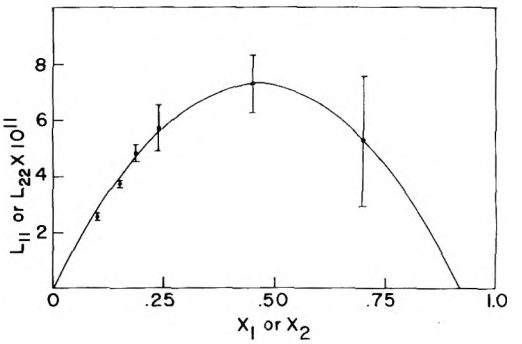

Figure 2. The diagonal Onsager diffusion coefficients, L_{11} and L_{22} ($mol^2\ cm^{-1}\ s^{-1}\ cal^{-1}$), vs. mole fraction.

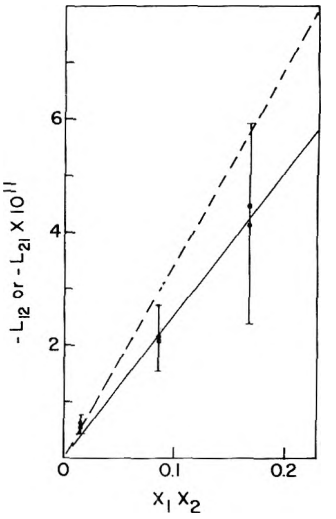

Figure 3. The off-diagonal Onsager diffusion coefficients, L_{12} and L_{21} ($mol^2\ cm^{-1}\ s^{-1}\ cal^{-1}$), vs. the mole fraction product, x_1x_2.

Discussion

With the results just presented, we have four tests of the theory which we can undertake (with the first three being the same as in ref 1): (I) we can compare the composition dependence of the diagonal Onsager coefficients with eq 1a; (II) we can compare the composition dependence of the off-diagonal coefficients with the predictions of eq 1b; (III) we can compare values of the off-diagonal coefficients with the predictions of eq 1b using the value of the parameter b from the diagonal coefficients; and (IV) we can compare the temperature dependence of the coefficients with the predictions of eq 3 and eq 4. We can also calculate the change in enthalpy, Gibbs free energy, and entropy of activation for the main diffusive process, since it again appears that a single process does predominate.

Test I: Figure 2 shows that the data at 40 °C agree with the prediction of eq 1a within experimental error. The composition dependence is fit by the parabola having the values given in eq 6 with a correlation coefficient of 0.9985.

Test II: Figure 3 shows that the data at 40 °C correspond to a linear dependence of L_{12} and L_{21} on the mole fraction product x_1x_2, within experimental error.

Test III: Figure 3 also shows that a marginal agreement between the numerical values of L_{12} and L_{21} and the values predicted by eq 1a using the value of b from the L_{11} and L_{22}

data is obtained. This agreement is not as good as was found at 25 °C.[1]

Test IV: This test is connected with the determination of the predominant molecular diffusion process. From eq 3 and eq 4, it is apparent that if a variety of molecular processes with different free energy changes of activation are important, a curvature in the plot of ln (L_{ij}) will result. The plot would be linear if a single process predominates, or if only processes having the same free energy changes of activation are important.

In ref 1, the relative experimental values of a and b were interpreted to indicate that only one molecular process, the exchange in position of two adjacent molecules, contributed significantly. This followed because only this process can in the assumed body-centered cubic close-packed lattice lead to contributions to $-b$ which are as large as the contributions to a. The values of a and b found at 25 °C were nearly equal in magnitude and opposite in sign.

In Figure 1, no significant curvature is found in the plot of ln (L_{22}) vs. $1/T$. This is in agreement with the conclusion that only a single molecular diffusion process is important at 25 °C. We conclude that the temperature dependence of the present data agrees with the predictions of the model theory of Mortimer and Clark[6] and that the molecular exchange process predominates in the temperature range from 25 to 45 °C. The composition dependence of the Onsager diffusion coefficients at 40 °C also is in agreement with this conclusion, with the values of a and $-b$ being equal within experimental error, as shown in Figures 2 and 3.

It is now possible to estimate changes in thermodynamic quantities for the predominant activation process. We delete all terms from eq 3 except those for the molecular exchange processes, and write

$$a \approx \frac{c}{Nh} \sum_{\gamma \in c} \mathcal{K}_\gamma \exp(-\Delta G^{\circ}{}_\gamma{}^{\ddagger}/RT)(z_{\alpha\gamma}{}^2 + z_{\beta\gamma}{}^2) \qquad (9)$$

where the sum now includes only terms for the exchange processes, which were called processes of type c in ref 6. From eq 17 of ref 1, eq 9 gives

$$a \approx \frac{24cz^2}{Nh} \mathcal{K}_c \exp(-\Delta G^{\circ}{}_c{}^{\ddagger}/RT) \qquad (10)$$

where we assume that the transmission coefficient, $\mathcal{K}_c$, is the same for all processes of type c, which differ only in direction of motion. The Gibbs free energy of activation, $\Delta G^{\circ}{}_c{}^{\ddagger}$, is also assumed to be the same for all of these processes. The nearest-neighbor lattice spacing is denoted by z.

Since the pressure was constant in our measurements,

$$\partial \ln (L_{ii})/\partial(1/T) = \partial \ln \mathcal{K}_c/\partial(1/T) - \Delta H^{\circ}{}_c{}^{\ddagger}/R \qquad (11)$$

where we assume that $\Delta H^{\circ\ddagger}$ is the same for all processes of type c.

The generalized transmission coefficient, $\mathcal{K}_c$, poses a problem, since it is subject neither to separate experimental measurement nor to practical theoretical estimation. We assume the same value of $\mathcal{K}_c$ assumed in ref 1, $\mathcal{K}_c \approx 0.1$, and assume it to be temperature independent. With this assumption, the average of the slopes of the least-squares lines for L_{11} and L_{22} gives

$$\Delta H^{\circ}{}_c{}^{\ddagger} = 2.46 \pm 0.42 \text{ kcal mol}^{-1} \qquad (12)$$

where the estimated experimental uncertainty was obtained using the 95% confidence limits on the Onsager diffusion coefficients, not the residuals in the least-squares fits.

With our estimate for $\mathcal{K}_c$, we can substitute into eq 10 and obtain an experimental value for $\Delta G^{\circ}{}_c{}^{\ddagger}$. Fortunately, $\Delta G^{\circ}{}_c{}^{\ddagger}$ is not very sensitive to the value taken for $\mathcal{K}_c$, but a realistic estimated error for $\Delta G^{\circ}{}_c{}^{\ddagger}$ is hard to obtain, since it is primarily due to uncertainty in $\mathcal{K}_c$. If we assume that $\mathcal{K}_c$ is within a factor of 2.5 of 0.1, an error of 0.5 kcal mol^{-1} is expected in $\Delta G^{\circ}{}_c{}^{\ddagger}$. We take a value of 5.73 Å for the solid-state nearest-neighbor lattice distance in CCl_4 as our value of z, as in ref 1, and obtain

$$\Delta G^{\circ}{}_c{}^{\ddagger} = 4.85 \pm 0.5 \text{ kcal mol}^{-1} \qquad (13)$$

This value is an average of 4.82 kcal mol^{-1}, obtained from the 25 °C data of ref 1, and 4.88 kcal mol^{-1}, obtained from the 40 °C data.

We can now compute $\Delta S_c{}^{\ddagger}$, again assumed to be the same for all processes of type c, and obtain

$$\Delta S^{\circ}{}_c{}^{\ddagger} = -7.82 \pm 2.0 \text{ cal deg}^{-1} \text{ mol}^{-1} \qquad (14)$$

These values for the changes of thermodynamic functions for the activation process seem plausible. One would expect a negative entropy change of activation, as the transition state (a state of maximum potential energy) is expected to be more highly ordered than an equilibrium state (a state of minimum potential energy).

Acknowledgment. The authors gratefully acknowledge partial support from a Cottrell College Science Grant of the Research Corporation, and thank Dr. Richard Wendt for bringing the conclusions of ref 10 to their attention.

References and Notes

(1) R. G. Mortimer, W. R. Marlow, and J. L. Shenep, *Ind. Eng. Chem., Fundam.*, **14**, 114 (1975).
(2) R. P. Wendt and M. Shamim, *J. Phys. Chem.*, **74**, 2770 (1970).
(3) J. K. Burchard and H. L. Toor, *J. Phys. Chem.*, **66**, 2015 (1962).
(4) T. K. Kett and D. K. Anderson, *J. Phys. Chem.*, **73**, 1262, 1268 (1969).
(5) E. L. Cussler, Jr., and P. J. Dunlop, *J. Phys. Chem.*, **70**, 1880 (1966).
(6) R. G. Mortimer and N. H. Clark, *Ind. Eng. Chem., Fundam.*, **10**, 604 (1971).
(7) H. T. Cullinan, Jr., and M. R. Cusick, *Ind. Eng. Chem., Fundam.*, **6**, 72 (1967).
(8) P. C. Carman, *Ind. Eng. Chem., Fundam.*, **12**, 484 (1973).
(9) S. R. DeGroot and P. Mazur, "Non-Equilibrium Thermodynamics", North Holland Publishing Co., Amsterdam, 1962.
(10) H. L. Toor, *Ind. Eng. Chem., Fundam.*, **6**, 454 (1975).
(11) P. R. Patel, E. C. Moreno, and T. M. Gregory, *J. Res. Natl. Bur. Stand., Sect. A*, **73**, 43 (1969).
(12) R. E. Williamson, R. H. Cromwell, and H. F. Trotter, "Calculus of Vector Functions", 3rd ed, Prentice-Hall, Englewood Cliffs, N.J., 1972, p 266.
(13) S. D. Conte, "Elementary Numerical Analysis", McGraw-Hill, New York, N.Y., 1965, p 27.
(14) D. G. Miller, *J. Phys. Chem.*, **63**, 570 (1959).

Relaxation Time of Dipole Orientation Around a Localized Excess Electron in Alcohols

Kenji Fueki,

Department of Synthetic Chemistry, Faculty of Engineering, Nagoya University, Nagoya, Japan

Da-Fei Feng,

Department of Chemistry, University of California, Davis, California 95616

and Larry Kevan*

Department of Chemistry, Wayne State University, Detroit, Michigan 48202 *(Received December 15, 1975)*

An improved method is developed for calculation of relaxation times for dipole orientation in liquid alcohols induced by localized excess electrons. The dielectric relaxation of the medium beyond the first solvation shell of the electron is explicitly incorporated. Results are presented for methanol, ethanol, and 1-propanol and compared to recent experiments. Although this increases the calculated relaxation times compared to calculations neglecting medium relaxation, the improvement in comparison with experimental values is small. This implies that orientational relaxation of molecular dipoles in the first solvation shell around a localized electron proceeds first and then the dielectric relaxation of the medium beyond the first solvation shell occurs to complete the electron solvation. The calculated temperature dependence for electron solvation in 1-propanol is non-Arrhenius and fits well with recent experimental data.

Introduction

The solvation time of electrons in polar liquids is currently one of the central problems in radiation chemistry. Recent developments in pulse radiolysis techniques have made it possible to directly observe changes in solvated electron spectra with time on nano- to picosecond time scales.[1-3] A theoretical study of electron solvation time based on a molecular model was first made by Fueki, Feng, and Kevan[4] utilizing quantities calculated from the Fueki, Feng, and Kevan semicontinuum model for solvated electrons.[5] In that study, we were able to predict the magnitude and temperature dependence of the solvation time of localized excess electrons or trapped electrons in liquid alcohols in reasonable agreement with experiment. For mathematical simplicity, the excess electronic charge distribution was assumed to be constant during dipole relaxation. Recently Tachiya and Mozumder[6] have considered explicitly a change in the charge distribution with dipole rotation in the electron solvation process. In their model, however, long-range electron–solvent interactions are neglected. Such an assumption does not seem justified for solvated electrons in strongly polar liquids such as alcohols. Also, such a model certainly overestimates the change in the charge distribution with dipole relaxation. In addition, they assumed zero cavity radius for the localized electrons which is not justified.

In this work, we develop a more refined theoretical treatment of the electron solvation rate, taking into account both the orientational relaxation of molecular dipoles in the first solvation shell around a trapped electron and the dielectric relaxation of the continuous medium beyond the first solvation shell, and apply it to solvated electrons in liquid methanol, ethanol, and 1-propanol.

Outline of Calculation

In this section we describe a method of calculation for the electron solvation time or the orientational relaxation time of molecular dipoles around a trapped electron. The rate of change in dipole orientation angle θ is given by[4]

$$\zeta \frac{d\theta}{dt} = -\mu \frac{C_{1s} e}{(r_d^0)^2} \sin \theta \tag{1}$$

where $-e$ is the electronic charge; μ is the permanent molecular dipole moment; ζ is the internal friction constant, $\zeta = 8\pi\eta a^3$ (η is the microscopic viscosity and a is the rotational radius of the molecule); r_d^0 is the distance between the center of a cavity and the center of a dipole in the first solvation shell at the configurational minimum; C_{1s} is the charge enclosed within r_d^0 for the ground state of a trapped electron. We have assumed that the radius changes are fast compared with the orientation changes so that r_d^0 is determined by the instantaneous dipole orientation. This seems justified based on recent ENDOR experiments on trapped electrons in which it is shown that the radius changes are small (<10%) during the process of electron solvation.[7]

Equation 1 is coupled with time dependent dielectric polarization in the continuous dielectric medium through C_{1s} and r_d^0. In solving eq 1, we start with the initial conditions: dipole orientation angle, θ_0, and high frequency dielectric constant, ϵ_∞. The time, $\tau_{\Delta\theta}$, required for a very small change, $\Delta\theta$, in dipole orientation angle, θ, can be expressed as[4]

$$\tau_{\Delta\theta} = \frac{\zeta (r_{d(0)}^0)^2}{\mu C_{1s(0)} e} \ln \left[\frac{\tan (\theta_0/2)}{\tan (\theta_1/2)} \right] \tag{2}$$

where $\theta_1 = \theta_0 - \Delta\theta$; $r_{d(0)}^0$ and $C_{1s(0)}$ are, respectively, the cavity radius at the configurational minimum and the charge enclosed within r_d^0 which can be determined from a semicontinuum model calculation[5] for θ_0 and ϵ_∞. Next, we calculate $r_{d(\Delta\theta)}^0$ and $C_{1s(\Delta\theta)}$ from the semicontinuum model with parameters θ_1 and ϵ_1. Here ϵ_1 is given by[8,9]

$$\epsilon(t) = \epsilon_\infty \left[1 - \left(1 - \frac{\epsilon_\infty}{\epsilon_s} \right) \left(1 - \exp \left[-t/\tau_1' \right] \right) \right]^{-1} \tag{3}$$

with $t = \tau_{\Delta\theta}$, $\tau_1' = \epsilon_\infty \tau_1 / \epsilon_s$ where τ_1 is the dielectric relaxation time which is attributed to hydrogen bond breaking processes,[10] and ϵ_s is the static dielectric constant. The time, $\tau_{2\Delta\theta}$, required for dipole orientation from θ_1 to θ_2 is then obtained where $\theta_2 = \theta_1 - \Delta\theta$. We cycle this procedure until the dipole

orientation angle attains the thermal equilibrium value, $\theta_{th} = \theta_n = \theta_{n-1} - \Delta\theta$.

Summing up all the relaxation time elements, $\tau_{j\Delta\theta}$ ($j = 1, 2, \ldots, n$), we obtain the dipole relaxation time around a trapped electron or the electron solvation time from

$$\tau_r = \sum_{j=1}^{n} \tau_{j\Delta\theta}$$

$$\tau_{j\Delta\theta} = \frac{\zeta(r_d^0(j-1)\Delta\theta)^2}{\mu C_{1s((j-1)\Delta\theta)}} \ln\left[\frac{\tan(\theta_{j-1/2})}{\tan(\theta_{j/2})}\right] \quad (4)$$

The physical constants used in the calculations are the same as those in the previous paper[4] and θ_0 is taken as 80° and $\Delta\theta = 1°$. Note that we have used the experimental macroscopic viscosity for the microscopic viscosity in eq 1. The values of τ_1' used are given elsewhere; see paragraph at the end of text regarding supplementary material.

We should comment that eq 3 applies strictly to conditions of constant electric displacement while under our conditions we have constant electric charge. However, the charge distribution $C_{1s}(R_0)$, where R_0 is the distance at which the dielectric continuum begins, changes only about 10% over the entire time range studied. The change in $C_{1s}(R)$ is even less for $R > R_0$. Therefore, the electric displacement is approximately constant and eq 3 is approximately valid.

Results and Discussion

The results of the calculations are given in Tables I and II and Figures 1–7.

A. *Electron Solvation Time.* Figures 1–3 show, respectively, the orientational relaxation time of molecular dipoles in the first solvation shell as a function of dipole orientation angle for trapped electrons in methanol, ethanol, and 1-propanol at room temperature. In these figures, N is the number of solvent molecules in the first solvation shell and θ_{th} is the thermal equilibrium angle of dipole orientation. It is seen that the time required for rotation of dipoles from θ_0 to a certain angle is greater for $N = 6$ than for $N = 4$. The dipole relaxation time, τ_r, increases in the order: methanol, ethanol, and 1-propanol. The calculated values of τ_r are given in Table I for trapped electrons in these alcohols at various temperatures. The τ_r values obtained in this work are only about 25% greater than those in the previous work.[4] In Table II are given the values of τ_r obtained in the present and previous calculations along with the observed electron solvation time, τ_{sol}.[11]

Although the improved model in this paper gives slightly better agreement with experiment, the improvement is not adequate to warrant the additional calculational complexity. It appears that neglect of the dielectric relaxation of the medium beyond the first solvation shell of the electron is an acceptable approximation.

Although the agreement of the calculated and experimental solvation times is not quantitative, the remarkable point is that better than order of magnitude agreement is found with *no* adjustable parameters. This suggests that simple dipole orientation of first solvation shell polar molecules plays the dominant role in electron solvation.

A quantitative comparison of τ_{sol} with τ_r reveals that the observed solvation time τ_{sol} is greater than that of τ_r by a factor of 4.5 for methanol, 2.8 for ethanol, and 1.7 for 1-propanol. This suggests that the present model is better for larger alcohols. This perhaps reflects the fact that our use of the macroscopic viscosity for the microscopic viscosity in eq 1 is more valid for the larger alcohols. However, we caution that the model may well fail when the solvent molecules attain such size that they can no longer be regarded as simple point dipoles.

One might also ask if this model can be extended to glassy matrices in which electron solvation times have also been measured.[12] The answer is no; the calculated relaxation times

TABLE I: Relaxation Time of Dipole Orientation by Solvated Electrons in Alcohols

	τ_r, s	
T, K	$N = 4$	$N = 6$
	Methanol	
160	9.90×10^{-11}	1.28×10^{-10}
183	2.81×10^{-11}	3.62×10^{-11}
195	1.70×10^{-11}	2.19×10^{-11}
243	4.32×10^{-12}	5.44×10^{-12}
294	1.83×10^{-12}	2.25×10^{-12}
	Ethanol	
140	4.02×10^{-9}	5.42×10^{-9}
155	8.47×10^{-10}	1.14×10^{-9}
173	2.25×10^{-10}	3.00×10^{-10}
195	7.34×10^{-11}	9.62×10^{-11}
234	2.03×10^{-11}	2.65×10^{-11}
296	6.08×10^{-12}	7.81×10^{-12}
	1-Propanol	
147	1.38×10^{-7}	1.86×10^{-7}
173	3.63×10^{-9}	4.80×10^{-9}
195	5.90×10^{-10}	7.79×10^{-10}
227	1.10×10^{-10}	1.45×10^{-10}
249	4.95×10^{-11}	6.55×10^{-11}
273	2.51×10^{-11}	3.28×10^{-11}
298	1.44×10^{-11}	1.88×10^{-11}

TABLE II: Electron Solvation Time at Room Temperature

	τ_r ($\theta_0 = 80°$, $N = 6$), ps		
Solvent	I[a]	II[b]	τ_{sol} (obsd),[c] ps
Methanol	2.25	1.92	10.7
Ethanol	7.81	6.97	23
1-Propanol	18.8	17.3	34

[a] This work. [b] Reference 4. [c] Reference 11.

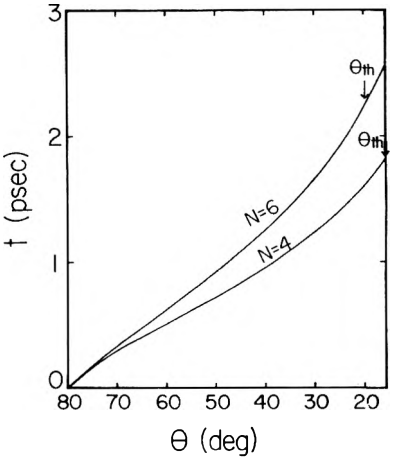

Figure 1. Solvation time as a function of dipole orientation angle for a trapped electron in methanol at 294 K.

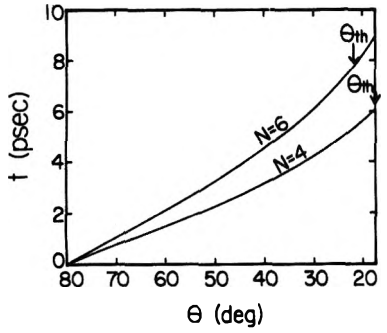

Figure 2. Solvation time as a function of dipole orientation angle for a trapped electron in ethanol at 296 K.

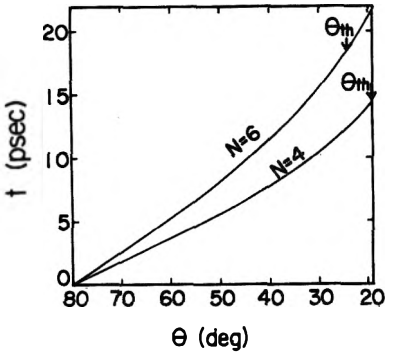

Figure 3. Solvation time as a function of dipole orientation angle for a trapped electron in 1-propanol at 298 K.

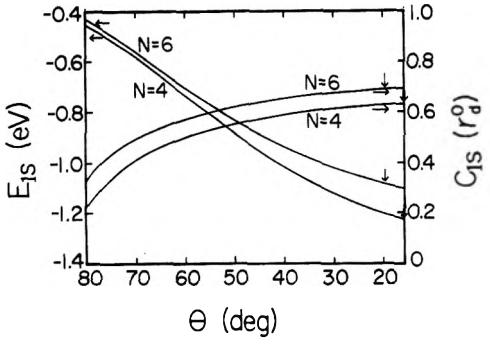

Figure 4. Charge distribution and ground state energy as functions of dipole orientation angle for trapped electron in methanol at 294 K. Vertical arrows indicate θ_{th}.

are several orders of magnitude too short. This appears to be a direct reflection of the inadequacy of equating macroscopic to microscopic viscosities in glassy matrices. Of course, we could always *define* a microscopic viscosity by fitting it to experimental electron solvation times via eq 1, but that would not give any new physical insight.

B. *Charge Distribution and Energy Levels.* Figures 4–6 show, respectively, the ground state charge distribution, $C_{1s}(r_d^0)$, and ground state energy level, E_{1s}, for trapped electrons in methanol, ethanol, and 1-propanol at room temperature as functions of dipole orientation angle, θ. It can be seen in these figures that C_{1s} increases with decreasing θ. The change in C_{1s} with θ is largest for methanol and smallest for 1-propanol. Also C_{1s} is greater for $N = 6$ than for $N = 4$. It should be pointed out that since a change in C_{1s} with θ for a trapped electron in 1-propanol is rather small, our previous treatment[4] of dipole relaxation time in 1-propanol is an especially good approximation to the present refined method

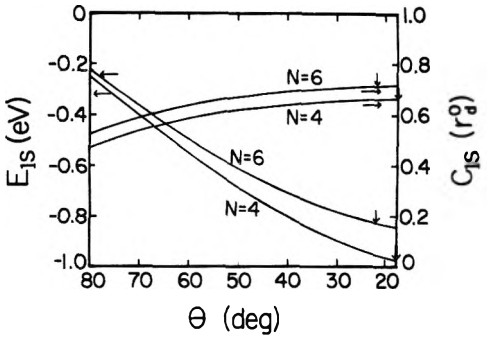

Figure 5. Charge distribution and ground state energy as functions of dipole orientation angle for a trapped electron in ethanol at 296 K. Vertical arrows indicate θ_{th}.

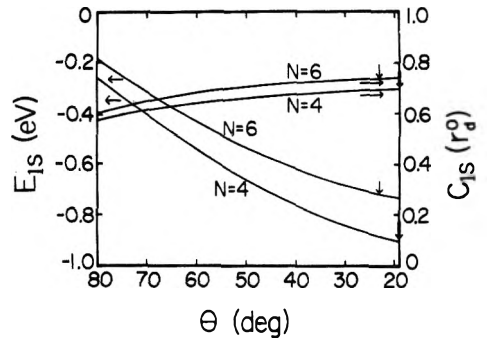

Figure 6. Charge distribution and ground state energy as functions of dipole orientation angle for a trapped electron in 1-propanol at 298 K. Vertical arrows indicate θ_{th}.

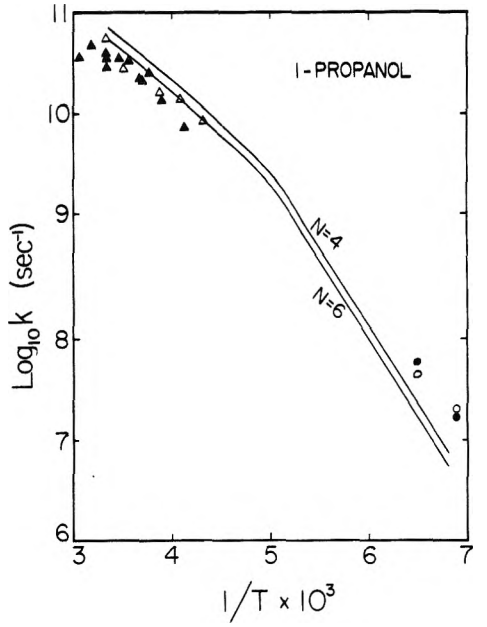

Figure 7. The solid lines show the calculated temperature dependence of the electron solvation rate in 1-propanol for $N = 4$ and $N = 6$ first solvation shell molecules. The experimental data of Hunt and Chase (ref 11) are given by (△) for formation of e_{sol}^- at 600 nm and by (▲) for decay of e_t^- at 1050 nm. The data of Baxendale (ref 13) are given by (○) for formation of e_{sol}^- at 550 nm and by (●) for decay of e_t^- at 1300 nm.

of calculation. This is also supported by the calculated dipole relaxation times as discussed above.

The energy level, E_{1s}, for trapped electrons decreases with

decreasing dipole orientation angle as anticipated. E_{1s} is in increasing order for methanol, ethanol, and 1-propanol for the same value of θ, and it is higher for $N = 6$ than for $N = 4$. It is also seen that the difference between the energy levels for $N = 4$ and 6 is in increasing order for methanol, ethanol, and 1-propanol.

C. *Cavity Radius and Dielectric Constant.* The cavity radius, r_d^0, increases only slightly with a decrease in dipole orientation angle from θ_0 to θ_{th}. The calculated values of r_d^0 at room temperature are 2.2–2.4 Å ($N = 4$) and 2.8–3.1 Å ($N = 6$) for methanol; 2.5–2.6 Å ($N = 4$) and 3.1–3.3 Å ($N = 6$) for ethanol; and 2.8–2.9 Å ($N = 4$) and 3.4–3.6 Å ($N = 6$) for 1-propanol.

The calculated results show that the time dependent dielectric constant, ϵ, remains nearly equal to the high-frequency dielectric constant, ϵ_∞, during dipole relaxation. These results arise from the fact that τ_r is shorter than τ_1'. This also implies that within the framework of the present model the orientational relaxation of molecular dipoles in the first solvation shell around a localized electron proceeds first and then the dielectric relaxation of the continuous medium beyond the first solvation shell follows to complete the electron solvation.

D. *Temperature Dependence of Theoretical and Observed Electron Solvation Rates.* Figure 7 shows plots of the calculated relaxation rate of dipole orientation, $k = 1/\tau_r$, vs. $1/T$, where T is absolute temperature, along with the observed solvation rate, $k = 1/\tau_{sol}$, for localized excess electrons in 1-propanol. Experimental points are taken from recent data of Chase and Hunt[11] and of Baxendale.[13] These theoretical curves are in reasonable agreement with the experimental data and well represent the temperature dependence of the electron solvation rate.

Note that the temperature dependence of k is non-Arrhenius. In our theoretical calculation this temperature dependence arises from the non-Arrhenius behavior of the macroscopic viscosity. In liquids that are not hydrogen bonded the macroscopic viscosity does follow an Arrhenius temperature dependence. Thus we may make the interesting prediction that experimental electron solvation rates in alkanes should follow Arrhenius behavior.

As already mentioned, the agreement between theory and experiment is not quite satisfactory for methanol and ethanol. In order to further improve the theoretical results on electron solvation rates, it would be necessary for us to have knowledge of the microscopic viscosity and to take into account dipole–dipole interactions in the calculation.

Acknowledgments. We thank Professor J. W. Hunt and Dr. W. J. Chase for helpful discussions and communication of results. This research was partially supported by the U.S. Energy Research and Development Administration under Contract No. E(11-1)-2086.

Supplementary Material Available: (Table III) dielectric relaxation times, τ_1' (1 page). Ordering information is available on any current masthead page. Also available from L. Kevan upon request.

References and Notes

(1) J. H. Baxendale and P. Wardman, *Nature (London)*, **230**, 449 (1971); *J. Chem. Soc., Faraday Trans. 1*, **69**, 584 (1973).
(2) G. Beck and J. K. Thomas, *J. Phys. Chem.*, **76**, 3856 (1972).
(3) L. Gilles, J. E. Aldrich, and J. W. Hunt, *Nature (London)*, *Phys. Sci.*, **243**, 70 (1973).
(4) K. Fueki, D.-F. Feng, and L. Kevan, *J. Phys. Chem.*, **78**, 393 (1974).
(5) K. Fueki, D.-F. Feng, and L. Kevan, *J. Am. Chem. Soc.*, **95**, 1398 (1973).
(6) M. Tachiya and A. Mozumder, *J. Chem. Phys.*, **63**, 1959 (1975).
(7) H. Hase, F. Q. H. Ngo, and L. Kevan, *J. Chem. Phys.*, **62**, 985 (1975).
(8) R. Schiller, *Chem. Phys. Lett.*, **5**, 176 (1970).
(9) A. Mozumder, *J. Chem. Phys.*, **50**, 3153 (1969).
(10) R. H. Cole and D. W. Davidson, *J. Chem. Phys.*, **19**, 1484 (1951); **20**, 1389 (1952).
(11) W. J. Chase and J. W. Hunt, *J. Phys. Chem.*, **79**, 2835 (1975).
(12) N. V. Klassen, H. A. Gillis, G. G. Teather, and L. Kevan, *J. Chem. Phys.*, **62**, 2474 (1975).
(13) J. H. Baxendale, private communication to J. W. Hunt; these data supercede those reported in ref 1 due to a correction in the temperature calibration.

A Kinetic Study of Ion Exchange in Tantalum Arsenate to Understand the Theoretical Aspects of Separations

J. P. Rawat* and Pritam Singh Thind

Department of Chemistry, Aligarh Muslim University, Aligarh (U.P.), India *(Received August 27, 1975; Revised Manuscript Received February 10, 1976)*

The exchange of the cations Ag^+, Mg^{2+}, Ca^{2+}, Sr^{2+}, Ba^{2+}, Y^{3+}, and Th^{4+} on tantalum arsenate in the H^+ form was studied. The slow step which determines the rate of exchange of these ions is diffusion through the particle. The diffusion coefficients, energies of activation, and entropies of activation were calculated and were used to determine the theoretical behavior of ion-exchange separations.

Introduction

Studies in the field of inorganic ion exchangers are increasing day by day due to their selectivity and stability under certain conditions. Preparation and properties of the ion exchangers of zirconium phosphate type have been established.[1] Analytical applications in the field of separation science have been reviewed by Inczedy[2] and Walton.[3-5] To understand the theoretical aspects of ion-exchange separations it is essential to study the thermodynamics and kinetics of this process. The kinetic studies on ion exchangers were mainly started by

Nachod and Wood[6,7] systematically. Their studies revealed that the exchange reactions were of second order, bimolecular, and that the values could be calculated by using concentrations instead of activities. Kinetics of ion exchange in the chelating resin Bio-Chelex-100 has been studied.[8] These authors studied the exchange of alkaline earth metal ions on the resin in the H^+ form. Nancollas and Paterson have described quantitative measurements upon hydrous thoria and zirconium phosphate using limited bath and infinite bath techniques.[9] Tantalum arsenate has recently been synthesized and used as a chemically stable exchanger.[10] The exchanger showed reproducible behavior and has been used for the separation of rare earths. In the present report the kinetic studies for the exchange of Ag^+, Mg^{2+}, Ca^{2+}, Sr^{2+}, Ba^{2+}, Y^{3+}, and Th^{4+} on tantalum arsenate (TaAs) are described. The values of activation energies, effective diffusion coefficients, and entropies of activation are calculated.

Experimental Section

Reagents. Tantalum pentoxide (BARC, India) and sodium arsenate (Riedel, Germany) were used. All other reagents used were of analar grade.

Tantalum pentoxide (22.10 g) was heated with 200 g of ammonium sulfate in 200 ml of concentrated sulfuric acid. The clear solution was diluted to 500 ml to obtain a solution which was 0.1 M with respect to tantalum. Sodium arsenate (0.1 M) solution was prepared in 2 M hydrochloric acid.

Synthesis of Tantalum Arsenate. Sodium arsenate solution was added to tantalum pentoxide solution slowly with constant stirring in the Ta:As ratio of 1:4. Sodium hydroxide solution was then added dropwise until the pH was zero. The precipitate was allowed to settle for 24 h at room temperature, and was then washed several times by decantation with water, filtered, and dried. The dried material broke down into small particles when immersed in water. The exchanger was then converted to the H^+ form by treatment with 2 M HNO_3 for 24 h. Finally it was washed several times with demineralized water and dried in an incubator at 40 ± 1 °C.

Kinetic Measurements. Rates of exchange were measured by the limited bath technique. Tantalum arsenate was ground well in order to give particles of different mesh size (50–250). Solutions of cations (0.1 N) were taken in conical flasks with constant ionic strength (μ = 1.0). The solutions were then brought to the desired temperature. When the desired temperature was reached a weighed amount of exchanger was added (0.2 g), and the flasks were thoroughly shaken. After appropriate intervals the contents of the flasks was filtered using Whatman No. 4 filter paper. The experiments were conducted at 32, 40, 50, and 55 °C with ±1 °C variation.

Analytical Methods. Cations Ba^{2+}, Sr^{2+}, Ca^{2+}, and Mg^{2+} were determined with EDTA using Erichrome black T as an indicator[11] while with yttrium and thorium xylenol orange[12] was used. Silver was determined spectrophotometrically.[13]

Results and Discussion

As the limited bath technique was used, the equation developed by Boyd et al.[14] and improved by Reichenberg[15] were used. The extent of reaction (F) is expressed as:

$$F = \frac{\text{the amount of exchange at time } t}{\text{the amount of exchange at infinite time}}$$

The rate of exchange can be determined by three different steps: (a) particle diffusion, (b) liquid film diffusion, and (c) mass action.

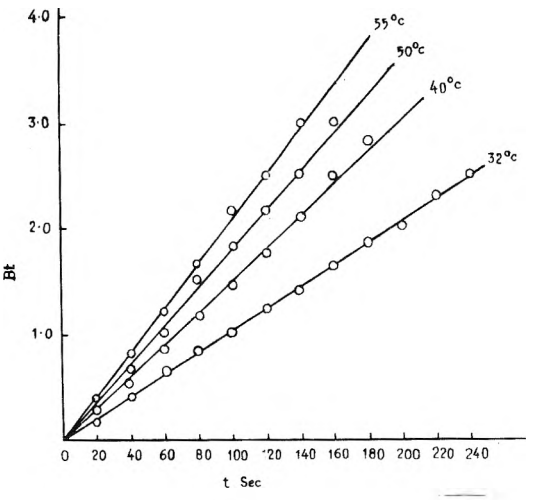

Figure 1. Plot of Bt vs. time for Mg^{2+} at different temperatures using TaAs (r = 1.05 × 10^{-2} cm).

The conditions of these experiments were set to study the particle diffusion mechanism only. As the rate-determining step is diffusion through the ion-exchanger particle, the following equation is valid:

$$F = 1 - \frac{6}{\pi^2} \sum_{n=1}^{\infty} \exp\left(\frac{-n^2 Bt}{n^2}\right)$$

where $B = \pi^2 D_i / r^2$, r = radius of the particle, D_i = effective diffusion coefficient of the two ions undergoing exchange within the exchanger.

Values of Bt as a function of F may be calculated as tabulated by Reichenberg.[15] The plot of Bt vs. t at four different temperatures for Mg^{2+} is presented in Figure 1, and similar plots were obtained for Ag^+, Ca^{2+}, Sr^{2+}, Ba^{2+}, Y^{3+}, and Th^{4+}. The B values are calculated from these plots and are given in Table I. Plots of Bt vs. t at different temperatures are straight lines passing through the origin. It indicates that the rate-determining step is diffusion through the particle. The results of variation of particle size of the exchanger are presented in Figure 2 in terms of plots of Bt vs. t for Mg^{2+}. These plots indicate that for larger particle size the rate is slower and the diffusion through the particle as the rate-determining step is independent of particle size.

The linear relationship between log D and $1/T$ K (Figure 3) enables the energies of activation (E_a) for the self-diffusion of cations to be calculated from the Arrhenius equation:

$$D = D_0 \exp(-E_a/RT)$$

The activation energy of the cation self-diffusion process reflects the ease with which cations can pass through the exchanger. Freeman and Stamires[16] observed an increase in E_a with ion size for the divalent ions Mg^{2+}, Ca^{2+}, Sr^{2+}, and Ba^{2+}. This increase was explained in terms of an increase in strength of bonding to two crystallographically separated sites for the large, more polarizable cations. Similar type of results are observed in the present report (Table II) but the values of E_a are lower than those reported by Freeman and Stamires. Calculation of D_0 and substitution into the following equation gives the entropy of activation (ΔS^*):

$$D_0 = 2.72\, d^2 KT/h \exp(\Delta S^*/R)$$

Here d is the ionic jumps distance assumed equal to 5 × 10^{-8} cm, K the Boltzmann constant, h Planck's constant, R the gas

TABLE I: *B* Values as a Function of Temperature and Particle Size

Metal ion	r,[a] cm	B, s^{-1} (32 °C)	B, s^{-1} (40 °C)	B, s^{-1} (50 °C)	B, s^{-1} (55 °C)
Ag^+	1.05×10^{-2}	1.88×10^{-2}	1.93×10^{-2}	2.0×10^{-2}	2.26×10^{-2}
Mg^{2+}	1.05×10^{-2}	1.03×10^{-2}	1.43×10^{-2}	1.66×10^{-2}	2.0×10^{-2}
Mg^{2+}	6.1×10^{-3}	1.07×10^{-2}			
Mg^{2+}	4.47×10^{-3}	1.22×10^{-2}			
Mg^{2+}	3.4×10^{-3}	1.44×10^{-2}			
Ca^{2+}	1.05×10^{-2}	1.38×10^{-2}	1.76×10^{-2}	2.21×10^{-2}	2.5×10^{-2}
Sr^{2+}	1.05×10^{-2}	1.66×10^{-2}	2.21×10^{-2}	2.60×10^{-2}	3.16×10^{-2}
Ba^{2+}	1.05×10^{-2}	2.66×10^{-2}	3.16×10^{-2}	4.93×10^{-2}	5.05×10^{-2}
Y^{3+}	1.05×10^{-2}	9.5×10^{-3}	1.16×10^{-2}	1.33×10^{-2}	1.71×10^{-2}
Th^{4+}	1.05×10^{-2}	6.66×10^{-3}	8.33×10^{-3}	1.0×10^{-2}	1.21×10^{-2}

[a] r = mean radius of the particle.

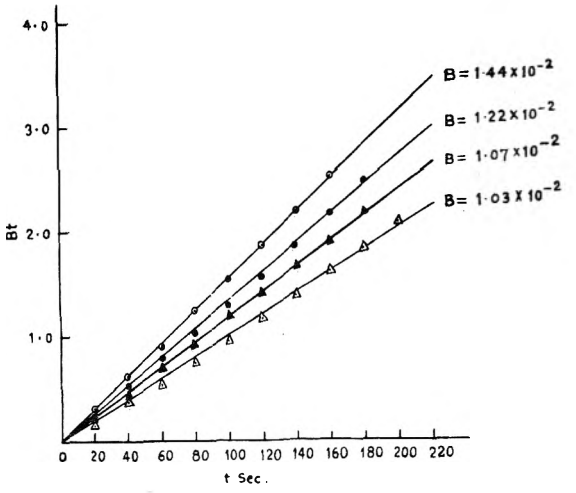

Figure 2. Plot of Bt vs. t for Mg^{2+} using different particle size of TaAs at 32 °C: (⊙) $r = 3.4 \times 10^{-3}$ cm; (●) $r = 4.47 \times 10^{-3}$ cm; (▲) $r = 6.1 \times 10^{-3}$ cm; (△) $r = 1.05 \times 10^{-2}$ cm.

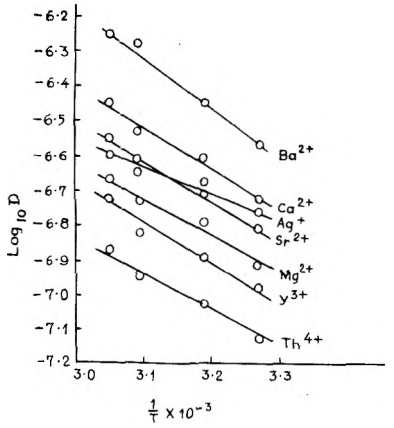

Figure 3. Plot of log D vs. $1/T$.

constant, and T is taken as 273 °C. D_0 and ΔS^* values are given in Table II.

In order to determine the rate of exchange at different temperatures, the values of F at various time intervals may be plotted. The results for Mg^{2+} are given in Figure 4. It is clear from this figure that as the temperature increases from 32 to 55 °C, the rate of ion exchange increases. This is due to the fact that with increasing temperature the mobility of the ion increases. Figure 4 also indicates that initially the uptake of Mg^{2+} is rapid. The uptake decreases with increasing time.

TABLE II: Self-Diffusion Parameters in Tantalum Arsenate

Migrating ion	D_0, cm^2/s	E_a, kcal/mol	ΔS^*, cal deg^{-1} mol^{-1}
Ag^+	2.09×10^{-7}	2.5	−24.010
Mg^{2+}	1.11×10^{-7}	4.9	−25.290
Ca^{2+}	1.55×10^{-7}	5.5	−24.605
Sr^{2+}	1.86×10^{-7}	5.7	−24.282
Ba^{2+}	2.72×10^{-7}	7.8	−23.490
Y^{3+}	1.05×10^{-7}	5.3	−25.366
Th^{4+}	7.49×10^{-7}	4.8	−26.047

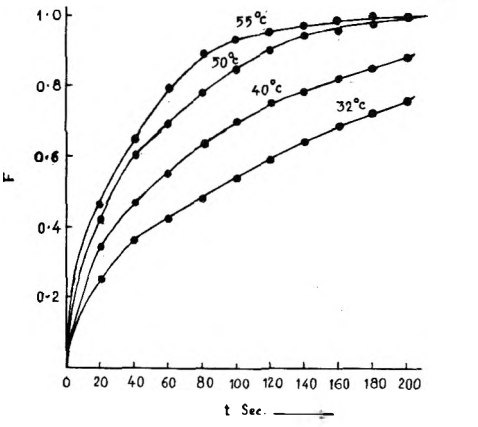

Figure 4. Rate of exchange of Mg^{2+} at different temperatures on TaAs.

Similar behavior is shown by the other cations used. These results are analogous with that of Heither-Wirguin and Markovits[8] but do not agree with those found for Ca^{2+} and Mg^{2+} by Turse and Rieman.[17] The results of ΔS^* show negative values (Table II). This is analogous to the behavior of divalent ions Mg^{2+}, Ca^{2+}, Sr^{2+}, and Ba^{2+} migrating through Y zeolites.[16]

Energies of activation show an increase in magnitude with decreasing hydrated ionic size for alkaline earth metal ions (Table II). This is analogous to the behavior of monovalent cations migrating through analcite.[18] This behavior indicate the feasibility of separating ions by exploiting difference in the rate of exchange toward tantalum arsenate.

Acknowledgment. The authors thank Professor W. Rahman for use of the research facilities. Thanks are also due to the Council of Scientific and Industrial Research (India) for financial assistance to P.S.T.

References and Notes

(1) C. B. Amphlett, "Inorganic Ion Exchangers", Elsevier, Amsterdam, 1964.
(2) J. Inczedy, "Analytical Applications of Ion Exchangers", Pergamon Press, New York, N.Y., 1966.
(3) H. F. Walton, *Anal. Chem.*, **42**, 86R (1970).
(4) H. F. Walton, *Anal. Chem.*, **44**, 256R (1972).
(5) H. F. Walton, *Anal. Chem.*, **46**, 398R (1974).
(6) F. C. Nachod and W. Wood, *J. Am. Chem. Soc.*, **66**, 1380 (1944).
(7) F. C. Nachod and W. Wood, *J. Am. Chem. Soc.*, **67**, 629 (1945).
(8) C. Heitner-Wirguin and G. Markovits, *J. Phys. Chem.*, **67**, 2263 (1963).
(9) G. H. Nancollas and R. Paterson, *J. Inorg. Nucl. Chem.*, **22**, 259 (1961).
(10) J. P. Rawat and S. Q. Mujtaba, *Can. J. Chem.*, **53**, 2586 (1975).
(11) R. Pribil, "Complexonii in Chimia Analitica", Edi, Tehn. Bucuresti, 1961, pp 254–255.
(12) A. Vogel, "Quantitative Inorganic Analysis", Longmans, Green and Co., London, 1961.
(13) E. B. Sandell, "Colorimetric Determination of Traces of Metals", Interscience, New York, N.Y., 1959, p 812.
(14) G. E. Boyd, A. W. Adamson, and L. S. Myers, *J. Am. Chem. Soc.*, **69**, 2836 (1947).
(15) D. Reichenberg, *J. Am. Chem. Soc.*, **75**, 589 (1953).
(16) D. C. Freeman and D. N. Stamires, *J. Chem. Phys.*, **35**, 799 (1961).
(17) R. Turse and W. Rieman, III, *J. Phys. Chem.*, **65**, 1821 (1961).
(18) R. M. Barrer and L. V. C. Rees, *Nature (London)*, **187**, 768 (1960).

COMMUNICATIONS TO THE EDITOR

Polyelectrolyte Membrane Electrets. Evidence for High Degree of Charge Storage Capacity

Publication costs assisted by the University of Illinois at Chicago Circle

Sir: In 1972 we[1,2] reported on persistent electrical polarization in membranes consisting of sodium polystyrenesulfonate in such polymer matrices as polyvinyl alcohol, polyacrylamide, and polyvinylpyrrolidone. In particular, we reported that a membrane consisting of the polyion in polyvinyl alcohol stored substantial amounts of electric charge in a stable fashion. In addition to the fact that the membranes stored several orders of magnitude more charge than did the usual dielectrics, these membranes also had substantial electrical conductivity. Typical values reported were polarizations of the order of 10^{-6} C/cm^2 with conductivities of the order of 10^{-12} (ohm cm)$^{-1}$. Both of these numbers were several orders of magnitude higher than the usual numbers reported in the literature for typical dielectrics.[3,4] It now appears that as a result of an unforseen contact resistance problem, the numbers we reported in 1972 were too low by almost 3 orders of magnitude.

Recently we performed some experiments in which the same membrane formulation utilized in the 1972 work was used. In this membrane formulation the components were Dupont Elvanol 71-30G (hot water soluble polyvinyl alcohol) and Dow sodium polystyrenesulfonate (mol wt = 6×10^6). The polystyrenesulfonate was washed with methanol six times and dialyzed against distilled water five times to remove such impurities as sodium bromide and unreactive monomer. The polyvinyl alcohol was similarly dialyzed for purification purposes. Appropriate mixtures of these ingredients in aqueous solution were cast on glass plates and dried at 70 °C in a circulating oven. Up to this point, the procedure was exactly the same as reported in 1972. However, in the recent work, the dried membranes were then coated with a suspension of purified colloidal graphite in chloroform. In addition, the electrodes were similarly coated.

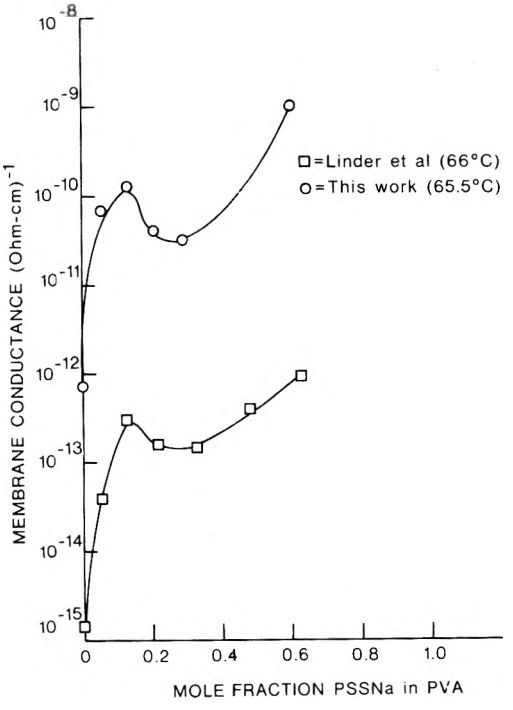

Figure 1. Membrane conductance as a function of mole fraction PSSNa in PVA.

After the membranes were dried, experiments were performed, utilizing several membrane formulations, in which the membranes were thermally charged and discharged using the same procedures and apparatus reported by Linder et al. In these experiments the membranes (ca. 0.005 cm thick) were charged by placing them in an electric field (22.5 V) at 66 °C, cooled to room temperature, after which the field was removed, and then reheated to about 76 °C while the membranes discharged through an electrometer (Keithley Model

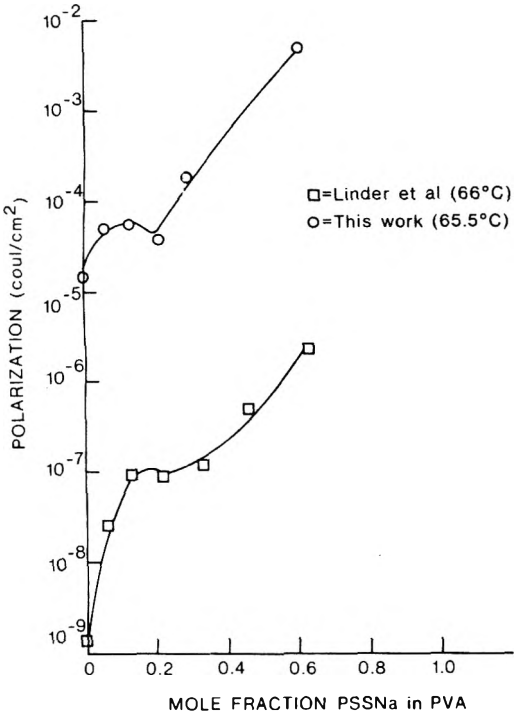

Figure 2. Membrane polarization as a function of mole fraction PSSNa in PVA.

610C). Figures 1 and 2 represent the results obtained. Each point reported is an average of a minimum of four experiments involving at least two separate membranes. The average standard deviation was 20.1% while the maximum standard deviation found was 36.4%.

Figure 1 is a comparision of the membrane conductance obtained in this work with the work of Linder et al. It should be noted that although the curves have essentially the same shape, the present curve is displaced upward by more than 2 orders of magnitude. This displacement is almost certainly a result of the reduced contact resistance between the electrodes and the membranes brought about by the presence of colloidal graphite. Figure 2 shows the membrane polarization obtained by integrating the measured current vs. time curves as compared with those of Linder et al. Again, it should be pointed out that although the curves have roughly the same shape, the present curve is displaced upward by more than 2 orders of magnitude.

The fact that the polarization curves now obtained have essentially the same shape as those reported by Linder et al. indicates that the model formulated to explain those results is still valid. The model (involving an electret formation and stabilization mechanism in which an ion became displaced in the direction of the applied field via a positive feedback between a local field and its reactive field components and the stabilization of these displacements by hydrogen bonding) was dependent on the shape of a polarization curve but not on the absolute values obtained.

The significance of the values now obtained lies in the very real possibility that membrane electrets of this type might prove to be practical sources of electrical power. On a weight basis the 0.6 mole fraction membrane stores approximately 1 C/g. Linder found that raising the polarization temperature from 66 to 93 °C increased the polarization of the membranes by about 1.5 orders of magnitude. It is reasonable to expect, therefore, that if the polarization temperature is 90 °C, the present membranes will store approximately 30 C/g at room temperature. The charged membranes (ca. 0.005 cm thick) retain a potential of about 2.5 V. For purposes of comparison, a commercial mercury battery, rated at 1.35 V, stores approximately 270 C/g. Taken in this light, the present results appear very promising.

Acknowledgment. We hereby acknowledge the generous support of the National Science Foundation under terms of grant GK 43294.

References and Notes

(1) C. Linder and I. F. Miller, *J. Phys. Chem.*, **76**, 3434 (1972)
(2) C. Linder and I. F. Miller, *J. Electrochem. Soc.*, **120**, 498 (1973).
(3) S. Bini and R. Capelletti in "Electrets", M. M. Perlman, Ed., Electrochemical Society, N.J., 1973, p 66.
(4) E. B. Podgorsak, G. E. Fuller, and P. R. Moran, ref 3, p 172.

College of Engineering **Irving F. Miller***
University of Illinois at Chicago Circle **Joaquin Mayoral**
Chicago, Illinois 60680

Received October 28, 1975

Nonideality of Mixing of Micelles of Fluorocarbon and Hydrocarbon Surfactants and Evidence of Partial Miscibility from Differential Conductance Data

Publication costs assisted by the Petroleum Research Fund

Sir: Although fluorocarbons and hydrocarbons are individually typical nonpolar substances, they exhibit considerable departure from ideality in their mixtures,[1,2] so much so that heptane and perfluoroheptane, for example, are only partially miscible at room temperature.[1] We wish to report some critical micellization concentrations (cmc) and differential conductance data on mixtures of sodium perfluorooctanoate (SPFO) with some hydrocarbon chain surfactants in aqueous solution which point out how intense this nonideality effect is in small systems such as micelles. These observations, along with some others recently made regarding the anomalous behavior of partially fluorinated surfactants,[2] suggest that such nonideality effects may be widespread and may significantly affect the properties of (a) carbon–fluorine compounds in biological systems,[3] (b) fluorine-labeled molecules for probing or studying hydrophobic environments of proteins, of enzymes, or of lipid membranes,[4-9] and, (c) surfactants at interfaces where fluorocarbon–hydrocarbon interactions are involved.

Figure 1 shows the cmc values of mixtures of SPFO with sodium laurate (SL) and sodium decyl sulfate (SDeS), in presence of 0.001 N NaOH added to suppress any hydrolysis. The data were obtained from plots of equivalent conductance against the square root of the concentration, C, in equivalents/liter, a procedure particularly useful for mixtures of ionic surfactants.[10] The conductance was corrected for the contribution of the NaOH.[11] Its effect on the high cmc values of Figure 1 through the common-ion effect[13] may be considered negligible for comparative purposes.

Previous studies have shown that the cmc's of binary mixtures of ionic hydrocarbon chain surfactants fall within the range of the values of the individual pure components,[10,14-17] and that the mixing of the chain moieties is nearly ideal,[14,15,18]

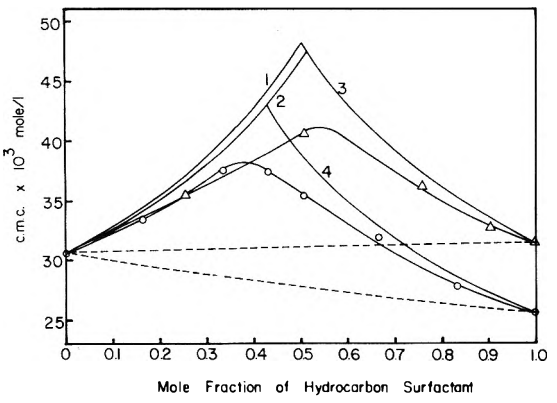

Figure 1. Critical micellization concentrations of mixtures of SPFO with SDeS (Δ) and SL (O) at 25 °C. Dashed lines show expected values on ideal mixing of the micelles,[18] assuming B (eq 2) = 0.645 for all three components. Curves 1, 2, 3, and 4 shows expected values for complete demixing of micelles (eq 3). Curves 2, 3, and 4 calculated for B = 0.645. Curve 1 calculated for B = 0.53.

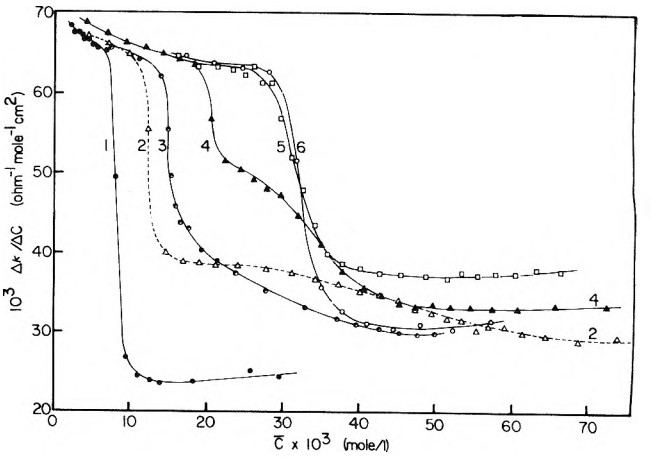

Figure 2. Differential conductance, $10^3(\kappa_2 - \kappa_1)/(C_2 - C_1)$, plotted against mean concentration $\bar{C} = (C_2 + C_1)/2$: curve 1, SDS; curve 2, SDS + SPFO (SDS mol fraction 0.5); curve 3, SDS + SDeS (SDS mole fraction 0.29, data from ref 10); curve 4, SDS + SPFO (SDS mole fraction 0.2); curve 5, SPFO; curve 6, SDeS.

presumably because their cohesive energy densities are comparable.[1] In our work, SL and SDeS were chosen to match the cmc of SPFO closely so that the pure surfactants are of comparable hydrophobic character. That the mixing of the carboxyl and sulfate head groups is of relatively little consequence by itself is shown by the cmc of an equimolar mixture of SL and SDeS, 0.0294 M as compared to 0.0256 M for SL and 0.0315 M for SDeS (all measurements in 0.001 N NaOH). The cmc values expected from ideal mixing of SPFO with SL and SDeS are shown by the dashed line in Figure 1. The experimental values, in contrast, are considerably higher, particularly in the middle of the mixing range. The higher cmc values are consistent with the positive deviations from Raoult's law that mixtures of fluorocarbons and hydrocarbons exhibit.[1] Such nonidealities lead to higher activity coefficients of the individual chains in the mixed micelles, resulting in lower stability of the mixed micelles as compared to homogeneous micelles.

To examine the magnitude of the nonideality of mixing, the cmc values of the mixed systems were calculated assuming the extreme case of complete demixing of micelles (Figure 1). In such a case, on increasing the overall concentration C of a binary mixture of components 1 and 2, micelle formation begins when the concentration of either 1 or 2 attains its cmc. If the surfactants are nonionic, the cmc–mole fraction diagram is composed simply of two curved lines for the two components given by the equation

$$\text{cmc} = \text{cmc}_0/X \tag{1}$$

where cmc_0 is the value for a pure surfactant, and X is its mole fraction. For ionic surfactants, however, the counterion of one component affects the cmc of the other through the common-ion effect.[13] On using the well-known relation between the cmc and the concentration of counterions (Na^+)

$$\log \text{cmc} = A - B \log [Na^+] \tag{2}$$

where A and B are constants,[13,14] the cmc of a mixed system is given by

$$\text{cmc} = \text{cmc}_0 \text{ antilog } \left(\frac{\log 1/X}{1 + B}\right) \tag{3}$$

Equation 3 must be applied to each component separately. A reliable experimental value of 0.645 for B has been obtained for SDeS.[19] We have used this representative value[13,14] for all three surfactants. For SPFO, a lower estimate of 0.53 from limited data for the potassium salt[20] is also used to indicate a measure of the uncertainty of this calculation (Figure 1).

Figure 1 shows that the experimental cmc data are not too far from the calculated case of no mixing of micelles, indicating that the nonideality of mixing is indeed severe.

Partially Miscible Micelles and "Phase Separation" in Small Systems. The intensity of the nonideality of mixing indicated by the cmc data of Figure 1 suggests the interesting possibility of the coexistence of two kinds of micelles, one rich and the other poor in the fluorocarbon component, under suitable conditions.[2] This phenomenon of a "phase separation" in small systems is likely to be of interest for lipid membranes. The cmc data by themselves do not provide conclusive evidence on this point. To investigate this possibility we have studied the conductance of mixtures of sodium dodecyl sulfate (SDS) and SPFO. The data are exhibited in Figure 2 as differential conductance, $10^3\Delta\kappa/\Delta C = 10^3(\kappa_2 - \kappa_1)/C_2 - C_1)$ where κ_2 and κ_1 are the specific conductance at two adjacent concentrations C_2 and C_1, plotted against the mean concentration $\bar{C} = (C_2 + C_1)/2$. $\Delta\kappa/\Delta C$ is thus an average value of $d\kappa/dC$ over the concentration range C_2–C_1. Its importance lies in its ability to indicate clearly the relatively abrupt change in solution composition at the cmc.[10,21] Curves 1, 5, and 6 of Figure 2 show data for the three single surfactants, SDS, SDeS, and SPFO, the latter two having similar cmc values. The $\Delta\kappa/\Delta C$ typically shows an abrupt drop in the region of the cmc and then attains a nearly constant value: each curve shows one inflection point. Mixtures of the two homologous surfactants, SDS and SDeS, have been studied by Mysels and Otter.[10] A representative example (curve 3, Figure 2) shows that here the initial sudden drop at the cmc is followed by a further gradual decrease over a wide concentration range, corresponding to a slow change in the composition of the mixed micelles and the monomers, before the final leveling off. When SDeS is replaced by SPFO, however (curves 2 and 4, Figure 2), the $\Delta\kappa/\Delta C$ curve changes its character and becomes biphasic: it shows two inflection points before leveling off at high concentrations. The first drop corresponds to the onset of micelle formation, i.e., the cmc. The high value of $\Delta\kappa/\Delta C$ at concentrations following this first transition and the presence of a second transition resembling the first one are consistent with the following explanation[2,22] initially

suggested for explaining some complex surface tension data.[2] The micelles that form first are composed primarily of the more hydrophobic SDS component. As the total concentration increases, the concentration as also the fraction of monomeric SPFO increases. At about the second inflection point, the activity of SPFO becomes high enough to form micelles which are composed primarily of the SPFO component. At the highest concentrations, the two kinds of micelles exist together.

The present work demonstrates that the severe nonidealities of interactions that fluorocarbons and hydrocarbons exhibit are present in small systems such as the micellar systems and that the surfactants show mutual phobia in addition to their well-known hydrophobiciy.[2]

Acknowledgment. Acknowledgment is made to the Donors of the Petroleum Research Fund, administered by the American Chemical Society, for support of this research. We are grateful to Karol J. Mysels for many helpful discussions.

References and Notes

(1) J. H. Hildebrand, J. M. Prausnitz, and R. L. Scott, "Regular and Related Solutions", Van Nostrand-Reinhold, New York, N.Y., 1970.
(2) P. Mukerjee and K. J. Mysels, *ACS Symp. Ser.*, **No. 9**, 239 (1975).
(3) "Carbon-Fluorine Compounds, Chemistry, Biochemistry and Biological Activities", Ciba Foundation Symposium, Elsevier, New York, N.Y., 1972.
(4) N. J. M. Birdsall, A. G. Lee, Y. K. Levine, and J. C. Metcalfe, *Biochim. Biophys. Acta*, **241**, 693 (1971).
(5) (a) N. Muller and R. H. Birkhahn, *J. Phys. Chem.*, **71**, 957 (1967); (b) N. Muller and R. J. Mead, Jr., *Biochemistry*, **12**, 3831 (1973).
(6) E. Zeffren, *Arch. Biochem. Biophys.*, **137**, 291 (1970).
(7) K. L. Gammon, S. H. Smallcombe, and J. H. Richards, *J. Am. Chem. Soc.*, **94**, 4573 (1972).
(8) J. T. Gerig and R. A. Rimerman, *J. Am. Chem. Soc.*, **94**, 7558 (1972).
(9) B. D. Sykes, *J. Am. Chem. Soc.*, **91**, 949 (1969).
(10) K. J. Mysels and R. J. Otter, *J. Colloid Sci.*, **16**, 462 (1961).
(11) Conductance measurements were carried out in a doughnut type dilution cell, equipped with a magnetic stirrer,[12] placed in an oil bath at 25 °C (controlled within ±0.015 °C). A Beckman Model RC-18A conductivity bridge, capable of capacitance balancing, was used for resistance measurements. The average precision of the measurements was about 0.03%.
(12) K. J. Mysels, *J. Phys. Chem.*, 65, 1081 (1961).
(13) P. Mukerjee, K. J. Mysels, and P. Kapauan, *J. Phys. Chem.*, **71**, 4166 (1967).
(14) K. Shinoda, T. Nakagawa, B. Tamamushi, and T. Isemura, "Colloidal Surfactants", Academic Press, New York, N.Y., 1963.
(15) H. Lange, *Kolloid Z.*, **131**, 96 (1953).
(16) F. Tokiwa, K. Ohki, and I. Kokubo, *Bull. Chem. Soc. Jpn.*, **41**, 2845 (1968).
(17) Y. Moroi, K. Motomura, and R. Matuura, *J. Colloid Interface Sci.*, **47**, 111 (1974).
(18) K. J. Mysels and R. J. Otter, *J. Colloid Sci.*, **16**, 474 (1961).
(19) K. J. Mysels and P. Kapauan, *J. Colloid Sci.*, 481 (1961).
(20) K. Shinoda and K. Katsura, *J. Phys. Chem.*, **68**, 1568 (1964).
(21) G. S. Hartley, "Aqueous Solutions of Paraffin-Chain Salts", Hermann, Paris, France, 1936.
(22) K. J. Mysels and P. Mukerjee, paper presented at the 169th National Meeting of the American Chemical Society, Philadelphia, Pa., 1975.

School of Pharmacy
University of Wisconsin
Madison, Wisconsin 53706
Pasupati Mukerjee*
Alex Y. S. Yang

Received December 8, 1975

The Low Apparent Permittivity of Adsorbed Water in Synthetic Zeolites

Publication costs assisted by the Naval Research Laboratory

Sir: Recent nuclear magnetic resonance studies have shown that the included water in synthetic zeolites is in many respects similar to the normal fluid, but with a viscosity 20-fold higher than that of the "bulk" variety.[1-3] In this study we report measurements of the relative dielectric permittivity of hydrated zeolites NaX and NaY over the frequency range 1–150 MHz; this range is too low at room temperature to include the dispersion region predicted for the included water from the NMR interpretation yet high enough so that the dispersion frequencies from Maxwell–Wagner[4] and ionic effects[4] are exceeded. We thus are able to estimate the upper limit to the magnitude of the zero frequency dielectric constant for the included water to be 14 for NaX and 21 for NaY. This apparently is an extreme example of the well-known ability of ions to depress the dielectric constant of water.[5,6] In effect, we have extended previous studies on the dielectric permittivity of concentrated electrolyte solutions to the very high concentrations (ca. 18 M) of mobile Na^+ ions present in the hydrated crystals.

The composition of zeolites NaX and NaY are described by the formulas:[7] $Na_{86}[(AlO_2)_{86}(SiO_2)_{106}] \cdot 264H_2O$ (NaX) and $Na_{56}[(AlO_2)_{56}(SiO_2)_{136}] \cdot 264H_2O$ (NaY). Their crystal structure consists of an open framework of aluminate and silicate tetrahedra enclosing interstitial voids of approximately 13 Å diameter. Negative charges in the lattice resulting from the substitution of Si^{4+} by Al^{3+} reside on lattice oxygen atoms, and are neutralized by Na^+ counterions which, in the fully hydrated crystal, float about in the interstitial voids.

A previous NMR study of H_2O and D_2O[3] adsorbed in NaX has shown that (1) the rotational and translational correlation times of the interstitial water molecules are equal and are about twenty times longer than those of bulk water molecules; and (2) the observed proton and deuteron relaxation times can be fit to theoretical expressions by assuming a relatively narrow distribution of correlation times (τ) of the form:

$$P(\tau)\,d\tau = (B\sqrt{\pi})\exp(-B^2z^2)\,dz$$

$$z = \ln(\tau/\tau^*)$$

$$\tau^* = \tau_0 \exp(A/(T - T_0))$$

$$B = \alpha(T - T_0)$$

where, for zeolite NaX, over the temperature range 250–450 K

$$\tau_0 = 1.86 \pm 0.6 \times 10^{-13}\ \text{s}$$

$$\alpha = 4.4 \pm 0.1 \times 10^{-3}\ \text{K}^{-1}$$

$$T_0 = 173 \pm 3\ \text{K}$$

$$A = 650 \pm 47\ \text{K}$$

(The quoted uncertainties are the standard errors in a least-square fit of the NMR data to theoretical expressions.) Observation (1) rules out the possibility of long-lived attachments ("binding") between the water and the lattice; (2) can be used to predict the water dipolar dielectric dispersion by integrating the Debye equations over this distribution (Figure 1a).[8] We assume the Debye correlation time (τ_D) to be given by the formula:

$$\tau_D = 3\tau^*$$

The rotational correlation time (and thus, the center frequency of the dielectric dispersion) of the interstitial water molecules is thus closely determined from the NMR data. Note that at room temperature the frequency range of this study does not include the dispersion region predicted by NMR; all data reported here at 100–150 MHz thus reflect

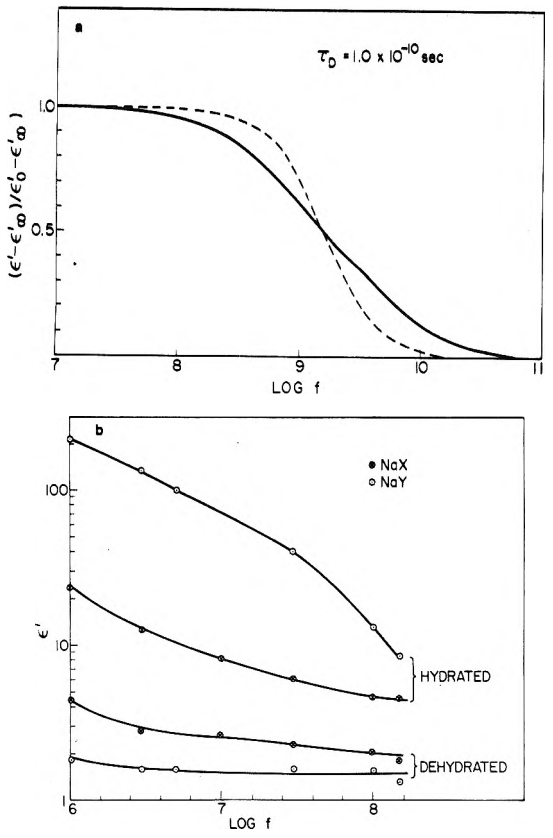

Figure 1. (a) (—) The anticipated dielectric dispersion of adsorbed water in zeolite NaX at 298 K, calculated from NMR data assuming the log normal distribution of correlation times given in the text. The dispersion resulting from a single rotational correlation time is given by (- - - -). (b) The observed permittivity ϵ' of zeolites NaX and NaY at 298 K.

TABLE I: Estimated Permittivity of Interstitial Water in Zeolites NaX and NaY (Linde) at 298 K

	NaX	NaY
Volume fraction, water	0.20	0.35
Volume fraction, dry zeolite	0.20	0.32
Measured permittivity, hydrated zeolite	4.5	8.5
Measured permittivity, dehydrated zeolite	1.9	1.6
Estimated permittivity, interstitial water	14	21

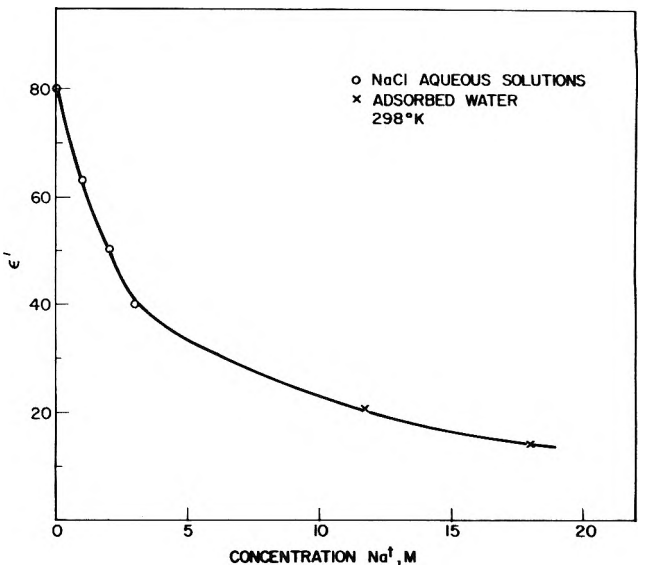

Figure 2. The observed dielectric permittivity of aqueous NaCl solutions from ref 6. Also shown is the calculated upper limit to the permittivity of the included water in zeolites NaX and NaY.

the low frequency dielectric constant of the adsorbed water.

A dielectric absorption peak has been observed[9] in hydrated NaX at 10 GHz (350 K), consistent with the NMR data. Jansen[4] reports a dielectric dispersion in hydrated NaX and NaY centered at frequencies between 1 kHz (205 K) and 6.7 MHz (260 K), attributed to interstitial water dipoles. At the lower temperatures his results are consistent with the NMR data; at higher temperatures, his estimated dispersion frequencies are an order of magnitude too low. These latter estimates are likely to be inaccurate, however, because of the limited frequency range of his measurements (<10 MHz) and the presence of several dielectric relaxation processes which overlap in frequency. While extensive NMR data on zeolite NaY are not available, its crystal structure is essentially the same as NaX; between 200 and 260 K the dipolar absorption which we attribute to water occurs at the same frequency in these two species.[4]

Samples of zeolites NaX and NaY were hydrated over saturated aqueous solutions of NaCl and packed by hand into the cup-shaped neutral terminal of a dielectric cell, described elsewhere.[10] The cell was designed to permit the sample to be removed without disturbing the powder. Capacitance measurements were performed with a Boonton RX meter and a Wayne-Kerr Model 601 impedance bridge, and corrected for the low residual inductance in the system. Samples were dehydrated by heating to 400 °C under a vacuum of 10^{-2} mmHg. The water content of the hydrated samples, as measured by weight loss during dehydration, agreed well with values calculated from the formulas given above.

Figure 1b shows the measured permittivity (ϵ') of the hydrated and dehydrated samples. Because of the lower powder density employed in this study (0.77 vs. 1.19 g/cm^3), the observed permittivities of NaX below 3 MHz are smaller by a factor of about 1.8 than those measured by another investigator.[11] The increase in permittivity at low frequencies is due to sample heterogeneity (the Maxwell–Wagner effect) and to the formation of electric dipoles by association between the mobile cations and the fixed anions in the lattice. From NMR data, the water dipolar absorption in NaX occurs at substantially higher frequencies than these other effects, at least at room temperature. This is evidently not quite the case with NaY.

The water dipolar absorption is surprisingly weak. The maximum possible change in permittivity resulting from this presumed dispersion is the difference between the permittivities of the hydrated and dehydrated samples, measured at 100 or 150 MHz. From these data, it is possible to estimate the maximum apparent permittivity of the interstitial water. We assume that the specific polarization, p, of the sample is additive:

$$p = v_{water}p_{water} + v_{lattice}p_{lattice}$$

where v_{water} or $v_{lattice}$ is the volume fraction of water or of dry zeolite in the powder. We also assume that the specific polarization is related to the permittivity by the Kirkwood expression:[12]

$$p = (\epsilon' - 1)(2\epsilon' + 1)/9\epsilon'$$

Although this formula is essentially empirical, it has been successfully used in other studies of adsorbed molecules,[12] and it predicts a bulk permittivity of 6.3 for dehydrated zeolite NaX, in good agreement with other estimates.[4]

Table I shows the results of these calculations. We find the maximum apparent permittivity of the interstitial water in NaX and NaY to be about 14 and 21, respectively, at 298 K. Assuming that the Na^+ cations are more strongly hydrated than either the lattice O^- charges (in the zeolite) or than simple anions (in bulk solution), our results can be compared to previous measurements of the permittivity of concentrated NaCl aqueous solutions (Figure 2). Although extensive association undoubtedly occurs between the lattice O^- ions and the mobile Na^+ counterions, most of the interstitial water molecules are probably located in the primary hydration spheres of these two ion species. Our results show that these water dipoles are "immobilized" (in the sense that their dipole moments do not contribute to the polarizability of the crystal), yet have rotational and translational "mobilities", estimated from NMR data, only twenty times lower than molecules in the bulk phase.

References and Notes

(1) H. A. Resing, *Adv. Mol. Relaxation Processes*, **3**, 199–266 (1972).
(2) H. A. Resing and J. S. Murday, *Adv. Chem. Ser.*, **No. 121**, 414–429 (1973).
(3) H. A. Resing, *J. Phys. Chem.*, **80**, 186 (1976).
(4) F. J. Jansen, Thesis, Katholieke Universiteit Leuven, Belgium, 1972; F. J. Jansen and R. A. Schoonheydt, *Adv. Chem. Ser.*, **No. 121**, 96–105 (1973).
(5) J. B. Hasted, D. M. Ritson, and C. H. Collie, *J. Chem. Phys.*, **16**, 1–21 (1948).
(6) J. A. Lane and J. A. Saxton, *Proc. R. Soc. London, Ser. A*, **214**, 531–545 (1952).
(7) D. W. Breck, *J. Chem. Educ.*, **41**, 678–687 (1964).
(8) N. E. Hill, Ed., "Dielectric Properties and Molecular Behaviour", Van Nostrand-Reinhold, New York, N.Y., 1969, p 56.
(9) V. K. Benzar and I. M. Rimkevitch, *J. Phys. Chem. USSR*, **47**, 435–436 (1973).
(10) C. T. O'Konski and A. Edwards, *Rev. Sci. Instrum.*, **39**, 1456–1458 (1968).
(11) R. A. Schoonheydt, personal communication.
(12) N. Hill, ref 8, p 427.

Armed Forces Radiobiology Research Institute
Bethesda, Maryland 20014
Kenneth R. Foster

Naval Research Laboratory
Washington, D.C. 20375
Henry A. Resing*

Received October 6, 1975

ADDITIONS AND CORRECTIONS

1975, Volume 79

Ira B. Goldberg, Harry R. Crowe, and Richard W. Franck: Peri Interactions in the Tetra-*tert*-butyl- and 1,3,8-Tri-*tert*-butylnaphthalene Anions. An Electron Spin Resonance Study.

Page 1744, Table III. The g factors of all of the naphthalene anions were based on the value of 2.002657 for the g factor of the perylene anion. The value of the g factor and $g - g_e$ for the naphthalene anion should be corrected to read 2.002736 and 0.417×10^{-3}, respectively.—Ira B. Goldberg

1975, Volume 79

J. L. Dye, C. W. Andrews, and S. E. Mathews: Strategies for the Preparation of Compounds of Alkali Metal Anions. Page 3068. Table IV has been revised as follows:

TABLE IV: Estimated Enthalpy Changes for Various Reaction Steps

Metal	M–M distance in metal, Å	Enthalpy change, kcal mol^{-1} (see Figure 2) ΔH_{vap}	ΔH_{ip}	ΔH_{ea}	ΔH_{le}	ΔH_F	Radius of cryptated cation, Å	$\Delta H°_{10}$, kcal mol^{-1}	$(\Delta H°_9 - \Delta H°_{9'})_{max}$, kcal mol^{-1}	$(\Delta H°_9 - \Delta H°_{9'})_{est}$, kcal mol^{-1}
Li	3.04	38.4	124.3	−14.3	−175.6	11.2	5.06	−74.2	−19.4	−22.2
Na	3.72	25.8	118.5	−12.6	−143.8	13.7	5.50	−67.6		
K	4.54	21.3	100.1	−11.6	−118.0	13.1	5.52	−64.4	21.5	14.9
Rb	4.95	19.5	96.3	−11.2	−108.3	15.8	5.53	−62.6	25.8	21.4
Cs	5.31	18.7	89.8	−10.9	−101.1	15.2	5.56	−61.3	30.4	37.6

—J. L. Dye

RARE GAS SOLIDS, Volume 1

edited by M. L. KLEIN and J. A. VENABLES

CONTENTS: *G. K. Horton.* Rare Gas Solids—Half a Century of Excitement and Progress. *R. J. Bell and I. J. Zucker,* Long Range Forces. *J. N. Murrell,* Short and Intermediate Range Forces. *J. A. Barker,* Interatomic Potentials for Inert Gases from Experimental Data. *N. R. Werthamer,* Self-Consistent Phonon Theory of Rare Gas Crystals. *M. L. Klein and T. R. Koehler,* Lattice Dynamics of the Rare Gas Solids. *H. R. Glyde,* Solid Helium. *U. Rössler,* Band Structure and Excitons. *K. F. Niebel and J. A. Venables,* The Crystal Structure Problem. Appendix A: Physical Constants, Units and Conversion Factors. Appendix B: Brillouin Zones and Band Structure Notation.

1976, 624 pp., $46.00/£25.30 ISBN: 0-12-413501-3

COLLOID FORMATION AND GROWTH

A Chemical Kinetics Approach

By JULIAN HEICKLEN

This book develops the science of colloid formation, growth, and removal from the viewpoint of chemical kinetics. It treats quantitatively the processes of homogeneous and heterogeneous nucleation, condensation, coagulation, vaporization, spontaneous fracture, diffusive loss, and gravitational settling. In some cases the book develops simplified easy-to-use approximate formulas for the various processes. The book features: complete and new derivation of all rate coefficients for all processes of consequence in colloid dynamics; exact treatment of small particles ($\lesssim$30 molecules); tables and figures of important results; discussion of theory of accommodation coefficients; review of previous work.

SECTION HEADINGS: Introduction. First-Order Physical Loss Processes. Bimolecular Processes. Thermodynamics and Reverse Reactions. Homogeneous Nucleation. Heterogeneous Nucleation. Accommodation Coefficients.

1976, 148 pp., $14.50/£8.00 ISBN: 0-12-336750-6

ADVANCES IN MAGNETIC RESONANCE

series editor: John S. Waugh

SUPPLEMENT 1/HIGH RESOLUTION NMR IN SOLIDS: Selective Averaging

By ULRICH HAEBERLEN

This book is addressed to all those wishing to understand thoroughly the principles of improving the spectral resolution in NMR. It will be invaluable to researchers in high resolution NMR in solids, and will also assist those interested in learning the physical and chemical information about matter which has resulted from "high resolution NMR in solids." Finally, it should appeal to the rapidly growing community of spectroscopists designing and applying experiments that are analogs to NMR experiments in the microwave and optical range of frequencies.

SECTION HEADINGS: Introduction. Nuclear Spin Hamiltonian. Manifestations of Nuclear Magnetic Shielding in NMR Spectra of Solids. Averaging in Ordinary Coordinate and Spin Spaces. Detailed Discussion of Multiple-Pulse Sequences Intended for High-Resolution NMR in Solids. Applications of Multiple-Pulse Techniques.

1976, 208 pp., $21.00/£11.55 ISBN: 0-12-025561-8

THE CHEMISTRY OF CYANO COMPLEXES OF THE TRANSITION METALS

by A. G. SHARPE

A Volume in *Organometallic Chemistry: A Series of Monographs*
series editors: P. Maitlis, F. G. A. Stone, and Robert West

This book is the first for many years to give a substantial account of the chemistry of complex cyanides of the transition metals. In a clear and authoritative review of the knowledge available on the subject, the author lays particular emphasis on recent investigations, but includes a summary of earlier research. In this comprehensive work, Dr. Sharpe discusses the advances that have been made and gives a balanced account of the preparation, the structures (excluding fine detail) and the chemical and physicochemical properties of cyano complexes.

1976, 314 pp., $25.75/£10.40 ISBN: 0-12-638450-9

THIRD REVISED AND ENLARGED EDITION

PROBLEMS IN QUANTUM MECHANICS

edited by D. TER HAAR

This collection of problems, most of which are provided with detailed solutions, can be used either in conjunction with any modern textbook, such as those by Schiff, Kramers, Landau and Lifshitz, Messiah, or Davydov, or independently as advanced reading by students familiar with the basic ideas of quantum mechanics from a more elementary textbook. For this new edition, the problems have been rearranged in a more logical order, further problems have been added to existing chapters and two new chapters, one dealing with many body problems and the density matrix, and one dealing with relativistic wave equations, have been added.

There are now 456 problems arranged in eleven chapters. The problems are of varying difficulty; some involve simple derivations or proofs, while for others the most advanced methods, both mathematical and physical, are needed. The emphasis throughout is on the building up of an understanding of the basic ideas of quantum mechanics and on the familiarization with the basic techniques.

1975, 472 pp., $19.50/£10.70 ISBN: 0-12-288656-9

N.B.: Postage plus 50¢ handling charge on all orders not accompanied by payment.
Prices subject to change without notice.

ACADEMIC PRESS
A Subsidiary of Harcourt Brace Jovanovich, Publishers
111 FIFTH AVENUE, NEW YORK, N.Y. 10003
24–28 OVAL ROAD, LONDON NW1 7DX

Now your J.T. Baker distributor can also ship you things he doesn't have!

How can your Baker distributor ship you things he doesn't have? Easy. He now can immediately contact the Baker Super Service Center and—in almost every instance—have the desired item shipped directly to you within 24 hours. *It's as though your J. T. Baker distributor has just added the largest reagent warehouse in the world to his backyard to serve you.* (To super-serve you.)

Now depend on your nearest Baker distributor for *all* of your laboratory reagent needs.

And do you have our new 428-page Catalog 750 featuring thousands of Baker quality laboratory chemicals? If not, please write. Thanks.

And, of course, J. T. Baker's Super Service is also available for...

NEW SPECIALLY-PURIFIED SPECTROPHOTOMETRIC SOLVENTS.

The J. T. Baker PHOTREX® line of high-quality spectrophotometric solvents has had 20 *new* additions:
Glycerol, Carbon Disulfide, Heptane, Methyl iso-Butyl Ketone, Reagent Alcohol (Denatured), Nitromethane, Pentane, Tetrachloroethylene, Methyl Ethyl Ketone, Plus 11 other new PHOTREX solvents.

Now the PHOTREX line numbers 35 superior solvents, all with the actual "lot analysis" on the label.

J.T.Baker®

J. T. Baker Chemical Co.,
222 Red School Lane,
Phillipsburg, N.J. 08865
201 859-5411